Study of Novae

Thesis Submitted for the Degree of

Doctor of Philosophy (Science)

in

Physics (Experimental)

By

Gesesew Reta Habtie

Department of Physics
University of Calcutta

2024

I dedicate this thesis to my parents;
Reta Habtie and Atalel Beyene.

Declaration

I, Gesesew R. Habtie hereby declare that this thesis titled, Study of Novae, and the work presented in it are carried out by me at S. N. Bose National Center for Basic Sciences under the supervision of Dr. Ramkrishna Das. Except where specific reference is made to the work of others, the contents of this dissertation are original and have not been submitted in whole or in part for consideration for any other degree or qualification in this, or any other university.

Gesesew Reta Habtie

2024

Dissemination

The work presented in this thesis was undertaken while the author was a TWAS-Bose research student under the supervision of Dr. Ramkrishna Das in the Department of Astrophysics & High-Energy Physics, S. N. Bose National Centre for Basic Sciences (SNBNCBS), affiliated to University of Calcutta. Portions of this work have appeared in the following papers (*):

1* **Habtie G. R.**, Das, R., Pandey R., Ashok N. M., Dubovsky P. A., (2024). Study of the fastest classical nova, V1674 Her: photoionization and morpho-kinemetic model analysis. MNRAS, 527, 1405 10.1093/mnras/stad3295.

2* **Habtie G. R.**, & Das, R. (2024). Spectroscopic study of the Quiescent Stages in between the 2006 and 2021 outbursts of RS Ophiuchi, (submitted), ArXiv. /abs/2402.03234.

3* **Habtie G. R.**, & Das, R. (2024). Optical Spectroscopy and Temporal evolution of Nova Cas 2021 (V1405 Cas), (Manuscript under preparation).

4 Pandey R., **Habtie G. R.**, Bandyopadhyay R., Das R., Teyssier F., Guarro Flo J., (2022a). Study of 2021 outburst of the recurrent nova RS Ophiuchi: Photoionization and morphokinematic modelling. MNRAS, 515, 4655 10.1093/mnras/stac2079.

Author also participated in the following discoveries reported on Astronomers Telegram;

1* **Habtie G. R.**, Das R., (2024). He II Emission Line Became the Most Intense Line in the Optical Spectrum of Nova V1405 Cas. Astron. Telegram, 16496, 1, https://ui.adsabs.harvard.edu/abs/2024ATel16496....1H.

2 **Habtie G. R.**, Das R., (2024). Optical Photometry and Spectroscopy of Nova Sco 2024 (V1723 Sco). Astron. Telegram, 16496, 1, https://ui.adsabs.harvard.edu/abs/2024ATel16454....1H.

Acknowledgements

First and foremost, I would like to thank my supervisor Dr. Ramkrishna Das for his invaluable guidance, support, and encouragement throughout the duration of my PhD studies. Dr. Ramkrishna Das has been a remarkable mentor, providing me with the intellectual freedom to explore my ideas while also offering insightful feedback and constructive criticism. His expertise, patience, and unwavering commitment to my academic and professional growth have been instrumental in the completion of this thesis. I count myself extremely fortunate to have worked under the supervision him. I thanks the members of my PhD research committee Professor Souman Mondal, Professor Sunandan Gangopadhyay and Dr. Tapas Baug for their insightful comments throughout my past evaluations. I am also immensely grateful to Prof. Archan Majumdar, my previous guide, for welcoming me to his group and for the freedom he gave me to follow my passion.

I acknowledge financial support from The World Academy of Sciences - TWAS and S. N. Bose National center for Basic Sciences, through the TWAS-BOSE PhD fellowship. My thanks to S. N. Bose National Center of Basic Sciences for hosting and providing me a very comfortable stay throughout my Ph.D.

My humble gratitude to the administration and staff of S.N. Bose National Center for the timely issuance of all the official papers I needed. My special thanks to Ms. Nibedita Konar for being there to help me from the beginning. I started communicating with her even before coming to India while starting the process of applying for my

visa. I received unwavering assistance from her for every problem I faced over the last 5+ years. I am extremely grateful for that. I am also thankful to Ms. Sara Dalafi of TWAS for being there from the beginning of my tenure, assisting me with any official requirements, and providing timely reminders for completing my tasks within the time frame.

Dr. Edwin Tendong, was the first good person I met at S.N. Bose as a friend. He remained my mentor and best friend until he completed his PhD and left. I am thankful for everything he did for me, from teaching me about life in India and resolving problems with my Python code or computer issues to sharing the hardest times during the pandemic. I had the best seniors: Dr. Ruchi Pandey and Dr. Rahul Bandyopadhyay. I have no words to express your kindness and willingness to help me on my PhD journey. I learned a lot from both of you, and I will remain grateful for that. I could not have survived without the immense love and support from my fellow graduate students and group members: Siddhartha Biswas, Subhajit Kar, Shashank Sarkhar Pandey, Rajib Kumbhakar, Dia Ram, Avijit Mondal, Ariful Hoque, Muhammad Usman Shehu, Dorothy Museo Mwanzia, Soumita Chakraborty, Aman Das, Nishant Gargi, Sk Sahil, Sudip Pramanik, and Avirup Chakraborty. I will remain in debt to all of you for the kindness you showed me throughout our time together. I would love to write more about the memories I shared with everyone, but time did not permit me. I am deeply grateful to my bay mates Dr. Sandip Saha, Dr. Rahul Karmakar, and Sagar Kumar Maity for being like family to me. Special thanks to all the friends who accompanied me for lunch, snacks, tea after snack, dinner, and tea after dinner. I can't imagine how dull my stay would have been without those gatherings. Those memories go beyond the food and tea we had together; they will remain in my heart forever. I also met many wonderful people outside of my department during my stay at S.N. Bose: Debatri Ghosh, Rajdip Biswas, Sreya Pal, Krishnendu Patra, Indrajit Ghose, Shivam Jani, and Ramesh Pramanik. Your kindness and greetings meant a lot to me, and I really appreciate it.

Last but not least, to my parents (Reta Habtie & Atalel Beyene): first of all, I want to apologize for leaving you alone for such a long time. Trust me, it wasn't my intention to do so; circumstances forced me to, and every day, every moment, I felt the pain of doing this to you. I appreciate your tolerance and patience. I promise that I won't do it again. I am deeply thankful to my elder brother Estifanos Reta for being a shoulder for me to lean on and for handling the problems back home, allowing me to focus on my work. I wouldn't have managed this achievement without you taking care of the family issues. Thank you for the love and support you always showed me. I am also thankful to my sisters Fikirte Reta, Kelem Reta, Gebeyanesh Reta, Aynalem Reta, my brother Dejen Reta, and their children for the excessive care, love, and trust in me, and for standing with me in every life struggle.

Abstract

Novae are transient astronomical events resulting from an eruption on the surface of an accreting white dwarf, caused by a thermonuclear runaway. These eruptions and their progenitors are ideal astronomical events/objects to study a variety of interesting topics, such as mass-transfer mechanisms, binary evolution, and thermonuclear and radiative emission processes. This thesis focuses on studying novae at different stages relative to their eruption dates; from eruption to post eruption. This research was undertaken mainly using spectroscopic and photometric observations, as well as photoionisation, and morphology-kinematic simulations. The three main results chapters in this thesis integrate the methods listed above to track the aging process of expanding nova shells and accretion disc. The first results chapter focuses on the spectral and photometric evolution of Nova Her 2021 (V1674 Her) from -0.0320 to 29 days relative to the discovery date. The spectral analysis revealed that nebular and coronal lines emerged on day +10.00 and +22, respectively, making it the earliest observed commencement for a classical nova to date, consistent with the photoionization model. This model provided estimates for the temperature and luminosity of the ionizing source, as well as the density, composition, and mass of the ejecta. The morpho-kinematic model determined the geometrical structure of the ejecta, including the inclination and position angle. The second results chapter focuses on the the quiescent phase of RS Oph between the 2006 and 2021 outbursts. The employed photoionization model showed a gradual increase in iron abundance in the accretion disk, while the helium abundance decreased. The

accretion rate, radius, mass, and density were estimated based on the photoionization model applied to seven epochs over approximately two years. The results indicated that the accretion rate is significantly higher as the nova approaches the next eruption compared to the initial stage of the quiescent phase. The third results chapter focuses on the the spectroscopic and photometric evolution analysis and modeling of the slowest Nova Cas 2021 (V1405 Cas) spectra in the first 1051 after outburst. Based on the photoionization modeling we estimated the temperature and luminosity of the source, as well as the density, abundances, and masses of the shell ejecta.

Table of contents

List of figures

List of tables

1 Introduction to Novae

Nova (Novae in plural) is a Latin term which is a short form of "stella nova (Stellae novae, in plural)", which is equivalent to a "new star". It refers to a sudden increase in the brightness of a star followed by a gradual decline to its original brightness. These events typically occur in binary star systems where a white dwarf, a remnant of a star like our Sun, accretes material from a companion star. As material accumulates on the surface of the white dwarf, it can trigger a runaway nuclear fusion reaction, releasing a burst of energy and causing a temporary increase in luminosity. Novae are one type among many other explosions which showed a sudden increase in brightness, such as Supernovae, Kilonovae, red nova, Millinova etc.

1. **Supernovae**: are violent explosions that occur when one of the stars in a close binary system is sufficiently massive and undergoes core-collapse. The result may be either a neutron star or a black hole orbiting the companion star (Carroll and Ostlie, 2017). These are the primary source of heavy elements, contributing significantly to the interstellar medium and the formation of new stellar systems.

2. **Kilonovae**: are rare but incredibly bright event resulting from the merger of two neutron stars or a neutron star with a black hole. These mergers release vast amounts of energy, including heavy elements like gold and platinum, into the universe (Gillanders et al., 2021). They are about 1000 times brighter than a typical novae (Zhu et al., 2021). These events are also linked to the

production of gravitational waves and gamma-ray bursts, making them significant for astrophysical research.

3. **Red novae**: are specific types of astronomical events where two stars in a binary system merge, resulting in a temporary increase in brightness that peaks in the red part of the spectrum. These are less energetic than standard supernovae but more luminous than regular novae (Molnar et al., 2017).

4. **Millinovae** : are smaller and less energetic than normal novae, and red novae, which involve merging stars in binary systems or other less common stellar interactions, resulting in a temporary increase in brightness.

This chapter presents a brief history of novae (Sec. 1.1), a detailed discussion of nova systems and eruption mechanisms (Sec. 1.2), the major classification schemes of novae (Sec. 1.3), the distribution of occurrences in the Milky Way galaxy and beyond (Sec. 1.4), the structure of the whole thesis (Sec. 1.6), and the scientific results within the thesis (Sec. 1.7).

1.1 Brief Historical Background of Novae

Since ancient times, Chinese astronomers documented "guest stars" that appeared for a few months before fading away, while in the West, they were referred to as "novae stellar" or "new stars". Even though the presence of novae discovered on the night sky long time ago, until 20^{th} century people barely know many things about them. For instance until twentieth century both novae and supernovae were considered as a same phenomenon, where it is completely different in reality. The typical modern understanding of nova was started in 1950s, with Schatzman (1951) discovery that ^{3}He triggers thermonuclear runaways and Walker (1954)'s identification of DQ Her as a binary system. Kraft (1963, 1964)'s articles showed binarity was common in cataclysmic variables (CVs)[1] and proposed explosive hydrogen burning on the surface

[1]CVs are binary star systems characterized by a primary star and a secondary star filling its Roche lobe. The white dwarf accretes hydrogen-rich material coming from the secondary star.

of degenerate stars. Paczyński (1965) revived this idea. Most of the theoretical research before 1950 are now seen as outdated. A major revolution occurred from 1985 onwards, when astronomers started observing novae in multiple wavelengths, such as UV, IR, radio, X-rays, and γ-rays (Cassatella et al., 1985; Das et al., 2006b; Diesing et al., 2023; Evans et al., 1988; Mason et al., 1987; Padin et al., 1985).

1.2 The Nova System

Novae are a close interacting binary systems consisting of a primary and a secondary star. They belongs to the non-magnetic class of CVs[2]. The primary star is a hot degenerate white dwarf, whereas the secondary star is typically a main-sequence star or a red giant.

1.2.1 The Primary Star; White dwarf

A white dwarf is the remnant core of a Sun-like star (with a mass of M $\leqslant$ 8 - 10 $M_{\odot}$) that has exhausted its nuclear fuel and shed its outer layers. These stars spend the majority of their lifetimes on the main sequence stage of the Hertzsprung-Russell (HR) Diagram (see Fig. 1.2), where they burn hydrogen in their cores into helium. When the core hydrogen is depleted, the star's size increases dramatically, turning it into a red giant (RG). During this phase, the required conditions for the nuclear fusion of helium into heavier elements such as carbon, nitrogen, oxygen, and even neon and magnesium are established, with a temperature around $\sim$ 10^8 K and a density of approximately $\sim 10^6$ kg m^{-3}. Eventually, most of the H is burned into He and heavier elements, depleting the star's nuclear fuel. After the core's nuclear reactions cease, the remaining energy is released, and over the following billion years, the core cools.

The white dwarf (WD) is among the densest objects in the universe, surpassed only by black holes and neutron stars. It possesses a mass similar to that of the Sun

[2]Non-magnetic cataclysmic variables (CVs) are a type of close binary star system where a WD accretes matter from a secondary star. Unlike their magnetic counterparts, non-magnetic CVs lack strong magnetic fields that influence the accretion process.

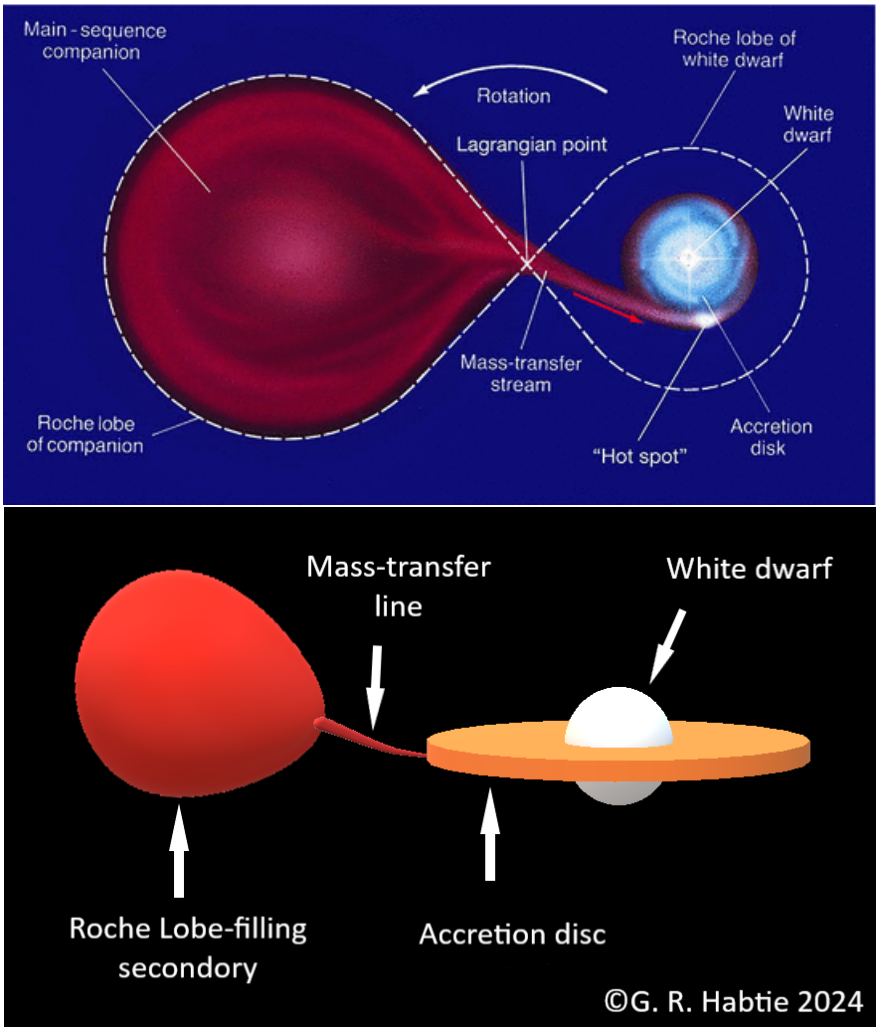

Fig. 1.1 Top: A schematic diagram depicting a pole-on view of a non-magnetic CV system (Credit: Pearson Prentice Hall, Inc. 2005). Bottom: A schematic diagram depicting an edge-on view of a non-magnetic CV system.

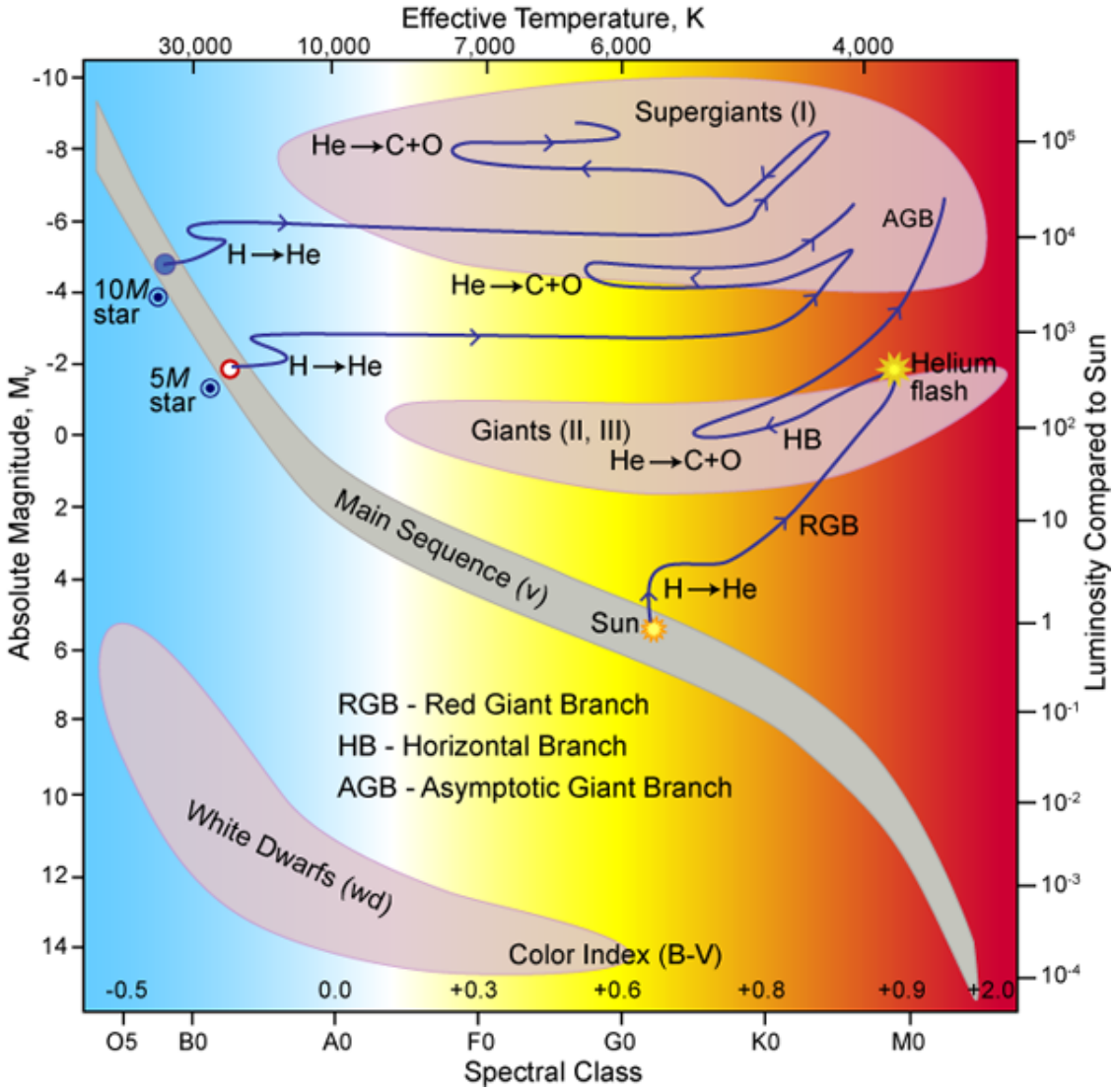

Fig. 1.2 Hertzsprung-Russell Diagram illustrating the evolution paths of a sun-like star. Credit: Carin Cain.

and a size comparable to that of the Earth. The WD remains stable due to electron degeneracy pressure, which prevents it from collapsing under its own immense gravity. In such high-density conditions, similar to the WD core, matter is prevented from further contraction because electrons cannot share the same set of quantum numbers, according to the Pauli exclusion principle. Since all of the lower energy levels are filled, electrons occupy higher energy levels as a result. Therefore, the gravitational energy of the WD is inadequate to cause further collapse or to convert protons and electrons into neutrons when its mass is below the Chandrasekhar limit (Koester and Chanmugam, 1990; Shapiro and Teukolsky, 1986).

White dwarfs are composed mainly of carbon and oxygen in their cores, with possible helium in less massive white dwarfs, as these elements are produced during the previous stages of stellar evolution. The composition depends largely on the mass of the progenitor star. For stars with an intermediate-mass, the nuclear fusion of heavy elements in the core halts at O , leading to the formation of a CO white dwarf (WD).

For intermediate-mass stars, nuclear fusion of heavy elements in the core halts at O , resulting in a CO white dwarf. However, for more massive stars (M $\leqslant$ 8 - 10 $M_{\odot}$), nuclear fusion can proceed after O as well to form heavier elements such as Neon and Magnesium, leading to the formation of an ONe WD. This indicates that the mass of an ONe WD ($M_{WD} > 1.1$ - 1.3 $M_{\odot}$) is greater than that of a CO WD ($M_{WD} \leqslant 1.2$ $M_{\odot}$) (Doherty et al., 2015; Gehrz et al., 1998; Iben and Tutukov, 1989; Weidemann, 2000).

White dwarf radius

A WD's gravitational energy and electron kinetic energy determine its radius. Nauenberg (1972) established a relationship between a WD's mass (MWD) and radius (RWD), demonstrating that the radius decreases as the mass increases:

$$R_{\mathrm{WD}} \approx 1.12 \times 10^{-2} \left[\left(\frac{M_{\mathrm{WD}}}{M_{ch}} \right)^{-2/3} - \left(\frac{M_{\mathrm{WD}}}{M_{ch}} \right)^{2/3} \right]^{1/2} R_{\odot}. \tag{1.1}$$

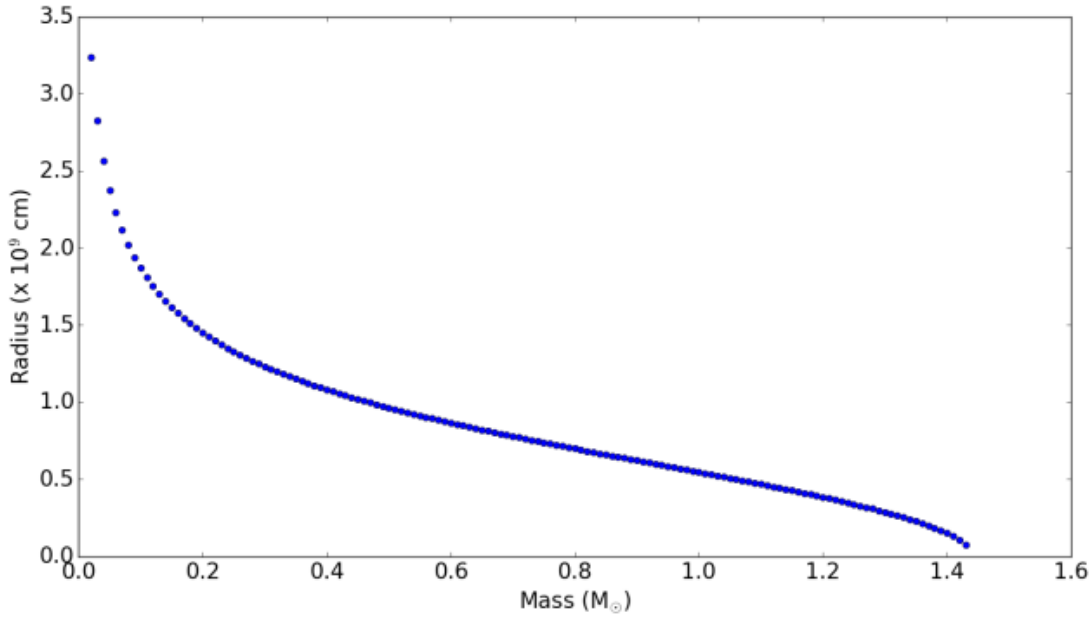

Fig. 1.3 An illustration for the relation between the WD mass and radius Nauenberg (1972).

This shows that the radius decreases with increasing mass and approaches zero as the WD mass gets closer to the Chandrasekhar limit (Fig. 1.3).

1.2.2 The Secondary Star

The secondary stars in novae could potentially be either main-sequence (MS) stars or red giant (RG) stars. The secondary in most CVs is on the main sequence because it evolves more slowly than the primary star, which is generally more massive at first. Systems with a more evolved secondary star, like an RG, feature strong stellar winds and are termed symbiotic systems, exhibiting different mass-transfer mechanisms compared to typical CVs . However, some of these systems can still experience nova eruptions. This is explained by the enormous mass of the white dwarf (WD) and the high mass-transfer rate onto the WD from the developed secondary. According to the evolutionary state of the secondary star, Darnley et al. (2012) proposed a new classification scheme for novae, which includes three types: RG-Nova (red giant secondary star), SG-Nova (sub-giant secondary star), and MS-Nova (main-sequence

secondary star). The radius of the secondary star could be given by:

$$R_{sec} = \frac{2a}{3^{4/3}} \left(\frac{q}{1+q} \right)^{1/3} \tag{1.2}$$

where a represents the separation between the binaries and q represents the ratio of the binary masses ($M_{\rm sec}/M_{\rm WD}$).

1.2.3 Accretion disc

Novae undergoes mass transfer from the secondary to the primary star, this matter of a hot gas will have sufficient angular momentum to form an accretion disc around the primary WD. Viscosity, which acts as internal friction, transforms the directed kinetic energy of the moving gas mass into random thermal motion. This process results in the orbiting gases losing energy and gradually spiraling inward toward the primary object. Studies show that this accretion results in a growing layer of hydrogen-rich gas on the WD surface (Starrfield et al., 2008).

1.2.4 Mass transfer mechanisms

1.2.4.1 Roche Lobe OverFlow (RLOF)

Within binary star systems, the combination of the primary and secondary stars produces the crucial equipotential surface, which includes the Roche lobe. In binary star systems, the Roche lobe is a part of the critical equipotential surface formed by the primary and secondary (see Fig. 1.4). The equipotential surface is given by eq. 1.3. Any material located outside or on the surface of this region will either escape the system entirely, orbit around it, or be drawn to the binary companion, depending on its initial position and momentum. Consequently, when the secondary star fills its Roche lobe, any material that escapes through the inner Lagrangian point (L_1) will fall onto the surface of the WD.(Lamers and Levesque, 2017; Warner, 1995).

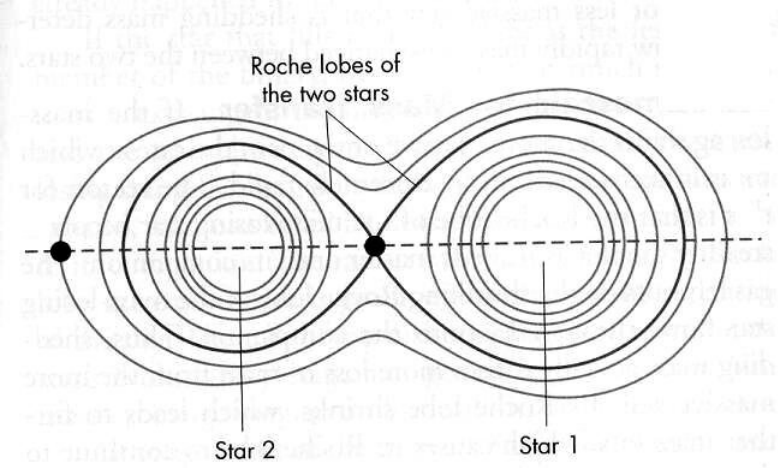

Fig. 1.4 The Roche lobe and equipotential surface of the binary system. The WD and companion stars are designated by star 1 and star 2 respectively. Adopted from: (Fix, 2001).

$$\Phi_R(r) = \frac{GM_{WD}}{|r - r_1|} - \frac{GM_{sec}}{|r - r_2|} - \frac{1}{2}(\omega \times r)^2 \tag{1.3}$$

where the last term accounts for the centrifugal force arising from the binary's rotation, and $\omega = \frac{2\pi}{P}$ denotes the binary system's angular frequency. The structure of the equipotential surfaces is determined by the mass ratio q. Each star's "Roche lobe" is the area that surrounds it. At the L_1 point, where the gravitational forces of both stars in the binary system are balanced, RLOF occurs when a star fills its Roche lobe.

The fundamental model that describes the mass-transfer mechanism from the secondary to the primary star is Roche Lobe Overflow (RLOF). The secondary star may fill its Roche lobe either due to a reduction in the size of the Roche lobe or because of the secondary star's expansion as it evolves off the main sequence. A decrease in orbital separation, which can occur for various reasons such as angular momentum loss, leads to a reduction in the Roche lobe's size (Linial and Sari, 2017; Warner, 1995).

After filling its Roche lobe, gas can escape from the atmosphere of the secondary into the Roche lobe of the primary (WD) through the L_1 point. Warner (1995) describes this flow as: "The flow resembles the escape of gas through a nozzle into a vacuum; the flow velocity is approximately the thermal velocity of the atoms in the gas". Because the

incoming gas has its angular momentum primarily in the plane, it forms an accretion disc in the orbital plane around the primary before hitting the WD's surface. Since the primary's gravitational potential predominantly affects the secondary, its influence on the disc is almost nonexistent. The particles' angular velocity is nearly Keplerian throughout much of the disc due to the conservation of angular momentum. Except at the disc's edge, where the conservation of angular momentum may necessitate an outward drift (see, e.g., Frank et al. (2002); Warner (1995)), the material inside the disc loses angular momentum due to factors like viscous shear and magnetic stresses. Consequently, it moves in towards the primary, where the material is accreted and accumulated on the WD's surface. The bright spot is the shock-heated, hot, and luminous region where the stream from the secondary meets the accretion disc's outer edge. As shown in Fig. 1.1, the energy emitted by the bright spot can match or even surpass that of the system's other components (primary, secondary, and disc).

1.2.4.2 Stellar Wind

In some close binaries, matter can transfer from the surface of the secondary to the primary star via solar wind, resulting in a nova eruption. AGB or RG stars, which are examples of secondary stars with powerful stellar winds (symbiotic systems; see, e.g., Starrfield et al. (2008)), may operate according to the stellar wind concept. In these systems, even when the secondary star's wind does not completely fill its Roche lobe, the WD still manages to accrete mass from it. The stellar wind model is the primary mass-transfer process in these systems, which often have higher orbital separations (Iben and Fujimoto, 2008). It is noteworthy, nonetheless, that in certain symbiotic systems, both mass-transfer mechanisms–RLOF and the stellar wind model–might be at work (Mikołajewska, 2012).

1.2.5 Nova Eruption mechanism: Thermonuclear runaway (TNR)

The white dwarf accretes material from its companion, mostly hydrogen. On the surface of the WD, a layer of unburnt hydrogen-rich gas ($\sim 10^{-4} - 10^{-6} M_{\odot}$) may accumulate, depending on the initial WD luminosity and the mass accretion rate onto the WD. The tremendous gravity of the WD compresses the bottom of this layer, which eventually becomes electron degenerate. In the case of degenerate matter, the pressure is temperature-independent, but the temperatures continue to climb with little to no expansion of these layers. The bottom of this layer reaches a temperature high enough to cause thermonuclear burning of the hydrogen at a critical pressure, (P_{crit}). This P_{crit} is related to the radius and mass of the accreted matter by the relation Fujimoto (1982);

$$P_{crit} = \frac{G M_{WD} M_{shell}}{4\pi R_{WD}^4} \tag{1.4}$$

where P_{crit} is in dynes cm^{-2} , $G = 6.67\times\ 10^{-8}$ dynes cm^{-2} , M$_{WD}$ and M$_{shell}$ are in grams, and R$_{WD}$ is in cm. When enough material accumulates on the surface of the white dwarf, satisfying the critical pressure and temperature at the bottom layer of the disc ($\sim 10^{15}$ N cm^{-2} and $\sim 7 \times 10^7$ K), triggering a thermonuclear runaway reaction (Starrfield et al., 2016; Truran and Livio, 1986). This reaction causes the temperature to surpass $\sim 7 \times 10^8$ K for a white dwarf of 0.6 $M_{\odot}$ and $\sim 4 \times 10^8$ K for white dwarfs with a mass closer to the Chandrasekhar limit (1.4 $M_{\odot}$) (Starrfield et al., 2016). This is followed by a violent explosion on the surface of the white dwarf, known as a nova eruption, resulting in a sudden and dramatic increase in brightness. . The eruption ejects a significant portion of the accreted matter into space as a shell ejecta. Following the eruption, the amplitude of the eruption ($A = m_{max} - m_{min}$) reaches $\sim$ 15 mag for the fastest novae and $\sim$ 7 mag for the slowest novae. The nova eruption can last for several weeks or months before gradually fading. Unlike supernovae, nova explosions do not destroy the white dwarf, allowing the process to repeat in the future by contributing a small percentage of mass gain to the white dwarf (approximately

10% of the accreted matter in every eruption) (Hachisu and Kato, 2000). This infers the gradual increase of WD mass with each outburst, and consequently, it may cross the Chandrasekhar limit of WD mass, resulting in a Type IA supernova. Therefore, the claim that novae are the progenitors of Type IA supernovae is valid.

1.2.5.1 Chain reaction

The cause of a nova eruption is a nuclear chain-reaction on the surface of the white dwarf. A thermonuclear runaway in a nova eruption is characterized by a chain reaction of nuclear fusion processes occurring on the surface of a white dwarf. This chain reaction is initiated when the white dwarf, part of a close binary system, accretes hydrogen-rich material from its companion star. Over time, this material forms an accretion layer on the white dwarf's surface, compressing and heating the underlying layers due to the intense gravitational field of the degenerate star. During the initial stages of accretion of matter onto WD, temperature at the base of the accreted layer reaches a few times 10^6 K. Near the bottom of the accreted layers, two mechanisms—the proton-proton chain reaction, which includes the pep reaction, and the CNO cycles—are activated by temperature increases, resulting in nuclear reactions. The reactions involved are: $p + e^- + p \longrightarrow d + \nu$ (where d is deuterium, e^- is an electron, p is a proton, and ν is a neutrino; see, for example, Hernanz (2005); Starrfield (1989)), and the CNO cycles (see Bahcall and May (1969); Schatzman (1958)). The temperature of the accreted material is raised by both nuclear processes and compressional heating until an eruption takes place.

When the accreted layers reach a temperature of approximately 10^6 K, the proton-proton chain reaction begins. In this process, two hydrogen nuclei (protons) fuse to form deuterium, with one of the protons converting into a neutron. This reaction releases two byproducts: a positron and a neutrino. Subsequently, the deuterium nucleus can capture another proton to form the helium isotope ^{3}He. This step is followed by one of three subsequent reactions that ultimately produce a $^4_2$He nucleus (Adelberger et al., 2011; Clayton, 1983). The total energy released in each cycle ranges between 20 and

30 MeV, and the rate of these reactions depends on the temperature, scaling as $\propto T^4$. Proton-proton chain reactions release energy, which raises the temperature. In the case of normal matter, this increase in temperature would typically lead to a rise in pressure, causing the material to expand and eventually cool. However, in degenerate matter, the pressure is dependent only on the density ($P \propto \rho^\gamma$, where P is the pressure, ρ is the density, and γ is the polytropic index). Thus, an increase in temperature does not result in an increase in pressure or expansion. Instead, it accelerates nuclear reactions, which can have uncontrollable consequences. The CNO cycles begin when the temperature reaches approximately 10^7 K, and at around 2×10^7 K, they become the primary energy release mechanism, replacing the proton-proton chain reactions.

The CNO cycles drive the later phases of the thermonuclear runaway (TNR) and the progression to the eruption's peak, even though proton-proton chain reactions are significant during the accretion phase of the eruption. In these reactions, CNO nuclei act as catalysts, allowing four hydrogen nuclei to be burned to produce a helium nucleus, releasing approximately 30 MeV of energy per cycle. Protons are captured by the heavy elements during these reactions, resulting in the formation of radioactive nuclei with half-lives of around 100 seconds. These radioactive nuclei subsequently decay via β^+-decay, releasing a significant amount of energy. The reactions in the CNO cycle are schematically shown in Fig. 1.5.

The envelope reaches full convection at $T \approx 10^8$ K, with a convective turnover timescale of about 100 seconds. This is comparable to the half-lives of the longest-lived unstable nuclei, which are transported to the surface by convection and deposit significant amounts of energy there. Depending on the enrichment, the energy generated at the surface by the decay of radioactive nuclei can exceed 10^{13} to 10^{15} erg s^{-1}. Simultaneously, convection brings new CNO nuclei to the high-temperature regions where they can undergo burning.

The longest-lived β^+-decay nuclei (^{13}N, ^{14}O, ^{15}O, and ^{17}F, with half-lives of 862 s, 102 s, 176 s, and 93 s, respectively) act as bottlenecks in the cycle, limiting the rate of nuclear energy generation at high temperatures ($T \geq 10^8$ K). At these temperatures,

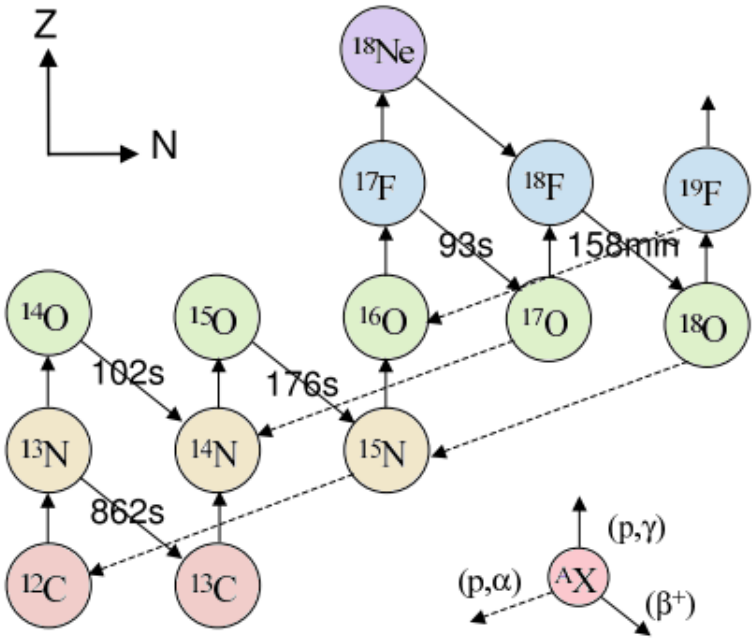

Fig. 1.5 Diagram showing the CNO cycle of hydrogen burning, which becomes out of equilibrium during nova explosions (Hernanz, 2005).

these nuclei become the most prevalent unstable nuclei in the envelope. CNO isotopes such as ^{13}C, ^{15}N, and ^{17}O are produced during these cycles. According to Hernanz (2005); Starrfield et al. (2008), novae are one of the primary sources of these isotopes in the Galaxy. The runaway continues until the temperature rises to a point where the gas pressure exceeds the degeneracy pressure. This causes the envelope (ejecta) to expand and relieves the degeneracy. The primary source of the envelope's expansion and the eruption's overall brightness is the energy deposited by the β^+-decay nuclei near the surface. The energy released by these radioactive nuclei is sufficient to match the observed luminosities ($\sim 10^5\ L_\odot$; see Starrfield (1989)) and expel material with expansion velocities similar to those observed (~ 1000 km s^{-1}).

This exponential increase in temperature and pressure due to the ongoing nuclear reactions leads to a violent explosion on the white dwarf's surface. The energy released in this explosion expels a significant portion of the accreted material into space, resulting in a dramatic and sudden increase in the star's brightness–a phenomenon known as a nova eruption. The chain reaction driving this process is a key aspect of

the thermonuclear runaway, illustrating the power of nuclear fusion under extreme conditions. These events do not destroy the white dwarf, allowing it to continue accreting material and potentially undergo future nova eruptions. The detailed study of these chain reactions provides critical insights into stellar evolution, nucleosynthesis, and the dynamic interactions within binary star systems.

1.2.6 Nova outburst observation

The fundamental features of the system can be inferred from the observed characteristics of the nova eruption. The following discussion outlines the evolution of novae and their observable properties at each stage of their optical development. As these concepts will be frequently referenced throughout this thesis, it is essential to have a basic understanding of these phenomena and the methods used to analyze them.

1.2.6.1 Optical light curve

The general morphology of the typical optical light curve of a nova outburst is presented in Figure 1.6. It is characterized by a sudden sharp increase in magnitude to the maximum $\sim$ 4 up to 9 mag for RNe and 8 up to 15 mag, followed by a rapid decline in brightness which is shown by the majority of novae. Various separate light-curve developments throughout the changeover period follow this. Eventually all the increased brightness will go away and return back to its initial brightness level until it starts the next accretion process and repeats the situation again.

The optical light curve of most CNe and RNe resembles at least on the general morphology given in Fig. 1.6. This light curve shows a typical common evolution characteristics pointed out as below;

(i) Rising phase: *initial rise, pre-maximum halt and final rise*

The nova undergoes several stages: the initial rise, the pre-maximum halt, and the final rise, until it reaches its peak brightness. The initial rise stage lasts for a brief period, typically not exceeding 2 or 3 days, even for slow novae. Following this is

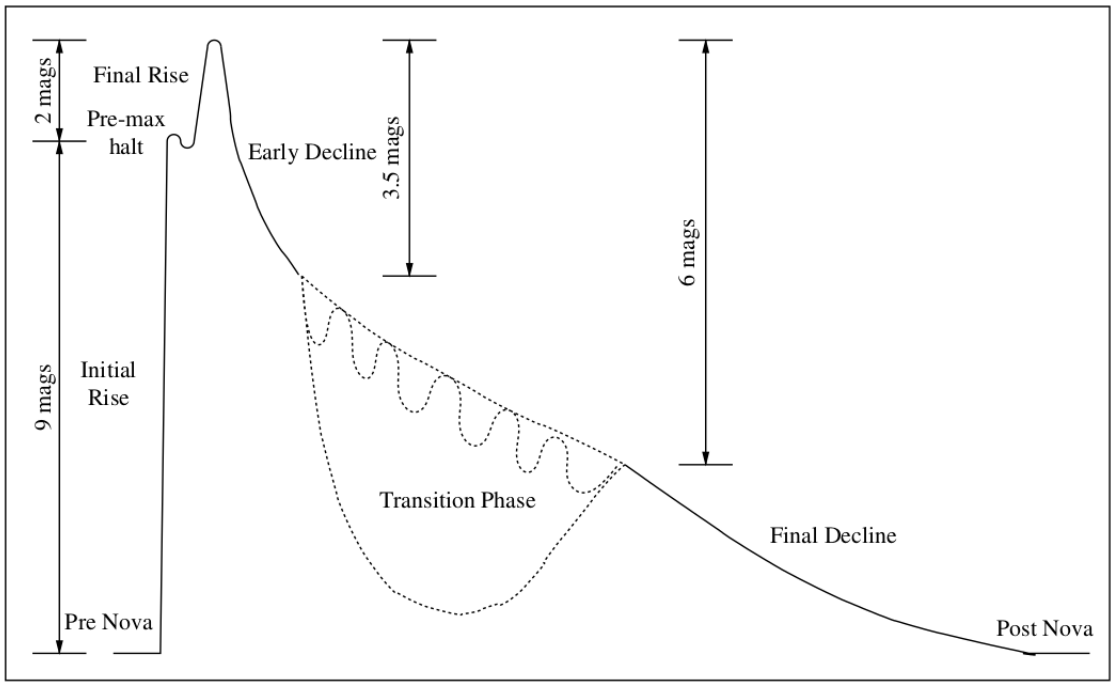

Fig. 1.6 Morphology of a nova light curve (Bode and Evans, 2008).

the pre-maximum halt, occurring about 2 magnitudes below the maximum brightness. During this stage, the brightness remains stable for a few hours in fast novae and for several days in slow novae. After the pre-maximum halt, the nova's brightness increases to its maximum. Fast novae reach their peak brightness in about a day, whereas slow novae may take several weeks or months.

(ii) Declining phase: *early decline, transition, and final decline phases*

The early decline phase starts within a few hours for fast novae and a few days for slow novae after reaching their maximum brightness, extending until the brightness has diminished by 3.5 mag. Although this phase is typically smooth, some novae, particularly the slower ones, show minor or significant irregularities. When the nova dims by approximately three magnitudes below maximum, it enters the "transition phase," the stage in the light curve evolution where novae display the greatest variety. During this phase, some novae exhibit large-scale quasi-periodic oscillations, while others transition smoothly without any distinct features. Some may even enter a deep

minimum phase lasting several months due to dust formation. After the transition phase concludes, the nova gradually declines to the post-nova phase.

1.2.6.2 Optical spectroscopic development

Most novae experience a consistent series of spectral evolution phases as they transition from the early outburst phase to the final quiescent phase. While the overall evolution of most novae—through the principal, diffuse-enhanced, and nebular stages—follows a similar pattern (Gaposchkin, 1957; Hack et al., 1993), there are notable variations in the specific emission properties of different objects. The evolution of the optical spectra of most novae during an outburst broadly follows the light curve evolution (McLaughlin, 1960). The correlated spectral and light curve evolution is summarized in Table 1.1.

After an outburst, the spectra of novae display signatures of expanding material. In the initial stages, the ionization of the ejecta is low, and the spectrum features permitted recombination emission lines. As the ejecta evolves, its density decreases and ionization increases, which is evidenced by the presence of forbidden and high-ionization emission lines. For a more detailed discussion on the spectral evolution of novae, please refer to McLaughlin (1943). In the following section, I will briefly discuss the evolution of nova ejecta spectra.

(i) Pre-maximum spectrum

The pre-maximum spectrum is observed when novae rise to their peak brightness. Slow novae, with spectra obtained during the pre-maximum halt, offer a better opportunity to study this stage (see Figure 1.6). This phase is characterized by a strong continuum and blue-shifted absorption lines, while emission lines are relatively weak. During this period, the nova's outburst involves the uniform expansion of an optically thick, cooling ejecta. The spectral line widths correspond to the expansion velocities, ranging from approximately -100 $\mathrm{km\,s^{-1}}$ for the slowest novae to around -1300 $\mathrm{km\,s^{-1}}$ for the

fastest novae. These pre-maximum spectra reflect the characteristics of a uniformly expanding, optically thick, cooling ejecta.

(ii) Principle spectrum

This phase, which occurs at 0.6 mag below maximum brightness, is characterized by strong absorption lines similar to those of supergiants of spectral types A to F, as well as increased CNO emission compared to the preceding phase. The speeds in this phase are higher than those observed earlier. The strongest emission lines include H , Ca II, Fe II, N , He , and O , and these lines emerge after the maximum. The early drop in brightness concludes with the development of the emission lines [O I] and [N II]. By the end of this phase, emission lines of [Fe II] and He II 4686 Å emerge. The average velocities of the absorption lines for slow novae are $\sim$ -150 $\mathrm{km\,s^{-1}}$, while the velocities are $\sim$ -1000 $\mathrm{km\,s^{-1}}$ for fast novae. According to McLaughlin (1960), ejecta velocities can be estimated using the following relationship:

$$\log \mathrm{V}_{ej}(\mathrm{km\,s^{-1}}) = 3.70 - 0.50 \log \mathrm{t}_3(d) = 3.57 - 0.50 \log \mathrm{t}_2(d) \tag{1.5}$$

(iii) Diffuse enhanced spectrum

The spectrum at this stage closely resembles the principal spectrum and occurs approximately one magnitude below the visual maximum. However, the speeds are twice as high as those in the principal spectrum. Depending on the speed class, this phase lasts from day 1 to day 20 following the outburst. The spectrum features metallic and hydrogen lines with blue-shifted absorption characteristics that are 1.5 to 2 times larger than those in the principal spectrum. These lines include Ca II, Mg II, O I, Fe II, and Na I. It is common for the broad absorption features to split into several distinct components in the later phases. The relationship described by McLaughlin (1960) can be used to determine the average velocities of the ejecta.

$$\log \mathrm{V}_{ej}(\mathrm{km\,s^{-1}}) = 3.81 - 0.41 \log \mathrm{t}_3(d) = 3.71 - 0.40 \log \mathrm{t}_2(d) \tag{1.6}$$

(iv) Orion spectrum

This phase occurs at approximately 2-4 magnitudes below maximum brightness and is characterized by highly blue-shifted absorption lines and emission lines of O I, He I, C II, N II, and H I. In the later stages, emission lines of N III and N V also appear in the spectrum. This phase is named due to its similarity to the stellar wind absorption lines seen in luminous OB stars. The absorption lines are blue-shifted between -2700 and -1000 $\mathrm{km\,s^{-1}}$, depending on the speed class, while the emission lines are broad and diffuse. Additionally, the Orion spectrum, both in emission and absorption, occasionally exhibits sudden changes in line strength.

(v) Nebular spectrum

This phase becomes appears at approximately 7 mag below the optical maximum. At this stage, intense ionization lines are produced. The expansion of the photosphere causes the density in the nova ejecta to decrease and the spectra to shift towards nebular characteristics. Alongside lines from the principal spectrum, broad forbidden emission lines of [O I], Ne V, Ne III, [N II], and O III dominate this phase. Apart from differences in the spectral composition and broader emission lines, the spectrum during this phase is quite similar to that of a planetary nebula. If the temperature of the ionizing radiation exceeds 10^6 K, coronal lines, including up to [Fe IV], will eventually appear.

(v) Post-nova / quiescence spectrum

This phase occurs a few years to decades after the outburst, when the ejected shell becomes spatially resolvable. The emission lines typically arise from the expanding ejected shell, while the continuum is mainly from the central ionizing white dwarf. As the nebula fades, the post-nova spectrum primarily displays permitted recombination lines of H , He , C , N , and O , along with [N III] and prominent Balmer continuum emission (Bode and Evans, 2008).

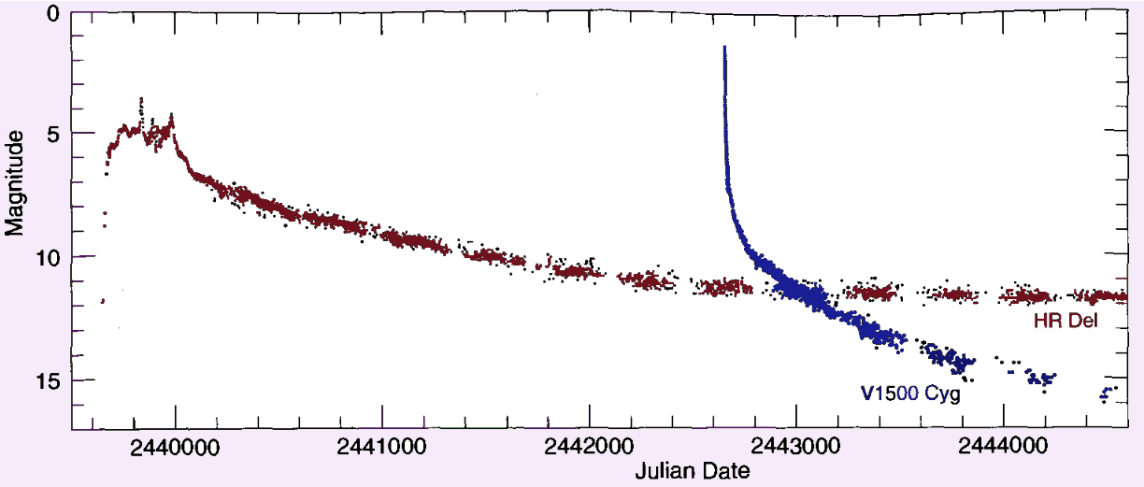

Fig. 1.7 Light curves of HR Del (Nova Del 1967) and V1500 Cyg (Nova Cyg 1975), illustrating the range from slow to fast novae (Hellier, 2001).

Table 1.1 Correlated spectral and light curve phases. Adopted from McLaughlin (1943).

Absorption system	Emission system	Duration,magnitudes from maximum	Part of light curve
Pre-maximum	Pre-maximum	-	Rise (decline)
Principal	principal	0.6 to 4.1	Early decline
Diffuse enhanced	Diffuse enhanced	1.2 to 3.0	Early decline
Orion	Orion(hazy bands)	2.1 to 3.3	Early decline
Nitrogen(Orion)	'4640' (Orion)	3 to 4.5	Transition
-	Nebular(principal)	4 to 11	Transition-final decline
-	Post-nova narrow stellar emissions	8 to min.	Final decline and post nova

In Chapters 4 and 5, I present examples of most of the aforementioned spectral phases. Chapter 4, Section 6.3.2 covers the stages from pre-maximum to coronal phase. In Chapter 5, Section 5.3, I provide several spectra from the quiescent phase of RS Oph.

1.2.6.3 Distance

For several decades, novae have been used as standard candles to measure the distances of galactic and extragalactic objects based an empirical relationship known as the Maximum-Magnitude-Rate of Decline (MMRD) relationship (see Fig. 1.8), Cao et al.

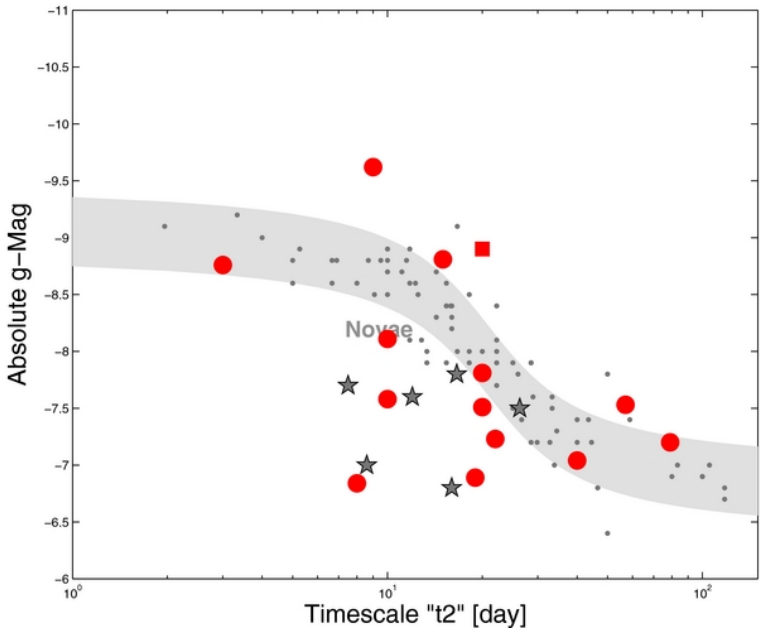

Fig. 1.8 The figure illustrates the MMRD empirical relation. The MMRD from della Valle and Livio (1995) is represented by the grey area, with their nova sample indicated by small, solid dark grey dots. The sample of feeble, rapid novae from Kasliwal et al. (2011) is represented by six grey stars. M31 novae from Cao et al. (2012) are shown by red circles and a red rectangle, while the brilliant recurrent nova M31N 2010-12a is marked by a red square.

(2012). This method was first proposed by Zwicky (1936) and subsequently refined by (Cao et al., 2012; della Valle and Livio, 1995; McLaughlin, 1939a; Mclaughlin, 1945). In Chapter 4 of this thesis, I used this method to estimate the distance of Nova Her 2021 (V1674 Her) (see Sec. 6.3.1.1).

1.2.6.4 Nova shell

Fundamental properties of the central binary system can be obtained by analyzing nova shells. One of the most significant applications of this analysis is the ability to calculate the distance to the system using the derived parameters. The following formula can be used to estimate the angular size of an expanding nova shell (Warner, 1995):

$$\Theta_r(t) = 0''.207 \frac{v_{exp}}{10^3\,\mathrm{km\,s^{-1}}} \frac{(t-t_0)}{d(\mathrm{Kpc})} \tag{1.7}$$

where, Θ_r is the angular radius, $(t - t_0)$ is the time elapsed in years, d is the distance in kpc, and v_{exp} is the expansion velocity in $\mathrm{km\,s^{-1}}$. One can determine when a nova shell will be resolvable using equation 1.7. The expansion parallax method, used across at least two epochs as in Harrison et al. (2013), is the most robust way to determine distances to novae.

Spectroscopic analysis provides details on the ionization structure and velocity of nova shell remnants. Long-established and fruitful in its application, imaging and spectroscopic observations have been utilized to infer the structure of nova shells (e.g., Hutchings et al. (1972); Lynch et al. (2006); Ribeiro et al. (2009, 2013)).

Expansion Velocity and Geometry of the ejecta

Using the Doppler shift relation, the expansion velocity of the ejecta (v_{exp}) can be measured from the spectral line-width:

$$V_{exp} = \left(\frac{FWHM}{\lambda_{\mathrm{centeral}}}\right) \times c, \tag{1.8}$$

where, c, the speed of light, $\sim 3 \times 10^5$ $\mathrm{km\,s^{-1}}$ and FWHM is the full width at half maxima of the spectral line at the central wavelength ($\lambda_{\mathrm{centeral}}$). The distinctive geometry of the ejecta can be discerned from the structure of individual emission line profiles during the optically thin period. The profiles of the emission peaks reveal the wind's direction and velocity. Additionally, the absorption line characteristics during the Fe-curtain phase, which occur well before the emission lines appear, also indicate the system's geometrical structure.

Shell ejecta elemental abundance

Observations have shown that nova ejecta are significantly enriched in metals (Bode and Evans, 2008). This enrichment is likely due to the mixing of accreted material with the white dwarf's core envelope before the final stages of the thermonuclear runaway (TNR) (see e.g., José (2012); Livio and Truran (1994)). Several mechanisms have been proposed

to explain this mixing, including one-dimensional models of diffusion-induced mixing, shear mixing at the disk-envelope interface, and convective overshoot-induced flame propagation. Additionally, two-dimensional models involving gravity wave breaking on the WD's surface and three-dimensional models of Kelvin-Helmholtz instabilities at the core-envelope interface have been suggested (see e.g., José (2012) and references therein). Consequently, the gases expelled during an outburst are a combination of WD material and accreted material from the secondary, processed by hot-hydrogen burning during TNR. The observed elemental abundance in nova ejecta is significantly influenced by the degree of thermonuclear processing during TNR and the composition of dredged-up matter from the underlying CO or ONe WD core. Therefore, accurately estimating the elemental abundances in nova ejecta after an outburst is crucial for understanding the causes and development of the nova outburst.

1.2.7 Nova at quiescent

During an outburst, only about 10-50% of the accreted hydrogen layer is ejected from the system. According to the TNR model, only a portion of the ejected envelope reaches velocities greater than the escape velocity as the nova evolves. The remaining expelled material, moving at speeds below the escape velocity, settles back into a quasi-static equilibrium and envelops the white dwarf (WD). This envelope undergoes nuclear reactions, causing the radius of the stellar photosphere to decrease while maintaining constant luminosity. The white dwarf's residual mass gradually decreases due to continuous mass loss from the wind. Once the WD exhausts its fuel, the hydrostatic burning phase slows, and the white dwarf begins to cool. The binary system eventually returns to a dormant state, marking the post-outburst or quiescence phase of nova evolution. During this phase, the system's brightness declines, and it reverts to its prior conditions, with the accretion process resuming in preparation for the next outburst. The nova spectra during the quiescence phase exhibit pronounced absorption features from the secondary companion and emission lines from the colder, outer region of

the accretion disc. These spectra can be used to reveal the nature of the secondary companion, study the physics of the accretion disc, and more .

1.3 Classifications of nova

Classifying novae from various perspectives allows astronomers to identify behavioral patterns and examine their evolutionary stages, as predicting these astronomical events is particularly challenging. Understanding these classifications helps in forecasting future eruptions and contributes to research on the chemical enrichment of the interstellar medium by nova ejecta. The following sections discuss the different classes of novae based on various criteria.

1.3.1 Based on recurrence period and eruption mechanism

1.3.1.1 Classical Novae (CNe)

Classical novae (CNe) are novae with one recorded outburst and are expected to erupt every 10,000 to 100,000 years. These outbursts are caused by thermonuclear runaways (TNR) on the surface of the white dwarf (WD). They exhibit a significant increase in brightness, ranging from 6 to 19 magnitudes, which is the difference between the pre-nova and nova outburst phases. This magnitude difference is primarily associated with the mass-transfer rate from the secondary star to the WD surface. CNe typically have relatively high WD masses, between 0.5 $M_\odot$ and 1.1 $M_\odot$, and accretion rates of approximately 10^{-9} to 10^{-10} $M_\odot$ yr^{-1} (Warner, 1995). This thesis includes a detailed investigation of the fastest classical nova, V1674 Her, in Chapter 4, and one of the slowest classical novae, V1405 Cas, in Chapter 6.

1.3.1.2 Recurrent Novae (RNe)

Recurrent novae (RNe) are a type of novae that have been observed to erupt multiple times, with a short recurrence period of approximately 10 to 100 years. These outbursts

are triggered by thermonuclear runaways (TNR) on the surface of the white dwarf (WD). The rapid recurrence of these novae is due to the high mass of the WDs, typically greater than 1.3 $M_\odot$, and correspondingly high mass transfer rates of up to $\dot{M} = 10^{-7}$ $M_\odot$ yr^{-1} . This means that it takes only a short time for enough matter to accumulate on the massive primary WD to trigger another TNR. The key differences between RNe and CNe are the presence of a massive WD close to the Chandrasekhar limit and a high mass accretion rate. RNe are essentially previously recognized CNe that show multiple outbursts within a short recurrence period. When a system is observed erupting more than once, it is classified as a recurrent nova. Due to the massive primary WD and often recurrence, RNe could be potential progenitors of Type Ia supernovae.

Recurrent novae are categorized into three groups based on the type of companion star (Kato and Hachisu, 2012):

i. **Slightly evolved MS stars:** CI Aql, V394 CrA, V2487 Oph, and U Sco.

ii. **Red-giant stars:** T CrB, RS Oph, V745 Sco, and V3890 Sgr.

iii. **Red dwarf stars:** IM Nor and T Pyx.

Among these, RNe with red-giant star companions are called symbiotic novae. These typically have a high WD mass and a quick recurrence period. Chapter 5 of this thesis presents a detailed investigation of one of the most famous symbiotic novae, RS Oph, during its quiescence period between the 2006 and 2021 outbursts.

1.3.1.3 Dwarf Novae (DNe)

Dwarf novae are eruptive variable stars that exhibit repeated outbursts with amplitudes of 2-5 magnitudes and typical recurrence times ranging from a few weeks to months (Osaki, 1997). Unlike CNe or RNe, DNe have a different underlying mechanism for their significantly weaker flares. The outbursts are thought to result from an instability in the accretion disc that abruptly pushes material onto the white dwarf's surface. This disc instability model, first proposed by Osaki (1997), suggests that fluctuations

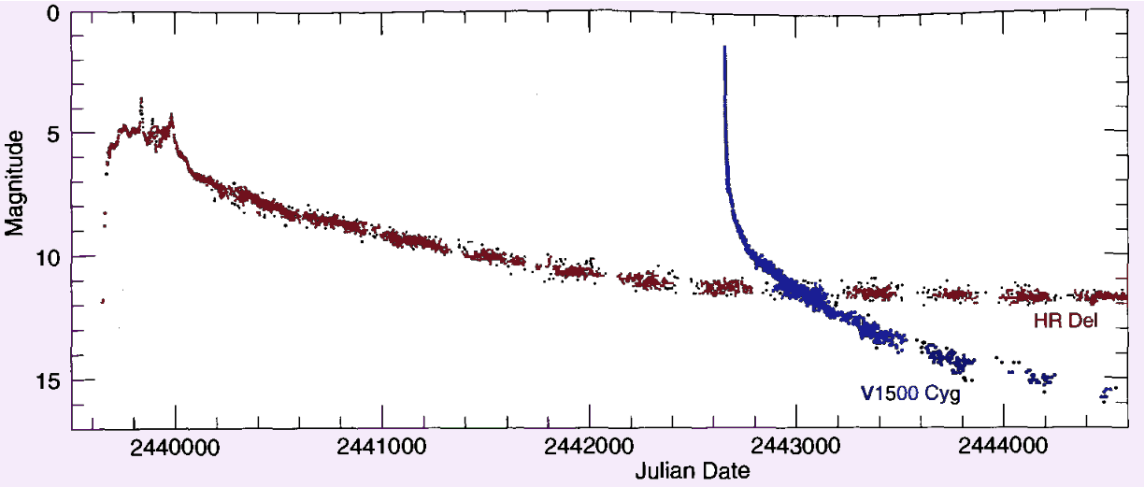

Fig. 1.9 Light curves of HR Del (Nova Del 1967) and V1500 Cyg (Nova Cyg 1975), illustrating the differences in light curve between the typical slow and fast novae (Hellier, 2001).

in the disc material's opacity and viscosity near the hydrogen photo-ionization point cause the instability, leading to a sudden increase in the accretion rate and resulting in the explosions observed in dwarf novae.

1.3.2 Based on speed class of the light Curve

Classifying novae into different subgroups based on the speed class has been started by Gerasimovic (1936). This classification grouped all novae in to two groups; *slow novae* and *flashing novae*. Fig. 1.9 illustrates the typical declining speed differences of the nova classified as very slow (HR Del; Nova Del 1967) and very fast (V1500 Cyg; Nova Cyg 1975) novae. The grouping was made based on evaluating the light curve of 18 galactic novae. But later on a serious of refinement have been done on this classification (see Table 1.2 for the complete series's of refinement through time). All the up-came classifications used the characteristics time to t_n which represents the the number of days that the nova takes to fall n magnitudes from the maximum. Therefore, t_2 and t_3 represent the number of days until the maximum magnitude decreases by 2 and 3 respectively (Bertaud, 1951; Gaposchkin, 1957; McLaughlin, 1939b; Mclaughlin, 1945).

Strope et al. (2010) presented an alternative method for categorizing novae based on the shape of their light curves during the transition phase and decline from

Table 1.2 Light curve based classification of novae. Adopted from Bode and Evans (2008).

Speed class	t_2	t_3	References
Flashing			Gerasimovic (1936)
Slow			
Fast	<29	<49	McLaughlin (1939b)
Average	30 - 49	50 - 84	
Slow	50 - 299	85 - 499	
RT Ser	>300	>500	
Very fast	<7	<15 (10)	Mclaughlin (1945)
Fast	8 - 24	15 -45 (30)	
Average	25 - 49	50 - 84 (60)	
Slow	50 - 250	85 - 449 (200)	
RT Ser	>570	>1000	
Rapid		<50	Bertaud (1951)
Lente		>50	
Very fast	<10	<20	Gaposchkin (1957)
Fast	11 - 25	21 - 49	
Moderately fast	26 - 80	50 - 140	
Slow	81 -150	141 - 264	
Very slow	151 - 250	265 - 440	

maximum brightness. They identified seven classes: P (plateau), D (dust dip), C (cusped secondary maximum), O (oscillations), F (flat-topped), J (jitters), and S (smooth), representing the classic nova light curves (see Table 1.3 for the defination and examples and Fig. 1.10 for a prototype of each class). Some novae exhibit a combination of these characteristics in their light curves and are categorized as uncommon. Theoretical modeling by Hillman et al. (2014) has demonstrated that varying the system's characteristics and attributes can produce a wide range of nova light curves.

1.3.3 Based on their spectra

The spectra of different novae exhibit significant diversity. Nevertheless, Williams (1992) organized them based on shared characteristics within this seemingly varied collection in an optical range. It has been observed that all novae spectra either display lines from Fe II or from He /N as the strongest non-Balmer lines in the early phases.

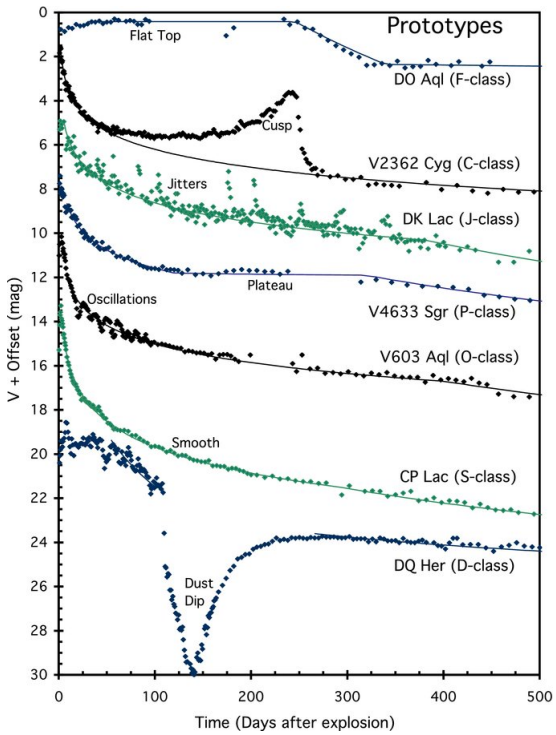

Fig. 1.10 The seven light-curve classes' prototypes from Strope et al. (2010). The binned light curves show the unique characteristics of every class.

Table 1.3 Definitions and Examples of Light Curve Classes. Adopted from Strope et al. (2010).

Class	Special feature	Example
S	Smooth	CP Lac, V1668 Cyg, V2275 Cyg
P	Plateau	V4633 Sgr, CP Pup, S Oph
D	Dust dip	DQ Her, FH Ser, V705 Cas
C	Cusp	V2362 Cyg, V1493 Aql, V2491 Cyg
O	Oscillations	V603 Aql GK Per, V1494 Aql
F	Flat topped	DO Aql, V849 Oph, BT Mon
J	Jitter	DK Lac, HR Del, V723 Cas

Definition: S–power-law decline with no major fluctuations; P–smooth decline interrupted by a long-lasting nearly flat interval followed by steeper decline; D–decline interrupted by fast decline, minimum, and recovery to just below original decline; C–power-law decline plus secondary maximum with steepening rise then steep decline; O–smooth decline with interval showing quasi-sinusoidal variations; F–smooth light curve with an extended interval at the peak with near constant brightness; and J–decline displays substantial variability often as short-duration brightenings.

Consequently, novae can be divided into two broad categories: the "Fe II" and the "He /N " classes (Williams, 1992). However, as will be discussed further, there are some novae that fall between these two classes, known as "hybrid" novae.

1.3.3.1 Fe II- type

The Fe II class of novae, which makes up about 60% of the total, is characterized by low ionization lines with the strongest non-Balmer lines being Fe II lines (see Figure 1.11). These novae display several low ionization Fe II lines along with CNO lines in the far red of the spectrum, excited by recombination and fluorescence scattering. The early spectrum is dominated by P Cygni absorption with velocities less than 2500 $\mathrm{km\,s^{-1}}$. Typically, Fe II novae are moderately fast and slow novae, with their spectra evolving over weeks. Some of the emission lines exhibit P Cygni profiles, indicating optically dense, expanding ejecta. The emission lines are narrow with rounded, peaked profiles. The expansion velocities of the ejecta spans between 1000 and 3500 $\mathrm{km\,s^{-1}}$. According to the spectra, these features are attributed to a substantial circumbinary gas envelope that originated from the secondary star (Williams, 1992). Additionally, early spectra show low ionization lines of Na I, Mg I, and Ca II.

1.3.3.2 He /N - type

The spectrum is dominated by the strongest non-Balmer lines, specifically helium (He I/He II) or nitrogen (N II/N III) lines (see Figure 1.11). It shows high ionization lines of He and N formed in the discrete shell of ejected gas. The P Cygni absorption is either weak or absent, and novae in the He /N class have higher excitation levels compared to the Fe II class. The spectrum features broad emission lines, indicating very high expansion velocities of the nova ejecta. Novae in this class are generally in fast and very fast speed classes, with their spectra evolving rapidly. The broad, flat-topped rectangular profiles with expansion velocities greater than 2500 $\mathrm{km\,s^{-1}}$ trace their origin to high-velocity, episodic ejection of gas (Williams, 1992).

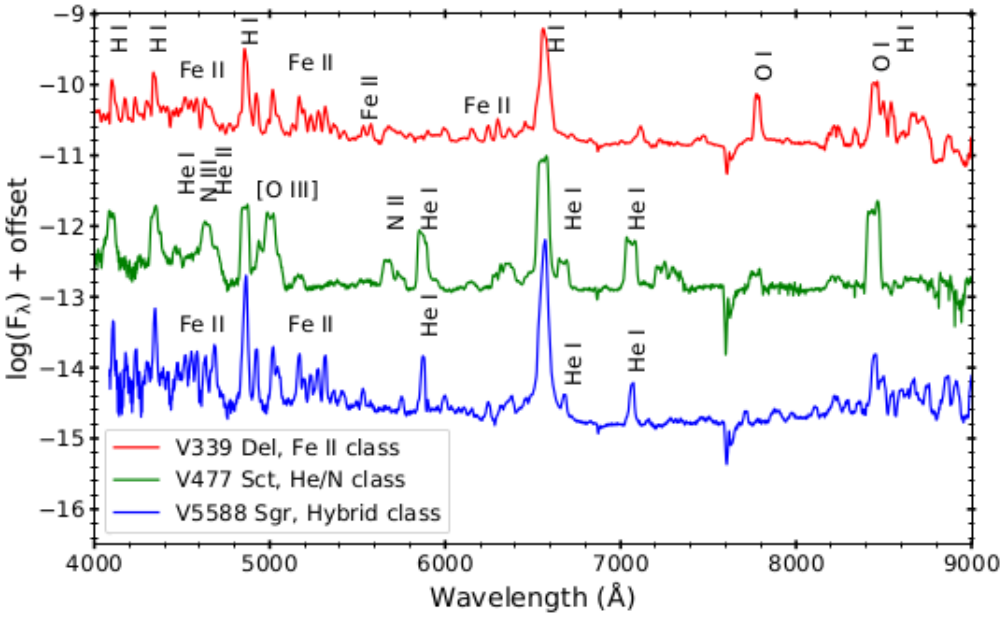

Fig. 1.11 Spectra of novae categorized into distinct spectral classes as indicated.

1.3.3.3 Hybrid type

These are nova systems whose spectral class changes from Fe II to He /N during the permitted lines phase, before the emergence of the forbidden lines (see Figure 1.11). The line-widths, in contrast to the Fe II class, suggest a faster expansion velocity. The line-profiles also show evidence for shell ejection as well as the ejection of matter through a weak wind. V5114 Sgr, a moderately fast nova with a smooth decline, is a notable example of a hybrid nova. In Chapter 4 of this thesis, we investigated the typical recent hybrid nova V1674 Her, which showed the quickest transformation from Fe II to He /N within just 10 days following the outburst.

1.3.4 Based on the WD

Novae can be further divided into two subtypes depending on the WD type.

1.3.4.1 CO - type

CO-type novae are outbursts that occur on the surface of low-mass carbon-oxygen (CO) white dwarfs (WDs). The vast majority of classical nova (CN) outbursts occur on CO WDs (Shore, 2012). However, only a small percentage of CO novae are known to produce a significant amount of dust following an outburst. CO nova outbursts fade more gradually than ONe novae because thermonuclear runaways (TNRs) on lighter WDs like CO WDs cause them to lose their envelopes and fade more slowly than those on heavier WDs (ONe type) (Shara et al., 2018). CO novae provide valuable insights into the synthesis of lighter elements and their rates of enrichment in the interstellar medium (ISM). Chapter 5 of this thesis is based on a thorough investigation on one of the CO nova, RS Oph.

1.3.4.2 ONe-type

ONe-type novae are outbursts that occur on the surface of massive oxygen-neon (ONe) white dwarfs (WDs). In contrast to CO novae, which have ejecta that evolve slowly with low expansion velocities, ONe novae exhibit quickly evolving ejecta with high expansion velocities. ONe novae accrete more massive envelopes than CO novae, leading to more violent outbursts due to higher degeneracy. This results in a partial extension of nuclear activity towards higher atomic number nuclei, due to the higher peak temperatures achieved in their envelopes. Novae with higher WD mass and faster ejection velocities release less mass ($\sim 10^{-6}$ to 10^{-5} $M_{\odot}$) compared to those with lower WD mass and slower speeds (Gehrz, 2008; Gehrz et al., 1998). Consequently, ONe novae eject smaller amounts of material than CO novae. Additionally, a massive WD requires comparatively less accreted matter to trigger a thermonuclear runaway (TNR) (Gehrz et al., 1998). ONe novae are crucial for understanding nucleosynthesis at high temperatures and contribute to the formation of heavier elements that play a significant role in the stellar lifecycle and the evolution of more massive stars. Chapter 4 and Chapter 6 of this thesis are based on thorough investigations of the ONe novae V1674 Her and V1405 Cas, respectively.

1.4 Distribution of Novae

1.4.1 Galactic Nova

The frequency of nova events in our galaxy is uncertain, as noted by Sharov (1972) and della Valle and Livio (1994). Mróz et al. (2015) measured a rate of 13.8 ± 2.6 yr^{-1} for the Galactic bulge alone. Figure 1.12 displays the Galactic distribution of novae brighter than m = 10 discovered since 1900, based on data from Shafter (2017), who estimates the Galactic nova rate to be between 50 and 100 per year. Shafter (2002) used the Bahcall and Soneira (1980) model for stellar density in the Milky Way to extrapolate the nova rate to faint magnitudes, finding a Galactic rate of 36 ± 13 yr^{-1}. Recently, Schaefer (2014) conducted a thorough analysis of observational selection biases against discovering even the brightest novae. After accounting for these biases, Schaefer (2014) suggested that only $43 \pm 6\%$ of Galactic novae are likely recovered. While some novae have been observed in the halo, indicating a Population II origin, most galactic novae are found in the bulge and along the Galactic plane. Additionally, della Valle et al. (1992) suggested that there are two distinct populations of novae: quicker and brighter ones on the Galactic plane, and slower and fainter ones in the bulge.

1.4.2 Extragalactic Nova

By the early 1990s, novae had been detected in eight extragalactic systems, with six systems having enough detections to estimate their nova rates. Ciardullo et al. (1990) conducted the first comparative study of nova rates across different galaxies, including NGC 5128, SMC, LMC, M31, M33, and a sample of Virgo ellipticals. Ongoing synoptic studies frequently discover novae in external galaxies, with approximately 1000 found in M31 alone. Darnley et al. (2006) calculated a nova rate of 65^{+16}_{-15} per year for M31. Shara et al. (2016) determined the rate in M87 to be 363^{+33}_{-45} per year. However, Shafter (2017) later reviewed this result and concluded that this figure was likely an upper limit due to uncertainties in identifying genuine novae from incomplete light curves

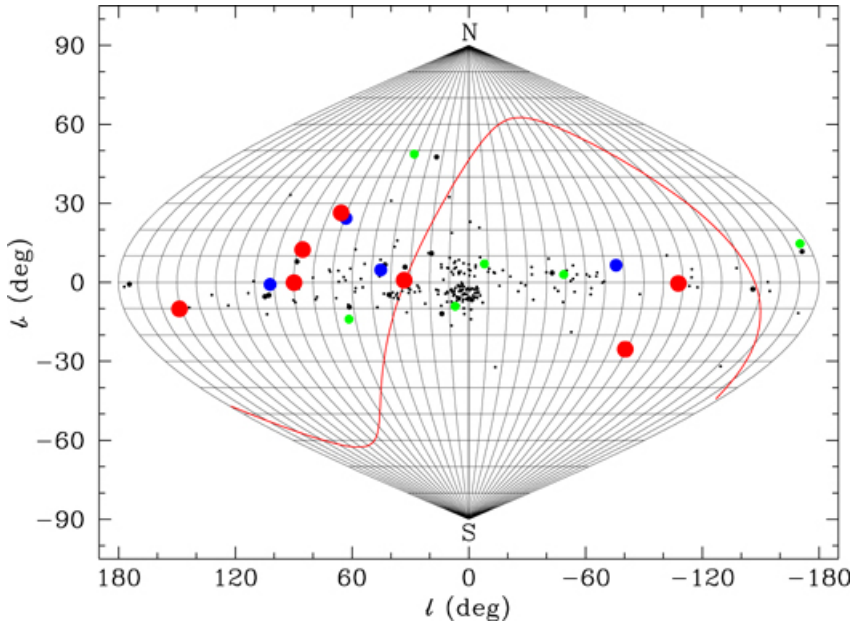

Fig. 1.12 The distribution of galactic novae brighter than $m = 10$ and recorded after 1900 is shown. The coordinates b and l denote the galactic latitude and longitude, respectively. The red, blue, green, black filled circles, and black dots represent novae with brightnesses of $m \leq 2$, $2 \leq m \leq 3$, $3 \leq m \leq 4$, $4 \leq m \leq 5$, and $5 \leq m \leq 10$, respectively. The celestial equator is indicated by the solid red line (Shafter, 2017).

and in extrapolating observations from near the galaxy's center to its entire extent. It was also found that M33, M32, NGC 205, the LMC, the SMC, and M81 are among the galaxies with notable counts of documented nova eruptions. After accounting for the various stellar populations, the nova rates in these galaxies are roughly similar to those in our Galaxy Shafter (2017).

1.5 Why do we study novae?

- Novae are crucial astronomical events for understanding the evolution of close binary systems and their contribution to the elemental abundances in the interstellar medium or the galaxy itself. They serve as ideal laboratories to study nuclear processes, accretion disk formation and destruction, and formation of dust grains in localized regions of space. These processes, which take place briefly in novae, particularly in recurrent novae, provide insights that are otherwise

challenging to observe in ordinary stars. Additionally, they contribute to the dust budget in the interstellar medium (Evans and Gehrz, 2012; Gehrz et al., 1998)."

- Novae represent a particular class of exploding stars where a white dwarf, after accumulating mass from a companion star, reignites nuclear fusion at its surface, resulting in a rapid increase in brightness. This phenomenon allows astronomers to better understand fusion processes and dynamic interactions within binary star systems. Novae are also considered one of the main sources of lithium in the Universe (Tajitsu et al., 2015) and other CNO isotopes such as ^{13}C, ^{15}N, and ^{17}O, which are formed through nuclear reactions during the eruption.

- Novae, particularly classical novae (CNe) and recurrent novae (RNe), are highly anticipated to be progenitors of type Ia supernovae due to the gradual increase in the white dwarf's mass with each outburst. This accumulation may eventually lead the white dwarf to surpass the Chandrasekhar limit ($M_{ch} = 1.40\ M_{\odot}$), which could lead to Type IA SNe (Hachisu and Kato, 2000; Osborne et al., 2011; Starrfield et al., 2024). Astronomers are intensively searching for the true progenitors of type Ia supernovae because of their significant contribution to cosmology, particularly the evidence they provide for the theory of the accelerating expansion of the Universe (Perlmutter, 1999; Riess et al., 1998). This is because, unlike core-collapse supernovae, Type Ia supernovae are standardizable candles that can be used to measure distances. Despite extensive research, the exact progenitor of Type Ia supernovae remains unclear. The single-degenerate channel is still considered a plausible progenitor pathway, even amidst numerous proposed scenarios. Consequently, studying classical and recurrent novae can provide valuable insights into the origins of Type Ia supernovae.

1.6 Structure of the thesis

In this chapter, I reviewed novae in general, starting from their early history and formation mechanisms to their various classification mechanisms and distribution in

the universe. In Chapter 2, I present the details of data acquisition and data reduction mechanisms, including information about the instruments utilized. In Chapter 3, I present the modeling tools and procedures for spectra and line profiles to obtain detailed information about the physical, chemical, and geometrical properties of novae during their outburst and quiescent phases. In Chapter 4, I present the photometric and spectroscopic study of the fastest classical nova, *V1674 Her*, which showed very unique characteristics in various ways. In Chapter 5, I present the quiescent phase (between 2006 and 2021) study of the most famous recurrent symbiotic nova, RS Oph. In Chapter 6, I present the spectroscopic and photometric study of one of the slowest novae, *V1405 Cas*, in 2021. In Chapter 7, I present the summary of the major findings presented in the thesis along with future plans in my research career.

1.7 Science results

Chapter 4 is based on a paper published as Habtie et al. (2024b), which presents the earliest appearance of nebular and coronal lines in the optical bands and the 3D geometrical structure of the ejecta of Nova Her 2021 (V1674 Her). Chapter 5 is based on a submitted paper, Habtie and Das (2024b), which reports a significant increase in the rate of accretion of RS Oph as it approaches the final stage of its quiescent phase and the onset of the next outburst. Chapter 6 is based on a completed paper, soon to be submitted for publication, which reports a significant enhancement of helium during the initial stages of the outburst and the bipolar geometry of the ejecta with an inclination angle of $\sim i = 35^{\circ}$ from the line of sight.

2

Data Acquisition and Reduction Techniques

SPECTROSCOPY and PHOTOMETRY are the most widely used techniques that astronomers employ to explore the intrinsic characteristics of astronomical objects, such as luminosity, temperature, radius, mass, and elemental compositions. Spectroscopy measures intensity as a function of wavelength, whereas photometry refers to the measurement of flux over a broad wavelength band of radiation. However, polarimetry and asteroseismology are also frequently used by astronomers to measure the degree of linear polarization and its direction, and to study oscillations of stars to understand their interior structures, respectively.

This thesis is mainly based on spectroscopic data acquired from both publicly available archives and personal observations using the 2m Himalayan Chandra Telescope. However, we also employed photometric measurements to develop the light and color curves of some objects and estimate the distance, mass, and radius of the target objects. The chapter begins with a brief introduction to publicly available archives, followed by a detailed description of observational techniques and data analysis methods for spectroscopic data using the Image Reduction and Analysis Facility (IRAF).

2.1 Spectroscopy

Spectroscopy is a cornerstone of modern astronomy, providing a wealth of information about astronomical objects, including their temperature, velocity, and composition

etc, which is unattainable through imaging alone. It provides the measurements of intensity as a function of wavelength, by dividing electromagnetic energy into its individual wavelengths. There are three different kinds of spectra: absorption line, emission line, and continuous (see Fig. 2.1). A continuous spectrum is produced by a hot, dense object, such as a star or incandescent solid, emitting light across a broad range of wavelengths without interruption. This type of spectrum appears as a seamless gradient of colors. An emission line spectrum, on the other hand, is generated by a heated, low-density gas. In this case, the gas emits light only at specific wavelengths, resulting in bright, discrete lines against a darker background. Each line corresponds to a particular element or molecule within the gas. Conversely, an absorption line spectrum occurs when light from a hot, dense source passes through a cooler, low-density gas. The gas absorbs light at certain wavelengths, creating dark lines within the continuous spectrum. These absorption lines are indicative of the composition and physical conditions of the intervening gas.

2.1.1 Spectrograph

A spectrograph uses a dispersing optical device, such as a prism, grating, or prism-plus-grating (grism), to separate the light into its constituent wavelengths. The light is delivered to the spectrograph from the source via a telescope. The dispersed spectrum is then recorded by a detector, commonly Charge Coupled Devices (CCDs). The following are the primary components of spectrograph;

1. **Entrance Slit:** It allows light from a specific part of the sky or a celestial object to enter the spectrograph. It helps to limit the field of view, background noise and wavelength degeneracy. It also increases spectral resolution by reducing the amount of light that can enter the instrument at one time. However, there is a loss of useful photons as the slit becomes narrower.

2. **Collimator:** It takes the divergent light from the entrance slit and makes it parallel. This is crucial for ensuring that the light rays are properly dispersed by the dispersing element. It typically consists of a lens and/or a mirror.

3. **Dispersing Element:** The dispersing element, which can be a prism, diffraction grating, or a grism, separates the incoming light into its component wavelengths.

    - **Prism:** It disperses light by refraction, bending different wavelengths by different amounts. This dispersion is disproportionately more in the blue regime than in the red.
    - **Grating:** It uses the principle of diffraction and interference to disperse light, often providing higher resolution than a prism. The dispersion is mostly linear in the case of the grating.
    - **Grism:** It is a combination of a prism and a grating. In this case the diffraction angle of the the transmission grating is canceled by the reflection angle of the prism such that the dispersed beam is in-line with the incoming radiation.

4. **Camera/Objective Lens:** It converges the dispersed light, producing an image of the spectrum onto the detector. It is a lens and/or a mirror.

5. **Detector:** It captures the dispersed light and records the spectrum. Modern spectrographs typically use charge-coupled devices (CCDs) for their high sensitivity and ability to record detailed spectral data across a wide range of wavelengths. CCDs are the standard visible and near-ultraviolet imaging sensors, which works based on the principle of photoelectric effect.

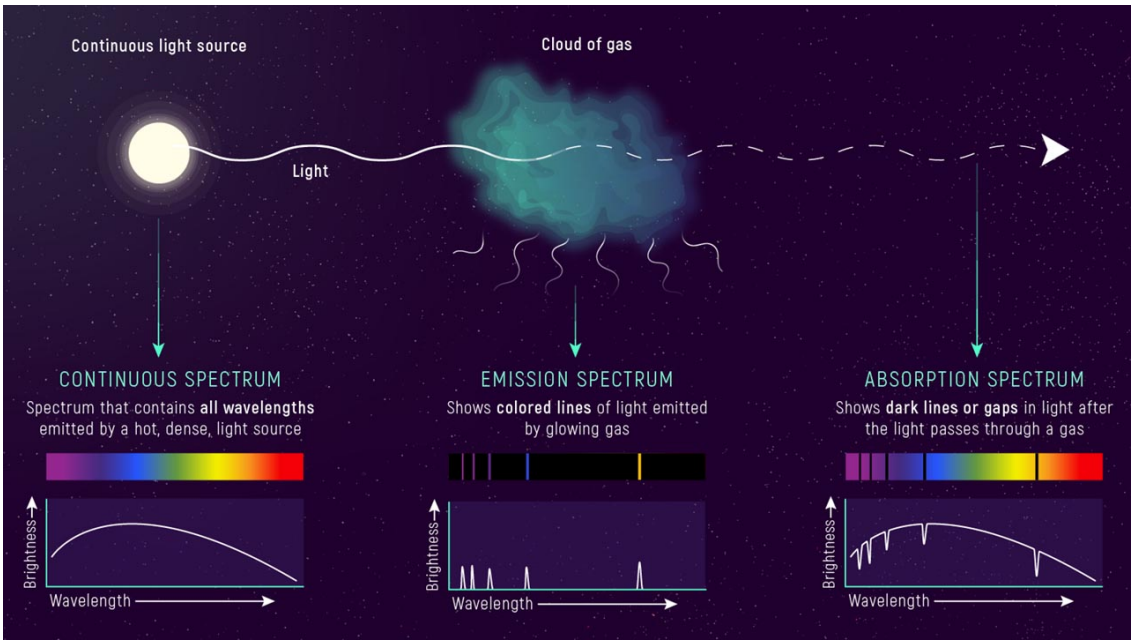

Fig. 2.1 Types of Spectra: Continuous, Emission, and Absorption *Credit*: NASA, ESA, Leah Hustak (STScI)

2.2 Archival data sources

2.2.1 ARAS

The Astronomical Ring for Amateur Spectroscopy (ARAS) is a volunteer organization dedicated to fostering collaboration in spectroscopy between amateur and professional astronomers. One of the key components of the Astronomical Ring for Amateur Spectroscopy (ARAS) initiative involves the spectroscopic monitoring of eruptive stars, including symbiotic binaries and classical novae, by amateur astronomers worldwide, spanning both the northern and southern hemispheres. ARAS observers utilize small telescopes ranging from 20 to 60 cm in diameter, equipped with spectrographs of varying resolutions, ranging from approximately 500 to 15000. These spectrographs cover the wavelength range from 3600 to nearly 8000 Å.

The majority of telescopes used by ARAS observers are reflectors, with notable models including Schmidt-Cassegrain, Newtonian, Dall-Kirkham, Cassegrain, and other variations. These telescopes typically range in size from 20 to 40 cm, with occasional

models reaching sizes of 50 or 60 cm. Due to the extremely small diameters of the telescopes, precise tuning of all equipment—especially the autoguider and focus—is necessary to achieve useful results with sufficient signal-to-noise ratio (SNR). Alpy200 ($R \sim 500$), Alpy600 ($R \sim 600$), and LISA ($R \sim 1000$) are some of the spectrographs widely used used by ARAS observers (Teyssier, 2019).

The spectra obtained undergo a standard data reduction processes, including dark subtraction and flat division, before being extracted and analyzed using the Integrated System for Images and Spectrometers (ISIS) software, developed by Christian Buil[1]. ISIS is a robust, interactive graphical tool designed for processing astronomical spectra. Additionally, it utilizes continuous integration testing alongside a proprietary test suite to monitor the overall quality of the code base and prevent code regressions (Rodriguez et al., 2021).

2.2.2 ESO

The European Southern Observatory (ESO) is an intergovernmental organization dedicated to astronomical research, established in 1962 with the support of 16 member nations. Operating some of the most advanced ground-based telescopes and observatories worldwide, such as the Very Large Telescope (VLT) at the Paranal Observatory in Chile, the Atacama Large Millimeter/submillimeter Array (ALMA), and the La Silla Observatory, ESO facilitates cutting-edge research in Astronomy and Astrophysics. Its mission is to provide the scientific community with access to state-of-the-art research facilities, enabling innovative studies across various domains of Astronomy and Astrophysics.

In this thesis, I utilized a spectrum of an M2III type star obtained from the ESO's library of spectra, which is accessible at the link provided ate the bottom of this page[2]. The spectrum is listed among published spectra by Pickles (1998). The data was processed and analyzed using standard procedures in IRAF.

[1] http://www.astrosurf.com/buil/isis-software.html
[2] https://www.eso.org/sci/facilities/paranal/decommissioned/isaac/tools/lib.html

2.2.3 AAVSO

The AAVSO, or Association of Variable Star Observers, is a non-profit organization established in 1911 to coordinate and assist amateur astronomers in observing variable stars at the Harvard College Observatory. Its mission is to promote broad participation in scientific research by ensuring that variable star astronomy is accessible to individuals worldwide, regardless of their location or level of expertise. The organization fosters collaboration between amateur and professional astronomers by collecting, analyzing, and archiving observations of variable stars. Additionally, the AAVSO shares variable star data and resources to facilitate scientific research, public outreach, and educational initiatives.

In this thesis, I utilized various optical photometric observation results (BVRI bands) to generate light curves for my target objects. The uploaded photometric data can be downloaded from the AAVSO International Database [3], while available spectra can be downloaded from the link[4], provided at the bottom.

2.2.4 The STONY BROOK / SMARTS Spectral Atlas of Southern Novae

The STONY BROOK / SMARTS Spectroscopic Atlas of (mostly) Southern Novae presents spectra and, in some cases, photometry of the novae since August 2003. The spectra are observed by Small & Moderate Aperture Research Telescope System (SMARTS). It is a network of telescopes which is primarily dedicated to astronomical research, to investigate a wide range of research topics, including variable stars, exoplanets, and transient astronomical events. The telescopes typically range from 0.3 to 1.5 meters in aperture, making them small to moderate in size. They are located at various observatories worldwide, including the Southern Astrophysical Research (SOAR) Telescope in Chile and the Cerro Tololo Inter-American Observatory (CTIO)

[3] https://www.aavso.org/aavso-international-database-aid
[4] https://app.aavso.org/avspec/search

in Chile. By providing researchers with access to observational data and time, the network contributes to the advancement of our understanding of the universe.

For this thesis I have utilized a spectrum obtained from Cerro Tololo Inter-American Observatory (CTIO). The spectrum has been downloaded from the STONY BROOK / SMARTS (mostly) Spectroscopic Atlas of (mostly) Southern Novae website[5] .

2.3 HCT observation

Some of the optical spectroscopic observations of novae presented in this thesis were conducted using the Himalayan Chandra Telescope (HCT). It is a 2-meter optical-infrared telescope located at the Indian Astronomical Observatory (IAO) in Hanle, Ladakh, India. The telescope is remotely controlled by Indian Institute of Astrophysics (IIA) from Centre for Research and Education in Science and Technology (CREST) in Hosakote through a specialized satellite link. It is equipped with cutting-edge instruments for optical and infrared observations, enabling astronomers to explore a diverse range of celestial objects and phenomena. The telescope situated at an altitude of approximately 4500 meters in the Himalayas; its high altitude and remote location offers optimal atmospheric conditions for astronomical observations, boasting clear, dark skies and minimal light pollution. Consequently, out of 365 days in a year, around 180 nights are cloud-free, and approximately 270-280 photometric nights available for observation. It has provided uninterrupted scientific observation services since May 2003 until the present. The telescope features three scientific instruments mounted on an instrument mount cube at the Cassegrain focus, allowing for easy attachment through the cube's four side ports and on-axis port. These instruments include; the Himalaya Faint Object Spectrograph (HFOSC), the TIFR NIR Imaging Spectrograph (TIRSPEC), and the Hanle Echelle Spectrograph (HESP). A brief description for each of these instruments is provided in the following subsections.

[5] http://www.astro.sunysb.edu/fwalter/SMARTS/NovaAtlas/

(a) Indian Astronomical Observatory (IAO)

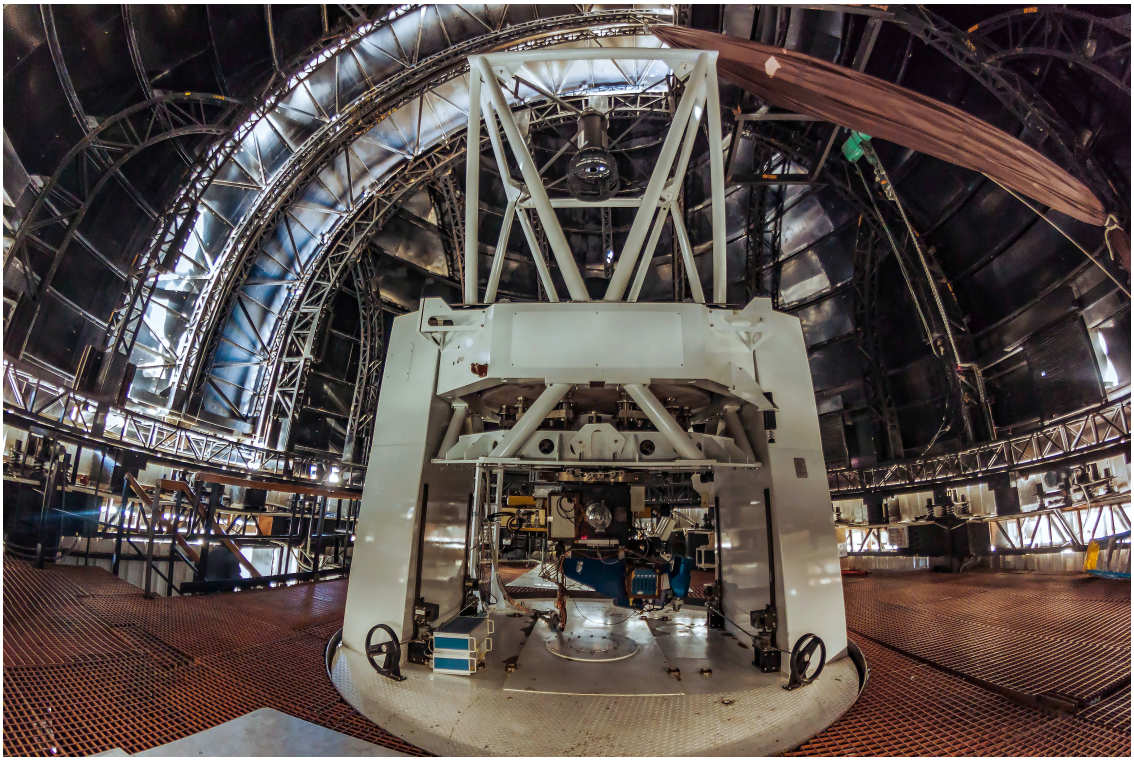

(b) Himalayan Chandra Telescope (HCT)

Fig. 2.2 These images were taken from https://www.indiatoday.in/interactive/photo-essay/hanle-inside-indian-astronomical-observatory-10-04-11-2022

2.3.1 HFOSC

The Himalaya Faint Object Spectrograph Camera (HFOSC)[6] is an optical imager combined with a spectrograph, is mounted on the central port of the instrument mount cube of HCT. It was designed and fabricated in collaboration with the Copenhagen University Observatory and is used for optical imaging and spectroscopy. It encompasses wavelengths spanning from 3500 - 9200 Å using a selection of 11 grisms, offering a spectral resolutions that vary from 150 - 4500. The telescope provides an unvignetted imaging field measuring 10 x 10 arcminutes onto a 2K x 2K section of the CCD camera. HFOSC utilizes Bessell U (3727 Å), B (4861 Å), V (5007 Å), R (6563 Å), and I (6724 Å) filters, achieving a signal-to-noise ratio of S/N = 22 for a 20-minute exposure time. In this study, grisms 7 and 8 were employed, encompassing the wavelength ranges of 4000– 7000 Å and 5200 – 9000 Å, with resolutions of 1200 and 2000, respectively.

2.3.2 TIRSPEC

TIFR Near Infrared Spectrometer and Imager (TIRSPEC)[7] is an NIR imager combined with a spectrometer mounted on HCT. It was developed by the Infrared Astronomy Group of Tata Institute of Fundamental Research (TIFR), Mumbai, in collaboration with Mauna Kea Infrared (MKIR), Hawaii. The instrument is equipped with a 1024 x 1024 Hawaii-1 detector array. Operating at a resolution of 0.3 arcsec per pixel, it offers a Field of View (FoV) of 307 x 307 arcsec^2 in imaging mode. In spectroscopy mode, it covers wavelengths ranging from 1 micron to 2.5 micron with a resolution of approximately 1200. In addition to the single order mode, which covers specific wavelength ranges such as Y(1.02-1.20), J(1.21-1.48), H(1.49-1.78), and K(2.04-2.35) micron, cross disperse modes are also available. These modes provide simultaneous coverage of wider wavelength ranges, including 1.02-1.49 micron and 1.50-2.45 micron. TIRSPEC uses the filters: Y, J, H, K, Methane off (1.584 μm); [Fe II] (1.645 μm);

[6] https://www.iiap.res.in/iao/hfosc.html
[7] https://www.tifr.res.in/~daa/tirspec/

Methane on (1.654 μm); H2 (1-0) (2.1239 μm); Br Gamma (2.166 μm); K-Cont (2.273 μm) and CO (2-0) (2.287 μm) (Ninan et al., 2014).

2.3.3 HESP

The Hanle Echelle Spectrograph (HESP)[8] is a fiber-fed spectrograph for the 2m HCT telescope mounted on a bench. The spectrograph offers two spectral resolution options: R=30000 and 60000. The low-resolution mode utilizes a 100-micron fiber as an input slit, while the high-resolution mode employs an image slicer. It utilizes an R2 echelle grating and two cross-dispersing prisms to ensure continuous wavelength coverage from 350 to 1000 nm. The CCD is a 4K x 4K system with a pixel size of 15 x 15 micron. The spectrograph design is a bench mark for compact size, large wavelength coverage and high throughput, based on a white pupil concept. It was constructed by Callaghan Innovation in New Zealand, while the instrument control interface was designed and developed by the Indian Institute of Astrophysics. A complete wavelength coverage over 350 - 1000 nm, will allow measurement of chemical abundances of key elements of stellar evolution. The high mechanical stability and double fibre mode will allow measurement of precise radial velocities, essential for programs such as exoplanet studies and astroseismology.

2.4 Optical Spectroscopic Data Reduction

Raw observational data obtained using a telescope frequently contain a multitude of artifacts, including atmospheric signatures, instrumental effects, and various sources of noise. Consequently, a sophisticated data reduction mechanism becomes essential to filter out extraneous signals while preserving the intended ones. This process, known as data reduction in astrophysics, aims to eliminate instrumental signatures and contaminant sources, particularly for ground-based observations, where atmospheric effects are prevalent. Only after these corrections can the true signal of the target

[8] https://www.iiap.res.in/hesp/Instrument_Specification.php

source be effectively extracted. Additionally, data reduction typically incorporates a noise model and error propagation calculations to assess uncertainties in the extracted signal accurately.

This thesis presents optical spectroscopic data obtained with the 2m HCT, processed using the standard procedures of the Image Reduction and Analysis Facility (IRAF)[9]. The basic procedures applied to reduce the spectra are discussed below.

2.4.1 CCD calibration

The CCD calibration consist of correcting for bias, flat-fielding, and removing cosmic rays. Bias frames captured on a specific night are merged to generate a median bias frame, which is then subtracted from each individual object frame. To correct for sensitivity variations of the CCD along the dispersion axis, flat frames from a halogen lamp are utilized. Subsequently, cosmic rays exceeding a predefined intensity threshold are eliminated from the spectra. The *zerocombine* and *cosmicrays* tasks in IRAF were utilized for combining bias frames and removing the cosmic rays effect, respectively. Additionally, the *ccdproc* task was employed to address and rectify various detector imperfections such as readout bias, zero level bias, dark counts, response variations, illumination discrepancies, and fringing effects. It also performs operations like trimming unwanted lines and columns and adjusting the pixel datatype for further analysis.

2.4.2 1D Spectrum Extraction

Initially, the two-dimensional spectral field is scanned along the spatial axis to identify the spectral band or bands captured from the science object. The aperture is positioned at the maximum intensity point, and its width is adjusted to encompass the spectral width along the spatial direction. The background level is determined where the

[9] http://iraf.noao.edu/, IRAF is a versatile software system designed for reducing and analyzing scientific data, developed at the National Astronomy Observatories (NOAO), USA. It offers a range of programs for image processing, graphics, and optical astronomy data analysis.

intensity reaches a minimum value. Subsequently, the spectrum is traced along the dispersion axis by identifying the positions of maximum intensity values. The *apall* task in IRAF is used for extracting one-dimensional spectra from two-dimensional spectra. It allows users to define the aperture and background regions, trace the aperture along the dispersion axis, and aggregate counts from multiple pixels to create a one-dimensional spectrum. This task is commonly used in the reduction and analysis of astronomical spectroscopic data. The extraction task needs to be performed for all the spectra of the science objects, lamps, and standard stars.

2.4.3 Wavelength calibration

The wavelength calibration is a procedure that involves converting pixel units into wavelengths. It utilizes lamp spectra as a reference, where the sources exhibit well-known spectral emission features. The lamp spectra are captured immediately after the object exposure frame. Iron-Argon (FeAr) and Iron-Neon (FeNe) serve as the arc lamps (laboratory standard sources) for Grism-7 & -8 respectively. Ideally, the lamp spectra should align with the exact pixels traced by the object spectrum on the CCD. The IRAF tasks *identify* and *refspectra* are used to identify the wavelengths of well-known spectral features in the lamp spectra and correlate them with the corresponding pixel numbers. Then, using the identified and labeled spectra as a reference, it is possible to calibrate the dispersion axis of the object spectra. The dispersion correction is performed by the IRAF command *dispcor*.

2.4.4 Flux calibration

Flux calibration is achieved through a two-step process. Firstly, the sensitivity function is derived from spectroscopic data obtained from standard stars like Feige 34 and Feige 110, which were observed on the same night. This function is determined using tasks like *standard*, which utilizes the magnitude of standard stars and atmospheric extinction, and *sensfunc*, which fits a polynomial to the observed magnitude as a

Table 2.1 HCT Submitted proposals and observation log.

Proposal code	Date of observation	wavelength	Instruments
HCT-2022-C2-P44	25-Jul-2022	No observation	-
	23-Aug-2022	Optical	HFOSC
HCT-2022-C3-T79	03-Dec-2022	Optical	HFOSC
	04-Dec-2022	Optical	HFOSC, HESP
HCT-2023-C1-T870	13-Jan-2023	No observation	-
	10-Mar-2023	Optical + NIR	HFOSC, TIRSPEC
HCT-2023-C2-P19	09-Jul-2023	No observation	-
	09-Aug-2023	Optical + NIR	HFOSC, TIRSPEC
HCT-2023-C3-P14	24-Sept-2023	Optical	HFOSC
	14-Nov-2023	Optical	HFOSC
HCT-2024-C1-P6	02-Feb-2024	Optical	HFOSC
	17-Feb-2024	No Observation	-
HCT-2024-C2-P48	26-Jun-2024	Optical	HFOSC

function of wavelength. Secondly, the standard star fluxes for the night of observation are calculated using known flux data and the calculated airmass. From these flux values, a sensitivity function is established across wavelengths. By incorporating this sensitivity function and the object spectrum's calculated airmass value, the final flux-calibrated object spectrum is generated.

2.5 Observation of Novae

Due to the catastrophic impact of Covid-19 at the beginning of my research tenure, I was unable to initiate the submission of proposals to available national facilities and conduct sufficient observations. My first successful observation night allocated on the HCT occurred on August 23, 2022. Subsequently, I successfully submitted six consecutive proposals, securing approximately eleven full nights for observation. Unfortunately, four nights were wasted due to unfavorable weather conditions in the telescope area. Despite these setbacks, we observed various novae on the remaining eight nights (see Table 2.1). However, due to time constraints for analysis, only a selection of the observed spectra is included in this thesis.

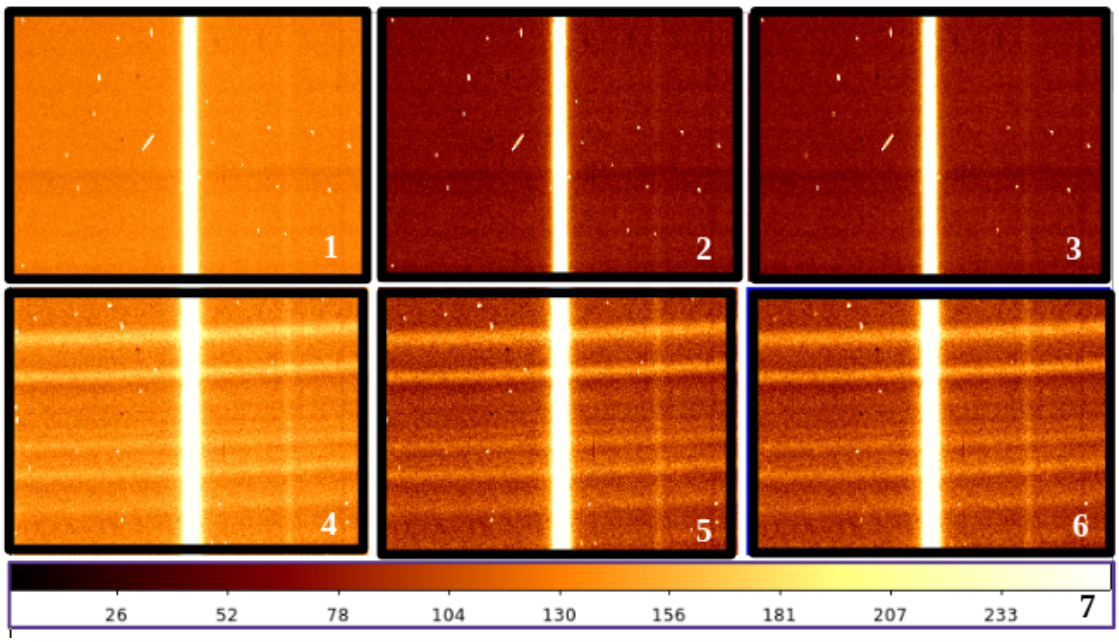

(a) 1 & 4 are Raw data; Grism 7 & 8 respectively, 2 & 5 after bias correction, 3 & 6 after cosmic rays removal, and 7 is a color bar (displaying the color mag, bias and contrast settings)

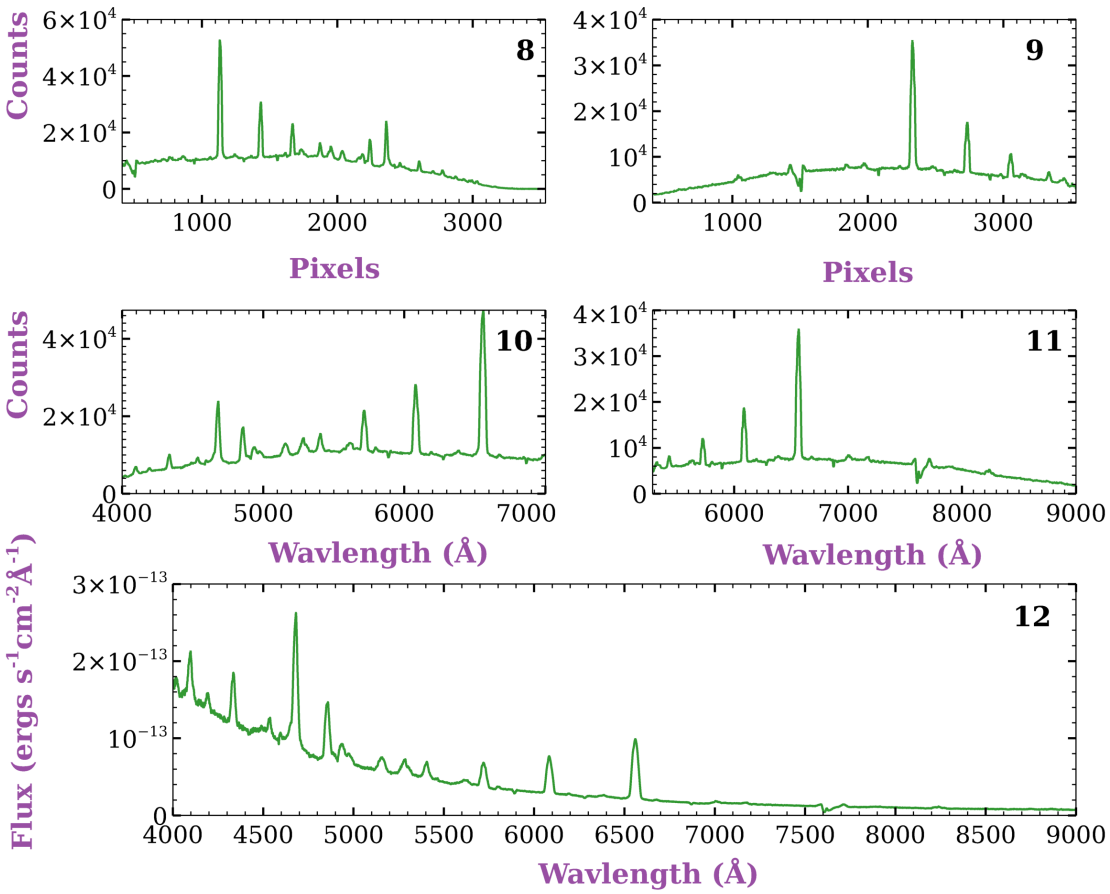

(b) 8 & 9 are Extracted 1D spectra, 10 & 11 are Wavelength Calibrated, and 12 is the combined and Flux calibrated spectrum

Fig. 2.3 Basic steps in Optical spectroscopic data reduction. The spectra are taken from HCT, for the object Nova cas 2021 (V1405 Cas).

3 Modelling Techniques

SPECTRAL MODELING has served as one of the powerful tools for studying the physical and chemical processes occurring within novae for several years. Researchers have utilized spectroscopic and spatially detailed data from nova shells to simulate the ejecta of nova systems. This endeavor aims to understand the evolution of physical conditions within the nova ejecta over time. Such analyses not only shed light on the characteristics of the binary system but also provide insights into its surrounding environment. Over time, additional techniques have been employed to enhance ejecta modeling efforts. Some of the modeling tools widely used for studying nova ejecta include PHOENIX, MOCASSIN, MAPPING, RAINY 3D, CLOUDY , SHAPE, DUSTY, and PYCLOUDY. Among the listed modeling tools above, two were utilized for the purpose of this thesis: CLOUDY and SHAPE. Brief descriptions of these two tools are provided below.

3.1 Photoionization Modeling

3.1.1 CLOUDY

CLOUDY is a widely used photoionization and plasma simulation code designed for astrophysical applications. It was initially developed in the late 1970s by Gary Ferland while he was a graduate student at the University of California, Berkeley (Ferland and Shields, 1978). Since then, it has undergone numerous updates and revisions to

incorporate new physical processes, improve computational efficiency, and expand its capabilities. Some notable updates and developments include:

1. **Version 13 (Cloudy 13):** Released in 2013, this version introduced improvements in the internal consistency and robustness of convergence for coupled physics problems. The result is far greater stability for simulations that extend into molecular gas. Additionally, due to the incorporation of newly added databases such as Chianti, Lambda, and Stout databases, the number of predicted lines in this version has been significantly increased.

2. **Version 17 (Cloudy 17):** Released in 2017, this version introduced significant performance improvement, approaching a factor of two compared with C13. Moreover several advances in the H- and He-like iso-electronic sequences incorporated.

3. **Version 23 (Cloudy 23):** Released in 2017, this version introduced a significant changes to the atomic and molecular data that improved the accuracy of CLOUDY predictions: the Chianti database upgraded from version 7 to 10; the H- and He-like collisional rates improved to theoretical values; the molecular data updated to the most recent LAMDA database, and several chemical reaction rates updated to their most recent UDfA (Updated Database for Astrophysics) and KiDA (KInetic Database for Astrochemistry) values.

For the purpose of making up this thesis we have utilized the last two most recent versions of CLOUDY (C17 & C23) (Chatzikos et al., 2023; Ferland et al., 2017).

CLOUDY is a microphysics code. It is designed to simulate physical conditions of non-equilibrium gas clouds exposed to external radiation fields, predicting emission lines spectrum based on assumptions about the gas's physical condition (ionization, density, temperature, and chemical composition). The clouds might be ranging from the intergalactic medium to the high-density LTE and STE limits. The range of temperatures extends from the CMB temperature up to 1.00×10^{10} K and the physical state ranges between fully molecular to bare nuclei. Through a self-consistent algorithm,

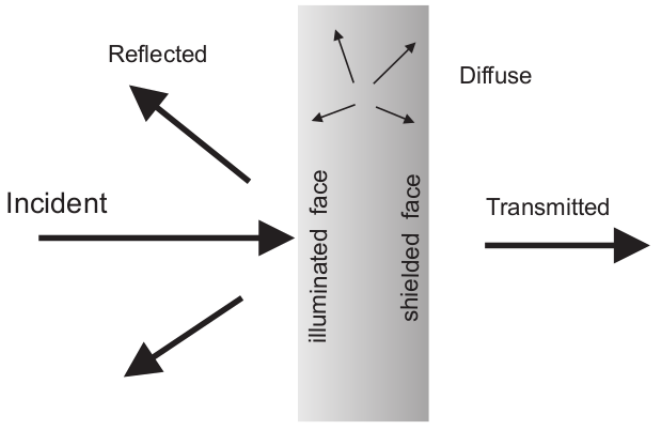

Fig. 3.1 Radiation fields included in the CLOUDY calculations. *Source*: Hazy 1 CLOUDY manual.

CLOUDY simultaneously solves thermal, statistical, and chemical equilibrium equations for input parameters, estimating both intensities and column densities of numerous spectral lines across the electromagnetic spectrum. Major ionization and recombination processes are accounted for in CLOUDY , such as photoionization, Auger ionization, collisional ionization, charge transfer, and three-body recombination. Model-generated spectra are compared to observations to deduce physical and chemical conditions. Input parameters comprise temperature (T), luminosity (L), hydrogen number density (n), filling factor, covering factor, elemental abundances, and inner and outer radii of the surrounding ejecta. For synthetic model spectra, these input parameters needs to be included and the abundances of elements with observed emission lines, whereas other elements were maintained at their solar values (Grevesse et al., 2010).

The calculations in the CLOUDY code incorporate various radiation fields, including: incident radiation field: emitted by the central object, reflected field: emitted by the illuminated face of the cloud back toward the source of the external field, transmitted radiation field: The net emission emerging from the shielded face of the cloud, diffuse radiation field: emitted by gas and grains within the nebula. This phenomenon is clearly illustrated in Figure 3.1.

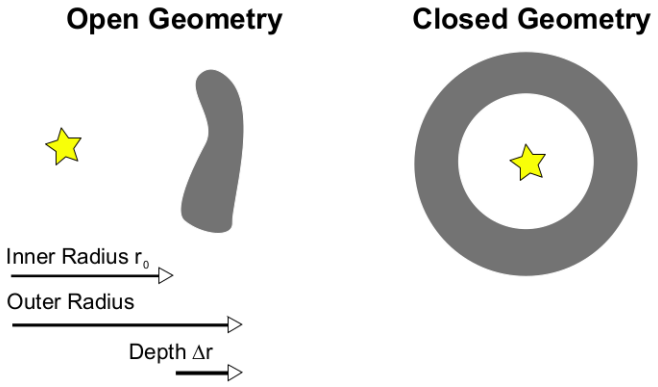

Fig. 3.2 A schematic diagram of open and closed geometry used in cloudy models. *Source:* Hazy 1, CLOUDY module

3.1.1.1 Geometry

The default geometry in CLOUDY is spherical or plane-parallel, depending on the ratio of the thickness of the cloud to the inner radius. Specifically, the geometry is: Spherical if $\frac{\triangle r}{r_0} \geq 3$, Thick shell if $\frac{\triangle r}{r_0} < 3$, and Plane-parallel if $\frac{\triangle r}{r_0} < 0.1$. The geometries in CLOUDY are grouped in an open or closed geometries. An open geometry is one in which the covering factor [1] of the gas is small, because the the gas cloud is not completely opaque or enclosed, where as a closed geometry has an emission-line gas covering $\sim$ 4πsr as seen by the central object. Fig. 3.2 illustrates this phenomenon.

3.1.1.2 During Expansion Phase

In this thesis, I employed CLOUDY to study the expansion phase of two novae: V1674 Her and V1405 Cas. For both cases, I assumed a spherical geometry and linear velocity expansion of the ejecta. The density variation for V1674 Her was $\rho \propto r^{-3}$, and for V1405 Cas, it was $\rho \propto r^{-2}$. This was related to the speed of the novae, as the fastest nova gets optically thin quicker than the slowest nova. As a result, the density of the cloud decreases more rapidly for the faster nova, whereas the slower nova may remain dense for a considerably longer time. The procedure we followed for modeling

[1]The covering factor is the fraction of 4πsr covered by gas, as observed from the radiation source at the center. Typically denoted as $\Omega/4\pi$, it ranges from 0 to 1, indicating the fraction of the radiation field emitted by the central object that directly interacts with the nebular gas.

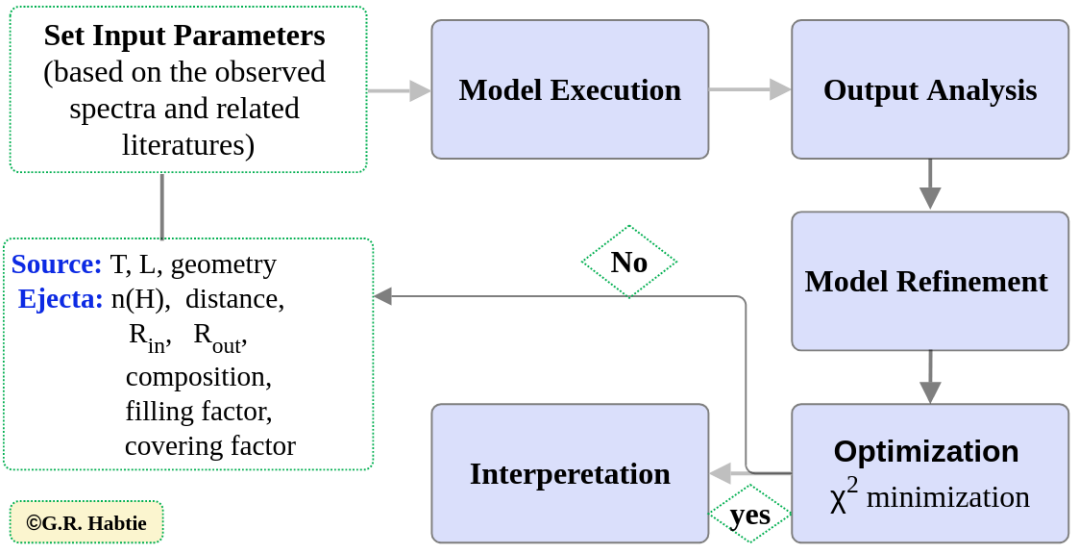

Fig. 3.3 The diagram shows the basic workflow of CLOUDY software.

is shown in the workflow in Fig. 3.3. First, I set the instruments based on preliminary estimations or some literature review results. Then, I executed a couple of models, evaluated the output, and worked on model refinement, which took the longest duration of time. I kept running models until satisfying results were achieved and the χ^2_{red} value fall in the scientifically acceptable range (i.e., between 1 and 2). Once satisfied with the model, I interpreted the results and wrote them in paper form (see Chapters 4 and 6 for detailed discussion and analysis of the results).

3.1.1.3 During Quiescent Phase

In this thesis, I also used CLOUDY to study the quiescent stage of the nova RS Oph. The modeling strategy is related to that of the expansion phase of the nova, but not exactly the same. For modeling the quiescent phase spectra of RS Oph, I assumed the geometry of the accretion disc to be a cylinder with a radius r and height h, instead of spherical unlike the expansion phase. In addition, we included the contribution of the secondary star, as its effect is clearly visible in every spectrum by a deep absorption line of TiO. Therefore, in this case, we considered three distinct parts: the white dwarf (WD), the accretion disc, and the secondary star. As the matter in the disc is not

moving or expanding at a very high speed like during the expansion phase, I was unable to estimate the inner and outer radii from the velocities. Therefore, I used the relations in (Hamada and Salpeter, 1961), (Gehrz et al., 1998), and Kepler's law to determine the inner and outer radii of the disc (see Sec. 5.5 for details).

3.2 Morpho-kinematic Modeling

3.2.1 SHAPE

In some parts of this thesis, I employed SHAPE, a morpho-kinematical code, for the purpose of 3D reconstruction of the shell ejecta structure. The code was developed by Steffen and López (2006) for analyzing and deciphering the 3D geometry and kinematic structure of nebulae and other astronomical phenomena (Steffen and Koning, 2017, 2012). Originally designed as a model for intricate AGN structures by Holloway et al. (1996), form enables the interactive and user-driven reconstruction of the 3D structure of astrophysical objects. This capability is particularly valuable when dealing with datasets that are not suitable for automatic reconstruction. Such datasets may not meet the fundamental assumptions of the reconstruction process or may lack the necessary precision. This versatile tool serves not only for studying intricate three-dimensional structures but also as a foundation for hydrodynamic and numerical photo-ionization computations. Additionally, Shape facilitates the calculation and visualization of spectrum information derived from these computations.

The user constructs morphologies using a variety of primitives, including fundamental shapes such as spheres, cylinders, torus, cones, and planes, among others. These primitives can be enhanced with modifiers, allowing for geometric alterations and distortions, as well as control over parameters like temperature, velocity, and density. Modifiers can be specified either analytically or interactively, and they can operate within spherical, cylindrical, or Cartesian coordinates. With skillful application, users can quickly apply density and velocity modifications to compare with data, enabling

the rapid construction of various common astrophysical morphologies in just a few minutes.

The general modeling procedure used to produce 3D morpho-kinematical models using SHAPE is outlined as follows. Initially, a careful and detailed analysis of the observed data is required. These observations typically consist of a spectrum or an image of an object, with a combination of both being preferred. Subsequently, by examining the velocity profile or the image captured by the telescope, one can construct the initial guess of the 3D structure using the primitive structures provided in the interactive 3D module window of the platform. Various modifiers, such as particle systems and vertex modifiers, can then be utilized to customize the reconstructed image. This process serves as an initial approximation of the system's three-dimensional structure. Enhancing this approximation involves incorporating velocity and emissivity fields. Rendering the constructed structures generates synthetic images and spectra, enabling us to compare the model-generated images or spectra with the observed data. Following comparison, a series of refinements on the initial parameters can be performed to find a closer replication of the observed spectral profile or 3D image described by a 2D format. For comparison, we can employ any of the error estimation mechanisms, such as χ^2 minimization or Root Mean Square. Once we are satisfied with the result, we can discuss the obtained outcome and utilize it for further analysis as needed. The general work flow for modeling in SHAPE is shown in Fig. 3.4.

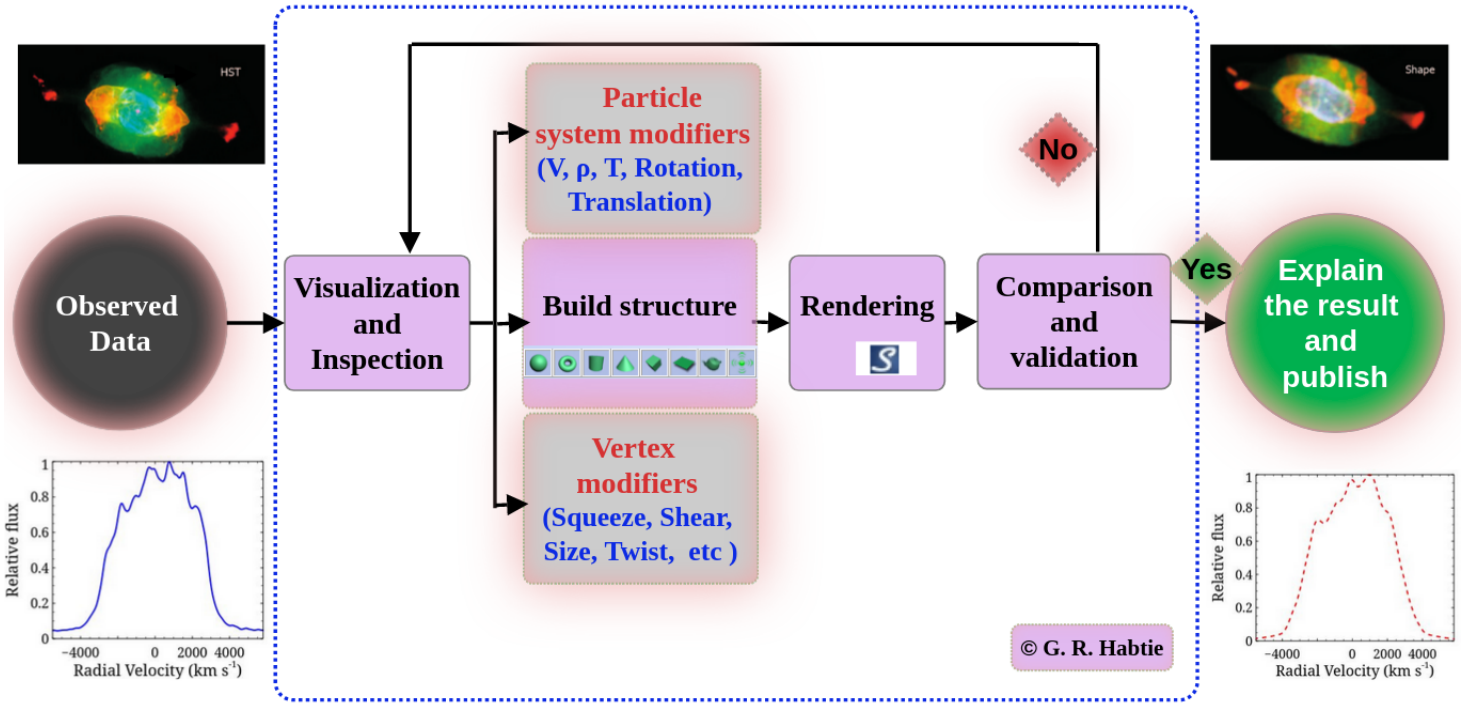

Fig. 3.4 SHAPE workflow diagram. The HCT image of the planetary nebula NGC 7009, on the left top and its SHAPE model on the right top are taken from Steffen et al. (2011).

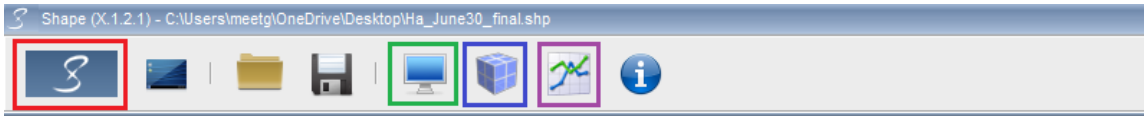

(a) Main toolbar

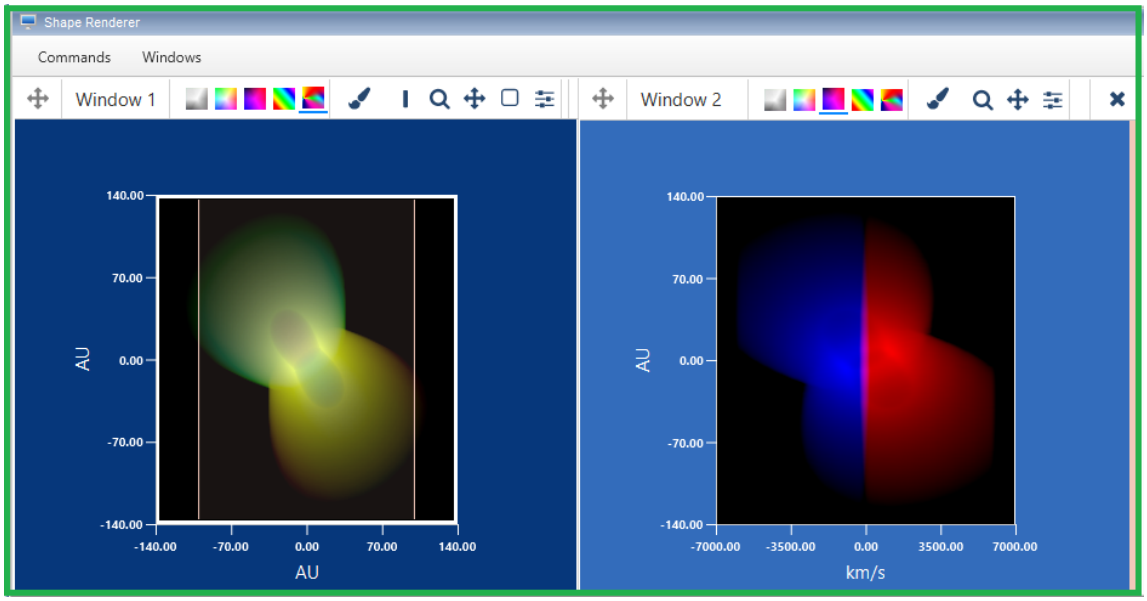

(b) Rendering window

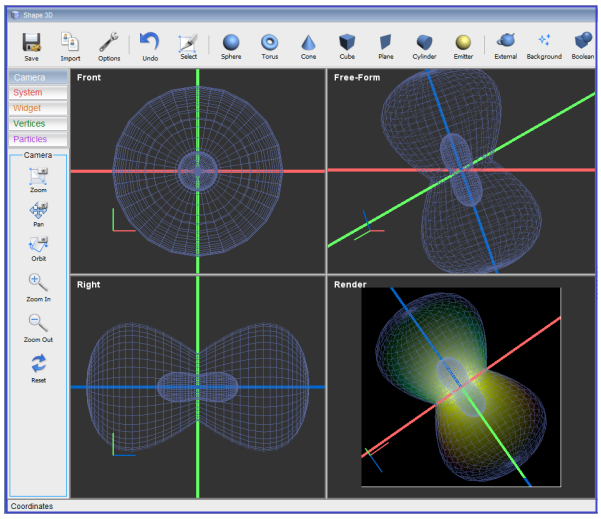

(c) 3D module

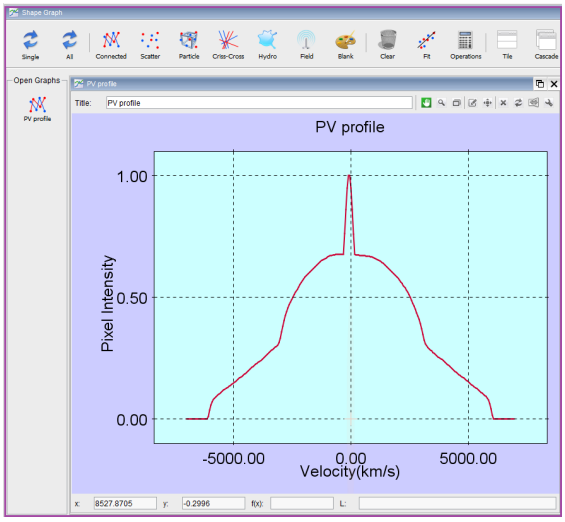

(d) Graph module

Fig. 3.5 Basic Components in the SHAPE Graphical User Interface; a) Toolbar displaying modules for rendering, 3D, and graphing. b) Rendering module containing input parameters. c) 3D module for configuring and adjusting the fundamental structure. d) Graph module displaying the generated spectrum or 1D line profile.

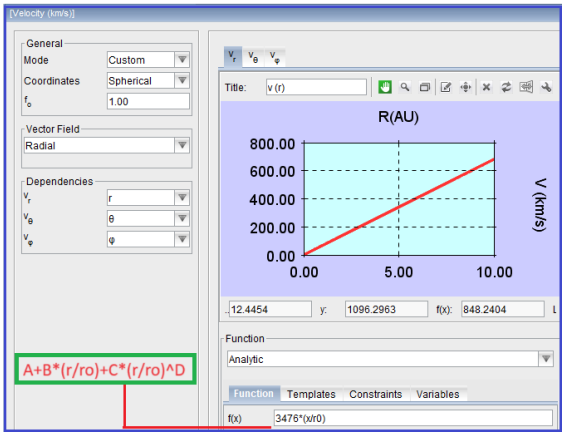

(a) Velocity field

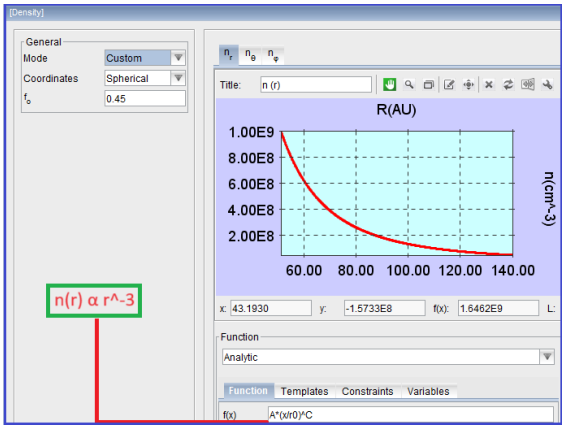

(b) Density field

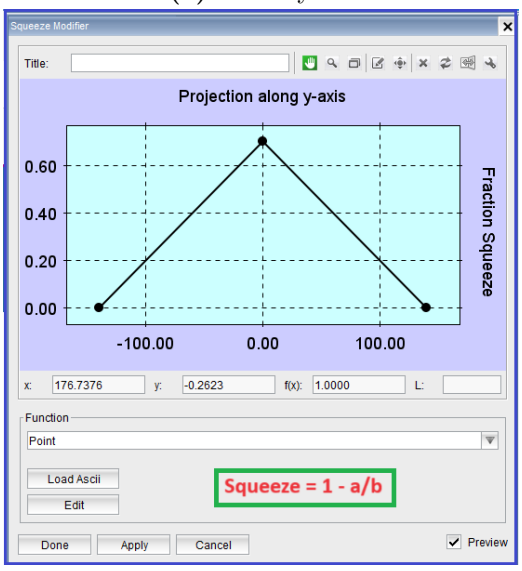

(c) Squeezing factor

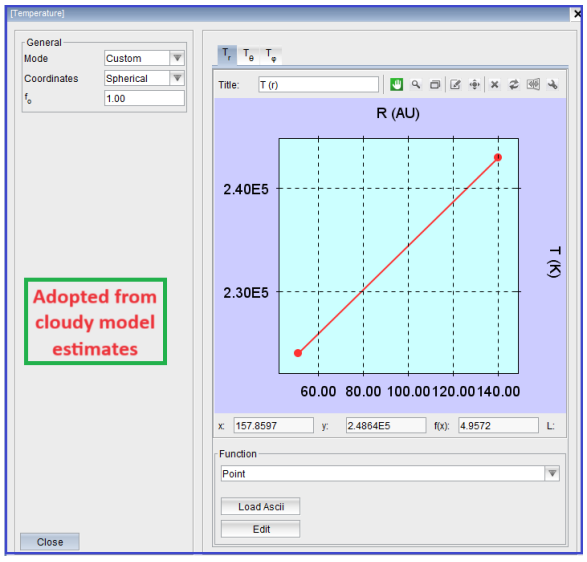

(d) Temperature field

Fig. 3.6 Few of the basic modifiers in SHAPE to establish and modify the particle system and vertex of the 3D structure. All the modifiers are the final state of the 3D structure constructed in Fig. 3.6

4 Study of the Fastest Classical Nova; V1674 Her

4.1 Introduction

The classical nova 'Nova Her 2021' (V1674 Her) was discovered by Seiji Ueda on 2021 June 12.5484 UT, (JD 2459378.0484), with a visual magnitude of 8.4 at a position $\alpha = 18^h57^m30^s.95$, $\delta = +16°53'9''.6$ (J2000) (CBET 4976)[1], which corresponds to the galactic coordinate $l = 048°.707$, $b = +06°.3114$. The nova reached its peak brightness on 2021 June 12.96 UT with a magnitude of V=6.14. The characteristic times t_2, t_3, and t_6 were estimated to be 1 day, 2.2 days, and 14 days, respectively (Woodward et al., 2021b).

The outburst of V1674 Her has been closely monitored across several wavelength domains, from radio to γ-rays (Aydi et al., 2021; Drake et al., 2021; Sokolovsky et al., 2021b; Vandenbroucke, 2021; Woodward et al., 2021b, 2022b). Li (2021) discovered an uncatalogued gamma-ray source at the nova's position using *Fermi-LAT* data in the range of 0.1-300 GeV. On 2021 June 14.41 UT (day 2.22), Swift observations with the *X-Ray Telescope (XRT)* detected the earliest X-ray emission from V1674 Her, while its super-soft source phase was detected on July 1.09 UT (day 18.9), (Drake et al., 2021; Page et al., 2021).

The Hϵ and Hζ lines displayed a high-velocity multiple absorption dip reaching $\sim$6500 kms^{-1} (Kuin et al., 2021). During the early phases of V1674 Her's evolution,

[1] http://www.cbat.eps.harvard.edu/unconf/followups/J18573095+1653396.html

optical and infrared observations revealed the presence of P-Cygni and flat-topped Balmer spectral line profiles. These profiles exhibited extensive substructures and line widths that increased over time, eventually reaching ∼11,000 kms^{-1} in width (Aydi et al., 2021; Woodward et al., 2021b, and references therein).

Radio observations with the *Karl G. Jansky Very Large Array (VLA)* at 2.6, 3.4, 5.1, 7.0, 13.7, 16.5, 31.1, and 34.9 GHz unveiled non-thermal emission (Sokolovsky et al., 2021b). Multiple observations suggested that the object might be classified as a Fe II type nova (Albanese et al., 2021; Aydi et al., 2021; Sokolovsky et al., 2021a; Woodward et al., 2021e), primarily due to the presence of several Fe II lines. Nevertheless, spectral analysis from observations conducted on the seventeenth day and onwards from the maximum magnitude revealed the emergence of several triply and more ionized neon lines (Wagner et al., 2021; Woodward et al., 2022b). Wagner et al. (2021) proposed that this nova belongs to a neon-type subclass of CNe originating from an ONe WD.

In this chapter, we study the nova V1674 Her, 2021 during the initial month following its outburst. We model the observed spectra using the photoionization code CLOUDY (V.17.02 (Ferland et al., 2017)). From the best-fitting model, we estimate the chemical and physical properties of the nova system, as well as their evolution. The photoionization modelling procedures, results, and discussions are presented in Section 6.3.3 of this chapter. We also employ SHAPE (Steffen and Koning, 2017, 2012), a morpho-kinematical software, to analyse and dissect the 3D geometry and kinematical structure of the ejecta (Section 4.3.4). The results obtained are summarised in Section 4.4.

4.2 Observations

In the present study, we used spectroscopic data collected from days -0.032 to +28.8 following the outburst of V1674 Her. The data was acquired from the publicly accessible Astronomical Ring for Access to Spectroscopy Database (ARAS Database[2]; Teyssier

[2]https://aras-database.github.io/database/novae.html

(2019)). The ARAS symbiotic project serves as an archival repository for data and encompasses a network of small telescopes, ranging from 20 to 60 cm in diameter, fitted with spectrographs with resolutions spanning from R $\sim$ 500 to 15,000, covering the wavelength range of 3600 to $\sim$ 9000 Å. In total, a set of 20 optical spectra (ranging from $\sim$ 3700 to 7800 Å) with resolutions varying from 300 to 1200 were employed. These spectra were acquired during the first month subsequent to the eruption and were contributed by various observers from different observatories. The observational details and the respective observatories are outlined in Table 4.1. The spectroscopic data were processed utilising the Integrated Spectroscopic Innovative Software (ISIS[3]) following standard procedures. Additionally, we analysed optical *BVRI* photometric data obtained from the American Association of Variable Star Observers (AAVSO)[4] database to investigate the photometric behaviour of the nova during the initial month post-outburst.

[3]http://www.astrosurf.com/buil/isis-software.html
[4]https://www.aavso.org/

Table 4.1 Log of optical spectral observation of V1674 Her.

MJD	Date 2021 (UT)	t[a](days)	Observer	Observatory	Spectrograph	Camera	R[b]	Coverage (Å)	TTE[c](s)
59378.454	June 12.927	-0.032	DBO[d]	WCO[i]	LISA	SXVR-H694	1023	3701-7391	4778
59379.447	June 13.947	0.988	DBO[d]	WCO[i]	LISA	SXVR-H694	941	3901-7381	3400
59381.445	June 15.945	2.986	DBO[d]	WCO[i]	LISA	SXVR-H694	1036	3900-7380	3041
59383.485	June 17.985	5.007	RLE[e]	THO[j]	ALPY[n]	ATK428	532	3760-7880	1821
59385.428	June 19.928	6.969	PAD[f]	VNT[k]	LISA	Atik 460EX	1027	3900-7550	3041
59387.364	June 21.864	8.905	PAD[f]	VNT[k]	LISA	Atik 460EX	1037	3900-7550	4867
59388.493	June 22.992	10.000	RLE[e]	THO[j]	ALPY[n]	ATK428	523	3800-7850	6485
59389.356	June 23.856	10.897	PAD[f]	VNT[k]	LISA	Atik 460EX	1056	3900-7550	3038
59391.721	June 26.221	13.230	FAS[g]	DCO[l]	LISA	Atik414ex	1068	3716-7304	5078
59393.367	June 27.867	14.908	PAD[f]	VNT[k]	LISA	Atik 460EX	1122	4000-7550	3038
59396.402	June 30.901	17.920	DDJ[h]	LSS[m]	ALPY[o]	Atik428	347	3750-7415	4519
59396.431	June 30.931	17.972	PAD[f]	VNT[k]	LISA	Atik 460EX	1149	4100-7550	1810
59397.408	July 01.908	19.880	PAD[f]	VNT[k]	LISA	Atik 460EX	1131	4200-7550	8010
59400.425	July 04.925	22.920	DDJ[h]	LSS[m]	ALPY[o]	Atik428	348	3750-7415	4519
59400.414	July 04.914	22.886	PAD[f]	VNT[k]	LISA	Atik 460EX	1132	4150-7550	6018
59402.411	July 06.910	24.883	PAD[f]	VNT[k]	LISA	Atik 460EX	1179	4000-7550	6020
59403.366	July 07.866	25.838	PAD[f]	VNT[k]	LISA	Atik 460EX	1120	4100-7500	6021
59404.372	July 08.872	26.844	PAD[f]	VNT[k]	LISA	Atik 460EX	1154	4100-7500	4816
59405.394	July 09.894	27.880	DDJ[h]	LSS[m]	ALPY[o]	Atik428	347	3762-7531	5425
59406.452	July 10.952	28.924	PAD[f]	VNT[k]	LISA	Atik 460EX	1138	4150-7500	4815

Note: [a]Number of days counted from t_0 (2021 June 12.959 UT, MJD 59378.459), [b]Resolution, [c]Total Time of Exposure, [d]David Boyd, [e]Robin Leadbeater, [f]Pavol A. Dubovsky, [g]Forrest Sims, [h]Daniel Dejean, [i] *West Challow Observatory* in England, [j] *Three Hills Observatory* in England, [k] *Vihorlat National Telescope* in Slovakia, [l] *Desert Celestial Observatory* in USA, and [m] *Labastide St Sernin* in France, ALPY^n represents ALPY200 lines/mm, and ALPY^o represnets ALPY_slit35

4.3 Results and Discussion

4.3.1 Optical light curve

The optical $BVRI$ light curve of nova V1674 Her over the initial 140 days, crafted using the AAVSO database, is shown in Fig. 6.1. Analysing the light curve, we ascertain that the peak of brightness, $V = 6.13$, was attained on 2021 June 12.959 UT (JD 2459378.459), inline with Munari et al. (2021b); Woodward et al. (2021b). As such, we adopted 2021 June 12.959 UT as the reference time for the outburst, denoted as t_0. Calculations for the characteristic times, t_2 and t_3, in V and B bands yield values of 0.90 and 1.94 days, and 1.19 and 6.39 days, respectively. It is notable that the B band has a more gradual rate of decline compared to the V band. This is because novae fade in brightness with age and become bluer in B-V (Van den Bergh and Younger, 1987). The $t_2 = 0.904$ days seems to be the quickest brightness decline time of any nova. This shows that the nova V1674 Her is the fastest classical nova ever observed, which is consistent with Wagner et al. (2021); Woodward et al. (2021b, 2022b). Other notable swift CNe include V838 Her, 1991 ($t_2 = 1$ day), V1500, 1975 ($t_2 = 2$ days), V1500 Cyg, 1975 ($t_2 = 2$ days), and V4160 Sgr, 1991 ($t_2 \sim 2$ days) (Strope et al., 2010). The optical light curve depicted in Fig. 6.1 demonstrates a smooth, rapid decline in brightness, suggesting that the nova did not produce an appreciable amount of dust.

4.3.1.1 Reddening and distance calculation

Using the established optical reddening law, which correlates interstellar extinction with colour excess as; $A_\lambda = R_\lambda E(B-V)$, we calculated the interstellar extinctions in the $BVRI$ -bands, corresponding to wavelengths of: 4400, 5500, 6540, and 8060 Å, respectively. We adopted the total-to-selective extinction ratio (R_λ) values: $R_B = 4.1$, $R_V = 3.1$, $R_R = 2.3$, and $R_I = 1.5$ (Richmond et al., 1994). The reddening value for V1476 Her has been calculated as $E(B-V) = 0.55$ (Munari et al., 2021b; Woodward et al., 2021e). Therefore, we employed the same value of $E(B-V) = 0.55$ in this study. Consequently, we derived the interstellar extinction values in the $BVRI$ -bands to be:

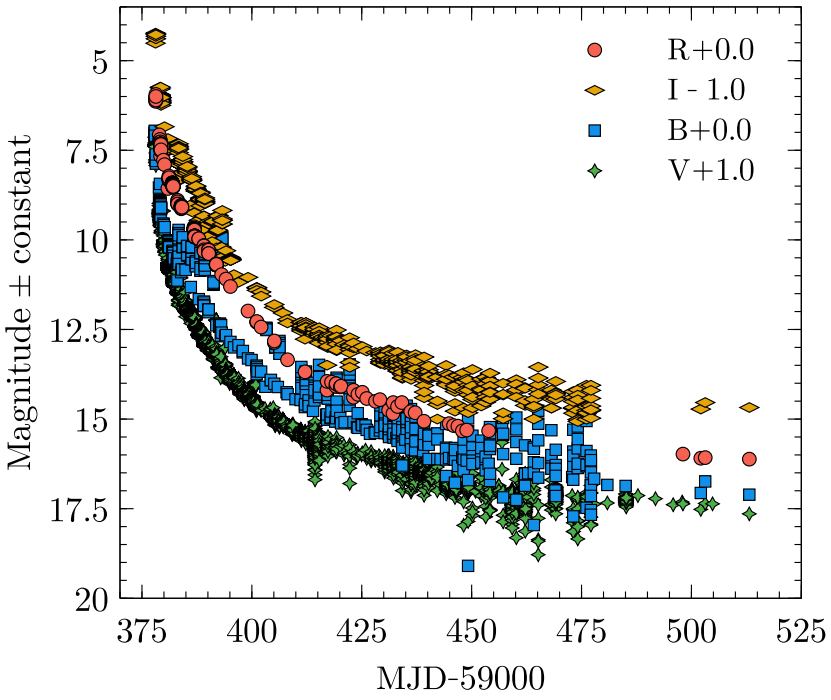

Fig. 4.1 *BVRI* Light curves of Nova Her 2021 generated using optical data from AAVSO. Offsets are applied to the V and I bands (as indicated in the legend) for the sake of clarity.

$A_B = 2.255$, $A_V = 1.705$, $A_R = 1.265$, and $A_I = 0.825$. Subsequently, we computed the absolute magnitude (M_λ) employing the Maximum Magnitude-Rate of Decline (MMRD) equation given below (della Valle and Livio, 1995).

$$M_\lambda = -7.92 - 0.81 \arctan\left(\frac{1.32 - \log t_2(\lambda)}{0.23}\right), \tag{4.1}$$

where $t_2(\lambda)$ corresponds to the t_2 values in the *BVRI* -bands, derived from AAVSO photometric data. These values are calculated to be: $t_2(B) = 1.149$ days, $t_2(V) = 0.904$ days, $t_2(R) = 1.96$ days, and $t_2(I) = 1.226$ days. Using these values, we calculated the absolute magnitudes in each band to be: $M_B = -9.057$, $M_V = -9.046$, $M_R = -9.013$, and $M_I = -9.043$. Subsequently, we employed the distance modulus equation to calculate distance values, which is given by,

$$m_\lambda - M_\lambda = 5log_{10}\left(\frac{d_\lambda}{10}\right) + A_\lambda, \tag{4.2}$$

where m_λ, d_λ, and A_λ are the apparent magnitude, distance, and extinction in the $BVRI$ -bands, respectively. The values of m_λ at t_2 were derived from the AAVSO photometric data as follows: $m_B = 8.962$ mag., $m_V = 8.147$ mag., $m_R = 7.901$ mag., and $m_I = 7.248$ mag. Using these values, we calculated distance of 4.97 kpc in V band, 5.60 kpc in B band, 5.48 kpc in R band, and 4.91 kpc in I band. Combining all these, the average measured distance across the four bands is found to be $5.24\pm^{+0.36}_{-0.33}$ kpc. Our estimate is in a good agreement previous estimates, e.g. Woodward et al. (2021b) estimated the distance in the V band to be $4.75^{+1.3}_{-1.0}$ kpc from the combination of MMRD with intersection of the extinction versus distance curve, and Bailer-Jones et al. (2021) estimated a distance of $6.0\pm^{+3.8}_{-2.8}$ kpc using *Gaia*-EDR3.

4.3.1.2 White dwarf mass and radius

The decline time t_3 can be utilized to estimate the mass of the WD, as at t_3, ∼85% of the entire shell mass is expelled (Shara, 1981). This indicates that a lengthy t_3 signifies a substantial ejecta shell mass and a relatively small WD mass. To compute the WD mass ($M_{\rm WD}$) of Nova V1674 Her, we employed the ensuing relationship, equation (4.3) (Livio (1992)):

$$t_3 = C\left[\frac{M_{\rm WD}}{M_{ch}}\right]^{-1}\left[\left(\frac{M_{\rm WD}}{M_{ch}}\right)^{-2/3} - \left(\frac{M_{\rm WD}}{M_{ch}}\right)^{2/3}\right]^{3/2} \text{days}, \tag{4.3}$$

where $C = 51.3$ (a constant calibrated from V1500 Cyg) (Livio, 1992, and references therein), $M_{ch} = 1.4\ M_\odot$ (Chandrasekhar mass limit), and $t_3 = 1.935$ days (Section 6.3.1). By solving equation (4.3) and plugging in the relevant values, we arrive at an estimate of $M_{\rm WD} \sim 1.36 M_\odot$. Such a substantial mass, nearing the Chandrasekhar limit, is necessary to account for the high ejection velocities ($\sim 6000\ \mathrm{km\,s^{-1}}$) (Woodward et al., 2021b). Drake et al. (2021) also estimated $M_{\rm WD} > 1.05 M_\odot$. The mass of WDs are a principal distinction between ONe and CO type novae. In case of ONe novae $M_{\rm WD} > 1.2\ M_\odot$, whereas in case of CO novae $M_{\rm WD} < 1.2 M_\odot$ (Gehrz et al., 1998). A more recent work by Doherty et al. (2015); Weidemann (2000) reported that the WD

mass in ONe novae is $> 1.0 M_{\odot}$. Using the following expression (Warner, 1995),

$$R_{\rm WD} \approx 0.90 \left[1 - \frac{M_{\rm WD}}{M_{ch}}\right]^{1/2} R_{\oplus}, \tag{4.4}$$

the possible smallest radius of the WD $R_{\rm WD}$ is $\sim$ 969 Km ($\sim$ 0.15 $R_{\oplus}$), where $R_{\oplus}$ denotes the radius of the Earth.

4.3.2 Spectral evolution

The spectral evolution of Nova V1674 Her during the initial month, spanning wavelengths of: $\sim$ 3700 – 7400 Å, 3920 – 7330 Å, 4170 – 7330 Å and 3800 – 7300 Å, is presented in Fig. 4.2 (a), 4.2 (b), 4.2 (c) and 4.3, respectively. All the notable emission features are identified. Fig. 4.4 illustrates the blue shifting of the P Cygni profile over time. All spectra are normalised to the H β line and corrected for reddening using $E(B-V) = 0.55$. The flux and widths of emission lines profiles were measured interactively using the tools provided by IRAF (Image Reduction and Analysis Facility)[5]. Analysis of dereddened spectra over the initial twenty-eight days, showed a notable reduction in observed flux during this period. Within the initial month of the outburst, the spectral evolution of nova V1674 Her underwent four distinct phases: pre-maximum, early decline, nebular, and coronal stages.

4.3.2.1 Pre-maximum Stage

The pre-maximum spectrum, observed on 2021 June 12.927 UT (i.e., 0.032 days before the visual maximum), is illustrated in Fig. 4.2 (a). This spectrum prominently featured Balmer, Fe II and He I lines, accompanied by distinct narrow and strong P Cygni profiles. The spectrum exhibited relatively weaker hydrogen Balmer emission lines, encompassing H 8, 3771 Å. This was because at this stage, a significant portion of the line-forming region was optically thick, leading to the attenuation of emission lines. The development of a large, optically thin region before reaching visual maximum is

[5] http://iraf.noao.edu/

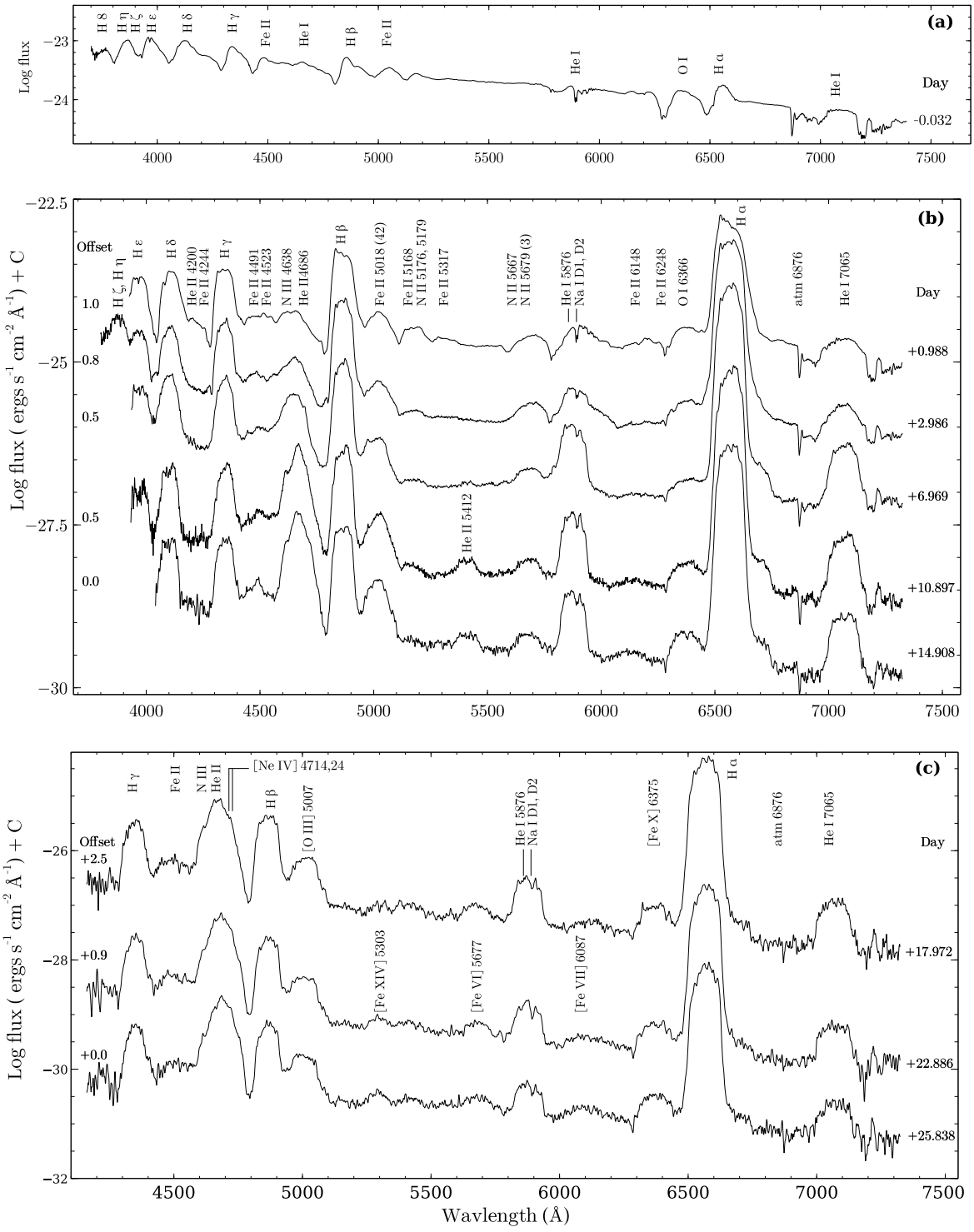

Fig. 4.2 Evolution of V1674 Her's medium-resolution optical spectra acquired: (a) on 2021 June 12.923 UT (-0.032 d); (b) from 2021 June 13.947 (+0.99 d) to June 27.867 UT (+14.91 d); and (c) from 2021 June 30.931 (+17.97 d) to July 07.866 UT (+25.84 d). For the sake of clarity, the spectra in (b) and (c) are offset by the amount indicated on the left side of the figure. The ordinate scale is logarithmic to emphasize the visibility of weaker features relative to the emission feature of H α . 'atm' stands for atmospheric absorption observed at around 6876 Å.

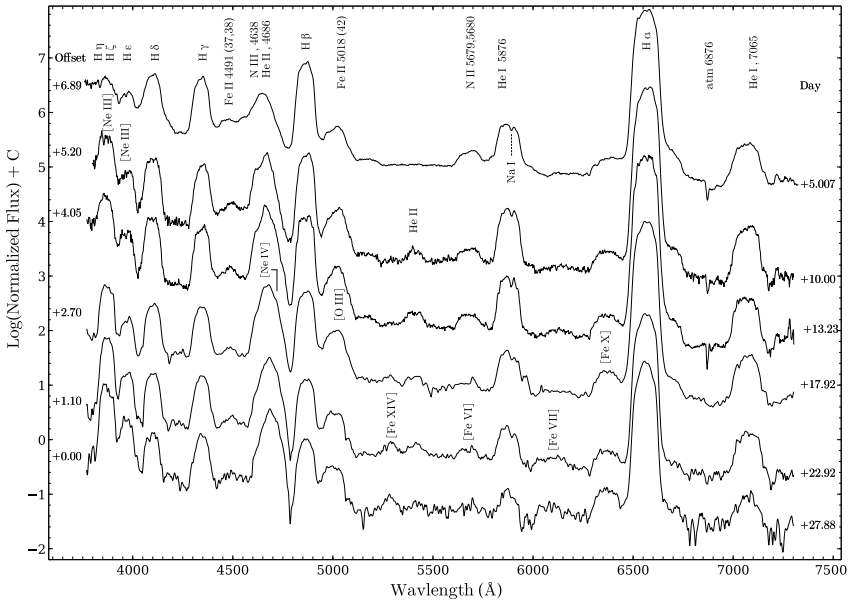

Fig. 4.3 Evolution of V1674 Her's low-resolution optical spectra obtained from 2021 June 17.985 (5.007 d) to July 09.894 (27.880 d). For the sake of clarity, the spectra are offset by the amount indicated on the left side of the figure. The ordinate scale is logarithmic to emphasize the visibility of weaker features relative to the emission feature of H α . 'atm' stands for atmospheric absorption.

an unusual occurrence for a nova (Schwarz et al., 2001). We noticed that the H η 3835 Å and H ζ 3889 Å lines appeared blended at this stage. The P-Cyg profiles of H α , He I, H β , and H γ were blue-shifted from the central maxima by -3598.88 ± 42, -3388.81 ± 46 , -3519.73 ± 50, and -3575 ± 60 km s^{-1}, respectively. Notably, these blue shifts were relatively lower for each line, as the blue shift of the P Cygni absorption line tends to increase after the outburst (refer to Fig. 4.4).

In addition to the P Cygni absorption features, a few other notable absorption features have also been observed among the considered spectra, including the pre-maximum spectrum. Firstly, the spectra displayed two adjacent absorption features on top of the He I 5876 Å line, namely: Na I D1 and Na I D2 lines. Notably, the Na I D2 line consistently appeared stronger than the Na I D1 line in all cases (see Fig. 4.5). These absorption lines might be attributed to the in-homogeneous nature of the ejecta, consisting of discrete emitting and absorbing clouds with a low filling factor (Williams et al., 1991). Despite a slight variation in the strength of these absorption lines, the

feature remains consistently present in every spectrum acquired within the initial month following the outburst. These features were evident in our medium-resolution spectra, as shown in Fig. 4.2, 4.3, 4.5, and 4.8. The Na I D1 and D2 absorption lines were red-shifted with respect to the rest frame (radial velocity, $V_{\rm rad} = 0\,{\rm km\,s^{-1}}$) of the He I 5876 Å line, by $+1078.00\pm^{+49.31}_{-64.09}$ and $+773.00\pm^{+57.72}_{-34.80}$ $\rm km\,s^{-1}$, respectively. These values were obtained by averaging the radial velocities of corresponding Na I D1 and D2 lines observed on days: 0.99, 8.91, 14.91, and 25.84. Secondly, all the spectra, including the pre-maxima stage spectrum, consistently exhibit a telluric feature at a wavelength of 6876 Å (see Fig. 4.2). Over time, the intensity of these absorption features diminished; nevertheless, their distinctive presence persisted in all spectra.

4.3.2.2 Early Decline Stage (0 to ∼10 days)

The set of spectra presented in Fig. 4.2 (b) are taken during the early decline phase. During this phase, the spectra displayed prominent and broad recombination lines, encompassing Balmer and Helium lines, as well as various iron multiplets. These spectra undeniably exhibited the typical features of Fe II novae, characterised by numerous low-excitation Fe II lines (Williams, 2012). Transitioning from the pre-maximum stage to the early decline stage, these recombination lines, notably the Balmer lines, became considerably stronger in relation to the continuum level. However, as time progressed, these emission lines gradually reduced in width, a trend commonly observed in novae initiated by thermonuclear runaways (TNRs) (Cassatella et al., 2004; Shore et al., 1996; Williams, 2012). This phenomenon is attributed to the diminishing contribution of the outermost ejecta region as they move away from the central object (Cassatella et al., 2004). As the expanding ejecta thin out, the ionization of the ejecta intensifies, owing to the ongoing illumination and ionization from the hot central ionizing source.

Fig. 4.4 illustrates the broad emission lines of H α , He I 5876, H β , and H γ , accompanied by their respective P Cygni profiles on days -0.032, +0.99, +2.99, and +6.969. On day 0.988, these P Cygni absorption lines exhibited blue shifts of -4988.93 ± 42, -4849.57 ± 46, -4841.05 ± 39, and -3998.23 ± 62 $\rm km\,s^{-1}$, relative to

the centre of emission line of H α , He I, H β , and H γ , respectively. Notably, the P Cygni profiles exhibited greater shifts compared to the pre-maximum stage. This shift is attributed to the increasing ejection velocity of novae with distance at least during the free expansion phase. Gradually, the P Cygni absorption features diminished and vanished in later days.

4.3.2.3 Nebular Phase ($\sim$ 10 to 22 days)

In this phase, a rapid reduction in the intensity of neutral emission lines has been observed. For instance, the measured flux in the H α , H β , H γ , H δ , He I 5876 Å, and He I 7065 Å emission lines is 3.69, 3.92, 4.00, 4.18, 3.8, and 3.22 times lower on day 10.897 than it was on day 6.969, respectively. This swift spectral progression indicates that almost all of the ejecta's clumps, have undergone ionization, signifying that the ejecta has entered the optically thin phase, commonly known as the nebular stage. During this phase, the collisionally excited nebular lines become prominent in the expanding ejecta's spectra (Schwarz et al., 2001). On day 10.00, the Balmer lines, H η and H ζ , became prominent in the observed spectra (see Fig. 4.3). This is due to the emergence of forbidden emission lines, such as [Ne III] 3869 Å, in the spectrum (see section 6.3.3.3, for the detail). Notably, the blended line at the spot of H η , H ζ , and [Ne III] 3869 Å stands out as the strongest emission line on this date, except for H α . These spectral characteristics often indicate the onset of the nebular phase. Similarly, H ϵ showed a significant increase in intensity, due to the appearance of [Ne III] 3968 Å(see section 6.3.3.3, for the detail). In Fig. 4.6, we provide a visualisation of how the intensity and structure of the emission lines changed between day 5.00, 10.00, and 22.90. These two lines, [Ne III] at 3869 and 3968 Å, were previously identified in nova V1674 Her on day 17.0 (Wagner et al., 2021; Woodward et al., 2022b).

The N III 4638 Å and He II 4686 Å emission lines displayed notably low intensity relative to the continuum level in the initial stages. However, they later exhibited a significant increase, and on day 14.908, they became the second strongest emission line after H α . This rapid evolution of the profile wasn't only due to the contributions of

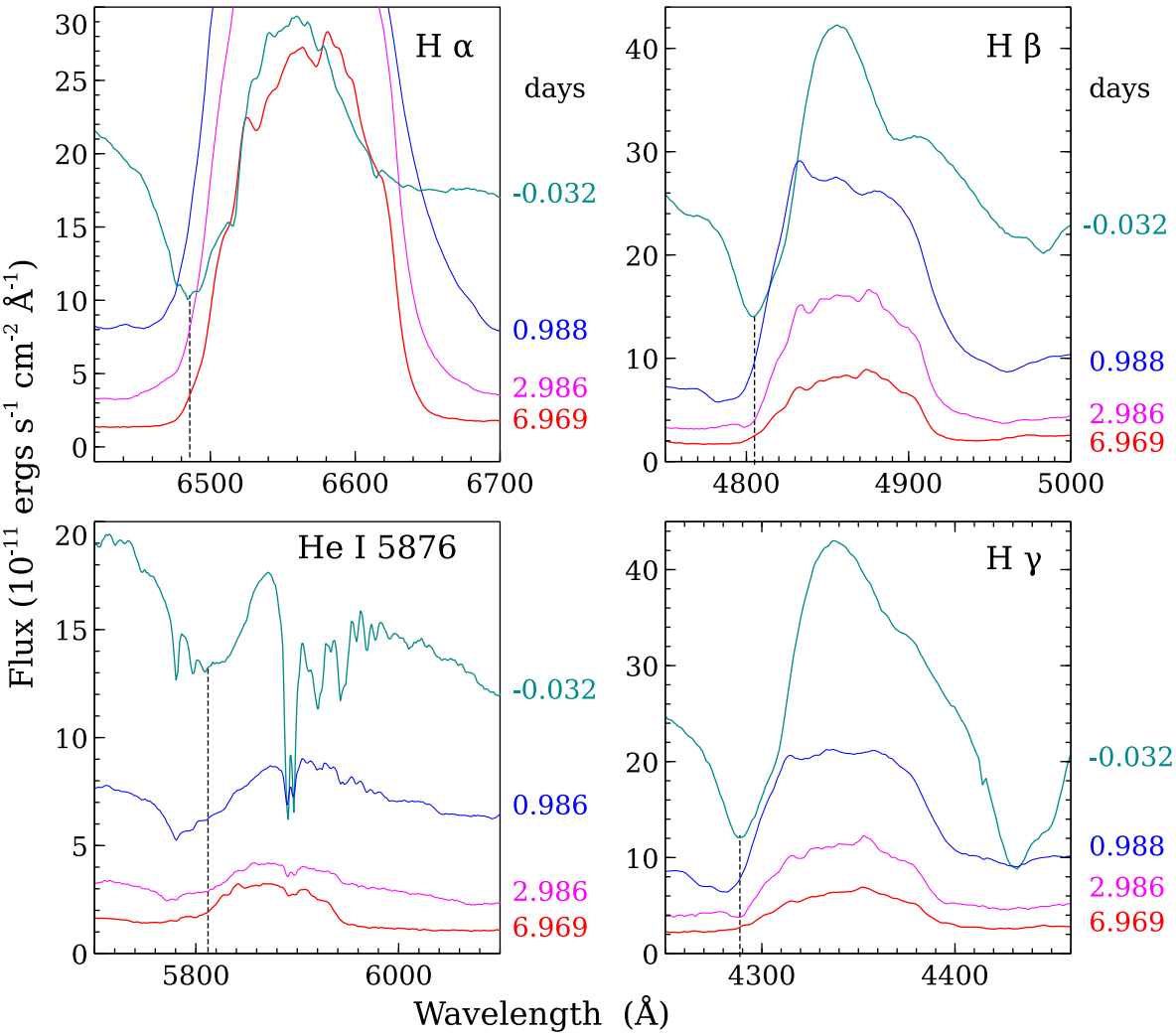

Fig. 4.4 Emission line profiles of H α , He I, H β , and H γ , along with their associated P Cygni profiles, displayed a blue shift as time progressed. The spectra are flux calibrated and deredenned with an extinction value *E(B-V)* of 0.55. In order to combine everything, we subtracted constants 19, 30, 35, and 50 from the flux component of the day -0.032 emission line profiles of the H α , He I, H β , and H γ lines, respectively. All these constants are in the same unit of flux.

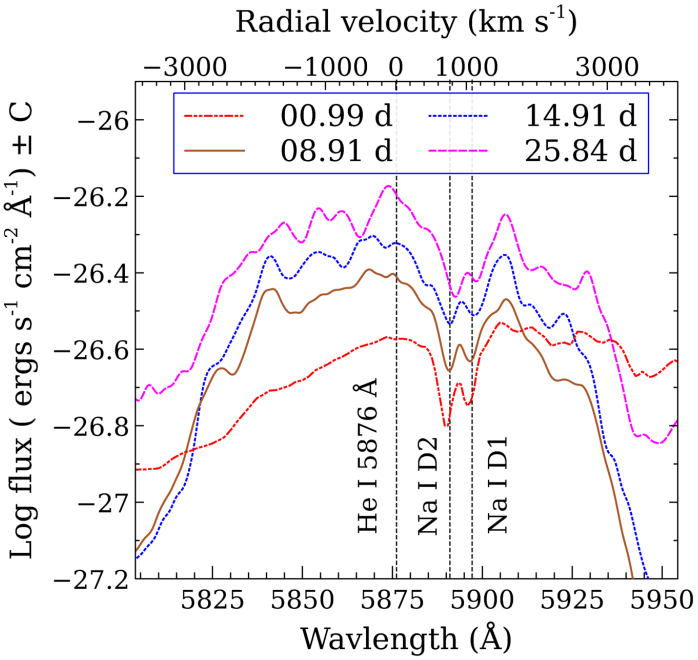

Fig. 4.5 Emission line profiles of He I 5876 Å on 2021 June 13 (0.99 d), June 21 (8.91d), June 27 (14.91 d), and July 07 (25.84 d). These emission lines show the Na I D1 and D2 doublets clearly. The Gray vertical dashed line represents radial velocity, $V_{rad} = 0$ km s^{-1}(i.e., 3876 Å), whereas the black dotted lines represent Na I D2 and D1 at $V_{rad} = 773$ and 1078 km s^{-1}, respectively, in left-to-right order.

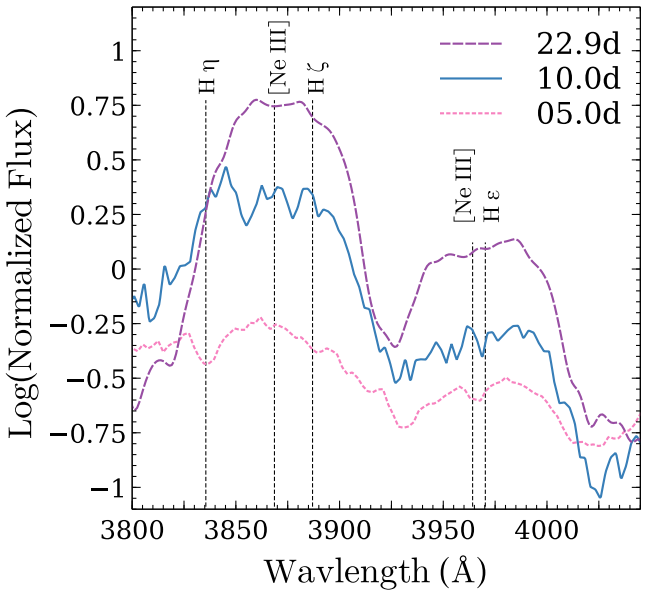

Fig. 4.6 Emission features of Balmer lines (H η 3835 Å, H ζ 3889 Å, and H ϵ3970 Å), on 2021 June 17.99 (5.0 d), June 22.99 (10.0 d), and July 04.925 (22.92 d). Starting from day 10.0 and onward, H η and H ζ became blended with [Ne III] 3869.07 Å, while H ϵ became blended with [Ne III] 3967.69 Å.)

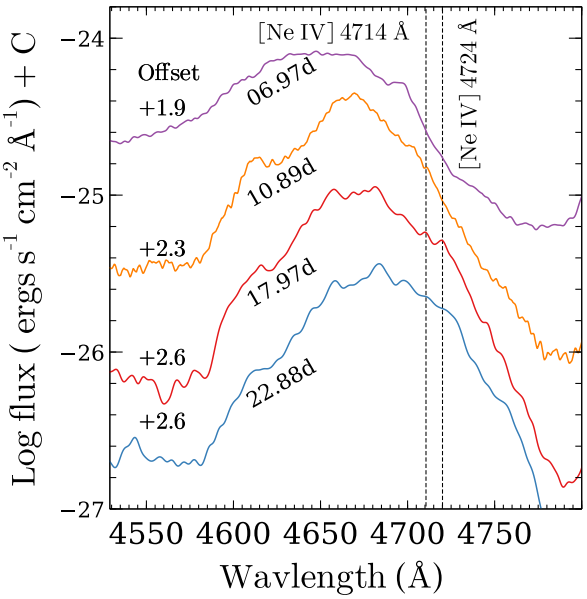

Fig. 4.7 Emission line profiles of N III 4638 Å, and He II 4686 Åon 2021 June 19.93 (06.97 d), June 23.86 (10.99d), June 30.93 (17.97 d), and July 04.91 (22.88 d). The black dashed vertical lines indicate the emergence of [Ne IV] 4714 and 4724 Å lines starting from at least day 17.97 and onward.

N III 4638 Å, and He II 4686 Å, but also the [Ne IV] 4714, 4724 Å lines on the right side of the profile (see the upper spectra in Fig. 4.2 (c) and 4.7). Although the [Ne IV] 4714, 4724 Å lines might have appeared earlier, it was on 2021 June 30 (17.972 d) that both forbidden neon lines became clearly observable. The presence of these neon lines in the spectra has also been reported by various researchers; for instance, Wagner et al. (2021) reported the detection of [Ne IV] 4714 and 4724 Å on day 15. Similarly, on day 17.92 (2021 June 30.90) we observed a notable increase in intensity in the line profile identified as Fe II 5018 Å during the early decline phase. This increase is mainly due to the emergence of [O III] 5007 Å in the spectrum (see Section 6.3.3.3 for details). The appearance of the [O III] line in the spectrum is usually considered a confirmation of the onset of the Nebular phase in the system. The presence of [O III] 5007 Å was also observed by Rudy et al. (2021) in the spectrum of day 15.00 (2021 June 28).

4.3.2.4 Coronal Phase (after ∼ 22 days)

The bottom two spectra in Fig. 4.2 (c) and 4.3 illustrate the emergence of several coronal emission lines commencing around day 22.89. It is possible that certain lines might have emerged prior to day 22.89. For example, a broad spectral line was observed on 2021 June 30, at ∼ 6375 Å, which aligns with the typical location of the coronal line [Fe X] . However, uncertainty remained whether this line is primarily influenced by the oxygen line, which appeared in the initial spectra phases, or by the forbidden iron lines resulting from an increase in ejecta temperature. From day 22.89 onwards, well-resolved higher forbidden ionization lines of iron, such as [Fe XIV] 5303, [Fe VI] 5677 Å, [Fe VII] 6087, and [Fe X] 6375 Å, became prominent in the spectra. According to the Tololo spectral classification outlined in Williams et al. (1991), it is explained that under any other circumstance of line strength, the nova spectrum can be considered in the coronal phase once the emission line [Fe X] 6375 Å has appeared and is stronger than [Fe VII] 6087 Å. These conditions are met for the case of V1674 Her on day 22.886 and thereafter. Therefore, based on spectral features and the appearance of forbidden emission lines of high ionization, we conclude that Nova Her 2021 has already entered the coronal phase by day 22.

According to Woodward et al. (2021b), the nova V1674 Her entered the coronal phase 11.5 days after the outburst (on 2021 June 24) in the IR band, marking the earliest coronal phase onset of any recorded classical novae. Prior to the discovery of V1674 Her, two of the fastest novae known were V1500 Cyg (with $t_2 = 2$ days) and V838 Her (with $t_2 = 2$ days), which entered the coronal phase on days 29 and 17 following the outburst, respectively (Benjamin and Dinerstein, 1990; Chandrasekhar et al., 1993). Hence, it is unsurprising that Nova V1674 Her, 2021, exhibits strong coronal emission lines at a quicker rate than slower novae, some of which barely generate these lines (Benjamin and Dinerstein, 1990; Ferland and Shields, 1978). However, optical spectra acquired during this period did not confirm the rapid onset of the coronal phase. This divergence is attributed to the lower opacity of IR compared to

optical and UV, resulting in the appearance of coronal lines in IR earlier than in the optical range (Gehrz et al., 1998).

4.3.2.5 Line Profiles

In Fig. 4.8, we illustrate the evolution of recombination line profiles for the H α , H β , H γ , He I 5876 Å, and He I 7065 Å lines. After the outburst, these lines exhibited intricate profiles characterised by a broad central component accompanied by multiple sub-peaks on the top of each line profiles. Broad lines denote fast-moving shell ejecta (Naito et al., 2022), while broad wings and peaks in emission lines indicate density and velocity in-homogeneities (i.e., slow-moving clumps embedded in diffuse gas) (Schwarz et al., 2007). On day +0.99, the emission line profiles of H α and H β appeared stronger on the blue side than the red side of the profile, resulting in an inclined top of the line profiles (see Fig. 4.8). This indicates asymmetric dispersion of the ejecta along the line of sight, involving both approaching and receding components. However, this condition didn't last long; by day +2.96, the red side of the H α and H β line profiles appeared somewhat stronger than the blue side. Further details are available in the morpho-kinematic section of this chapter (Section 4.3.4).

The evolution of Balmer line flux ratios of H α and H γ relative to H β from day +0.988 to +28.924 is shown in Fig. 4.9. In the graph, we have included two horizontal lines to comprehend how closely the observational results align with the theoretically estimated value of the Balmer line flux ratio for Case B at 10^4 K, as calculated by (Osterbrock, 1989). The upper and lower horizontal lines represent H α / H β and H γ / H β ratios, having values of 3.08 and 0.46 respectively (Osterbrock, 1989; Schwarz et al., 2001). As depicted in the Fig. 4.9, the H α / H β ratio during the period between days +6.969 and +14.908, as well as the overall H γ / H β ratio, exceeds the expected value based on recombination under optically thin circumstances. This stipulates the presence of a high-density region contributing to the emission. This result is inline with the photoionization model result discussed in Section 6.3.3.2.

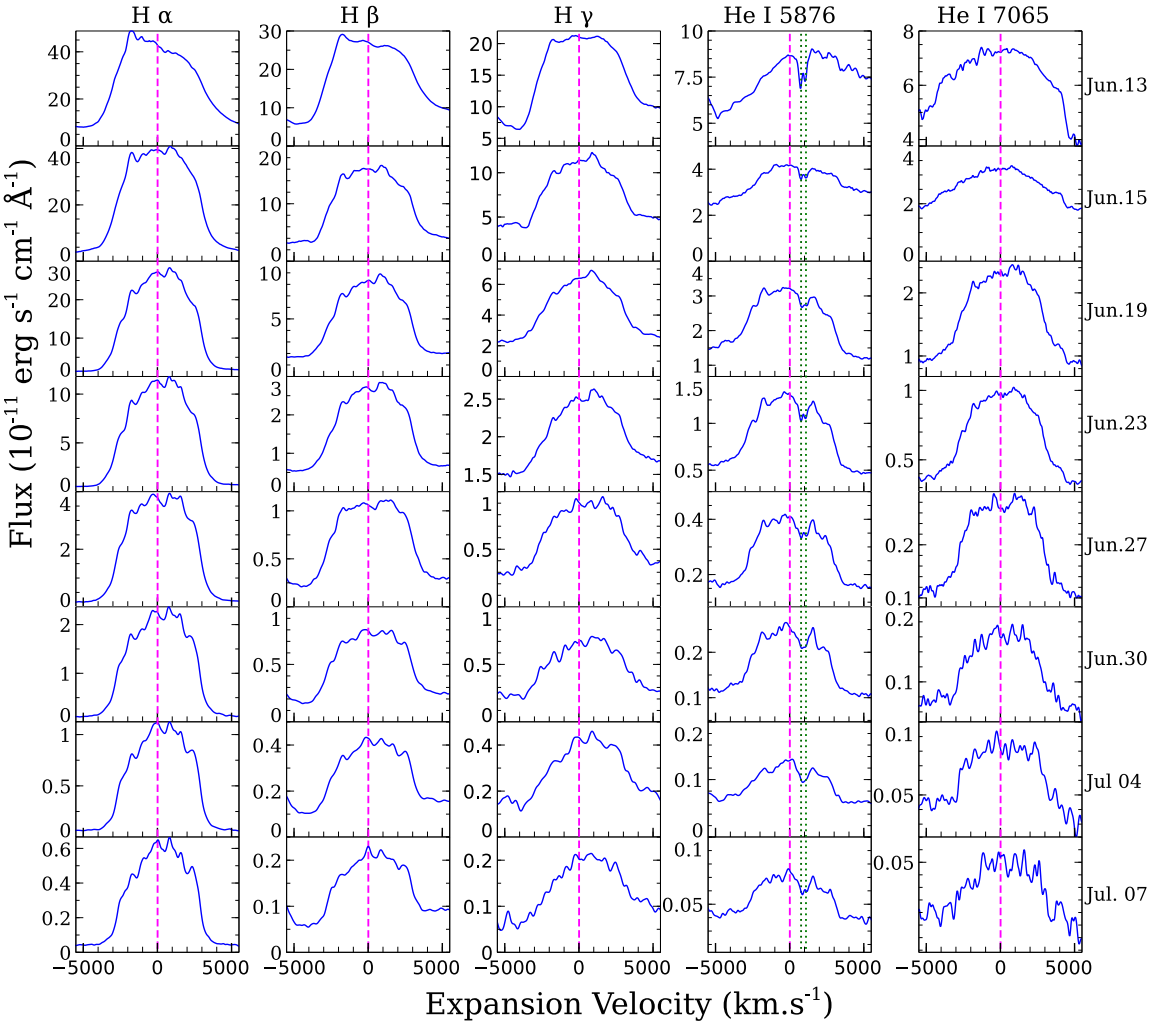

Fig. 4.8 Emission line profiles for H α , H β , H γ , He I 5876 Å, and He I 7065 Å observed on 2021 June 13.95, June 15.95, June 19.93, June 23.86, June 27.87, June 30.93, July 04.91, and July 07.87 UT. Interstellar extinctions are corrected with $E(B\text{-}V) = 0.55$. The horizontal axis represents expansion velocity in $\mathrm{km\,s^{-1}}$, while the vertical axis represents observed flux in $\mathrm{erg\,s^{-1}\,cm^{-2}\,\AA^{-1}}$ units. The vertical broken magenta line denotes the centre (rest frame) of each profile. The green dotted vertical lines in column four indicate Na I D1 (right) and D2 (left) lines.

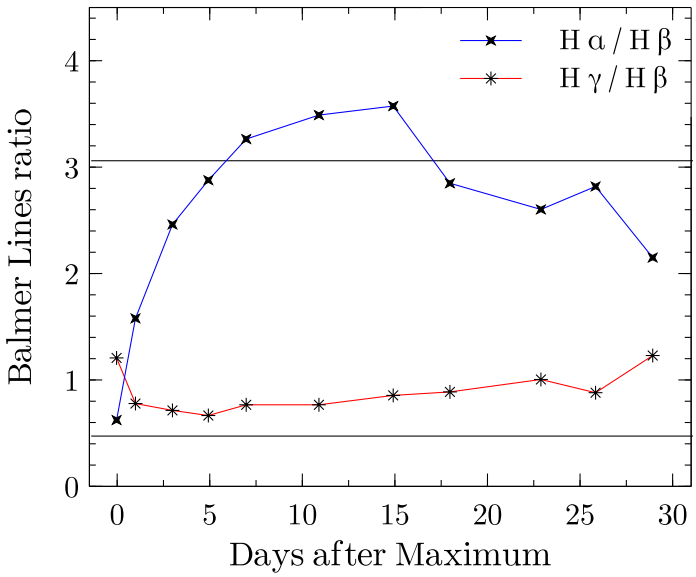

Fig. 4.9 Evolution of ratios of reddening corrected Balmer line fluxes (H α / H β and H γ / H β), from day +0.988 to 28.924. The horizontal lines represent the Balmer lines ratio for case B at 10^4 K. The upper and lower horizontal lines represent the theoretical estimation of H α / H β and H γ / H β , respectively.

4.3.2.6 V1674 Her as a neon nova

V1674 Her exhibited a variety of distinct characteristics of neon novae. For instance, Firstly, neon novae are distinguished by a substantial WD mass. The estimated WD mass of V1674 Her is $\sim$ 1.36 $M_{\odot}$ (Section 4.3.1.2), aligning with the typical WD mass range for neon novae. Secondly, ONe novae tend to cluster more closely towards the galactic plane than lower-mass CO novae (della Valle et al., 1992). Similarly, V1674 Her is positioned at galactic coordinates ($l = 048°.707$, $b = +06°.3114$), in closer proximity to the galactic plane, as anticipated. Thirdly, the optical light curve in Fig. 6.1 reveals a smooth and rapid decline in brightness without any evident signs of dust formation. Woodward et al. (2021a,c) also noted the absence of significant dust formation in the first two months following the nova's outburst. According to Williams et al. (2013), fast neon novae tend to produce minimal dust, while CO novae generate more dust due to their lower-mass WDs, resulting in higher mass ejections at slower speeds (Gehrz et al., 1998). Fourthly, neon novae exhibit prominent neon emission lines, and their ejecta often achieve higher velocities compared to CO novae (Hachisu and Kato, 2016;

Starrfield et al., 1986; Vanlandingham et al., 1996). As clearly depicted in Fig. 4.3, neon lines began to emerge in the spectra along with Balmer and helium lines around day +10.00 following the outburst. The Fe II multiplets gradually diminish, while neon lines become stronger than most of the permitted lines, except H α . This transition suggests that the nova shifted from an Fe II-dominant type to a neon nova on day 11, consistent with previous studies (Wagner et al., 2021; Woodward et al., 2021b, 2022b). The estimated elemental abundances obtained from photoionization modelling also support the gradual decrease in iron content and simultaneous increase in neon abundance (Section 6.3.3.3). Such hybrid characteristics are atypical within the Nova system.

4.3.3 Photoionization Model

In this study the photoionization code CLOUDY[6] (V17.02; Ferland et al. (2017)) was employed to simulate the emission line spectra of the nova V1674 Her. Previous studies, including Schwarz (2002); Schwarz et al. (2007); Shore et al. (2003); Vanlandingham et al. (2005) have also used CLOUDY to study various kinds of novae. This code models the physical conditions of non-equilibrium gas clouds exposed to external radiation fields, predicting emission lines spectrum based on assumptions about the gas's physical condition (ionization, density, temperature, and chemical composition). Through a self-consistent algorithm, CLOUDY simultaneously solves thermal, statistical, and chemical equilibrium equations for input parameters, estimating both intensities and column densities of numerous spectral lines across the electromagnetic spectrum. Major ionization and recombination processes are accounted for in CLOUDY, such as photoionization, Auger ionization, collisional ionization, charge transfer, and three-body recombination. Model-generated spectra are compared to observations to deduce physical and chemical conditions. Input parameters comprise temperature (T), luminosity (L), hydrogen number density (n), filling factor, covering factor, elemental abundances, and inner and outer radii of the surrounding ejecta. For synthetic model spectra, we included

[6] https://trac.nublado.org/

these input parameters and the abundances of elements with observed emission lines, whereas other elements were maintained at their solar values according to (Grevesse et al., 2010).

We initiated our modelling by assuming a central ionizing source with a high temperature ($T > 10^4$ K), whose physical properties are determined by the temperature and luminosity parameters across all of our models. This central ionizing source is enveloped by a spherically symmetric ejecta, whose density is governed by the parameter of hydrogen number density. The density distribution of this ejecta follows a power-law profile dependent on radius, as proposed by Bath and Shaviv (1976), i.e., $\rho \propto r^{\alpha}$, where α represents the power-law index. The degree of clumpiness, indicating the proportion of gas within the total volume, is established by the filling factor parameter, denoted as f(r). Notably, CLOUDY employs radial-dependent hydrogen density and filling factor, which are defined as follows:

$$\frac{n(r)}{n(r_0)} = \left(\frac{r}{r_0}\right)^{\alpha} \text{cm}^{-3}, \tag{4.5}$$

$$\frac{f(r)}{f(r_0)} = \left(\frac{r}{r_0}\right)^{\beta}, \tag{4.6}$$

where α and β represent the exponents of the power laws, r_0 denotes the inner radius, and n(r) and f(r) indicate the hydrogen density and filling factor at a radius r, respectively. The shell's density is governed by a hydrogen density parameter with a power-law density profile and an exponent of -3, chosen to maintain a steady mass per unit volume throughout the model shell ($\dot{\text{M}}$ = const.) and a linear velocity law (v $\propto$ r). Ederoclite et al. (2006); Shore (2008) estimated that the maximum filling factor of a nova shell ejecta, which typically occurred at the beginning of the shell expansion, was 0.1. This value could decrease as the shell expands. Thus, as our model covered the first month following the outburst, we adopted a filling factor value of 0.1, resulting in a power law exponent of $\beta = 0.0$. The inner and outer shell radii were determined using the minimum and maximum expansion velocities obtained from the FWHM of

all emission lines and the time between the outburst and discovery. The minimum velocity for each of the six selected epochs ranged between 2893.5 and 3290 $\mathrm{km\,s^{-1}}$, and the maximum velocity ranged between 5260 and 6566.6 $\mathrm{km\,s^{-1}}$.

The set of synthetic spectra were generated by simultaneously varying all the aforementioned input parameters in smaller increments across a wide range of values. Temperature was varied between $10^{4.5}$ and 10^{6} K, luminosity between 10^{36} and 10^{41} $\mathrm{erg\,s^{-1}}$, and ejecta density between $10^{6.5}$ and $10^{13}, \mathrm{cm^{-3}}$, along with elemental abundances. Multiple test models were iterated across all epochs numerous times before arriving at the final model. Initially, the models were visually assessed, and those not aligning with the observed spectrum were discarded. Ultimately, to assess the fitting quality, we computed the χ^2 and χ^2_{red} values of the model, expressed by the following relation:

$$\chi^2 = \sum_{i=1}^{n} \frac{(M_i - O_i)^2}{\sigma^2}, \qquad \text{and} \qquad \chi^2_{\mathrm{red}} = \frac{\chi^2}{\nu}, \tag{4.7}$$

where O_i and M_i represent the ratios of observed and modelled line fluxes to the H β line flux, respectively, and σ_i denotes the error in the observed flux ratio. The degrees of freedom, ν, are given by $n - n_p$, where n is the count of observed lines and n_p is the number of free parameters. Typically, σ falls within the range of 10 to 30 percent, depending on its strength relative to the continuum and its potential for blending with other spectral lines (Helton et al., 2010). Interactive flux measurements were conducted by fitting Gaussians using the *splot* task within the *onedspec* package in IRAF. An ideal model should yield a $\chi^2 \approx \nu$ (Schwarz et al., 2001). Thus, a desirable χ^2_{red} value should be low, typically ranging from 1 to 2, indicating a satisfactory and well-fitted model. The values of the best-fitting model parameters along with their corresponding uncertainties are presented in Table 4.2. These uncertainties were determined by individually varying each parameter while keeping others fixed at their best-fitting values until χ^2_{red} reaches 2, thereby establishing parameter uncertainties. This approach results in a free parameter uncertainty of about 3σ (Schwarz et al., 2001).

In this study, we modeled a total of five spectra, which offer broader spectral coverage and feature a greater number of emission lines. These spectra span the initial

month following the outburst, specifically at epochs 1, 2, 3, 4, and 5, corresponding to days +10.00, +13.23, +17.92, +22.92, and +27.88, respectively. When selecting the spectra for modelling, we intentionally excluded the initial days after the outburst to ensure that photoionization remains the primary ionization mechanism (Albanese et al., 2021; Page et al., 2021; Woodward et al., 2021b). Among these five epochs, the first three pertain to the nebular phase, while the last two belong to the coronal phase.

Initially, we ran several one-component models in an attempt to replicate the observed spectra. However, we encountered difficulties in reproducing certain prominent lines in the spectra, such as [N II] 5669, 5680 Å, and O I 6366 Å, which are clearly evident in the observed spectrum. Additionally, many other lines, including [Ne IV] 4714, 4724 Å, Fe II 4491 Å, and nearly all Balmer lines, were underestimated by the one-component model. Similar limitations of the one-component model have been noted in several previous studies, such as V1974 Cyg (Vanlandingham et al., 2005), V4160 Sgr (Schwarz et al., 2007), RS Oph 2006 (Mondal et al., 2018), and V1280 Sco (Pandey et al., 2022a). The primary reason behind these limitations in the one-component model lies in the heterogeneous density distribution within the Nova ejecta shell. It consists of clumpy material with high-density embedded in a more diffuse gas (Mondal et al., 2018; Pandey et al., 2022b; Paresce et al., 1995; Shore et al., 1993). To address this issue, we employed a two-component model, based on the assumption that the ejecta comprises two density components: clumps and diffuse regions. The clump region is responsible for generating lines of low ionization, which constitute the majority of observed lines. On the other hand, the diffuse region generates highly ionized emission lines without affecting the clump contribution to the spectrum. For fitting each epoch's spectrum, we executed two distinct models with the two densities, and then scaled each model by the respective covering factor, ranging from 0 to 1. The resulting models were combined to produce the final model, incorporating contributions from both density regions.

Fig. 6.12 illustrates the best-fitting CLOUDY model profiles (shown in red) superimposed on the observed optical spectra (shown in black) for five distinct epochs. Table

4.3 presents a comparison of relative fluxes between the best-fitting model-predicted lines and the observed lines during the early phase, along with corresponding χ^2 values. For computing χ^2 values, emission lines appearing in both observational and modelled spectra were selected. The observed and modelled line fluxes were determined using IRAF, and profiles with multiple components were decomposed using multiple Gaussian functions. To mitigate inaccuracies related to flux calibration across different epochs, flux ratios of observed and modelled emission lines relative to H β were calculated.

Table 4.2 Best fit CLOUDY model parameters during outburst phase of Nova Her 2021.

Parameters	Values				
	Epoch 1	Epoch 2	Epoch 3	Epoch 4	Epoch5
Black Body Temperature ($\times 10^5$K)	1.99 ± 0.05	2.04 ± 0.10	2.19 ± 0.05	2.24 ± 0.10	2.34 ± 0.10
Luminosity ($\times 10^{38}$ erg s^{-1})	1.26 ± 0.33	$1.99^{+0.24}_{-0.41}$	$2.00^{+0.52}_{-0.41}$	$3.16^{+0.39}_{-0.34}$	$3.16^{+0.31}_{-0.28}$
Clump Hydrogen density ($\times 10^8$cm^{-3})	$10.0^{+1.22}_{-1.19}$	$8.13^{+0.19}_{-0.09}$	$7.94^{+0.19}_{-0.18}$	$6.32^{+0.15}_{-0.14}$	$5.62^{+0.69}_{-0.38}$
Diffuse Hydrogen density ($\times 10^7$cm^{-3})	$6.31^{+1.63}_{-1.29}$	$3.98^{+0.43}_{-1.03}$	$3.16^{+0.39}_{-0.34}$	$1.99^{+0.24}_{-0.21}$	$1.00^{+0.05}_{-0.05}$
α	-3.00	-3.00	-3.00	-3.00	-3.00
Inner radius ($\times 10^{14}$cm)^a	2.51	3.98	4.68	5.75	7.08
Outer radius ($\times 10^{14}$cm)^a	5.62	7.94	8.51	10.00	15.14
Filling Factor^a	0.10	0.10	0.10	0.10	0.10
β ^{a}	0.00	0.00	0.00	0.00	0.00
Clump to diffuse Covering factor	62/38	55/45	53/47	53/47	55/45
He/He$_\odot$	$2.80^{+0.70}_{-0.30}$	$2.50^{+0.30}_{-0.20}$	$2.90^{+0.50}_{-0.30}$	$2.90^{+0.30}_{-0.50}$	$2.90^{+0.1}_{-0.2}$
O/O$_\odot$	$5.00^{+0.50}_{-0.50}$	$5.50^{+2.00}_{-1.00}$	10.0 ± 2.5	$6.00^{+1.50}_{-2.00}$	$8.00^{+0.10}_{-0.20}$
N/N$_\odot$	$50.0^{+30.0}_{-20.0}$	$50.0^{+25.0}_{-5.00}$	$50.0^{+20.0}_{-15.0}$	30.0 ± 10	$40.0^{+3.00}_{-10.0}$
Ne/Ne$_\odot$	$10.5^{+2.00}_{-1.50}$	$15.5^{+1.00}_{-1.50}$	$12.5^{+3.50}_{-2.50}$	$15.5^{+4.00}_{-2.00}$	$30.5^{+5.00}_{-4.00}$
Fe/Fe$_\odot$	$2.50^{+1.00}_{-1.00}$	$2.50^{+4.00}_{-3.00}$	2.50 ± 0.5	1.00 ± 0.3	1.00 ± 0.2
Ejected matter mass ($\times 10^{-5}$ $M_\odot$)	0.867	2.138	2.918	3.825	8.93
Number of lines	16.0	17.0	15.0	16.0	14.0
Number of free parameters	10.0	10.0	10.0	10.0	10.0
Degrees of freedom	6.00	7.00	5.00	6.00	4.00
$\chi^2_{\rm tot}$	10.91	7.53	5.24	6.13	6.86
$\chi^2_{\rm red}$	1.82	1.08	1.05	1.02	1.71

Note: ^{a} stands for the quantity is not considered as a free parameter.

4.3.3.1 Temperature and Luminosity

The parameter values as deduced from the best-fitting CLOUDY models, are provided in Table 4.2. The optimal CLOUDY models indicate that the central ionizing source exhibited a temperature of $\sim 1.99 \times 10^5$ K during epoch 1, which subsequently increased to around 2.34×10^5 K by epoch 5. Furthermore, the luminosity of the central ionizing source is found to be 1.26×10^{38} erg s^{-1} during epoch 1 and then raised to 3.16×10^{38} erg s^{-1} by epoch 5. These derived temperature and luminosity values from the best-fitting CLOUDY model reasonably align with the previously estimated values of T $\geq 4 \times 10^5$ K and L $\sim 1.0 \times 10^{38}$ erg s^{-1}) for day 16 (Rudy et al., 2021). Both the effective temperature and luminosity of the central ionizing source exhibited lower values in the initial days and showed an increase in the subsequent epochs (refer to Fig. 4.11). This rise in the central ionizing source's temperature is due to the compression of leftover matter within the pseudo-photosphere as the ejecta expands during its collapse. This compression process results in elevated gas temperatures, consequently leading to higher rates of radiation emission (Bath and Shaviv, 1976). The heightened radiation output subsequently triggers the expansion and cooling of the outer layers of the WD.

4.3.3.2 Ejecta Density

Throughout epochs 1 to 5, the diffuse hydrogen density varied from 6.31×10^7 to 1.00×10^7 cm^{-3}, while the clump hydrogen density ranged from 1.00×10^9 to 5.60×10^9 cm^{-3}. During the expansion phases of a nova outburst, the density of the ejected material undergoes a substantial decrease over time. This occurs as the ejecta expands at high velocities after an outburst, with some material being absorbed by interstellar clouds or the surrounding gas from the companion star. This absorption releases extra energy from the nova mechanism, causing a gradual shift towards an optically thin atmosphere and a subsequent reduction in density. The diminishing density exposes the ionizing radiation emitted by the central WD to the expanding ejecta, resulting in an increased ionization potential. This, in turn, facilitates the emergence of emission

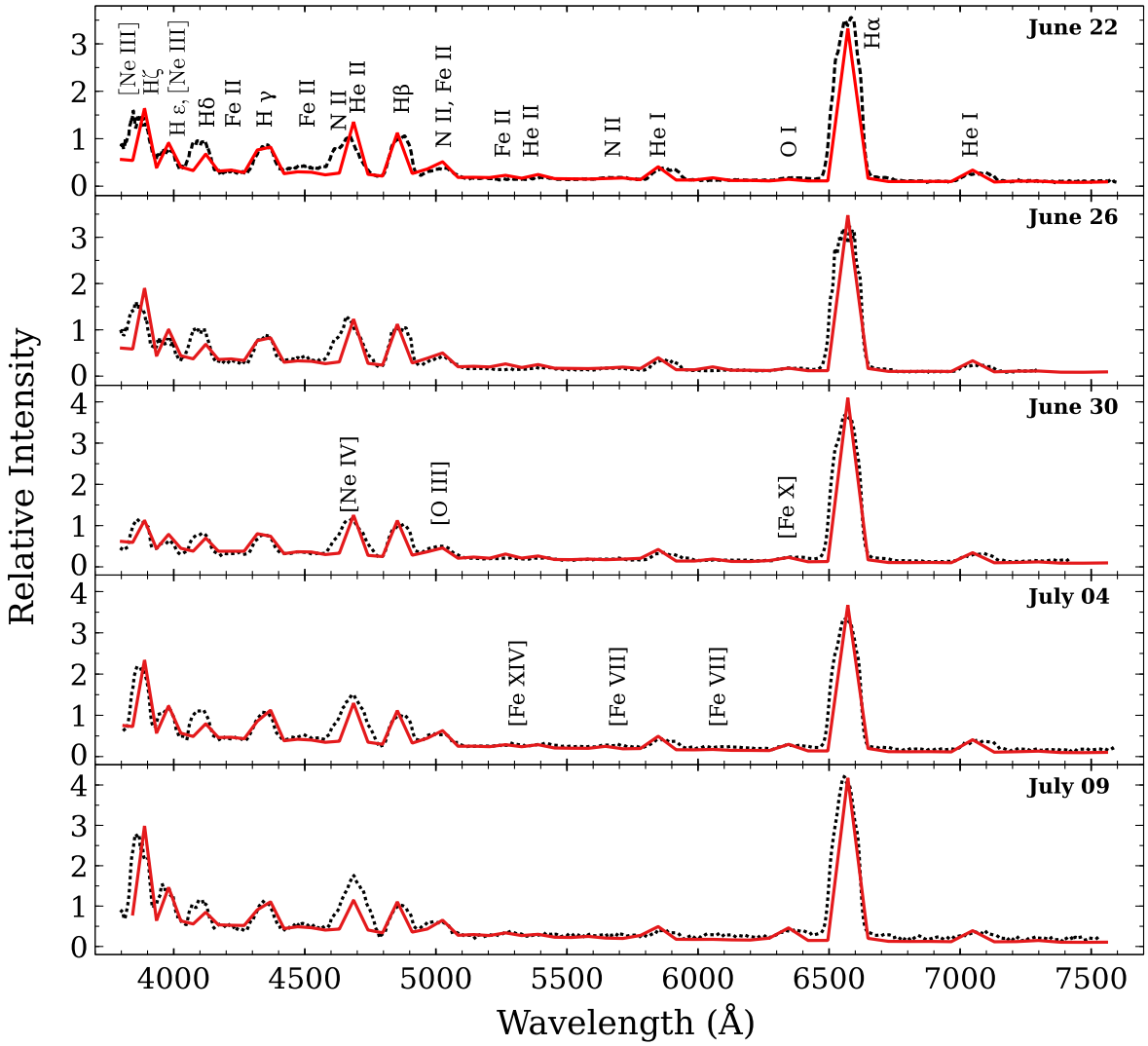

Fig. 4.10 Best-fitting CLOUDY synthetic spectrum (red solid line) plotted over the observed spectrum (dashed black line) of V1674 Her obtained on 2021 June 23, June 27, June 30, July 4, and July 7, from top to bottom, respectively.

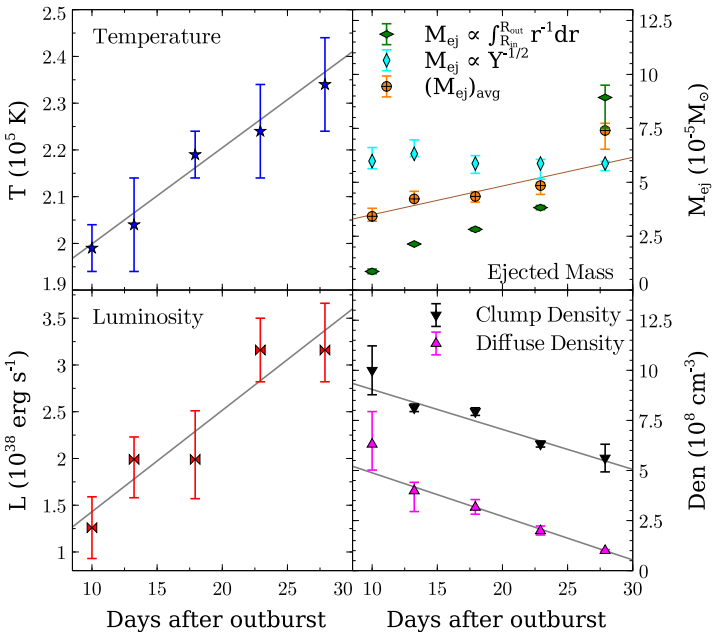

Fig. 4.11 Variations in the cloudy best-fitting parameters: temperature, luminosity, ejected mass, and number density. The panel for ejected mass comprises ejected masses calculated by two methods and their averages (for more information see 6.3.3.4) .

lines with higher ionization potentials. The density evolution observed in novae, along with the subsequent ionization processes, can generally be attributed to the interplay between expanding ejecta, matter absorption, and ionizing radiation from the central WD.

The ratio of clump-to-diffuse covering factors from the best-fitting model was calculated to be 62/38, 55/45, 53/47, 53/47, and 55/45 for epochs 1, 2, 3, 4, and 5, respectively. We observed that the majority of emission lines originated within regions of higher ejecta density, as earlier predicted in Section 6.3.2.1. The best-fitting CLOUDY model revealed that the He I 5878 and 7065 Å lines exclusively originated from the clump component of the ejecta. Conversely, the [N II] 5669, 5680 Å, and O I 6366 Å lines were observed to be produced solely from the diffuse component of the ejecta. Thus, the modelling clearly illustrates that the observed spectra cannot be adequately replicated by a one-component model, and it is not possible to deduce the physical and chemical attributes of the source and ejecta solely from such spectra.

4.3.3.3 Elemental Composition

During epochs 1, 2, and 3 (nebular phases), oxygen, nitrogen, iron, helium, and neon were found to be overabundant relative to the solar value. With the exception of iron, whose abundance decreased to a solar value during epochs 4 and 5 (coronal phases), these elements continued to be overabundant. Furthermore, the model suggested a twofold increase in neon abundance within the initial days of the coronal phase. The notable increase in Ne abundance and decrease in Fe II abundance could be attributed to Nova V1674 Her's shift from a Fe II type to a Neon-type nova, as suggested earlier by Wagner et al. (2021); Woodward et al. (2022b). Moreover, the neon overabundance in the ejecta indicates that the WD was an ONe type as predicted in Section 4.3.1.2 (Evans and Gehrz, 2012).

Helium abundance across all epochs was determined by fitting the prominent He I (5876, 7065 Å) and He II (4686, 5412 Å) lines. During modelling, we observed that the He I lines originated from high-density regions, whileHe IIlines arose from both higher and lower densities. Oxygen abundance in epoch 1 was determined using O I 6366 Å alone, while in subsequent epochs, [O III] 5007 Å was also considered. O I originated from a lower density zone, whereas [O III] emerged from higher density areas. Nitrogen abundance for all three epochs was estimated through fitting N II 5680 Å, which originated from the lower density region. Neon abundance for epochs 1 and 2 was derived from [Ne III] (3869, 3968 Å), and for epochs 3, 4, and 5, the [Ne IV] 4714 Å line was included. Both [Ne III] and [Ne IV] primarily originated from the clump region. Iron abundance in epochs 1, 2, and 3 was determined by fitting Fe II (4200, 4487, 5018, 5168, 6247 Å), with epoch 3 contributing from the coronal line [Fe X] 6375 Å. These lines were mainly generated from higher density regions, although the lower density area also contributed. Enhanced iron abundance over the solar value during the first three epochs implied helium enrichment in the nova ejecta, potentially indicating that the companion star had evolved beyond the main-sequence level (Bode and Evans, 2008). For epochs 4 and 5, iron abundance was measured by fitting [Fe X]

6375 Å, [Fe VII] 6087 Å, [Fe VI] 5677 Å, [Fe XIV] 5303 Å, Fe II 5167 Å, and Fe II 4487 Å.

A notable increase in intensity was observed in emission features such as H η 3835.4 Å, H ζ 3889 Å, and H ϵ 3970 Å starting on day 10 (2021 June 22.99). Similarly, the Fe II 5018 Å emission feature and an emission line identified as a blended feature of N II 4638 Å and He II 4686 Å exhibited similar behaviour on day 17.9 (2021 June 30). By varying the hydrogen density, effective temperature, and luminosity of the source, we could not generate these features in the model spectra, to match the observed one. These characteristics were exclusively generated by enhancing the abundances of neon and oxygen beyond their solar values (Grevesse et al., 2010). Consequently, the emission features of [Ne III] 3869, 3968 Å, [Ne IV] 4714, 4724 Å, and [O III] 5007 Å became stronger, and the intensity of the blended features at $\lambda = 3889, 4686,$ and 5018 Å increased. This result strongly supports the claim we made in Section 4.3.2.3 that the nebular phase of Nova V1674 Her began on day 10, marking one of the quickest transitions in history.

Table 4.3 Observed and best-fit CLOUDY model line flux values for nebular and coronal phase epochs.

		Epoch 1 (June 22)			Epoch 2 (June 26)			Epoch 3 (June 30)		
Line ID	λ (Å)	modelled	Observed	χ^2	modelled	Observed	χ^2	modelled	Observed	χ^2
H ζ ,[Ne III]	3889	1.519	1.748	2.339	1.508	1.567	0.152	1.195	1.114	0.292
H ϵ ,[Ne III]	3970	1.080	0.964	0.600	1.106	1.013	0.381	0.852	0.747	0.491
H δ	4101	0.785	0.921	0.814	0.867	0.879	0.007	0.805	0.770	0.053
Fe II	4180	0.653	0.594	0.153	0.800	0.700	0.444	-	-	-
H γ	4340	1.266	1.047	2.145	1.204	1.033	1.288	1.239	1.015	2.223
Fe II	4415	0.806	0.745	0.166	0.860	0.821	0.067	0.715	0.669	0.097
N III	4638	0.512	0.804	3.793	0.694	0.654	0.069	-	-	-
He II	4686	0.745	0.729	0.010	0.659	0.984	4.712	0.919	1.097	1.397
[Ne IV]	4724	-	-	-	-	-	-	0.192	0.117	0.249
H β	4861	1.000	1.000	0.000	1.000	1.000	0.000	1.000	1.000	0.000
[O III]	5007	-	-	-	-	-	-	0.768	0.699	0.210
Fe II,He I	5016	0.839	0.716	0.671	0.671	0.644	0.030	-	-	-
Fe II	5276	0.274	0.246	0.035	0.304	0.224	0.278	0.335	0.280	0.135
[Fe XIV]	5303	-	-	-	-	-	-	-	-	-
He I	5412	0.264	0.242	0.021	0.282	0.279	0.0004	0.267	0.240	0.031
[Fe VI]	5677	-	-	-	-	-	-	-	-	-
N II	5679	0.339	0.325	0.009	0.322	0.298	0.027	-	-	-
He I	5875	0.423	0.384	0.066	0.367	0.333	0.051	0.359	0.331	0.034
Fe II	6248	-	-	-	0.164	0.180	0.011	-	-	-
O I	6366	0.223	0.233	0.005	0.164	0.164	0.4E-4	-	-	-
[Fe VII]	6087	-	-	-	-	-	-	0.084	0.069	0.008
[Fe X]	6375	-	-	-	-	-	-	0.245	0.232	0.008
H α	6562	3.453	4.429	10.906*	4.983	4.248	13.494*	3.179	2.706	5.605*
He I	7002	0.369	0.326	0.082	0.282	0.296	0.008	0.299	0.283	0.0114

Note: The symbol * denotes that the value is not taken into account while calculating the total χ^2 for each epoch.

Figure 4.3 Continued: Observed and best-fit CLOUDY model line flux values for nebular and coronal phase epochs.

		Epoch 4 (July 04)			Epoch 5 (July 09)		
Line ID	λ (Å)	modelled	Observed	χ^2	modelled	Observed	χ^2
H ζ,[Ne III]	3889	1.909	1.90	0.002	2.138	2.485	5.352
H ϵ ,[Ne III]	3970	1.288	1.089	1.754	1.438	1.525	0.342
H δ	4101	1.124	1.077	0.095	1.059	1.143	0.31892
Fe II	4180	-	-	-	-	-	-
H γ	4340	1.469	1.358	0.546	1.537	1.415	0.669
Fe II	4415	1.049	0.937	0.564	1.292	1.291	0.2E-4
N III	4638	-	-	-	-	-	-
He II	4686	0.642	0.878	2.481	1.009	1.014	0.0013
[Ne IV]	4724	0.383	0.445	0.172	-	-	-
H β	4861	1.000	1.000	0.000	1.000	1.000	0.000
[O III]	5007	0.896	0.807	0.351	0.897	0.935	0.063
Fe II,He I	5016	-	-	-	-	-	-
Fe II	5276	-	-	-	-	-	-
[Fe XIV]	5303	0.427	0.407	0.016	0.396	0.418	0.023
He I	5412	0.326	0.304	0.021	0.351	0.374	0.024
[Fe VI]	5677	0.243	0.217	0.031	0.286	0.281	0.0011
N II	5679	-	-	-	-	-	-
He I	5875	0.356	0.324	0.046	0.454	0.422	0.046
Fe II	6248	-	-	-	-	-	-
O I	6366	-	-	-	-	-	-
[Fe VII]	6087	0.121	0.123	1.7E-4	-	-	-
[Fe X]	6375	0.180	0.155	0.029	0.371	0.370	0.3E-4
H α	6562	2.806	2.048	14.351*	2.936	2.546	3.812*
He I	7002	0.321	0.298	0.024	0.251	0.232	0.016

Note: The symbol * denotes that the value is not taken into account while calculating the total χ^2 for each epoch.

4.3.3.4 Ejected mass Calculation

The ejected mass within the model shell could be calculated using the following equation, (Schwarz et al., 2001):

$$M_{\rm ej} = n(r_0) f(r_0) \int_{R_{\rm in}}^{R_{\rm out}} \left(\frac{r}{r_0}\right)^{\alpha+\beta} 4\pi r^2 dr, \tag{4.8}$$

where $n(r_0)$ represents the hydrogen density ($\rm cm^{-3}$) and $f(r_0)$ stands for the filling factor at the inner radius of the shell (r_0). The exponents α and β correspond to the power laws. The values for density, filling factor, α, and β are directly adopted from the best-fitting CLOUDY model parameters (refer to Table 4.2). The estimation of the total ejected shell mass involved multiplying the mass in both density components (clump and diffuse) with their corresponding covering factors and subsequently adding them together. Consequently, the ejected hydrogen shell masses for epochs 1, 2, 3, 4, and 5 are estimated to be: $0.87 \times 10^{-5} M_{\odot}$, $2.14 \times 10^{-5} M_{\odot}$, $2.92 \times 10^{-5} M_{\odot}$, $3.83 \times 10^{-5} M_{\odot}$, and $8.93 \times 10^{-5} M_{\odot}$, respectively. The ejected mass could also be estimated from the helium abundance factor Y (Shore et al., 1993),

$$M_{\rm ej} = {\rm Y}^{-1/2}\ 10^{-4}\ M_{\odot}, \tag{4.9}$$

where Y represents the helium abundance enhancement factor, which was adopted from our CLOUDY best-fitting model parameters (Table 4.3). This approach has been successfully applied to various novae, including neon novae like QU Vul Shore et al. (1993) and V1974 Cyg (Vanlandingham et al., 2005). Based on this method, the estimated mass of the ejecta shell for epochs 1, 2, 3, 4, and 5 are found to be: $\sim 5.98 \times 10^{-5}\ M_{\odot}$, $6.33 \times 10^{-5}\ M_{\odot}$, $5.87 \times 10^{-5}\ M_{\odot}$, $5.87 \times 10^{-5}\ M_{\odot}$, and $5.87 \times 10^{-5}\ M_{\odot}$, respectively.

We chose to use the average values of the ejected masses obtained from the two aforementioned approaches as the most plausible estimates for the expelled masses during epochs 1, 2, 3, 4, and 5, which are approximately $3.42 \times 10^{-5}\ M_{\odot}$, $4.23 \times 10^{-5}\ M_{\odot}$,

4.35×10^{-5} $M_{\odot}$, 4.85×10^{-5} $M_{\odot}$, and 7.40×10^{-5} $M_{\odot}$, respectively. Given the considerable fluctuations in ejected mass observed across the five distinct epochs, particularly in the first and last epochs, adopting the average is considered a more reliable estimation. These estimates of ejected mass across the five distinct epochs are consistent with the typical expectations for a neon nova, which ejects a smaller mass ($\sim 10^{-6} - 10^{-5}$ $M_{\odot}$) (Duerbeck, 2008; Gehrz, 2008; Gehrz et al., 1998). However, it is important to note that the obtained values of ejected mass could be considered as their minimum value because a large amount of neutral or much hotter gas might remain undetected or require a more intricate approach to be detected (Bode and Evans, 2008; Ferland, 1998).

TNRs on massive WDs, like V1674 Her, lose their envelopes and fade more swiftly than those on small WDs (CO type) (Shara et al., 2018). Those novae with higher WD mass and faster ejection velocities release less mass ($\sim 10^{-6} - 10^{-5}$ $M_{\odot}$) than lower WD mass and slower speed novae (Duerbeck, 2008; Gehrz, 2008; Gehrz et al., 1998). As a result, novae of ONe type eject smaller amounts of material than CO novae. A massive WD requires comparatively less accreted matter to trigger a TNR (Gehrz et al., 1998; Shara, 1994), a concept reflected in the mass-radius relationship ($M_{\rm WD}^{1/3} R_{\rm WD}$ = constant) and the binding energy formula $(GM_{\rm WD}\ M_{\rm ej})/R_{\rm WD} \propto M_{\rm WD}^{4/3}\ M_{\rm ej}$. Woodward et al. (2021b) suggested a maximum possible ejected mass of $\sim \sim 1.4^{+0.8}_{-1.2} \times 10^{-3} M\odot$ for Nova V1674 Her. Conversely, Drake et al. (2021) predicted an ejection mass range of 2×10^{-5} $M_{\odot}$ to 2×10^{-4} $M_{\odot}$ for such a rapid nova. This study estimates ejected masses at five epochs between 3.42 and 7.40×10^{-5} $M_{\odot}$, reasonably consistent with prior research. Additionally, the central WD mass is estimated at $\sim$ 1.36 $M_{\odot}$, also in line with previous studies.

4.3.4 Morpho-kinematic modelling

We performed a morpho-kinematical analysis of the outburst of Nova V1674 Her in 2021, using the latest version of SHAPE[7] (i.e., SHAPEX; Steffen and Koning (2017,

[7] https://wsteffen75.wixsite.com/website/

2012)). Our aim is to generate the 3-D structure of the ejecta by modelling prominent emission lines in the observed spectra and studying how the structure evolves with time. Through morpho-kinematic analysis, one can determine the inclination angle, position angle, geometrical size, and structure of the ejecta shells. Similar studies are conducted for a few other novae, (for example, Harvey et al., 2020; Linford et al., 2015; Munari et al., 2011; Pavana et al., 2020, etc).

4.3.4.1 Gaussian decomposition of H α line

Due to the remarkably high ejection velocity of the nova, the majority of line profiles exhibit broad characteristics, accompanied by a series of ripples on top of each profile (see Fig. 4.12). To identify components with different velocities, we performed Gaussian fitting on H α emission lines using the FITYK[8] software (Wojdyr, 2010). It is a customizable peak-fitting application with a user-friendly graphical interface, designed to manage a wide variety of non-linear functions, and enables users to perform continuum subtraction and Levenberg-Marquardt least squares fitting.

We fitted the emission line profiles of H α observed on 2021 June 15.945 (2.96 d), June 23.856 (10.897 d), June 27.867 (14.91 d), June 30.931 (17.972 d), July 04.914 (22.886 d), and July 07.866 (25.838 d) UT, spanning over the first month. H α was chosen to be modelled because it stands out as the broadest and most distinct line across all time frames. To fit the observed line profiles, we required at least seven Gaussian components for each epoch (see Fig. 4.12). This enabled us to obtain the radial velocities and the FWHM values of the individual components. Reasonable velocity symmetry appears to exist between the fast-moving components, 1 and 7, as well as the slower-moving components, 2 and 6, and 3 and 5. Table 4.4 and 4.5 provides the radial and FWHM velocities of each ripples. All profiles exhibit good correspondence in radial velocity for the same ripple, indicating that they are kinematically identical. These kinds of ripples occur due to various circumstances: (1) when novae eject large, distinct blobs of matter at various angles to the line of sight

[8] https://fityk.nieto.pl/

Table 4.4 Calculated radial velocity of the ripples numbered on the H α emission line profile in V1674 Her.

	Component Radial velocity ($km\,s^{-1}$)						
Day	1	2	3	4	5	6	7
2.96	-1791.20	-1755.56	-933.19	-24.12	940.36	1477.00	1858.72
10.90	-2141.98	-1698.25	-1098.42	-39.36	1028.17	1616.80	2270.14
14.91	-1946.50	-1774.17	-1180.35	-180.07	943.69	1550.36	2176.99
17.97	-2151.20	-1793.28	-1222.92	-211.49	923.76	1522.17	2213.57
22.89	-2385.42	-1751.07	1091.41	-0.74	893	1535.41	2416.47
25.84	-2099.2	-1681.79	-1042.08	67.60	978.70	1590.10	2323.21

Table 4.5 Calculated FWHM velocity of the ripples numbered on the H α emission line profiles in V1674 Her.

	Component FWHM velocity ($km\,s^{-1}$)						
Day	1	2	3	4	5	6	7
2.96	2205.21	418.14	914.73	1355.92	767.73	486.29	2412.79
10.90	1632.34	415.02	884.39	1518.62	859.59	584.94	1605.69
14.91	1804.5	378.35	723.22	1518.31	893.25	499.43	1617.06
17.97	1525.48	393.76	746.32	1511.60	895.77	498.56	1391.97
22.89	729.04	164.66	1144.26	1475.42	672.94	751.66	1031.64
25.84	1351.17	402.03	819.33	1302.66	852	511.85	1170.44

(Munari et al., 2006), (2) when the density distribution appears in-homogeneous and speed variation results from it (Schwarz et al., 2007), and (3) when brightness increases as a result of the polar and projection effects of equatorial rings (Munari et al., 2006, and references therein).

4.3.4.2 SHAPE modelling

We estimated the 3D morphological structure and density distribution in the ejecta of Nova V1674 Her by modelling the prominent emission line profiles. Line profiles from the expanding ejecta provide insights into how morphology and kinematic properties correlate along the line of sight. We can observe this correlation in either 1D or 2D spectral profiles, enabling us to attain the position-velocity (PV) profiles. These profiles usually encompass both the position and velocity of a specific point across the shell ejecta.

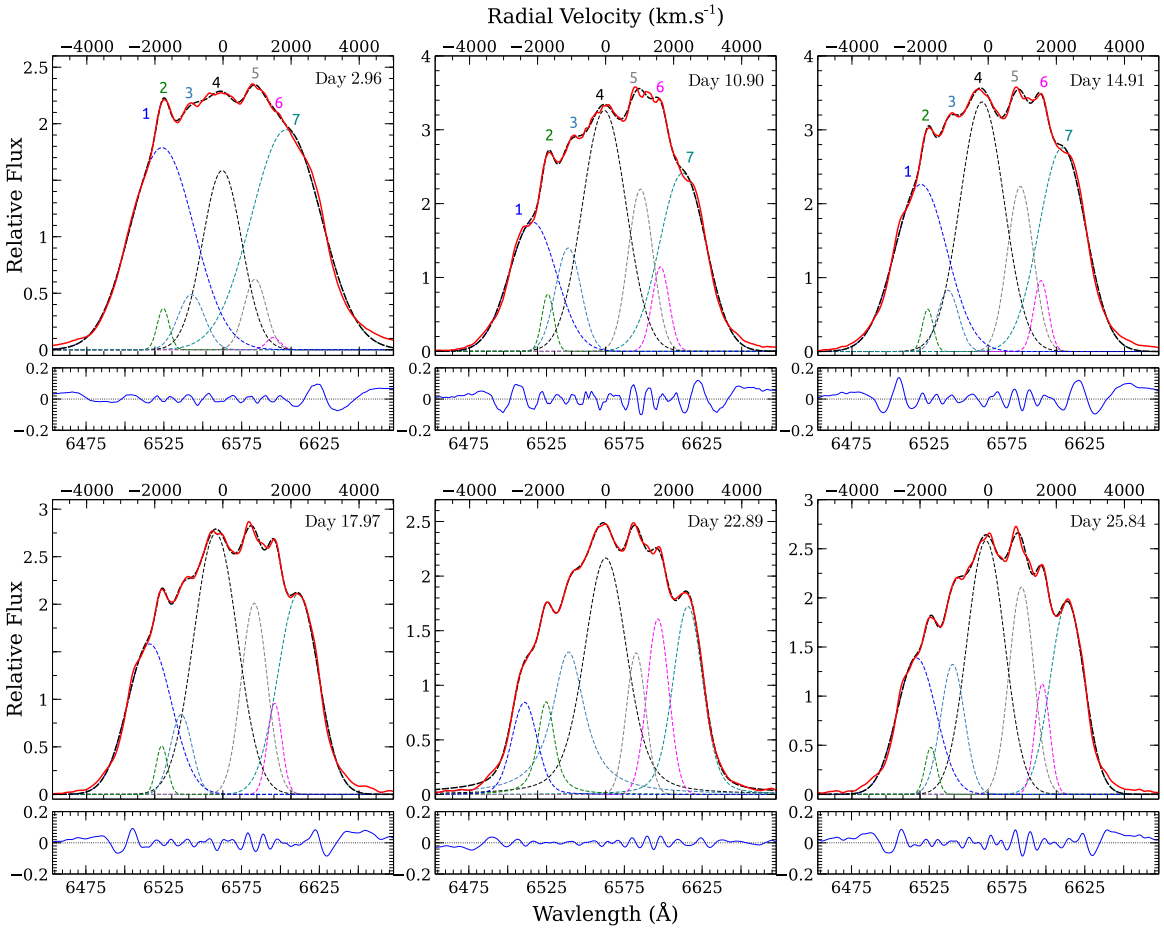

Fig. 4.12 The best fit for the Gaussian components of the H α line profile of V1674 Her on days 2.96, 10.897, 14.91, 17.972, 22.886, and 25.838 following the outburst. The combined Gaussian components are depicted with black broken lines, while the observed spectrum are represented by red solid lines. Each individual Gaussian component is distinguished by a unique colour scheme shown in each panel. Component numbers 1 through 7 correspond to peaks listed in increasing wavelength order. Additionally, the residuals from the overall fit are displayed at the bottom of each panel.

Within SHAPE, we possessed the capability to construct diverse 3D multi-component structures, including polar blobs, prolate structures with tropical rings, prolate structures exhibiting equatorial rings, and bipolar structures. These structures were constructed using a variety of elementary geometries, such as spheres, cylinders, cones, or toroids, either individually or in combination. Moreover, the fundamental geometry can be tailored by employing various structural modifiers like squeeze, spiral, twist, and others. Each component was assigned a density profile and velocity field using corresponding modifiers. The SHAPE code conducts all the radiation transfer calculations through the ejecta and generated the 3D model, along with the PV diagram.

In this study, we reconstructed the 3D structure of the nova ejecta using the H α -PV spectral profile of the ejecta. The line profiles of H α generally provided a well-resolved view of the position-velocity correlation characteristics towards the line of sight. Our main objective is to develop a 3D model characterized by a designated density distribution and expansion velocity field, ensuring that the PV profile generated by the model corresponded with the observed position-velocity profile. To achieve this, we utilised fundamental modifiers related to velocity, density, squeeze, and translation, which offered additional characterization for each constituent. Through the utilization of these modifiers, we adjusted all unconstrained variables to generate synthetic line profiles that closely resembled the observed ones. One important modifier in the SHAPE software package is the 'squeeze' modifier, as defined by (Ribeiro et al., 2013):

$$\text{squeeze} = 1 - \frac{a}{b}, \tag{4.10}$$

where a and b represent the semi-minor and semi-major axes of the ejecta shell, respectively. This equation was utilised to transform a spherical shell configuration into a bipolar structure. A higher value of the squeeze indicates a more pronounced deformation at the ejecta's waist, while a squeeze value of zero implies a spherical shape. In this study, we adjusted the values of the squeeze modifier within the range of 0.0 to

1.0. Translation modifiers were employed to reposition the polar caps along with their corresponding coordinate systems to their respective poles. The study encompasses the modification of both the parameters of the modifiers and the inclination and position angles of the binary system. These angles ranges from 0 to 90° and 0 to 180°, respectively. To determine the optimal model, various configurations were computed prior to discovery. The same radius-density power-law relation as in photoionization modelling, i.e., $\rho \propto r^{-3}$ (Section 6.3.3), was employed. The initial density guess was adopted from the best-fitting models produced by CLOUDY (see Table 4.2). The determination of the radius for each component was based on the observed line profile's FWHM and the elapsed time since the outburst. To portray the radial velocity distribution in all directions, we employed the Hubble-flow type linear velocity field equation given by (Ribeiro et al., 2009):

$$v(r) = \frac{3200}{\sin i}(\frac{r}{r_0}), \tag{4.11}$$

where i, r_0, and r represent the inclination angle, inner, and outer radii of the ejected shell. In all epochs, the shell's radius was calculated based on the expansion velocities. Previous studies (Drake et al., 2021; Woodward et al., 2021e) estimated that the maximum expansion velocity could reach up to 11,000 $\mathrm{km\,s^{-1}}$. In this study, we explored the parameter space by varying the expansion velocity (V_{exp}) in the range of 1,000 to 11,000 $\mathrm{km\,s^{-1}}$, with increments of 100 $\mathrm{km\,s^{-1}}$.

Initially, a comparison between the observed and model images, as well as the PV diagrams, was conducted through visual estimation. Once a satisfactory visual alignment between the observed and modelled line profiles was achieved, the goodness of fit was assessed using two quantitative measures: the root mean square (rms) and the quality (q) factor. The rms value was computed as a metric to quantify the overall differences between the synthetic and observed profiles, providing an estimation of the mean disparity between the two. On the other hand, the q-factor served as a measure of similarity based on the relative positions and strengths of the features present in

the line profile. The rms was calculated using the following equation:

$$rms = \sqrt{\frac{1}{n}\sum_{i}\left[1 - \frac{M_i}{O_i}\right]^2}, \tag{4.12}$$

where M_i and O_i represent the modelled and observed flux values of the i^{th} observable, respectively. In this case, we focused on a single observable per model, so i is equal to 1, resulting in a total number of observables (n) also being unity. A model is considered acceptable if the root mean square (rms) is less than one (Bandyopadhyay et al., 2020). Additionally, to assess the quality of fitting, we computed the quality factor q, given by (Morisset and Georgiev, 2009).

$$q = \frac{\log(\frac{M}{O})}{\tau}, \qquad \text{where,} \quad \tau = \log(1+\delta), \tag{4.13}$$

where δ represents the corresponding error between the modelled and observed line profiles. Similarly, the fitting process is deemed successful within the specified tolerance limit if the absolute value of q is less than 1. Consequently, upon closer examination, we determined that a 10% discrepancy could be attributed to inaccuracies in the model parameters.

The sample of various attempts to find the best fitting synthetic line profile to the observed spectral line observed on June 15, 2021, by using various geometries have been provided in figure 4.13.The polar caps are responsible for peaks on the center of the line profile. The peaks on on the red side shows some of the trials we made to find the best fit model for epoch 1 (June 15, 2021). We follow similar procedures for the other epochs as well.

Figure 4.14 shows how the individual model components generated by using different geometries (dashed magenta, red and green lines) and sum of those components (solid blue line) fit with the observed line profile of H α (dashed gray line) on June 15, 2021. As we follow similar procedure to fit the other epochs as well, we didn't include

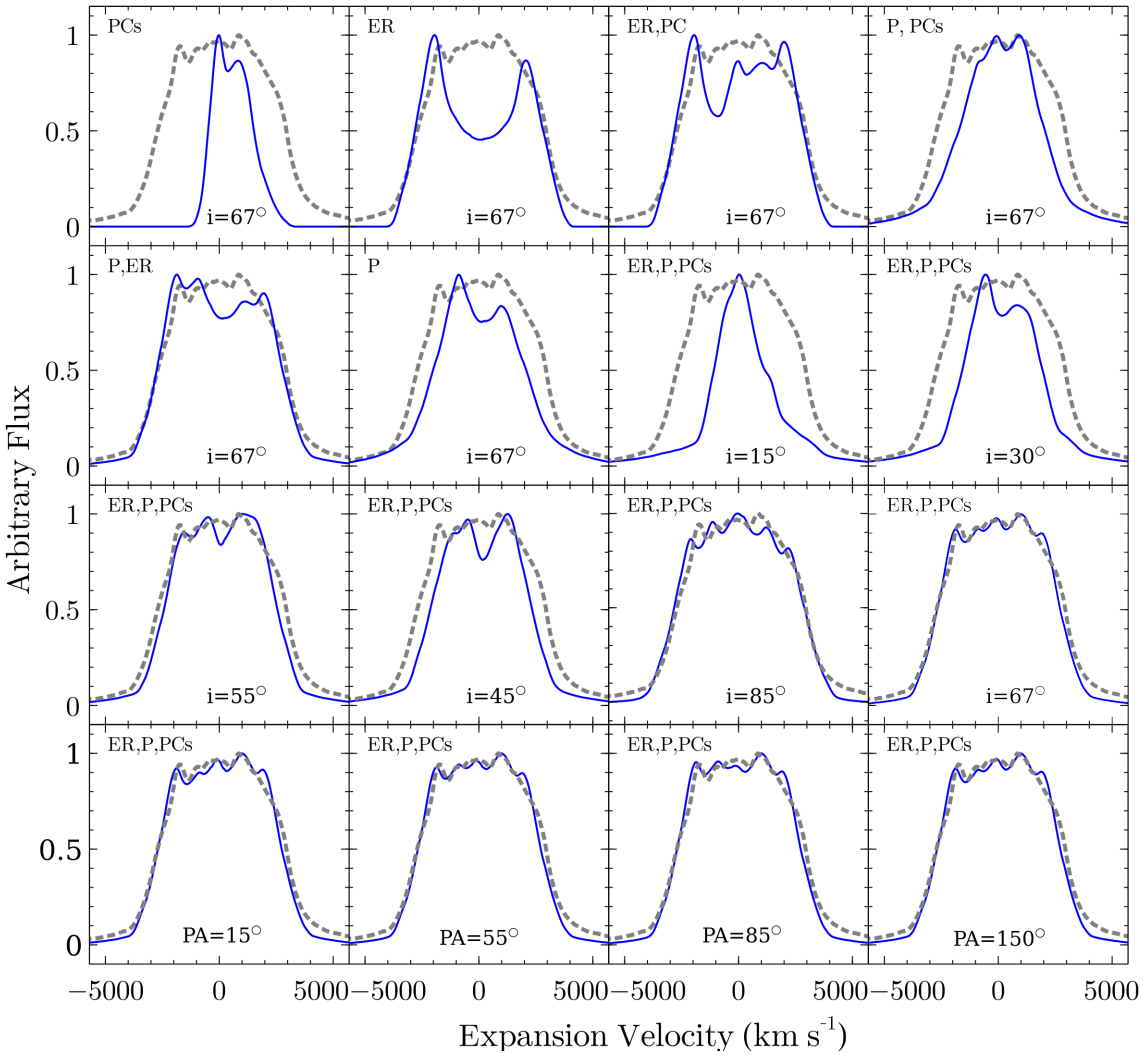

Fig. 4.13 Optimizing geometries to fit the observed spectral line profiles. In the plot above, geometries are plotted in blue solid lines at their best fit inclinations and the observed spectral line profiles in gray dashed lines. In the upper three rows the position angle PA= 35°, where as in the last row the inclination i= 67°. The abbreviations in the plot are ER=Equatorial Ring, PCs= Polar Capes, P= Prolate.

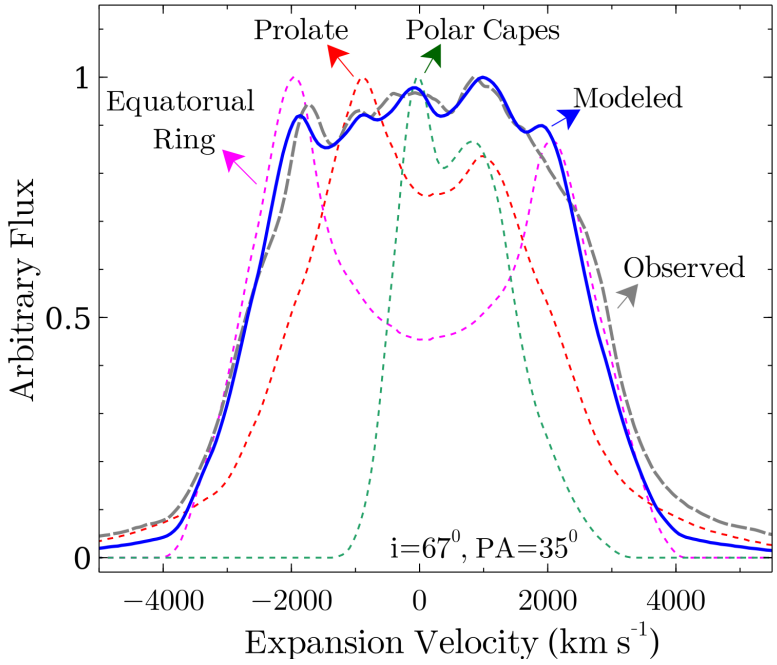

Fig. 4.14 Individual fitting components to the observed line profile (dashed gray line) at day 3 after outburst (i.e June 15, 2021). The model spectrum (solid blue line) is the sum of the individual components, Equatorial Ring (dashed magenta line), Prolate (dashed red line), and Polar Capes (dashed green line)

the corresponding figures of figure 4.14 for the other epochs, rather we provided all the best fit plots in figure 4.15.

We reconstructed the 3D ejecta geometry of V1674 Her for six epochs: days 2.96, 10.91, 14.91, 17.97, 22.89, and 25.84 following the outburst. Across all epochs, the modelled ejecta consistently exhibit a bipolar geometry characterised by a central equatorial ring surrounding the major axis. The bipolar structure consists of symmetrical bipolar morphology resulting from a squeezed oblate shape and asymmetrical polar caps. The presence of an equatorial ring in the H α morphology suggests potential interaction between the outflow and a secondary component. This phenomenon was observed in other previously analysed novae, such as V2672 Oph (Nova Oph 2009) (Munari et al., 2011; Ribeiro et al., 2011), and nova ASASSN-18fv (Pavana et al., 2020).

Despite the reconstructed geometries exhibiting similarities across epochs, notable variations were identified in most of the free variables, including density, velocity, and

Table 4.6 Comparison between observed and modelled line fluxes of V1674 Her.

Day	O. Flux	M. Flux	Mod./Obs.	rms	q
2.96	110.0	118.0	1.0727	0.0727	0.7366
10.90	103.0	103.7	1.0068	0.0068	0.0711
14.91	110.1	117.3	1.0065	0.0654	0.6646
17.97	102.4	108.8	1.0625	0.0625	0.6361
22.89	100.2	109.0	1.0878	0.0878	0.6758
25.84	93.12	99.2	1.0653	0.0653	0.6636

radius. The inclination angle (i)[9] and position angle (PA)[10] experienced changes within a limited range. For all the modelled line profiles, we determine $i = 67 \pm 1.5°$ as the optimal value for the ejecta morphology's inclination, while the position angle is $PA = 35^{+20}_{-15}$. Fig. 4.15 displays the best-fitting model profiles of H α overlaid on the observed line profiles. To assess the model's appropriateness, we calculated and provided the rms and q-factor values in Table 4.6 using equations (4.12) and (4.13).

The 3D configuration of H α within the V1674 Her ejecta is depicted in Fig. 4.16. This figure illustrates the density variations within the ejected material shell along both the bipolar axis (Z-axis) and the equatorial ring axis (X-axis). According to the model, the density in the equatorial region of the ejecta shell is higher than that of the polar components on the specified days, which is evident in Fig. 4.16 where the denser areas are represented in white. The sum of each ejecta geometries collected for the six different epochs are shown in Figure 4.17. The graphical representation also visualises the gradual expansion of the shell's geometrical dimensions during the intervals between the six epochs. The asymmetric features observed along the bipolar axis arise from the polar caps, and they are common among all model geometries within the context of the entire ejecta model. This asymmetry is attributed to unconstrained factors such as ejecta density, velocity, and angular radii within the polar cap regions. The red component of the polar caps exhibits a significantly higher magnitude compared to the blue component, with respective ratios of ∼3.11, 4.88, 3.88, 4.8, 4.49, and 3.13. This

[9]The i is the angle made between the plane of observation and the orbital plane of the binary, which is expected to be the same as the shell equatorial structure.

[10]The PA is measured in degrees counterclockwise with respect to the north celestial pole.

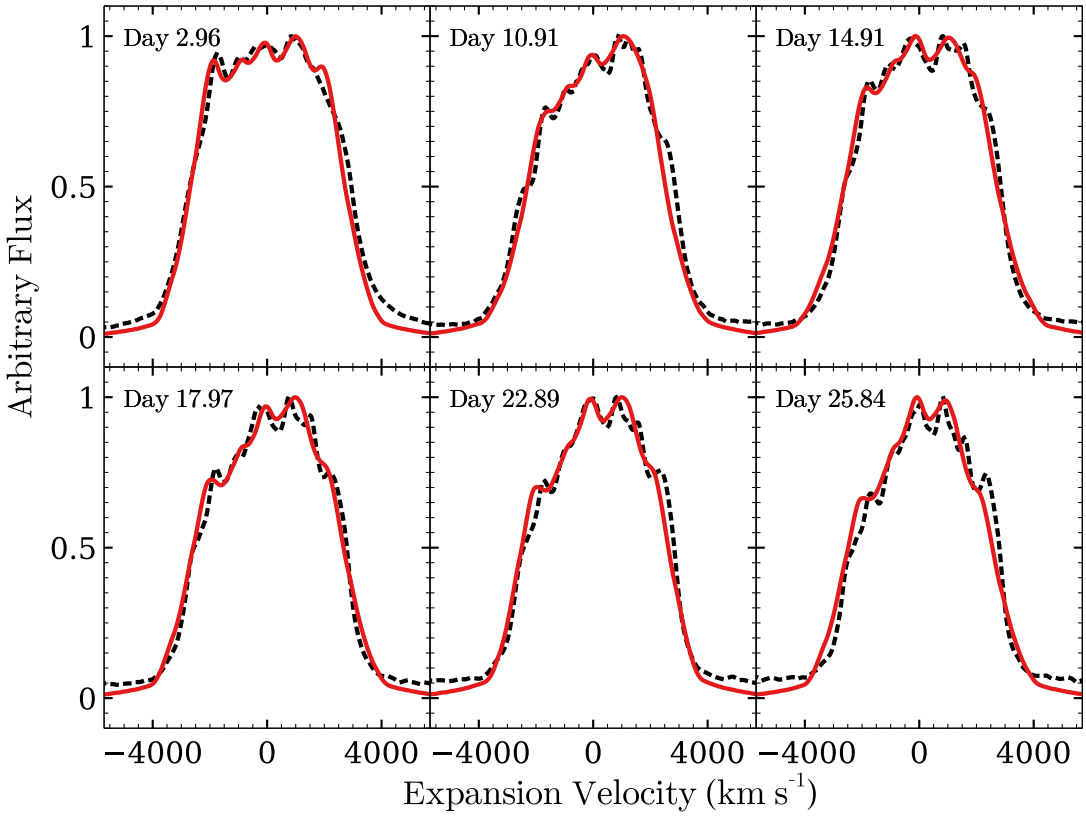

Fig. 4.15 Best-fit modelled velocity profile (the red solid line) overlaid on the observed H α profile (dashed black line) of V1674 Her on the following dates in 2021: June 15.95 (2.96 d), June 23.86 (10.91 d), June 27.87 (14.91 d), June 30.931 (17.97 d), July 04.91 (22.89 d), and July 07.87 (25.84 d).

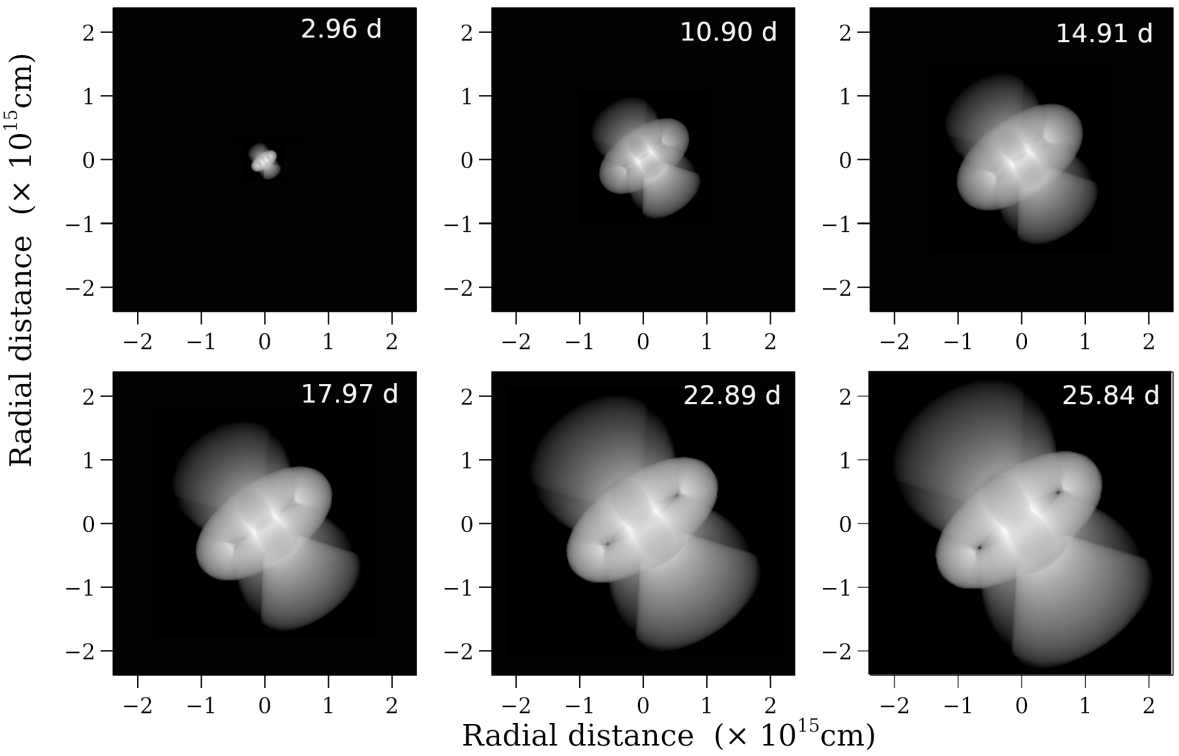

Fig. 4.16 2D representation of the asymmetric 3D model result, obtained for the H α geometry of the ejecta of V1674 Her. The model images of the ejecta are derived from the best-fit to the H α line profile on the following dates in 2021: June 15.95 (2.96 d), June 23.86 (10.90 d), June 27.87 (14.91 d), June 30.931 (17.97 d), July 04.91 (22.89 d), and July 07.87 (25.84 d).

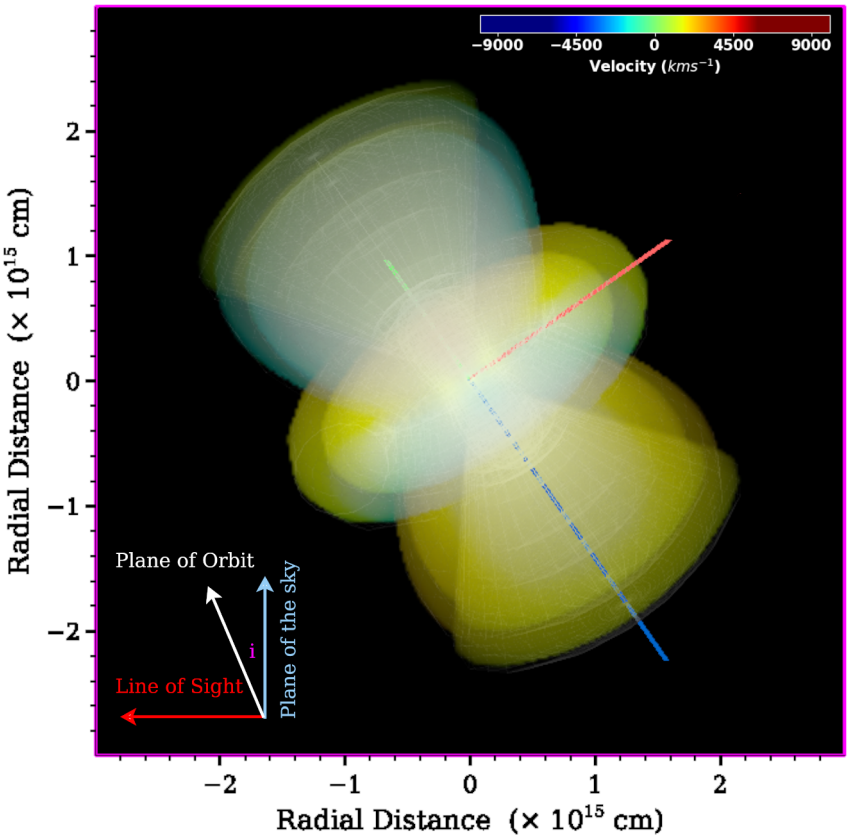

Fig. 4.17 2D representation of three dimensional expanding structure of H α on days 3, 11, 15, 18, 22, 1nd 25 of V1674 Her for the outburst in 2021. The overall structure is that a dumbbell structure with polar blobs and equatorial torus.

comparison is based not solely on geometric magnitude but also considers the density differences between the two poles. It indicates a larger amount of matter moving away from the line of sight (towards the red region) compared to that moving towards the line of sight (towards the blue region). With the exception of the polar cap elements situated on the red and blue sides of the bipolar major axis, all other components display symmetrical morphology.

4.3.5 Constraints of the model

Low values of $\chi^2_{\rm red}$ (between 1.0 and 2.0) indicate a close match between the simulated spectra and the observed ones. As shown in Table 4.3, the estimated $\chi^2_{\rm red}$ falls within this range for the majority of emission lines. However, some emission lines have $\chi^2_{\rm red}$

red values that exceed the expected range. Notably, the most significant discrepancies were observed in the H α lines. As indicated in Table 4.3, the χ^2 values for each epoch are notably higher than expected. This discrepancy is likely due to the fact that the observed H α line in the spectrum appears as a broad rectangular shape, whereas CLOUDY typically generates a triangle-shaped emission line. Consequently, we chose to exclude the H α line from the computation of $\chi^2_{\rm red}$ in our model, as it becomes challenging to precisely match the line flux ratios to the observed values. Other lines contributing to higher χ^2 values include H γ on epochs 1 and 3, H ζ on epochs 1 and 5, He II (4686 Å) on epochs 2 and 4, and N III (4638 Å) on epoch 1. These discrepancies may originated from the lines being suppressed either due to the model's inability to fully account for high optical depth or because the two-component model cannot adequately represent the intricate density structure of the nova ejecta.

Our model includes two distinct ejecta density components with higher and lower densities. This approach is considered more realistic than the one-component model, which assumes a uniform density across the ejecta shell. However, it may still fall short, as CLOUDY treats these components individually even if they are not truly distinct. The CLOUDY model is unlikely to incorporate clumpy components embedded within a larger diffuse component, a common feature in novae. This limitation arises because CLOUDY is a one-dimensional code and is not suitable for describing such complex environments. In such cases, dynamical models would be more appropriate. While CLOUDY can perform dynamical simulations, they are nearly 1000 times slower than time-steady calculations (Pandey et al., 2022a). The primary goal of this research is to develop a model that adequately explains the key characteristics of the shell ejecta from V1674 Her and its ionizing source. Currently, we have found that non-local thermal equilibrium (NLTE) time-independent snapshot models suffice. Using the employed modelling methods, we have successfully replicated a wide range of observational effects.

The morpho-kinematic 3D model in this study suggests that the ejecta structure associated with H α consists of a non-spherical bipolar shape overlaid with an equatorial ring within the ejecta. However, for the purposes of simplicity in the cloudy modelling,

we considered the geometry to be a homogeneous symmetric sphere, which does not entirely reflect reality. Temperature was held steady in our morpho-kinematic modelling since we observed that it had an insignificant impact on line profile fitting and 3D morphology. Consequently, temperature was not treated as a free parameter. Harvey et al. (2020) have also supported the notion that temperature has minimal effects on the structure of emission lines, particularly under conditions of higher densities.

4.4 Summary

We have investigated the spectroscopic and photometric evolution of V1674 Her, the fastest-recorded nova. We employed the ionization code Cloudy to model the observed spectra and estimate the physical and chemical parameters of the nova system. Additionally, we determined the morphology and inclination angle of the nova system using the morpho-kinematical analysis tool SHAPE. The main findings from our analysis are summarised below:

1. The decline time scales, t_2 and t_3 are estimated to be $\sim$ 0.91 days and 1.94 days, respectively, classifying it as an exceptionally rapid nova.

2. Utilising the MMRD relationship and a mean extinction of $A_V = 1.705$ in the V band, we estimate the distance to the nova to be $\sim$ 4.97 kpc.

3. We deduce the mass and radius of the WD to be $\sim$ 1.36 $M_\odot$ and $\sim$ 0.15 $R_\oplus$, respectively, confirming the ONe-type nature of the WD and thus categorising the nova as a Neon-type.

4. P Cygni absorption lines displayed an initial blue shift, evolving over time due to increasing velocity with distance.

5. The nova V1674 Her transformed from a Fe II-type to a He/N-type nova within ten days of the explosion.

6. The nova entered the nebular phase more rapidly than any recorded CNe, beginning on day 10 in the optical band.

7. photoionization modelling of the observed spectra through CLOUDY provided estimates for the source's temperature and luminosity, as well as the ejecta's density and elemental composition (refer to results in Table 4.2).

8. Our model, spanning one month after the outburst, unveiled an overabundance of He , Ne , O , N , and Fe relative to solar abundances. After ∼17 days from the outburst, the Fe abundance normalised to its solar value, while the neon abundance increased by a factor of 2, favouring the transition that occurred.

9. Based on our CLOUDY model, the ejected mass of V1674 is predicted to be $3.42 \times 10^{-5}\ M_{\odot}$, $4.23 \times 10^{-5}\ M_{\odot}$, $4.35 \times 10^{-5}\ M_{\odot}$, $4.85 \times 10^{-5}\ M_{\odot}$, and $7.40 \times 10^{-5}\ M_{\odot}$ for epochs 1, 2, 3, 4, and 5, respectively. These values align with theoretical predictions and prior findings for this nova.

10. The H α morphology of the nova ejecta during the initial month after the outburst exhibited asymmetry, featuring both bipolar and equatorial ring geometries. The presence of equatorial rings in the H α geometry suggests potential interactions of outflows with a secondary companion. We estimate the inclination angle of the ejecta geometry to be $\sim i = 67 \pm 1.5°$.

5

Quiescent Stages of RS Ophiuchi (2006-2021)

5.1 Introduction

The Recurrent Nova (RN) RS Ophiuchi (RS Oph) is a symbiotic nova belonging to a rare class of binary star systems, consisting of a massive white dwarf ($M_{WD} = 1.20{-}1.40\ M_{\odot}$) and a red-giant (RG) of type M0–2 III with a mass range of $0.68 - 0.80\ M_{\odot}$ (Brandi et al., 2009; Hachisu et al., 2007; Mikołajewska and Shara, 2017; Mondal et al., 2020; Osborne et al., 2011; Pandey et al., 2022b; Parthasarathy et al., 2007; Sokoloski et al., 2006). The binary has an orbital period, $P_{\rm orb}$, of 453.60 ± 0.40 days (Brandi et al., 2009). Hjellming et al. (1986) estimated the distance to RS Oph of d = 1.60 kpc from H I absorption line measurements. In this system, the white dwarf (WD) accretes material from the RG's stellar wind, leading to a buildup of hydrogen on the WD's surface. When the accumulated hydrogen reaches a critical pressure, it ignites in a thermonuclear runaway (TNR), resulting in a nova outburst (Gehrz et al., 1998). Previously RS Oph has undergone nine repeated outbursts in 1898, 1907, 1933, 1945, 1958, 1967, 1985, 2006 (Schaefer, 2010), and 2021 (Pandey et al., 2022b). However, the 1907 and 1945 outbursts lack full confirmation due to their alignment with the sun (Schaefer, 2004, 2010). The recurrence of these outbursts is interspersed with quiescent periods lasting approximately between 9 and 21 years (Schaefer, 2010).

The massive white dwarf, in conjunction with its high mass-transfer rate of ($\sim\ 2.00 \times 10^{-7} M_{\odot}\ \mathrm{yr}^{-1}$) (Booth et al., 2016; Walker, 1977), provides compelling

evidence that RS Oph is a likely candidate for a Type Ia supernova. The gradual increment in the WD's mass, due to the accumulation of about 10% of the accreted matter during each quiescent stage (Hachisu and Kato, 2000), supports this likelihood. The recent study by Starrfield et al. (2024) also showed a gradual increase in the WD's mass after outbursts, as the accreted mass appeared to be less than the ejected mass in each epoch of the hydrodynamical simulations conducted. Similarly, Hernanz and José (2008) conducted an evolutionary model indicating that the ejected mass is smaller than the accreted mass. Consequently the WD mass may eventually exceed the Chandrasekhar limit ($M_{ch} = 1.40\ M_{\odot}$) sometime in the future (Osborne et al., 2011). The net increasing rate of the WD mass has been calculated to be $1.20 \times 10^{-8}\ M_{\odot}\ \mathrm{yr}^{-1}$ (Hachisu and Kato, 2000), further supporting the premise that RS Oph holds the potential for evolving into a Type Ia supernova.

Several systematic multi-wavelength observations and studies of RS Oph have been conducted, mainly after the 1985 outburst. For example, γ-ray (Acciari et al., 2022; H. E. S. S. Collaboration et al., 2022), X-ray (Bode et al., 2006; Nelson et al., 2011; Page et al., 2022; Sokoloski et al., 2006), ultraviolet (Cassatella et al., 1985; Nelson et al., 2011), optical (Anupama and Mikołajewska, 1999; Buil, 2006; Skopal, 2009; Taguchi et al., 2021b), infrared (Banerjee et al., 2009; Das et al., 2006a,b, 2008; Evans et al., 1988, 2007; Woodward et al., 2021d), and radio (Kantharia et al., 2007; O'Brien et al., 2006; Rupen et al., 2008).

The comprehensive analysis of optical spectroscopy, particularly from 1958 onward (Eskioglŭ, 1963; Pottasch, 1967), revealed complex emission line profiles during outbursts, which are crucial for understanding the dynamics of the ejected material and its interaction with the surrounding environment. These profiles, including P Cygni profiles, indicate the presence of high-velocity winds and mass ejection from the system (Anupama and Mikołajewska, 1999; Bode et al., 2006). The UV observations in 1985, revealed significant differences in the emission line profiles of RS Oph compared to other classical novae Cassatella et al. (1985). They reported the early appearance of high ionization species in the UV range. The complex UV emission line profiles are also

crucial in studying the dynamics of the ejection and the geometry of the system. Das et al. (2006b); Evans et al. (1988) made IR observation and reported the rare detection of an infrared shock wave as the nova ejecta plows into the preexisting wind of the secondary in the RS Oph system consisting of a WD primary and a RG secondary. Padin et al. (1985), reported the first detection of the radio emission from RS Oph, and suggested a non-thermal origin of high brightness temperature. RS Oph has been detected as a very strong soft X-ray source using the European X-ray Observatory Satellite (EXOSAT) Mason et al. (1987). The early radio and X-ray emissions from RS Ophiuchi are predominantly non-thermal, resulting from the interactions between the shock waves and the surrounding nebular material (Eyres et al., 2009; Nayana et al., 2024). Abe et al. (2023) reported the detection of very high-energy (VHE) gamma rays at a significant level of 13.2 during the first four days of RS Oph using the MAGIC telescopes. In August 2021, the Fermi Large Area Telescope, H.E.S.S., and MAGIC all detected GeV and TeV γ-ray emission from the 2021 outburst of the RN RS Ophiuchi (Diesing et al., 2023). This marks the first observation of very high-energy γ-rays from a nova, opening a new avenue for studying particle acceleration. Both H.E.S.S. and MAGIC attributed the observed γ-rays to a single, external shock.

Relative to the outburst phase of RS Oph, its quiescent phase has been studied to a lesser extent. Some of the studies conducted on it are; (Anupama and Mikołajewska, 1999; Brandi et al., 2009; Mondal et al., 2020; Zemko et al., 2018). The quiescent phase of a nova is crucial for understanding various characteristics of nova eruptions and their development. This includes exploring interactions between binary components, the impact of eruptions on accretion discs and mass-transfer rates, recurrence intervals, and inter-class correlations among cataclysmic events (Kamath, 2008; Mondal et al., 2020). This study aims to investigate the temporal evolution of the chemical and physical characteristics of the RS Oph system during its quiescent phase from 2008 to 2020.

We describe our datasets in Section 5.2. In Section 5.3, we discuss the spectral characteristics observed during quiescence between the 2006 and 2021 outbursts.

Sections 5.4 and 5.5 detail the model analysis and technique, respectively, using the CLOUDY photoionization tool. In Section 5.6, we present the results and discussion of the model, and finally, we provide our conclusions in Section 5.7.

5.2 Data Set

We selected eight spectra spanning a time range of $\sim$ 13 years, from 2008 Feb. 22.38 UT to 2021 Mar. 8.15 UT, with an interval of about two years. These spectra cover the wavelength range of $\sim$ 3900 to 7500 Å and have a resolution range of $\sim$ 620 to 14,000. They were selected for spectral analysis purposes, encompassing the quiescent period between the two consecutive outbursts (2006 and 2021). All the spectra are normalized to the line flux of H β, and correct for reddening by E(B-V)= 0.73 (Pandey et al., 2022b; Snijders, 1987).

Out of the eight spectra selected for analysis, six were obtained from the ARAS database, one from Stony Brook/SMARTS, and one from Astrosurf. For the present study, we used spectroscopic data available in Astronomical Ring for Access to Spectroscopy Database (ARAS Database)[1] (Teyssier, 2019), Stony Brook/SMARTS Atlas of (mostly) Southern Novae [2](Walter et al., 2012), and Astrosurf Recurrent Nova[3]. The ARAS Symbiotics Project is composed of a cluster of compact telescopes, with diameters spanning from 20 cm to 60 cm. These telescopes are outfitted with spectrographs featuring resolutions ranging from R $\sim$ 500 to 15,000. The instruments cover a wavelength spectrum from 3600 Å to $\sim$ 9000 Å and are specifically designed for monitoring eruptive variable stars. The Stony Brook/SMARTS Atlas database contains both spectroscopic and photometric data obtained since 2003. This database facilitate systematic studies of the nova phenomenon and correlative studies with other comprehensive data sets. We also utilized a spectrum of an M2III type star, obtained from the European Southern Observatory (ESO) website[4], to match the absorption

[1] https://aras-database.github.io/database/novae.html
[2] http://www.astro.sunysb.edu/fwalter/SMARTS/NovaAtlas/rsoph/rsoph.html
[3] http://astrosurf.com/buil/us/rsoph/rsoph.htm
[4] https://www.eso.org/sci/facilities/paranal/decommissioned/isaac/tools/lib.html

features in the spectra originating from the secondary star. The instrumentation and observation details for each observatory and the log of observations are presented in Table 5.1.

Table 5.1 Log of optical spectral observation of Rs Oph, during its quiescent stages between the 2006 and 2021 outbursts.

Date (UT)	t_0^a (days)	t_q^b (days)	Obs.r	Obs.y	Spectrograph	Camera	R^c	Coverage(Å)	TTE^d(s)
2008 Feb. 22.38	739.550	300.00	SB^e	CTIO[1]	venerable RC	1K CCD	-	2720-9558	300
2010 Aug.15.82	1644.99	1205.00	BUI^f	CTO[2]	LISA	QSI583	620	3829-7317	4200
2012 Jun. 26.94	2326.11	1886.00	BUI^f	CTO[2]	LISA	Atik314L$^+$	1000	3829-7317	2113
2014 Jul. 24.95	3084.12	2644.00	DBO^g	WCO[3]	LISA	SXVR-H694	870	3800-7591	4441
2016 Aug. 20.93	3842.12	3402.00	JGF^h	SMMO[4]	LHIRES	ATIK 460EX	1101	3917-7475	4019
2018 Jul. 20.02	4540.09	4100.00	LES^i	MRO[5]	echelle	ASI1600mm	12000	4031-7950	8590
2020 Apr. 06.34	5166.50	4726.00	LES^i	MRO[5]	echelle	ASI1600mm	14000	4031-7955	7397
2021 Mar. 08.15	5502.32	5062.00	PAD^j	VNT[6]	LISA	Atik 460ex	824	4000-7500	1822

Note: $^{(a)}$Number of days counted from outburst date (t_0) (2006 Feb. 12.83 UT), $^{(b)}$Number of days counted from the start of quiescent phase (t_q) (2007 April 26), $^{(c)}$Resolution, $^{(d)}$Total Time of Exposure, $^{(e)}$Stony Brook using $^{(1)}$Cerro Tololo Inter-American Observator (CTIO), $^{(f)}$Christian Buil using $^{(2)}$Castanet-Tolosan Observatoty, $^{(g)}$David Boyd using $^{(3)}$ West Challow Observatory, ^{h}Joan Guarro Flo using $^{(4)}$Santa Maria de Montmagastrell Observatory, $^{(i)}$Tim Lester using $^{(5)}$Mill Ridge Observatory, $^{(j)}$Pavol A. Dubovsky using $^{(6)}$Vihorlat National Telescope, Obs.r stands for "Observer", and Obs.y stands for "Observatory".

5.3 General descriptions of the spectra

Fig. 5.1 illustrates the evolution of the quiescent spectra of RS Oph from day 739.55 (2008 Feb. 22.38 UT) to day 5502.32 (2021 Mar. 8.15 UT), after the outburst (on 2006 Feb. 12.83 UT), covering $\sim$ 4762 days of the quiescent period. The respective observation dates are indicated at the top-left corner of each panel. For this study, we selected eight spectra with nearly two-year intervals, except for the last one, which has only a one-year difference. These spectra show strong and broad emission lines attributed to hydrogen, helium, and iron, but the broadness of the lines decreases over time (see Table 5.2). The spectra are mostly dominated by Balmer lines (from H α to H 8) and He I (4922, 5016, 5876, 6678, and 7065 Å) lines. The presence of iron also becomes clear, especially in the later phases of the quiescent stage. Fe II (4233, 4491, 4584, 4924, 5018 Å) are some of the iron lines that appear in the spectra. The absence of higher ionization lines in the spectrum is likely due to the high-energy photons from the accretion disc being absorbed by the surrounding material. These photons are then re-emitted at lower energies, resulting in the softening of the radiation. The emission lines observed in these spectra during quiescent phase appear broad due to the expanded discs (Anupama and Prabhu, 1989). Intens optical Fe II emission lines originate from the outer, lower density portion of the disc (see Sec. 6.3.3.3). The strong TiO absorption features at 5448 and 6180 Å originate from the cool secondary star, indicating the resumption of accretion processes. Additionally, the appearance of optical flickering is considered another sign of the resumption of accretion (Zamanov and Bruch, 1998). Based on the presence of TiO molecular lines, Mondal et al. (2018) reported that accretion resumed approximately on day 250 following the outburst. In contrast, Worters et al. (2007, 2008) reported that accretion process resumed on day 241, based on their photometric observations, which showed a strong optical flickering (Sokoloski et al., 2001). However, the full quiescent phase began on April 26, 2007 (Mondal et al., 2018, 2020). Therefore, by taking the average of the two, we adopted day 245 as the resumption of the accretion process, and day 440 as the onset of the

quiescent phase. In Table 5.1, we present the number of days from the onset of the quiescent phase (t_q) until the date the spectra in Fig. 5.1 were taken.

5.3.1 Emission Line profiles

The emission line profiles of the four strongest Balmer lines (H α, H β, H γ, and H δ) are depicted in the two panels of Fig. 5.2. The left column comprises the profiles of the H α and H β lines, while the right column encompasses the profiles of the H γ and H δ lines. Both columns comprises the profiles of eight distinct epochs. The H α profiles of 2018 Jul. 20.02 UT (day 4540) and 2020 Apr. 6.34 UT (day 5165.50), acquired through a high-resolution telescope, distinctly exhibit a central deep absorption feature which cut the broad emission line into two adjacent peaks (see the left column of Fig. 5.2). This is possibly due to a slow, very dense wind in the system (Anupama and Mikołajewska, 1999; Van Winckel et al., 1993). In addition, the double peak feature of H α suggests that it originates from the accretion disc (Horne and Marsh, 1986; Zamanov et al., 2024). The double peak feature detected in H α is also mirrored in H β, indicating that it too originates from the accretion disc. This feature, previously observed in various prior outbursts (Anupama and Mikołajewska, 1999; Brandi et al., 2009; Van Winckel et al., 1993; Worters and Rushton, 2014; Zamanov, 2011). The red-side peak of both H α and H β emission lines of both epochs, appeared stronger than the blue one in both epochs, consistent with observations during the quiescent period of the 1985 outburst of RS Oph (Brandi et al., 2009; Van Winckel et al., 1993).

The core of the H α line displays subtle positional shifts toward either the blue or red side (see Fig. 5.2). For instance, on days 739.55, 2326.11, 3084.12, and 5502.32, the core has been shifted blueward by -35.50, -65.93, -150.47, and -132.73 km s^{-1}, respectively, while on day 3842.12, the core has been shifted to the red by +92.83 km s^{-1}. Conversely, on day 1644.99, the peak has not been shifted to either side. On days 4540.09 and 5165.50, the peak on the red side shifted blueward by -9.14 and -6.86 km s^{-1}, respectively, whereas the peak on the fainter side is also shifted to the blue side by -68.57 and -73.14 km s^{-1}, respectively. The central deep absorption noticed

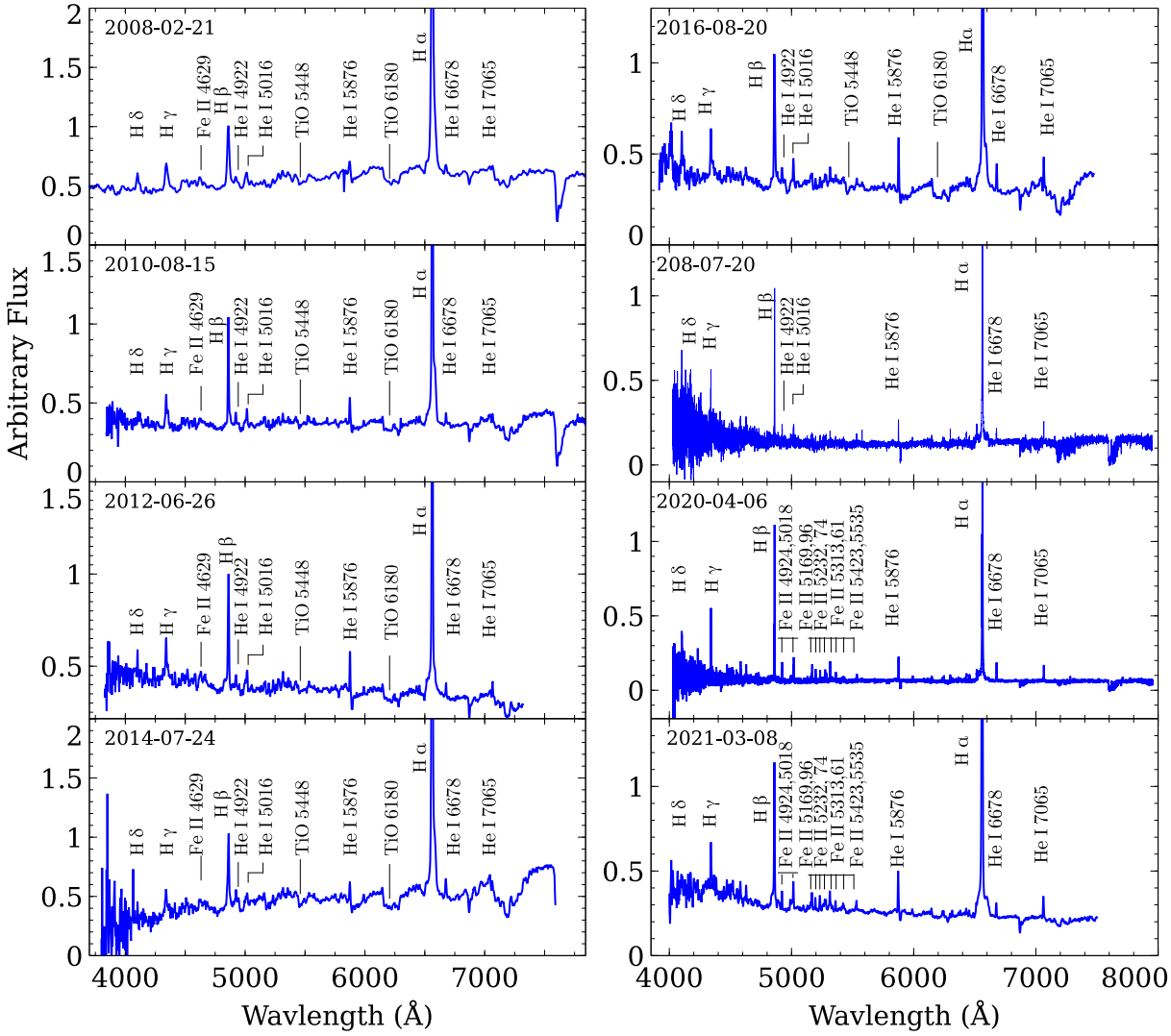

Fig. 5.1 Dereddened spectra of Rs Oph, illustrating the spectroscopic evolution from days 740 to 5504 following the 2006 outburst. All the prominent lines are labeled. The ordinate represents arbitrary normaized flux to H β line whereas the abscissa represents the wavelength in in Åunit. All spectra are corrected for reddening by a factor of E(B-V)=0.73.

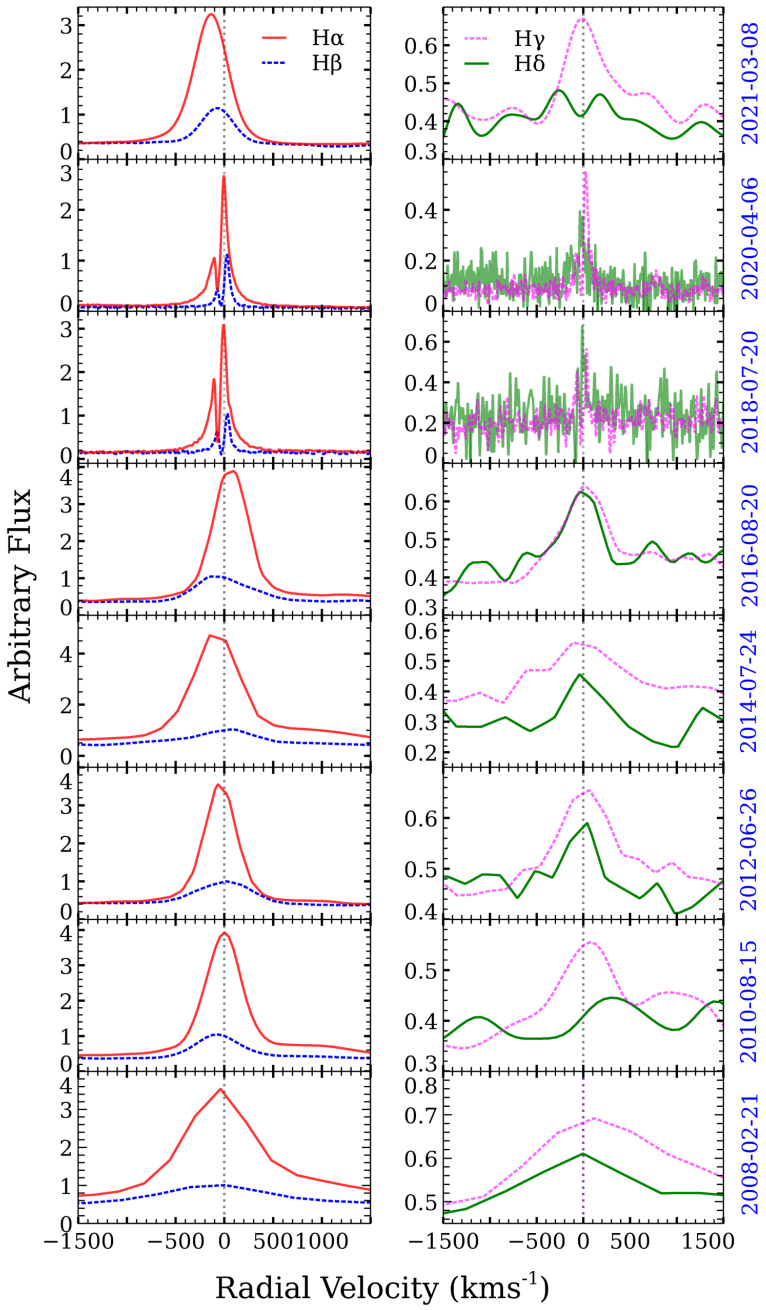

Fig. 5.2 Plot of H α, H β, H γ, and H δ emission line profiles of RS Oph during the quiescence phase between the 2006 and 2021 eruption. The legends on the top panels of each column apply to all the panels below, and the number of days provided on the right side of the second column serve as labels for the corresponding rows in the left column as well.

on these two days (4540.09 and 5165.50) have been also shifted bluewards by -68.57 and -73.14 $\mathrm{km\,s^{-1}}$. The reason for these shifts of peaks of emission lines could be the orbital motion of the primary and secondary stars around their common center of mass. This orbital motion induces periodic Doppler shifts in the emission lines (Horne and Marsh, 1986). The observed positional shift of the peaks might be due to fluctuations in the accretion rate. Anupama and Mikołajewska (1999) reported that accretion rate fluctuations were the primary reason for various variabilities, including changes in emission flux. A similar phenomenon was observed in nova V3890 Sgr (Zemko et al., 2018). Comparable shifts in central position are noted in other Balmer lines (H β, H γ, and H δ), albeit to a lesser extent in most cases.

The most noticeable characteristic observed in the emission lines of the spectra in this study is a decrease in the width of the Balmer lines over time. Table 5.2 presents the FWHM values of H α and H β for the eight spectra. The table clearly shows that these emission line profiles were widest on 22 Feb. 2008 compared to any other spectra captured later. Despite a slight increase on 24 Jul. 2014, the FWHM values of both emission profiles decrease monotonically up to 06 Apr. 2020. The reason for this narrowing of line width could be the slowing down of the remaining shell ejecta rom the outburst phase due to its interaction with the surrounding interstellar medium. As a result, the Doppler broadening of the emission lines is reduced, causing the lines to become narrower. Deceleration of the shell ejecta has also been observed in T Pyx (Schaefer et al., 2010). To the contrary of line width decrement through the course of time, a significant broadening has been observed on 08 Mar. 2021, about five months before the next outburst. This might be due to an increased accretion rate as the system approaches the critical limit, resulting in a higher velocity dispersion of the accreted material in the accretion disc. Additionally, the increased mass accreted onto the WD may create turbulence in the accretion disc, contributing to the broadening (Frank et al., 2002; Warner, 1995). Our photoionization modeling in Sec. 5.6.4 confirmed the significant increase in the accretion rate.

Table 5.2 FWHM values of most prominent emission lines (H α and H β) in all quiescent phase spectra.

Epochs	FWHM(H α) (km s^{-1})	FWHM(H β) (km s^{-1})
22 Feb. 2008	1114.43	1499.70
15 Aug. 2010	912.85	633.20
26 Jun. 2012	442.02	723.93
24 Jul. 2014	658.24	1020.78
20 Aug. 2016	469.91	743.06
20 Jul. 2018	246.84	127.13
06 Apr. 2020	185.13	129.79
08 Mar. 2021	459.85	448.98

Note: Each FWHM are subjected to $\pm$ 10 to 30 km s^{-1}error, which is estimated by taking three measurements for each and averaging them.

Disc size estimation from the H α and H β double peaks

In Section 5.3.1, we discussed that the H α and H β emission profiles showed double peaks on 2018 Jul 20.02 UT (day 4540) and 2020 Apr 6.34 UT (day 5165.50) (see Fig. 5.2). These features are attributed to emission lines originating from the disc. Assuming the accretion disc surrounding the white dwarf of RS Oph is a Keplerian disc, where the disc orbits the white dwarf under the influence of gravity. Zamanov et al. (2024), also assumed the accretion disc of the T CrB as a Keplerian disc. By using the separation of double peaks $\triangle V_{H\,\alpha}$ on the lines originated from the Keplerian disc, the outer radius R_{AD} can be estimated using the relation given by (Huang, 1972):

$$\triangle V_{H\,\alpha} = 2 \sin i \sqrt{\frac{G M_{WD}}{R_{AD}}} \tag{5.1}$$

where G is the gravitational constant (6.67×10^{-11} m^{3}kg^{-1}s^{-2}), M_{WD} is the mass of the white dwarf in RS Oph, and i is the inclination angle of the disc axis to the line of sight. We adopt the values $M_{WD} = 1.35 M_{\odot}$ (Hachisu et al., 2007) and $i = 30°$ (Pandey et al., 2022b). The separation of the peaks for H α and H β were found to be 98 ± 0.28 km s^{-1} and 101 ± 0.83 km s^{-1}, respectively. By applying these values in Eq. 5.1, we found $R_{AD1} = 1.87 \pm 0.01 \times 10^{12}$ cm for H α and $R_{AD2} = 1.76 \pm 0.03 \times 10^{12}$ cm

for H β. Taking the average of both results gives the radius of the accretion disc to be $R_{AD} = 1.82 \pm 0.10 \times 10^{12}$ cm

5.4 Photoionization Model Analysis

We used the 2023 released version of the CLOUDY code (C23)[5]; (Chatzikos et al., 2023) to model the quiescent spectra of RS Oph. CLOUDY has been effectively applied to study novae including the quiescent stage of a nova (Das and Mondal, 2015; Mondal et al., 2018, 2020; Pavana et al., 2019). CLOUDY simulates the physical conditions of non-equilibrium gas clouds exposed to an external radiation field by using detailed microphysics. It predicts the emission-line spectrum based on assumptions about the gas's physical conditions (ionisation, density, temperature, and chemical composition). The photoionization code CLOUDY uses a set of input parameters to compute the ionization, thermal and chemical state of a non-equilibrium gas cloud, illuminated by a central source, and it predicts the resulting spectra. The input parameters include the temperature (T) in Kelvins and luminosity (L) in erg s^{-1} of the central ionising source, hydrogen number density (n) in cm^{-3}, filling factor, covering factor, elemental abundances, and inner and outer radii (cm) of the surrounding ejecta. To generate synthetic model spectra, we incorporated all of these input parameters in our model along with the abundances of only those elements whose emission lines are observed in the spectra, while other elements are kept at their solar values (Grevesse et al., 2010). In CLOUDY hydrogen density and filling factor varies radially as $n(r) = n(r_o)(r/r_o)^{\alpha}$ cm^{-3} and $f(r) = f(r_o)(r/r_o)^{\beta}$, respectively, where α and β are the exponents of the power laws, and r_0 is the inner radius. The density of the shell is controlled by a hydrogen density parameter with a power-law density profile and an exponent of -2 because it provides a steady mass per unit volume throughout the model disc ($\dot{M}$ = const). The ratio of the filled to vacuum volumes in the ejecta are set to 0.1, which is the value used in other recent CLOUDY studies (Das and Mondal, 2015; Mondal et al., 2018, 2020).

[5] https://trac.nublado.org/

The goodness of our model fit is estimated from the χ^2 and χ^2_{red} (reduced-χ^2) of the model; using $\chi^2 = \sum_{i=1}^{n} \frac{(M_i - O_i)^2}{\sigma^2}$, and $\chi^2_{red} = \frac{\chi^2}{\nu}$ respectively, where O_i and M_i are the ratios of observed and modelled line fluxes to the H β line flux, respectively, σ_i is the error in the observed flux ratio, ν is the degrees of freedom given by $n - n_p$, n is the number of observed lines, and n_p is the number of free parameters. An ideal model has a $\chi^2 \approx \nu$ (Schwarz et al., 2001). Thus, the χ^2_{red} value of a model has to be low (typically in the range of 1-2) in order to be considered acceptable and well fitted. Normally, σ ranges from 10 to 30 percent, depending on how strong it is relative to the continuum and whether it can blend with other lines in the spectrum (Helton et al., 2010).

5.5 Modeling Procedure

We modeled a total of seven spectra, offering broader spectral coverage ($\sim$ 3900 to $\sim$ 7500 Å) and featuring a greater number of emission lines ($\sim$ 12 to 18 lines).We chose seven spectra to cover the entire quiescent period, with approximately two-year intervals. The modeled spectra span $\sim$13 years (2008-2020), however, the whole quiescent phase span for in between the 2007 and 2021 outbursts. The chosen seven epochs are Epoch 1 (2008-Feb-22), Epoch 2 (2010-Aug-15), Epoch 3 (2012-Jun-26), Epoch 4 (2014-Jul-24), Epoch 5 (2016-Aug-20), Epoch 6 (2018-Jul-20), and Epoch 7 (2020-Apr-2020); corresponding to days 740, 1645, 2326, 3085, 3843, 4542, and 5168, respectively after the 2006 outburst.

Initially, during the early years of the quiescent phase (from 2008-2016), we employed a one-component density profile across the radial distance of the accretion disc. However, as the nova approached to the next outburst (in 2021), the accretion disc increased in size significantly, leading to density gradient which is responsible for the emergence of diverse spectral lines. To account for this, we divided the accretion disc into two components (see Fig. 5.3) with distinct density and temperature profiles, and we adjusted them to match the emission features by multiplying with

the corresponding covering factors. While slightly varying the temperature, keeping the luminosity constant in each component, we noticed that the fitting procedure was not very sensitive to small changes in luminosity. This could be attributed to the minimal variation in geometrical extension with the luminosity parameter (Gallagher and Starrfield, 1978; Pandey et al., 2022b; Starrfield et al., 1976). Iron lines observed in the spectrum were mostly generated from the outer, lower-density region of the disc, whereas the helium lines primarily originated from the inner, higher-density and higher-temperature region.

In addition to the accretion disc, we also incorporated the primary (white dwarf) and secondary stars into our model. The primary star's contribution was added to the synthetic spectrum by generating a blackbody for each corresponding temperature, which fit the continuum. The secondary star's contribution was included by using the spectrum of an M2 III type red-giant star. Inclusion of the secondary star's spectrum in our model fits the absorption features originating from the cool secondary star. The accretion disc was responsible for all the emission lines in the spectra, and we adjusted its parameters for the best fit.

The inner radius ($R_{\rm in}$) and outer radius ($R_{\rm out}$) of the accretion disc were calculated as follows. The R_{in} was calculated from the relationship between the radius and mass of the white dwarf (i.e., $M_{\rm WD}^{(1/3)}\ R_{\rm WD} \propto$ constant) (Gehrz et al., 1998), and using the result that a WD of $1M_{\odot}$ has a radius of $10^{8.9}$cm (Hamada and Salpeter, 1961). The $R_{\rm in}$ is obviously equals to R_{WD}, as the inner portion of the disc is in physical contact with the outer surface of the WD. Therefore by equating the two relations we obtained $R_{in} = 10^{8.86}$ cm. The R_{out}, was estimated using the relation $R_{\rm AD}({\rm max})/a = 0.60/(1+q)$, where $R_{\rm AD}({\rm max})$, a and q represent the maximum accretion disc radius (i.e., equivalent to R_{out}), separation and ratio between the primary and secondary stars, respectively (Lasota et al., 2008; Paczynski, 1977; Sun et al., 2023). We took the average of the lowest and highest possible masses of the secondary (0.68 - 0.8 $M_{\odot}$) (Mikołajewska and Shara, 2017), which is $0.74M_{\odot}$. Using Kepler's third law and substituting the mentioned values along with the orbital period of 453.6 days (Brandi et al., 2009),

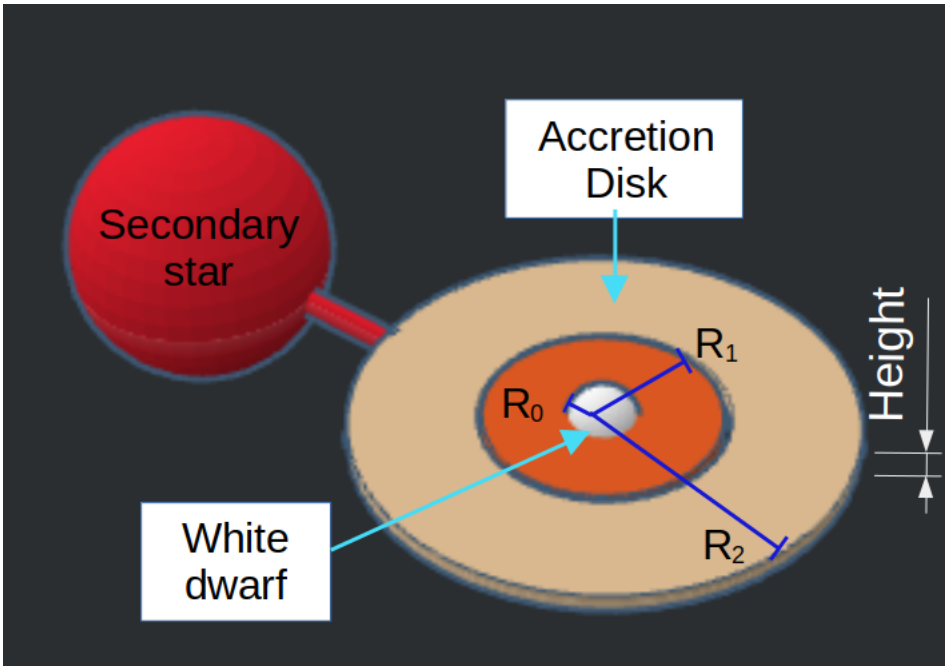

Fig. 5.3 Schematic diagram of a nova system at the quiescence stage. The accretion disk is assumed to be cylindrical in shape and has two components of density and temperature. The symbols R_0, R_1, and R_2 represent the radius of the white dwarf (inner radius of the inner disk component), the outer radius of the inner disk component (the inner radius of the outer disk component), and the outer radius of the outer disk component, respectively.

we obtained the separation (a) to be 2.22×10^{13}cm, and the ratio (q) to be 0.54. By substituting these all in the equation above, we obtained $R_{out} = 10^{12.94}$ cm. This estimate of the disc size is consistent with our estimation of the disc size from the double peak features of H α and H β in (Section 5.3.1). In our model of accretion disc we used $R_{in} = 10^{8.85}$cm and $R_{out} = 10^{13}$cm.

The inner radii for all epochs, except for the outer components of the last two epochs where we have considered a two-component model, are the same. However, as the accretion disc continuously grows radially, the outer radii of each epoch had to vary. In the initial years of the quiescent stage (particularly from 2008-2016), the outer radii were varying almost linearly with time. However, in the last few years (2018-2020), the outer radii of each epoch were increasing so rapidly. Fig. 5.5 illustrates this phenomenon effectively.

From the best-fitting model, we have obtained values for various physical and chemical parameters of the RS Oph system during its quiescent phase. These parameters include the temperature and luminosity of the source, hydrogen number density, dimensions, and composition of the accretion disc formed on the surface of the white dwarf (see Table 5.4). In Fig. 5.4, we present the best-fitting synthetic spectra overlaid on the observed spectra of RS Oph for seven epochs. Both the modeled and observed spectra are normalized to the line flux of H β, and the observed spectra are dereddened by E(B-V)=0.73 (Pandey et al., 2022b; Snijders, 1987).

To minimize the number of free parameters, the density power, filling factor, and inner and outer radii are held constant during the iterative process of fitting the observations. The hydrogen density, underlying luminosity, and effective blackbody temperature were varied. In addition, only the abundances of elements of observed lines were varied. All others are either set fully off or fixed at their solar values (Grevesse et al., 2010).

Following the procedure, we computed a set of synthetic spectra by simultaneously varying all the aforementioned input parameters in smaller increments across a broad sample space. The temperature ranged from $10^{3.5}$ to 10^{6} K, luminosity was

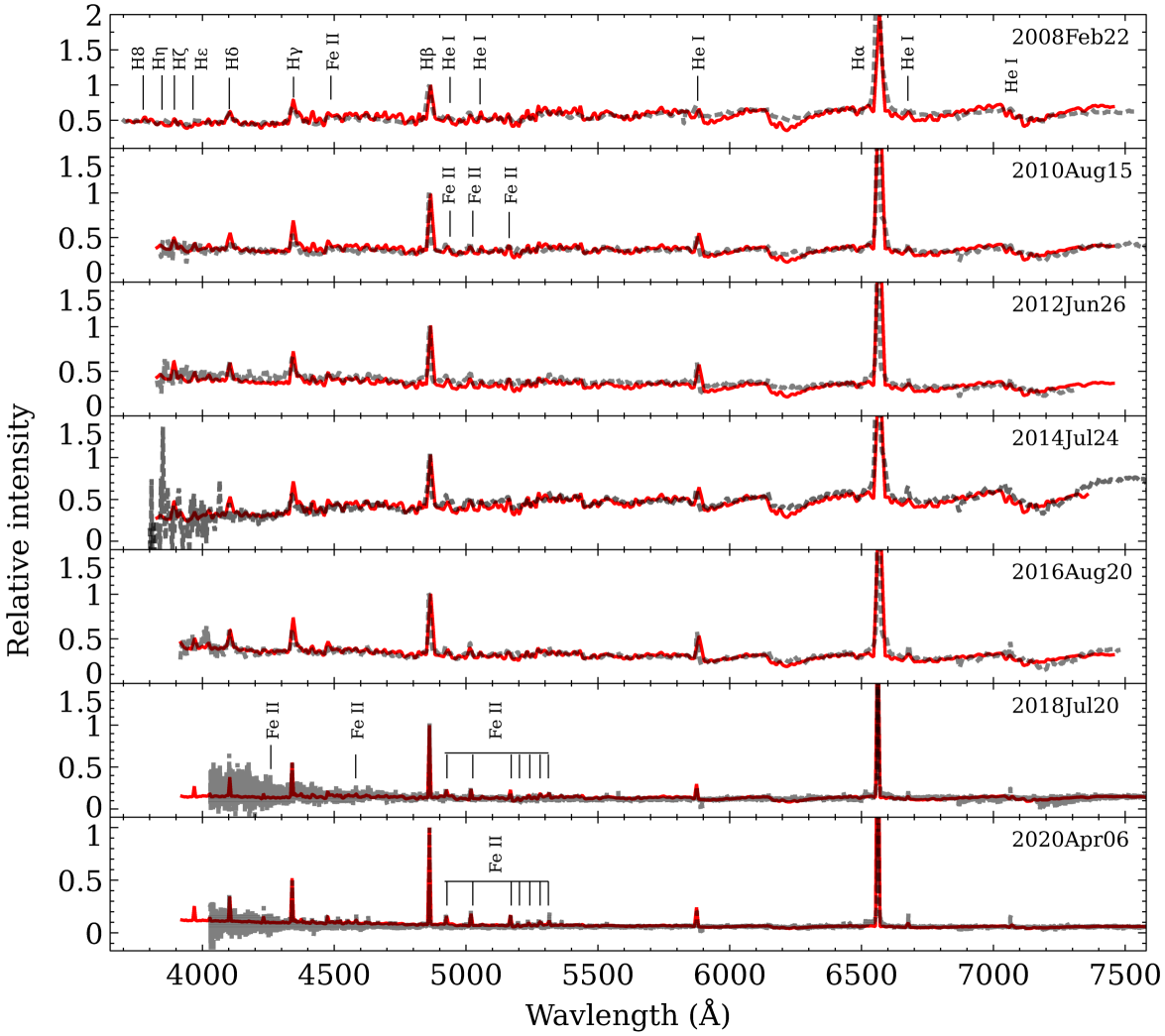

Fig. 5.4 Observed spectra during the quiescence phase of novae RS Oph (grey dashed line) alongside model-generated spectra (red solid line). Dates of observation for each epoch are indicated on the right side of each panel. Spectra have been normalized with respect to the H β line. Prominent emission lines are marked in the figure. For more details, please refer to Section 5.6.

varied between 10^{37} and 10^{38} erg s^{-1}, and ejecta density spanned $10^{6.5}$ to 10^{13}cm^{-3}, concurrently with the elemental abundances. Multiple test models were iterated across all epochs before arriving at the final model. Initial visual examinations were conducted, and model spectra that did not align with the observed spectrum were discarded. To assess the fit quality, we calculated the χ^2 and $\chi^2_{\rm red}$ values of the model, as discussed in section 5.4. A comparison of the relative fluxes for the best-fitting model-predicted lines and the observed lines during the early phase is presented in Table 5.3, along with the corresponding χ^2. We selected emission lines that appear in both observational and modeled spectra, for the calculation of χ^2. To determine the line fluxes in individual emission lines, interactive flux measurements were performed by fitting Gaussians using the *splot* task of the *onedspec* package in IRAF.

5.6 Results and Discussion

5.6.1 Temperature & Luminosity

From the first epoch (2008) to the fifth (2016), we applied a one-component model. The temperature and luminosity of the system increased from 1.05×10^4 K and 1.00×10^{29} erg s^{-1}to 1.20×10^4 K and 1×10^{30} erg s^{-1}, respectively. In the initial couple of years, the system was relatively cool and less luminous system, possibly indicating that it had fully entered the quiescent phase with minimal matter accretion at that moment. Over time, both the temperature and luminosity increased. We opted not to vary the luminosity, as we observed that the fitting process was somewhat insensitive to small variations in luminosity (see Sec. 5.5). Similar to the patterns observed in the previous epochs, the temperature and luminosity continued to increase in these cases as well (see the values in columns 7-10 of Table 4.2).

5.6.2 Density & Radius

Our model shows that the hydrogen density in the accretion disk increased from 3.16×10^9 cm^{-3} to 6.31×10^{10} cm^{-3} from 2008 to 2016. After 2016, we used two density components: the inner density increased from 6.31×10^{10} cm^{-3} to 3.16×10^{11} cm^{-3}, while the outer density decreased from 6.31×10^{10} cm^{-3} to 3.16×10^{10} cm^{-3}. This clearly demonstrates that as the accretion disk forms, the inner region becomes denser than the outer region due to higher gravitational compression in the lower layers of the disk. The model also show that the outer radius of the accretion disk increased from 3.20×10^9 cm to 6.31×10^{11} cm during the period from 2008 to 2016. From 2016 to 2020, it further increased from 6.31×10^{11} cm to 1.00×10^{13} cm. This indicates that the radial expansion of the accretion disk was faster in the later stages of the quiescent phase compared to the earlier stages.

5.6.3 Elemental composition

The spectra show prominent lines of hydrogen, helium, and iron. All spectra are primarily dominated by Balmer lines, such as H α, H β, H γ, and H δ. These lines are the strongest in all spectra, indicating that hydrogen is the major constituent of the system.

Our model reveal a significant decrease in the abundance of helium throughout the quiescent stage of the nova RS Oph. For example, the He/He$\odot$ ratio was 2.4 in the first epoch but decreased to the solar value on epochs 6 and 7. The helium abundance across all epochs was determined by fitting the prominent He I lines (4026, 4471, 4922, 5016, 5048, 5876, 7065 Å). Our model clearly shows that the majority of these lines originate from the inner portion of the accretion disc, which is denser than the outer portion. However considerable amount of He has been generated from the lower density region as well. In addition, during modeling, we observed that a higher density needed to be set to achieve a better fit for these lines, consistent with Zemko et al. (2018). The generation of helium from higher density regions is also

common during active phases of novae (e.g., V1674 Her (Habtie et al., 2024a,b); RS Oph (Pandey et al., 2022b)).

In the initial three epochs (2008, 2010, and 2012), Fe exhibited subsolar abundances in the accretion disc. However, from the fourth epoch (2014) onward, it showed a considerable increase, appearing overabundant (see Table 5.4). The Fe /Fe$\odot$ ratio in the first and last epochs was obtained as 0.50 and 2.50, respectively. This indicates a significant enhancement in iron abundance as the nova approaches the upcoming outburst, possibly due to the continuous supply of substantial amount of iron rich matter from the secondary. The iron abundance for each epoch was determined by fitting specific lines from Fe II (4233, 4415, 4491, 4584, 4629, 4924, 5018, 5169, 5232, 5276, 5361, and 5538 Å). These lines predominantly originated from lower-density regions of the disc, with some contributions observed from higher-density areas. Fe II signifies a low ionization stage, suggesting its origin in a zone characterized by low kinetic temperature. During the initial four years from 2008, the abundance of iron was significantly lower than the solar value. This discrepancy could be attributed to the limited quantity of accreted matter, resulting in an insufficient amount of iron reaching the disc. The model predicts that the iron abundance surpasses the solar value from 2014 onward, increasing rapidly. This trend aligns with the notion that iron originates from the secondary star.

5.6.4 Accretion mass & rate

We calculate, the ejected mass within the model disc using the following equation, (Schwarz et al., 2001):

$$M_{\rm disc} = n(r_0) f(r_0) \int_{R_{\rm in}}^{R_{\rm out}} \left(\frac{r}{r_0}\right)^{\alpha+\beta} 2\pi r dr \int_0^h dz, \tag{5.2}$$

where $n(r_0)$ represents the hydrogen density (cm^{-3}) and $f(r_0)$ stands for the filling factor at the inner radius of the shell (r_0). The exponents α and β correspond to the

power laws. The values for density, filling factor, α, and β are directly adopted from the best-fitting CLOUDY model parameters (refer to Table 5.4).

The total ejected shell mass for the two-component model was estimated by multiplying the mass in each density component (clump and diffuse) by their corresponding covering factors and then adding them together. Similarly, for the one-component model, the mass was multiplied by its covering factor. Consequently, the ejected hydrogen shell masses are estimated to be: $8.94 \times 10^{-16} M_{\odot}$, $5.39 \times 10^{-15} M_{\odot}$, $2.52 \times 10^{-14} M_{\odot}$, $4.03 \times 10^{-14} M_{\odot}$, $8.02 \times 10^{-14} M_{\odot}$, $3.65 \times 10^{-8} M_{\odot}$, and $1.63 \times 10^{-7} M_{\odot}$ on the seven, respectively. In the first epoch, as anticipated, the white dwarf (WD) accreted a relatively small mass. The accretion mass showed a gradual increase during Epochs 2, 3, 4, and 5. In these epochs, the accretion mass exhibited a relatively slower growth rate. During Epochs 6 and 7, the accretion disc's mass increased rapidly. Fig. 5.5 illustrates the growth of the accretion disc over time in terms of both mass and radius. The observed acceleration of accretion rate can be attributed to the overall increase in the mass of the system (white dwarf and accretion disc) caused by the accumulation of matter on the white dwarf's surface. This results in a more efficient extraction of material from the secondary star's surface, utilizing the enhanced gravitational pull.

Counting from the resumption of the accretion disc on the surface of the WD (April 2007) to the last epoch of our model (April 2020), the time span of the accretion disc formation is $\sim$ 13 years. Utilizing the accreted masses estimated from the best-fit parameters of our photoionization model, we calculated a mean accretion rate of $\sim 1.25 \times 10^{-8} M_{\odot}$ yr^{-1}. This value is in excellent agreement with previous estimates independently made by Hachisu and Kato (2000) and Nelson et al. (2011), both of which were $\sim 1.20 \times 10^{-8} M_{\odot}$ yr^{-1}.

The critical accretion disc mass necessary for initiating thermonuclear runaway (TNR) can be estimated by considering the critical pressure in the inner layers of the disc (10^{15} N cm^{-2}) (Truran and Livio, 1986), as expressed by the formula:

$$M_{\rm acc} \approx \frac{4\pi R_{\rm WD}^4}{G M_{\rm WD}} P_{\rm crit}, \tag{5.3}$$

where $G = 6.67 \times 10^{-11}\ Nm^2kg^{-2}$, and $R_{\rm WD}$ and $M_{\rm WD}$ represent the radius and mass of the white dwarf (WD). Additionally, we determine the WD radius using the Nauenberg (1972) mass-radius approximation given in Yaron et al. (2005):

$$R_{\rm WD} \approx 1.12 \times 10^{-2} \left[\left(\frac{M_{\rm WD}}{M_{ch}} \right)^{-2/3} - \left(\frac{M_{\rm WD}}{M_{ch}} \right)^{2/3} \right]^{1/2} R_{\odot}, \tag{5.4}$$

Adopting the white dwarf mass of RS Oph as $M_{WD} = 1.35 M_{\odot}$ (Hachisu et al., 2007), we obtained a white dwarf radius ($R_{\rm WD}$) of approximately 1.72 $\times 10^8$ cm. The critical mass required to be accreted onto the white dwarf was then computed using Equation 5.3 to be $M_{\rm acc} = 3.07 \times 10^{-7} M_{\odot}$. This is considered as the critical mass of the accretion disc essential for initiating thermonuclear runaway (TNR) for a white dwarf mass of $1.35 M_{\odot}$.

Based on our model, we found that the accreted mass onto the white dwarf up to epoch 6 (July 20, 2018) totaled approximately $3.65 \times 10^{-8} M_{\odot}$, leaving a deficit of $2.70 \times 10^{-7} M_{\odot}$ to reach the calculated critical mass of $3.07 \times 10^{-7} M_{\odot}$. This result indicates that only about 12% of the critical mass had been accreted by July 20, 2018 (in approximately 10 years), whereas the remaining 88% of the critical mass had to accrete in the subsequent 3 years, up to the outburst that occurred in August 2021.

On April 6, 2020, our model estimated an accreted mass of $1.63 \times 10^{-7} M_{\odot}$, leaving a deficit of approximately $1.44 \times 10^{-7} M_{\odot}$ to reach the critical mass. This shows that about 53% of the critical mass required for triggering the TNR processes had been accreted up to April 6, 2020 (in approximately 13 years), whereas the remaining substantial mass (about 47%) accreted onto the white dwarf over the subsequent 16 months.

This observation underscores that the accretion rate in the final years is significantly higher compared to earlier periods, driven by the increased gravitational attraction resulting from the mass already deposited onto the white dwarf.

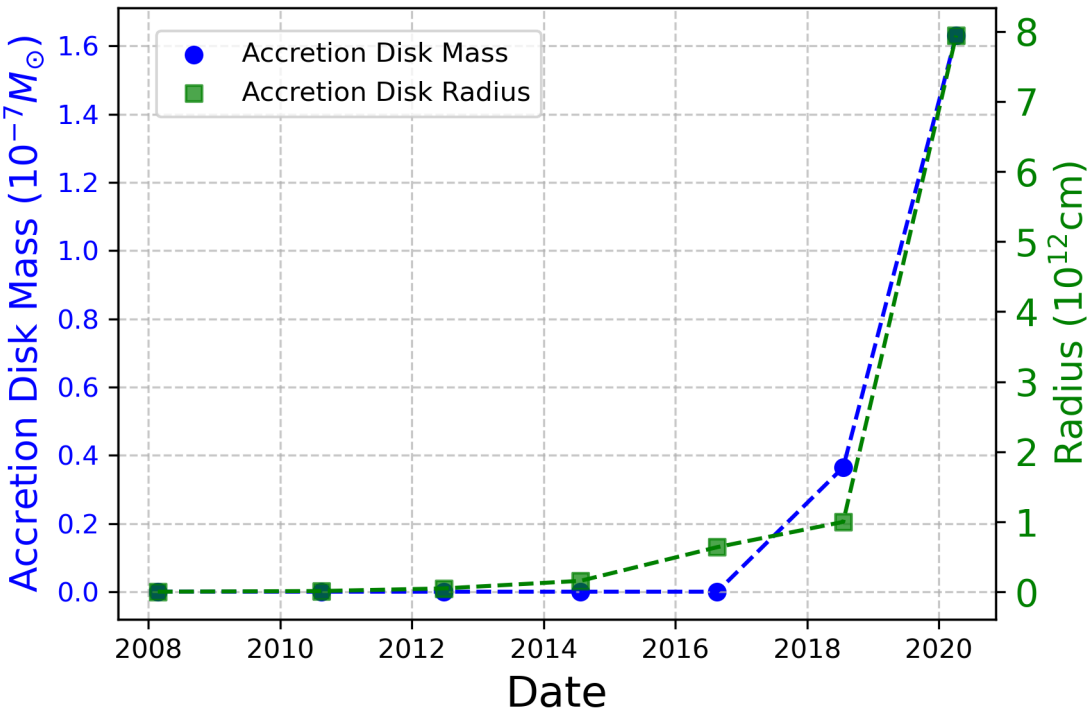

Fig. 5.5 Temporal Evolution of Accretion Disk Mass and Radius: This plot showcases the dynamic interplay between accretion disk mass and radius over time, providing a comprehensive view of the system's evolution.

Table 5.3 Observed and best-fit CLOUDY model line flux values for quiescent phase epochs of Rs Oph.

Line		Epoch 1 (2008Feb22)			Epoch 2 (2010Aug15)			Epoch 3 (2012Jun26)			Epoch 4 (2014Jul24)		
ID	λ (Å)	mod.	Obs.	χ^2	mod.	Obs.	χ^2	mod.	Obs.	χ^2	mod.	Obs.	χ^2
H 8	3770	0.304	0.271	0.074	-	-	-	-	-	-	-	-	-
H η	3835	0.190	0.185	0.002	-	-	-	-	-	-	-	-	-
H ζ	3889	0.511	0.125	0.048	0.312	0.331	0.038	0.290	0.287	0.001	0.366	0.172	2.239
H ϵ	3970	0.100	0.188	0.539	0.144	0.248	1.071	0.181	0.441	2.991	0.225	0.336	0.727
He i	4026	-	-	-	-	-	-	0.315	0.376	0.164	0.197	0.111	0.439
H δ	4101	0.247	0.355	0.812	0.812	0.424	0.005	0.375	0.277	0.432	0.389	0.334	1.885
Fe II	4233	0.091	0.088	0.001	0.079	0.220	1.988	0.076	0.242	1.228	0.082	0.087	0.002
H γ	4340	0.885	0.743	1.403	0.738	0.688	0.250	1.083	0.869	1.284	0.861	0.661	2.376
Fe II	4415	0.226	0.110	0.938	0.184	0.154	0.090	0.174	0.412	2.521	0.230	0.303	0.311
He I	4471	-	-	-	-	-	-	-	-	-	-	-	-
Fe II	4491	0.212	0.237	0.042	-	-	-	-	-	-	-	-	-
Fe II	4584	0.312	0.318	0.003	0.246	0.351	1.117	0.420	0.500	0.283	0.367	0.552	2.016
Fe II	4629	0.517	0.527	0.006	-	-	-	0.547	0.765	2.119	-	-	-
H β	4861	1.000	1.000	0.000	1.000	1.000	0.000	1.000	1.000	0.000	1.000	1.000	0.000
He I	4922	0.398	0.591	2.589	0.252	0.703	0.703	0.280	0.459	1.422	0.469	0.458	0.007
Fe II	4924	-	-	-	-	-	-	-	-	-	-	-	-
He I	5016	0.318	0.515	2.682	0.224	0.035	0.035	0.341	0.547	1.887	0.526	0.651	0.911
Fe II	5018	-	-	-	-	-	-	-	-	-	-	-	-
He I	5048	0.372	0.349	0.035	-	-	-	-	-	-	-	-	-
Fe II	5169	0.199	0.290	0.572	0.200	3.681	3.681	0.191	0.075	0.602	0.425	0.505	0.385
Fe II	5232	0.241	0.356	0.915	0.238	0.013	0.013	0.414	0.355	0.156	0.273	0.463	2.151
Fe II	5276	0.364	0.585	3.394	0.267	2.275	2.275	0.237	0.383	0.944	0.419	0.291	0.973
Fe II	5361	0.533	0.785	4.396	0.346	0.606	0.606	0.351	0.468	0.600	0.520	0.616	0.547
Fe II	5538	-	-	-	-	-	-	-	-	-	-	-	-
He I	5876	0.509	0.565	0.216	0.519	0.558	0.152	0.499	0.391	0.523	0.734	0.456	4.554
H α	6563	-	-	-	3.462	3.376	0.738	-	-	-	-	-	-
He I	6678	0.599	0.730	1.201	0.281	0.348	0.454	0.219	0.252	0.049	0.294	0.458	1.588
He I	7065	0.555	0.682	1.145	0.251	0.325	0.535	0.209	0.264	0.133	0.374	0.452	0.369

Figure 5.3 Continued: Observed and best-fit CLOUDY model line flux values for quiescent phase epochs of Rs Oph.

Line		Epoch 5 (2016Aug20)			Epoch 6 (2018Jul20)			Epoch (2020Apr06)		
ID	λ (Å)	mod.	Obs.	χ^2	mod.	Obs.	χ^2	mod.	Obs.	χ^2
H 8	3770	-	-	-	-	-	-	-	-	-
H η	3835	-	-	-	-	-	-	-	-	-
H ζ	3889	-	-	-	-	-	-	-	-	-
H ϵ	3970	0.153	0.066	0.339	-	-	-	-	-	-
He i	4026	0.122	0.134	0.006	-	-	-	-	-	-
H δ	4101	0.356	0.470	0.821	0.090	0.202	0.027	0.211	0.232	0.027
Fe II	4233	0.00.104	0.116	0.007	1.117	0.073	0.014	0.054	0.095	0.014
H γ	4340	0.737	0.533	1.849	0.438	0.284	1.641	0.430	0.204	1.641
Fe II	4415	0.180	0.082	0.428	0.151	0.040	0.853	0.043	0.030	0.853
He I	4471	0.222	0.339	0.604	0.128	0.037	0.568	0.128	0.037	0.568
Fe II	4491	-	-	-	-	-	-	-	-	-
Fe II	4584	0.328	0.162	1.227	0.143	0.107	0.087	0.057	0.059	0.087
Fe II	4629	0.450	0.249	1.966	0.189	0.026	1.841	0.025	0.071	1.841
H β	4861	1.000	1.000	0.000	1.000	1.000	0.000	1.000	1.000	0.000
He I	4922	0.162	0.283	0.659	-	-	-	-	-	-
Fe II	4924	-	-	-	0.205	0.111	0.607	0.099	0.099	0.607
He I	5016	0.166	0.311	0.942	-	-	-	-	-	-
Fe II	5018	-	-	-	0.156	0.125	0.066	0.128	0.124	0.066
He I	5048	0.100	0.272	1.316	-	-	-	-	-	-
Fe II	5169	0.149	0.214	0.188	0.190	0.169	0.031	0.139	0.082	0.031
Fe II	5232	0.148	0.116	0.046	0.192	0.111	0.449	0.042	0.060	0.449
Fe II	5276	0.213	0.308	0.394	0.244	0.082	1.827	0.076	0.068	1.827
Fe II	5361	-	-	-	0.295	0.072	3.457	0.067	0.061	3.457
Fe II	5538	0.181	0.228	0.098	0.277	0.063	3.183	0.031	0.043	3.183
He I	5876	0.506	0.454	0.119	0.315	0.233	0.466	0.243	0.138	0.468
H α	6563	3.537	4.017	10.223	-	-	-	-	-	-
He I	6678	0.146	0.252	0.498	0.075	0.105	0.063	0.073	0.064	0.063
He I	7065	0.116	0.129	0.008	0.079	0.097	0.022	0.049	0.070	0.022

Table 5.4 Best Fit CLOUDY Model Parameters for Quiescent Stages of RS Oph: 2006 to 2021 Outburst.

Parameters	Values				
	Epoch 1	Epoch 2	Epoch 3	Epoch 4	Epoch5
Black Body Temperature ($\times 10^4$K)	1.047	1.072	1.096	1.148	1.202
Luminosity ($\times 10^{30}$ erg s^{-1})	0.100	0.158	0.316	0.501	1.000
Hydrogen density ($\times 10^{10}$cm^{-3})	0.316	1.000	3.162	3.981	6.309
α	-2.000	-2.000	-2.000	-2.000	-2.000
Inner radius ($\times 10^9$cm)^a	0.708	0.708	0.708	0.708	0.708
Outer radius ($\times 10^{11}$cm)^a	0.032	0.126	0.50	1.584	6.309
Filling Factor^a	0.100	0.100	0.100	0.100	0.100
β ^{a}	0.000	0.000	0.000	0.000	0.000
Covering factor (AD:BB:SE)	45.5:15.5:39.0	62.5:15.5:22.0	63.0:17.5:19.5	59.0:10.0:33.0	65.0:16.0:17.0
He/He$_\odot$ ^{b}	2.400	1.800	2.100	2.100	2.100
Fe/Fe$_\odot$ ^{b}	0.500	0.500	0.800	1.900	2.100
Number of lines	22.00	17.00	20.00	18.00	19.00
Number of free parameters	6.000	6.000	6.000	6.000	6.000
Degrees of freedom	16.00	11.00	14.00	12.00	13.00
$\chi^2_{\rm tot}$	28.314	16.203	27.834	16.652	17.8561
$\chi^2_{\rm red}$	1.771	1.473	1.988	1.388	1.374

Note: ^{a} stands for the quantity is not considered as a free parameter.

^{b} Abundances are given in logarithmic scale, relative to the solar value. Due to an unprecedented mismatch between the model and observed spectra, we have excluded the presence of certain elements in our model spectra, including Carbon, Oxygen, Nitrogen, and Neon.

Figure 5.3 Continued: Best Fit CLOUDY Model Parameters for Quiescent Stages of RS Oph: 2006 to 2021 Outburst.

Parameters	Values			
	Epoch6		Epoch7	
	disk_{in}	disk_{out}	disk_{in}	disk_{out}
Black Body Temperature ($\times 10^4$K)	1.698	1.096	1.778	1.122
Luminosity ($\times 10^{30}$ erg s^{-1})	3.981	3.981	7.943	7.943
Hydrogen density ($\times 10^{10}$cm^{-3})	10.00	1.000	31.62	3.162
α	-2.000	-2.000	-2.000	-2.000
Inner radius ($\times 10^9$cm)[a]	0.708	31.62	0.708	31.622
Outer radius ($\times 10^{11}$cm)[a]	0.316	10.00	0.316	100.0
Filling Factor[a]	0.100	0.100	0.100	0.100
β [a]	0.000	0.000	0.000	0.000
Covering factor (AD:BB:SE)	42.0:3.0:8.0	44.0:3.0:8.0	43.0:2.0:3.0	49.0:3.0:3.0
$\text{He/He}_\odot$ [b]	1.100	1.100	1.000	1.000
$\text{Fe/Fe}_\odot$ [b]	2.400	2.400	2.500	2.500
Number of lines	19		19	
Number of free parameters	6.000		6.000	
Degrees of freedom	13		13	
χ^2_{tot}	13.263		14.471	
χ^2_{red}	1.020		1.113	

Note: [a] stands for the quantity is not considered as a free parameter.

[b] Abundances are given in logarithmic scale, relative to the solar value. Due to an unprecedented mismatch between the model and observed spectra, we have excluded the presence of certain elements in our model spectra, including Carbon, Oxygen, Nitrogen, and Neon.

5.6.5 Electron density and temperature Vs Depth

Using our model we showed the how electron density and temperature varied in the disk for each epoch, starting from the illuminating portion of the disk designated as R_1 in Fig. 5.3. From our model we found that the electron temperature on the illuminated face of the accretion disc in all epochs (i.e. at depth = 0 cm or at radius = 7.08×10^8 cm from the center of the WD) to be $3.47 \pm 0.42 \times 10^4$K. The electron density in all epochs showed a considerable increment from 3.76×10^9 to 3.40×10^{10} cm^{-3}. Fig. 5.6, illustrates the variation of the electron temperature and density with the depth into the accretion disc from the illuminated face to the WD. Both the electron temperature and densities in each epoch showed a gradual decrease in going from the inner radius to the outer radius.

5.6.6 Lines Volume Emissivity in the disk

The volume emissivity of a line describes the energy emitted in a specific spectral line per unit time and per unit volume. From our best-fit model, we have obtained the volume emissivity of selected prominent lines in the disk with respect to depth (the distance between the illuminated face of the disk and a point within the disk). Figure 5.7 shows how the volume emissivity of lines H α, H β, H γ, H δ, and He I 5876 Å varies relative to depth measured from the illuminated face of the disk to a point within the disk. The figures clearly show that the emissivity decreases from the inner to the outer portions of the accretion disk. The volume emissivity has a direct relationship with the square of the electron density and the square root of the electron temperature ($4\pi j_{br} \propto N_e^2 T_e^{1/2}$), where j_{br} stands for bremsstrahlung emissivity (Frank et al., 2002). This demonstrates that the obtained emissivity is consistent with the T_e and n_e values in Fig. 5.6.

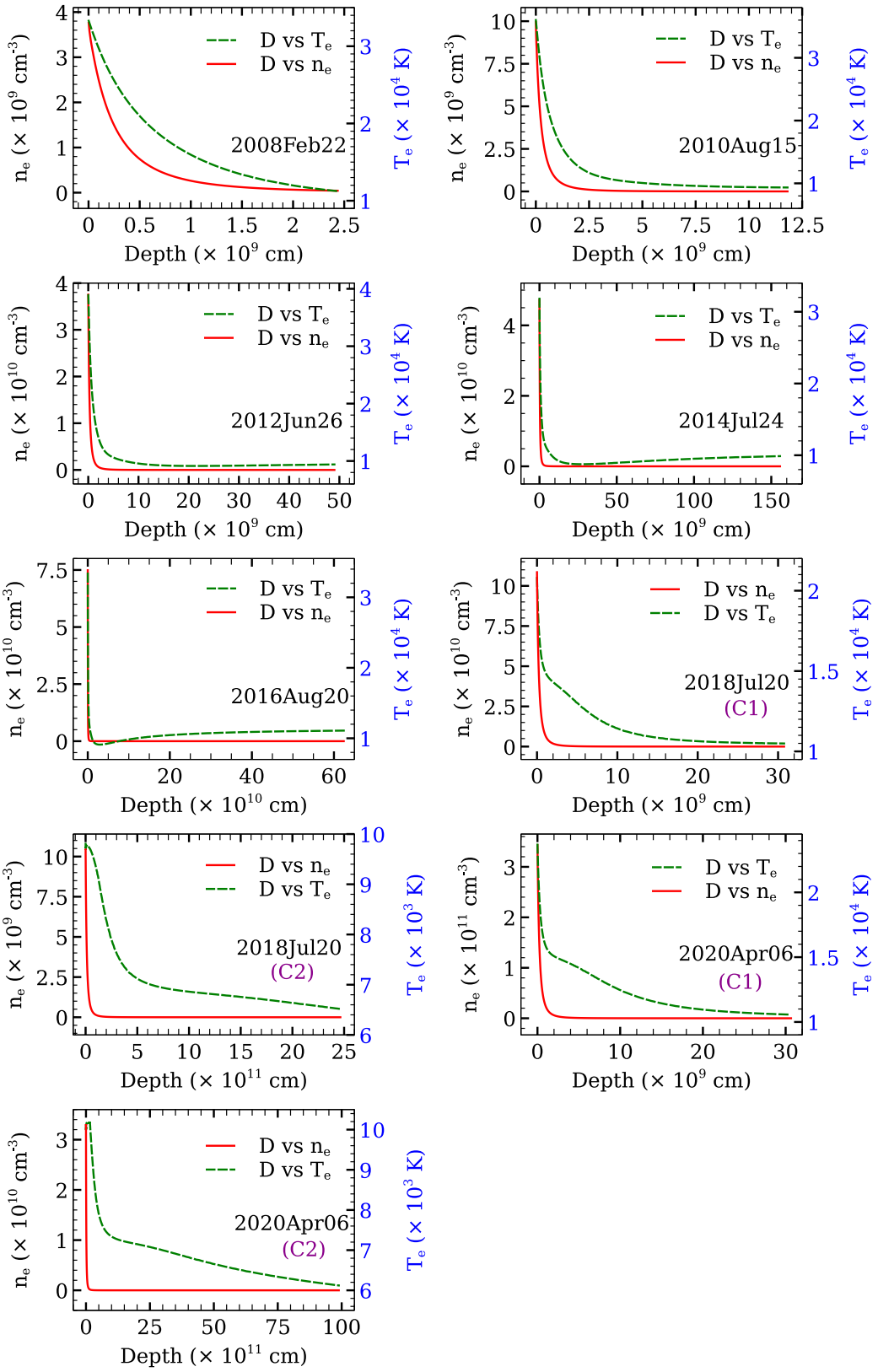

Fig. 5.6 An illustration showing how the electron density (n_e) and electron temperature (T_e) inside the accretion disk vary with respect to the depth (D). The red solid line represents D vs. n_e, and the green dashed line represents D vs. T_e. The C1 and C2 labels in the last two epochs indicate components 1 and 2, representing the inner and outer portions of the disk, respectively.

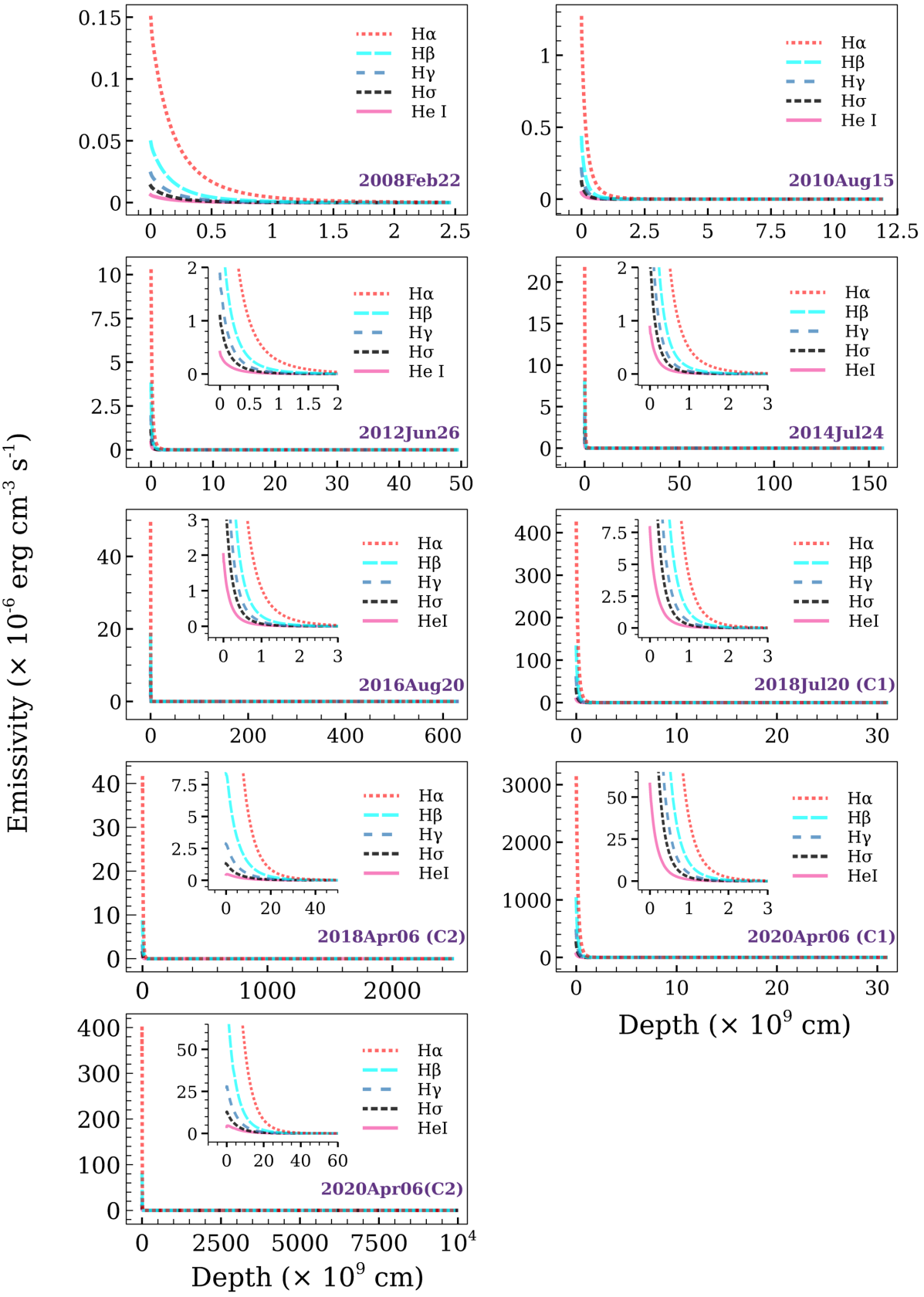

Fig. 5.7 Volume emissivity of H α, H β, H γ, H δ, and He I 5876 Åin disk with respect to depth (D). The C1 and C2 labels in the last two epochs indicate components 1 and 2, representing the inner and outer portions of the disk, respectively.

5.7 Conclusions

Our investigation of RS Oph during the quiescent phase between the 2006 and 2021 outbursts employed photoionization-based modeling and spectroscopic analysis to elucidate the accretion disc formation process, encompassing its composition, mass, and dimensions. The key findings are summarized below:

1. The spectra during the quiescent phase shows low-ionization emission features, including hydrogen, helium, iron, and TiO absorption features.

2. The high-resolution spectral profiles of H α and H β showed a deep absorption at the top, resulting in double-peaked profiles. This is due to the slow and dense wind in the system.

3. The core of H α showed a significant shift over time towards the blue and red edges of the profiles, which is due to the orbital motion of the primary and secondary around their common center of mass. Fluctuations in the accretion disc could be another possible reason for this shift.

4. The width of the Balmer lines showed a continuous decrease except for the last spectrum, which was taken approximately five months before the outburst in 2021. The possible reason for this might be an increase in the accretion rate, which leads to an increase in the velocity dispersion of the accreted material.

5. Using the double peak features observed in the H α and H β lines, we have estimated the accretion disc size to be $R_{AD} = 1.82 \pm 0.10 \times 10^{12}$ cm.

6. Utilizing the CLOUDY photoionization code, we determined that the central ionizing sources exhibit temperatures in the range of $1.05 - 1.80 \times 10^4$ K and luminosities between $0.10 - 7.90 \times 10^{30}$ erg s^{-1}.

7. The abundance of He displayed temporal variations, showing an overabundance from 2008 to 2016, returning to solar values by 2020. Meanwhile, Fe appeared subsolar from 2008 to 2014 but became overabundant from 2006 onward.

8. The mean accretion rate, as calculated from the model, is approximately $1.25 \times 10^{-8} M_{\odot}$ yr^{-1}. However, it is important to note that this value does not imply uniform accretion dynamics over time. About 47% of the critical mass was accreted in the last 16 months, and approximately 88% of the critical mass was accreted after July 20, 2018. This non-uniform accretion rate suggests a more rapid approach towards reaching the critical mass in the final years. This phenomenon could be attributed to the heightened gravitational pull resulting from previously accreted matter, influencing the accretion dynamics as the system approaches the critical mass limit.

9. The critical mass of the accretion disc is calculated to be $3.07 \times 10^{-7} M_{\odot}$.

10. From our model we found that the electron temperature (T_e) and electron density (n_e) to be $3.47 \pm 0.42 \times 10^4$K and 3.76×10^9 to 3.40×10^{10} cm^{-3}, respectively.

6 Study of Temporal Evolution of Nova V1405 Cas, 2021

6.1 Introduction

Nova Cas 2021 (V1405 Cas) was initially spotted as a transient candidate by Yuji Nakamura, registering at 9.6 magnitudes (unfiltered) on 2021-03-18.4236 UT (JD 2459291.9236) [1]. Subsequently, it was confirmed to be a classical nova by Maehara et al. (2021) and Taguchi et al. (2021a). The nova exhibited He/N type spectra initially, but approximately a month later, it transitioned to displaying Fe II type spectra (Munari et al., 2021a; Shore et al., 2021a). Subsequently, as its luminosity decreased, it reverted to He/N type spectra again (Shore et al., 2021b). Eventually, at approximately t = +618 days, its classification was updated to a neon nova due to the detection of predominant neon lines (Munari and Valisa, 2022).

It is widely accepted that the rate of brightness decline during a nova outburst is influenced by the mass of the hosting white dwarf (WD), with heavier WDs leading to faster declines in brightness, and vice versa for lighter WDs (Hachisu and Kato, 2010; Kato and Hachisu, 1994). Neon Novae, characterized by heavy WDs (>1.1 M$\odot$), are typically classified as fast novae (Doherty et al., 2015; Gehrz et al., 1998; Habtie et al., 2024b; Lauffer et al., 2018; Taguchi et al., 2023; Weidemann, 2000). However, the case of V1405 Cas presents an unexpected scenario. Despite being classified as a neon nova,

[1] http://cbat.eps.harvard.edu/unconf/followups/J23244760+6111140.html

V1405 Cas is remarkably slow, suggesting the possibility of a smaller WD mass. This unpredictability is reminiscent of other novae such as V723 Cas, which is the only very slow nova classified as a neon nova (Taguchi et al., 2023). The estimated WD mass of nova V237 is approximately $\sim$0.7M$\odot$ (Hachisu and Kato, 2015), consistent with expectations regarding nova speed and WD mass. The contrasting behavior of novae V1405 Cas and V237 Cas suggests that these novae represent different facets of nova behavior, warranting further exploration.

The aim of our project is to study the physical processes and characteristics of nova V1405 Cas. To achieve our objectives, we conducted an extensive spectral analysis and modeling. We employed the photoionization modeling tool CLOUDY to estimate various physical and chemical properties of the white dwarf, accretion disk, and secondary star. The study covers an extended period ($\sim$ 1050 days) starting from the outburst in 2021, as the nova is notable for being one of the slowest novae in history. The chapter is arranged as follows: in Section 6.2, we discuss the observation techniques and data reduction, in Section 6.3, we provide the analysis and discussion of the obtained results, including light curve analysis in Section 6.3.1, spectroscopic evolution in Section 6.3.2, and modeling results and discussion in Section 6.3.3.

6.2 Observations

For our current study, we utilized the 2-meter Himalayan Chandra Telescope (HCT) situated in Hanle, Ladakh, operated by the Indian Institute of Astrophysics (IIA) in Bangalore, India. Obtaining observing nights was facilitated by submitting the observation proposal titled 'Optical and NIR observations of Classical, Recurrent, and Symbiotic Novae'. Throughout the available observation period, we collected spectra of various novae. Among these, we focused on exploring the spectroscopic data of V1405 Cas across the optical range of 4000–9200 Å. This chapter presents the results of our optical analysis of this nova. The observation log is provided in Table 6.1 .

The optical spectra from the HCT were acquired using the Himalayan Faint Object Spectrograph Camera (HFOSC) equipped with Grism 7 (with a resolution of approximately 1500) covering the wavelength range of 4000–7000 Å and Grism 8 (with a resolution of approximately 2200) covering the range of 5200–9200 Å. Standard reduction procedures were applied to all spectra using various tasks within the Image Reduction and Analysis Facility (IRAF) package[2], including bias subtraction and cosmic ray removal. Subsequently, the spectra were extracted using the optimal extraction method implemented in the APALL task in IRAF. Wavelength calibration was performed using arc lamp observations, specifically iron–argon (FeAr) for Grism 7 and iron–neon (FeNe) for Grism 8. Flux calibration was achieved using sensitivity functions derived from spectroscopic data of standard stars Feige 34 (O-type subdwarf) and Feige 110 (OB-type subdwarf), observed concurrently. We present Grism 7 (Fig. 6.2 - 6.9) and 8 (Fig. 6.10) spectra separately because a little mismatch due to the resolution differences. To account for interstellar extinction, all spectra were dereddened using the corresponding color excess values. Additionally, normalization with respect to the H β line was performed for consistency across spectra.

Apart from the observation using HCT, we have also used spectroscopic data obtained from archive. The archival data is acquired from the Astronomical Ring for Access to Spectroscopy Database (ARAS Database[3]; Teyssier (2019)). The ARAS symbiotic project serves as an archival repository for data and encompasses a network of small telescopes, ranging from 20 to 60 cm in diameter, fitted with spectrographs with resolutions spanning from R $\sim$ 500 to 15,000, covering the wavelength range of 3600 to $\sim$ 9000 Å. In total, a set of 20 optical spectra (ranging from $\sim$ 3700 to 7800 Å) with resolutions varying from 300 to 1200 are employed. These spectra are acquired during the first month subsequent to the eruption and are contributed by various observers from different observatories. The observational details and the respective observatories

[2] http://iraf.noao.edu/
[3] https://aras-database.github.io/database/novae.html

are outlined in Table 6.1 . The spectroscopic data was processed utilising the Integrated Spectroscopic Innovative Software (ISIS[4]) following standard procedures.

[4]http://www.astrosurf.com/buil/isis-software.html

Table 6.1 Log of optical spectral observation of V1674 Her.

MJD	t[a](days)	Observer	Telescope	Spectrograph / Camera	R[b]	Coverage (Å)	TTE[c](s)
59293.342	1.918	DBO[d]	WCO-UK[h]	LISA / SXVR-H694	1030	3900-7380	2718
59531.391	239.967	PAD[e]	VNT[i]	LISA / Atik 460EX	976	3800-7550	1231
59814.658	523.234	GRH[f]	HCT[j]	HFOSC - Gr7	1300	4000-7000	60
59814.670	523.246	GRH[f]	HCT[j]	HFOSC - Gr8	2200	5200-9000	60
59916.660	625.236	GRH[f]	HCT[j]	HFOSC - Gr7	1300	4000-7000	600
59916.675	625.251	GRH[f]	HCT[j]	HFOSC - Gr8	2200	5200-9000	600
59974.577	683.153	SK[g]	HCT[j]	HFOSC - Gr7	1300	5200-9000	1200
59974.603	683.179	SK[g]	HCT[j]	HFOSC - Gr8	2200	5200-9000	600
60165.857	874.433	GRH[f]	HCT[j]	HFOSC - Gr7	1300	4000-7000	1500
60165.891	874.467	GRH[f]	HCT[j]	HFOSC - Gr8	2200	5200-9000	1200
60271.763	980.390	GRH[f]	HCT[j]	HFOSC - Gr7	1300	4000-7000	1200
60271.779	980.355	GRH[f]	HCT[j]	HFOSC - Gr8	2200	5200-9000	1200
60342.559	1051.135	GRH[f]	HCT[j]	HFOSC - Gr7	1300	4000-7000	1200
60342.602	1051.178	GRH[f]	HCT[j]	HFOSC - Gr8	2200	5200-9000	1200

Note: [(a)]Number of days counted from t_0 (2021 March 19.4236 UT, JD 2459291.924), [(b)]Resolution, [(c)]Total Time of Exposure, [(d)]David Boyd, [(e)]Pavol A. Dubovsky, [(f)]Gesesew R. Habtie, [(g)]Subhajit Kar, [(h)] *West Challow Observatory* in England, [(i)] *Vihorlat National Telescope* in Slovakia, [(j)] *Hemaliyan Chandra Telescope* in India.

6.3 Results and Discussion

6.3.1 Optical light curve

The optical *BVRI* light curve of nova V1405 Cas over the initial 1200 days, constructed using the AAVSO database, is shown in Fig. 6.1. Upon analyzing the light curve, we determined that the peak brightness, $V = 5.082 \pm 0.061$, was reached on 2021 May 10.297 UT (JD 2459344.797). Therefore, we designate 2021 May 10.297 UT as the reference time for the primary maximum. Apart from the primary maximum, we observed multiple outbursts of the nova at different times, but all of them were less brighter than the primary maximum. Among all maxima the top five prominent maxima are listed in Table 6.2. The Table includes the maximum V-magnitude value for each successive re-brightening's, along with the corresponding t_2 and t_3 values. For this study, we utilized the t_2 and t_3 values which are estimated from the last maxima of the re-brightening's, where the nova's brightness continued fading afterwards. Valisa et al. (2023) estimated the rate of flux decline after the final significant brightening using an exponential model of the form $F \propto (t - t_0)^{-2.33}$. For our further analysis, we adopted the t_2 value obtained from the last maxima, which are $t_2 = 164.517$ days and $t_3 = 174.611$ days. Similarly, we calculated the characteristic times t_2 and t_3 for the B-band to be 175.28 and 175.79 days, respectively. The obtained t_2 value is in good agreement with (Aydi et al., 2024). These are not the only t_2 and t_3 values observed in this nova; rather, they represent the last t_2 and t_3 values seen during the declining process of the nova. The estimated t_2 and t_3 values of the V1405 Cas outburst clearly indicate that the nova belongs to the speed class of very slow novae.

6.3.1.1 Reddening and distance calculation

All the spectra in this chapter have been corrected for reddening using $E(B-V) = 0.53$ (Munari and Valisa, 2022; Valisa et al., 2023). Using this value, we have estimated the distance of nova V1405 Cas from Earth.

Table 6.2 The t_2 and t_3 values of the Nova Cas 2021 outburst for its several brightening it showed. All the Date in UT are in the year 2021.

Date (UT)	(t-t_0)	V (mag)	t_2	t_3
May 10.297	52.855	5.082 ± 0.061	6.607	-
Jun. 7.094	80.652	6.421 ± 0.141	27.814	-
Jul. 27.406	130.964	5.819 ± 0.193	79.759	82.590
Sept. 10.119	175.677	6.455 ± 0.004	124.619	126.821
Sept. 22.262	187.819	6.481 ± 0.004	135.514	140.900
Oct. 19.744	215.302	6.835 ± 0.004	164.517	174.611

Note: (t-t_0) stands for the number of dates counted from the date of discovery (2021-03-18.4236 UT) to each brightening.

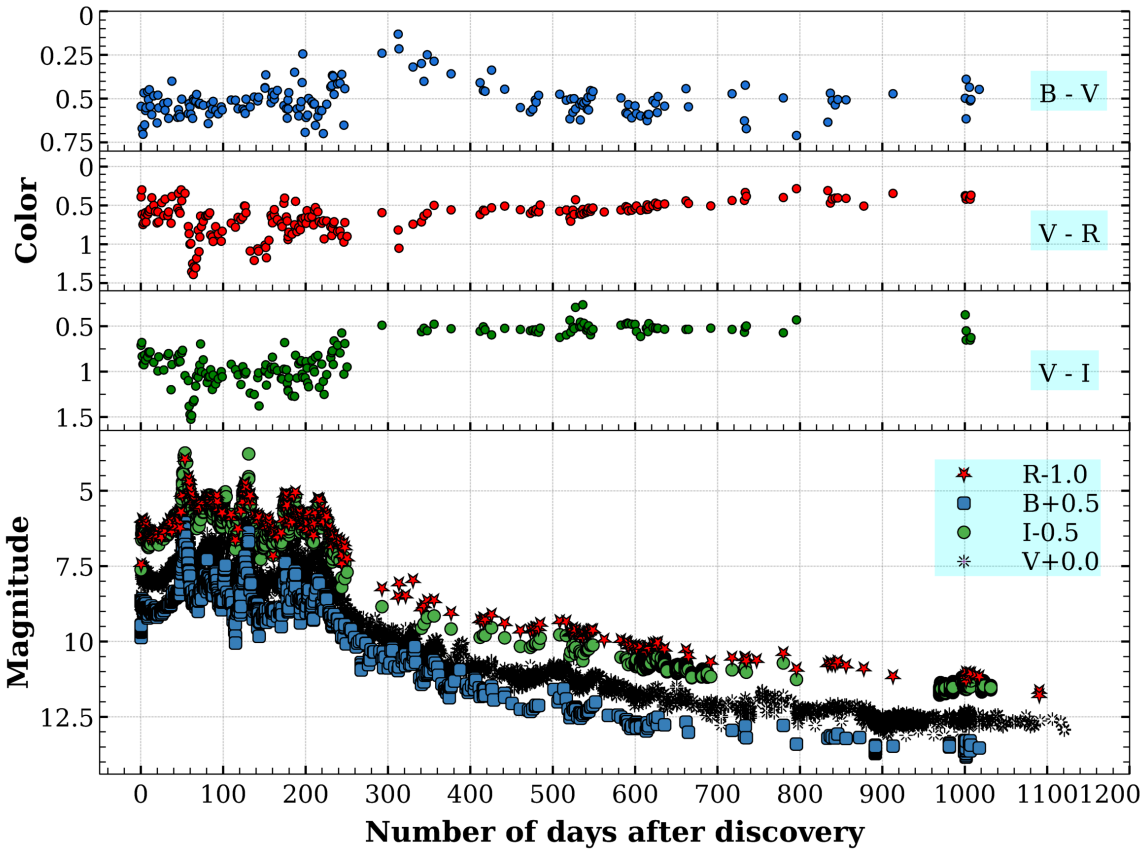

Fig. 6.1 *BVRI* Light curves of Nova Cas 2021 generated using optical data from AAVSO. Offsets are applied to the V and I bands for the sake of clarity.

First, we calculated the visual extinction A_V using the relation $A_V = R_V \times E(B-V)$, where the standard total-to-selective extinction ratio $R_V = 3.1$ (Richmond et al., 1994). Then, we utilized the relation of visual absolute magnitude and t_2 as given by Downes and Duerbeck (2000):

$$M_V = -8.02 - 1.23 \arctan\left(\frac{1.32 - \log t_2}{0.23}\right)$$

By substituting the value $t_2 = 164.517$, we obtained $M_V = -6.397$ mag. Finally, employing the distance modulus equation and substituting the derived parameters and visual apparent magnitude obtained from AAVSO, we estimated the distance of nova V1405 Cas from Earth to be approximately 2.091 ± 0.004 kpc. This result is in reasonable agreement with the previous Gaia estimate of about $1.73^{+0.08}_{-0.07}$ kpc (Taguchi et al., 2023).

6.3.2 Spectral evolution

The evolution of optical spectra for V1405 Cas up to 1052 days following the outburst on 2021 March 18.4236 UT (JD 2459291.924) is presented in Fig. 6.2 to 6.10. The first two spectra (Fig. 6.2 and 6.3) are taken from publicly available sources (see Table 6.1); spanning from 3900 to 7380 Å and from 3810 to 7550 Å , respectively. The remaining spectra (Fig. 6.4 to 6.10) are based on our observations from HCT. Due to considerable resolution differences between grism 7 (gr-7) and grism 8 (gr-8) (see Table 6.1), we preferred to present the spectra for each wavelength range separately. Since most of the emission lines across the optical region are concentrated on the blue side, we presented each spectrum separately for better visibility (see Figures 6.4 to 6.9). In contrast, the red side has fewer emission lines, so we presented all of them together in Figure 6.10. The spectra cover the range from 3700 to 7000 Å for gr-7 and from 5200 to 9000 Å for gr-8. However, for gr-8, we presented only the range from 6600 to 9000 Å, as gr-7 already covers the bluer side.

The spectra from day +1.918 (Fig. 6.2) and day +239 (Fig. 6.3) are dominated by strong hydrogen Balmer and helium lines. In addition to these recombination lines, the emergence of iron multiplets are observed in the spectra. These include Fe II multiplets 27, 29, 37, 38, 41, 42, 46, 49, 55, 73, and 74. Valisa et al. (2023) reported that these lines formed quite early, from day +31.4 onwards, while the He I lines weakened. Furthermore, very strong P Cygni profiles were persistent up to day 239, representing one of the longest durations of such absorption features. In contrast, these features disappear much more quickly in faster novae, such as RS Oph 2021, and V1674 Her (Habtie et al., 2024b; Pandey et al., 2022b). In both spectra, He I lines at 4028, 4471, 4922, 5016, 5876, 6678, and 7065 Å appeared stronger and broader than in any other spectra from later days. The strength of these He lines significantly reduced over time, and higher ionization levels of helium were introduced.

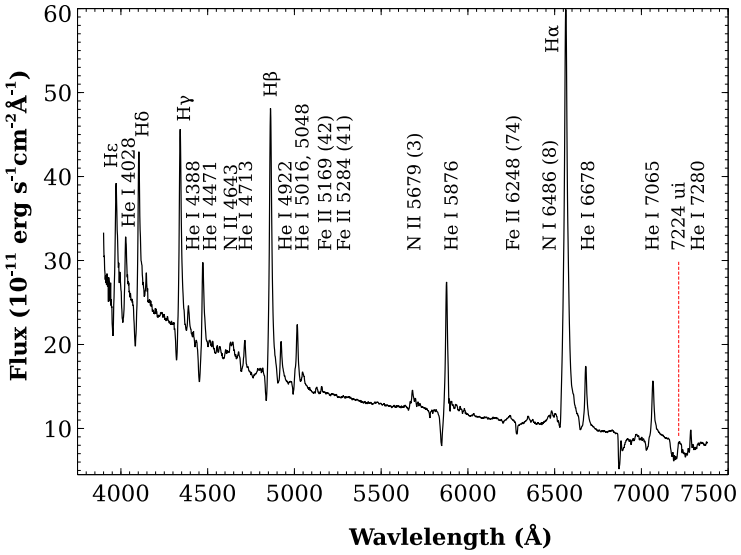

Fig. 6.2 A spectrum of V1405 Cas on 2021 March 20.342 UT.

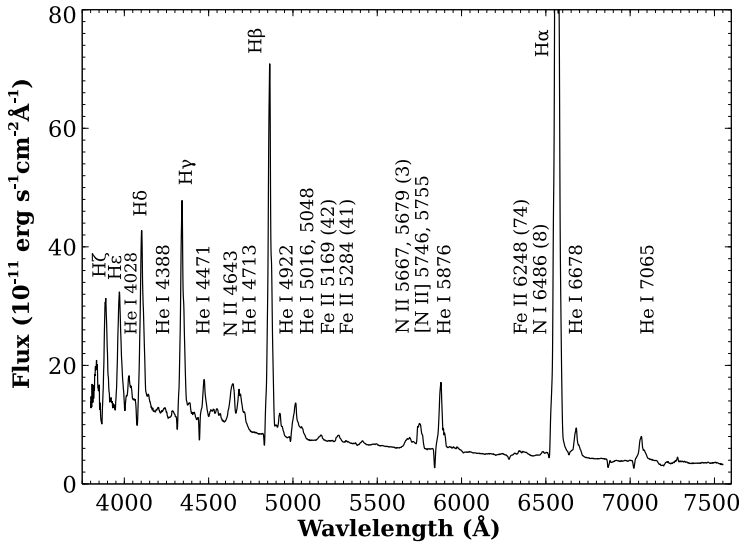

Fig. 6.3 A spectrum of V1405 Cas on 2021 November 13.391 UT.

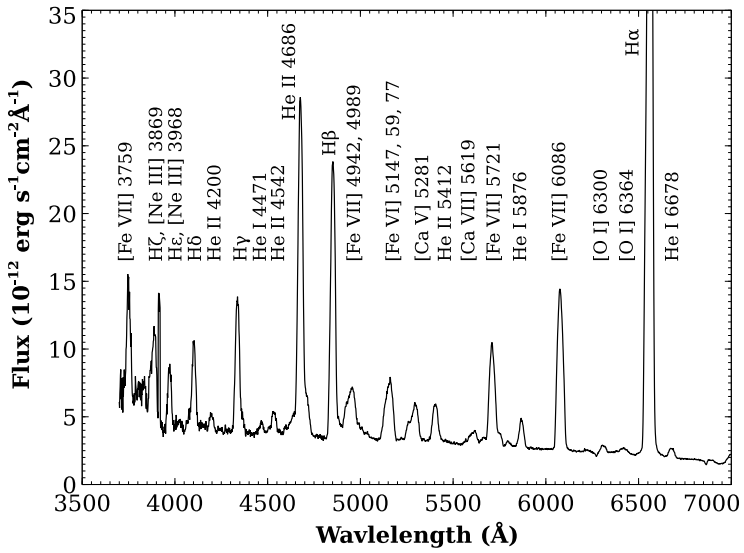

Fig. 6.4 A spectrum of V1405 Cas on 2022 August 23.658 UT.

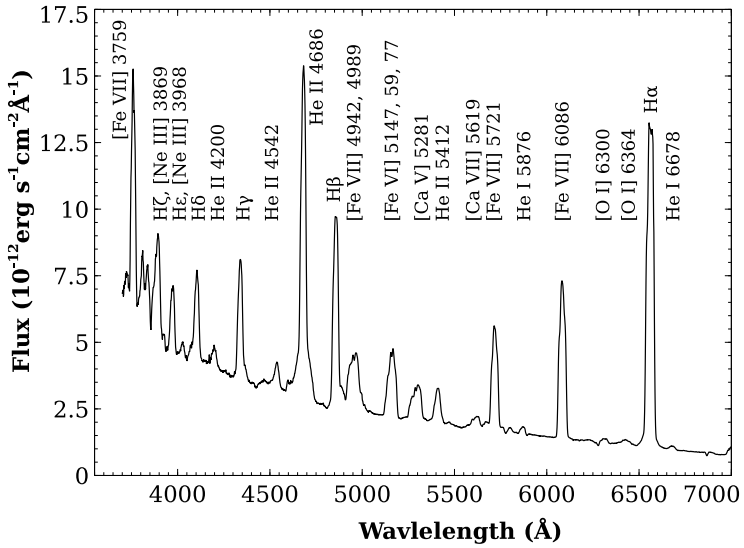

Fig. 6.5 A spectrum of V1405 Cas on 2022 December 3.66 UT.

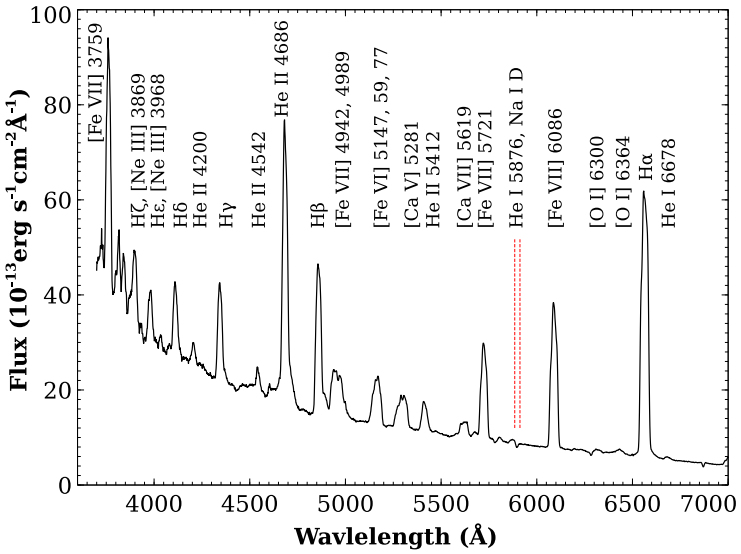

Fig. 6.6 A spectrum of V1405 Cas on 2023 January 30.577 UT.

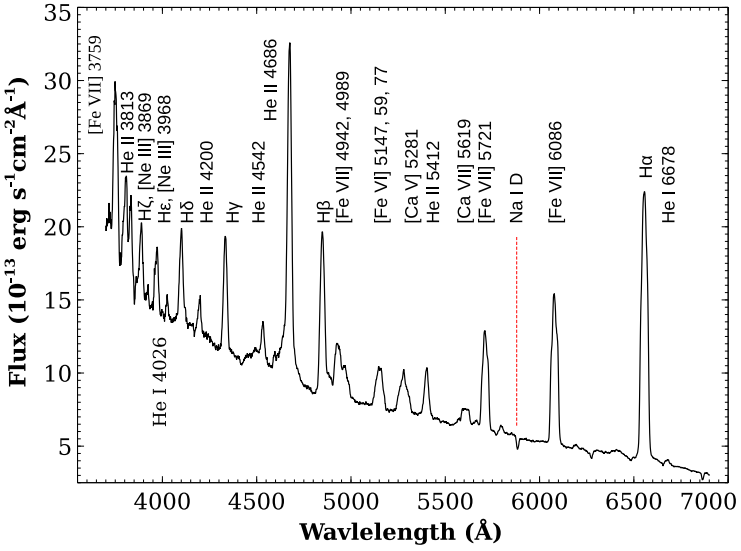

Fig. 6.7 A spectrum of V1405 Cas on 2023 August 9.857 UT.

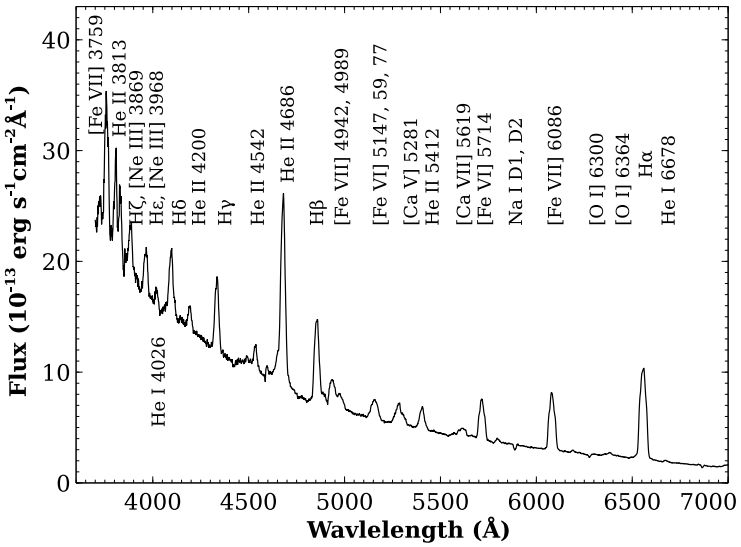

Fig. 6.8 A spectrum of V1405 Cas on 2023 November 23.763 UT.

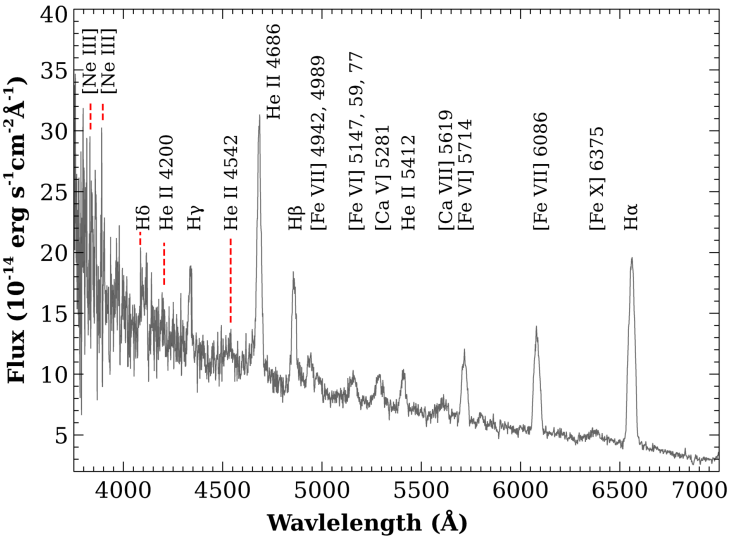

Fig. 6.9 A spectrum of V1405 Cas on 2024 February 2.559 UT.

Figures 6.4 to 6.9 illustrate the spectra observed from HCT. All the prominent lines are labeled accordingly. In Table 6.3, we provide corresponding tables for each spectrum, which contain information such as flux ($\mathrm{erg\,s^{-1}cm^{-2}\AA^{-1}}$), FWHM ($\mathrm{km\,s^{-1}}$), and EQW (Å) of the most prominent emission lines, including H α, H β, H γ, H δ, He II 5412 Å, He II 4686 Å, [Ca V] 5288 Å, [Fe VI] 5160 Å, [Fe VII] 5721 Å, and [Fe VII] 6086 Å.

Figure 6.4 shows the spectrum from 2022 Aug 23.658 UT (+523.23 d). This spectrum demonstrates significant evolution of emission lines in many aspects. For instance, the strength of various low ionization permitted lines has diminished significantly, whereas higher ionization permitted and forbidden lines have become stronger. Specifically, the He I 5876 line has significantly diminished in this spectrum compared to the spectra in Figures 6.2 and 6.3. In contrast, the higher ionized He II line has shown rapid growth in intensity, becoming the strongest emission line among the non-Balmer lines and the second strongest emission line in the entire optical wavelength range (see Table 6.3). This event has been reported by various researchers (Habtie and Das, 2024a; Woodward et al., 2022a). Similarly, all other He I lines, such as 7065, 6678, 5016, 4922, 4713, 4471, and 4388, have either significantly weakened or completely disappeared from the spectrum. Whereas, He II lines like 4542, 4200, and 5412 Å emerged in the spectrum. On the other hand, most of the Fe II lines have disappeared, and replaced

by various coronal lines such as [Fe VI] 5147, 5179, 5277 Å, [Fe VII] 4942, 5721, 6086 Å, [Va V], and [O I], which evolved to higher ionization forbidden lines.

Figure 6.5 shows the spectrum from December 3, 2022, at 3.66 UT (+625.24 d). In this spectrum, the most detectable change is the drastic increase of [Fe VII] 3759 Å. The He II line is still the strongest line without subtracting the continuum (see Fig. 6.5). In contrast, most of the lower ionization lines, such as He I 5876, have almost completely vanished compared to the previous epochs. Similarly, in the remaining three epochs represented in Figures 6.6, 6.7, 6.8, and 6.9, most of the recombination low ionization lines disappeared, and higher ionization nebular and coronal lines became stronger, indicating that the nova is in the coronal phase.

6.3.2.1 Line Profiles

Fig. 6.3.2.1 comprises the line profiles of prominent emission lines such as; H α, H β, H γ, He II 4686 Å, [Fe VII] 5721 Å, and [Fe VII] 6086 Å of eight different epochs. For each line profiles heliocentric correction has been applied for the purpose of accounting the Earth's motion relative to the Sun. Two positions of heliocentric radial velocity in each profile are indicated by vertical dashed lines.

In the Table 6.3, we presented the values of de-reddened flux ($\mathrm{erg\,s^{-1}\,cm^{-2}\,\AA^{-1}}$), FWHM ($\mathrm{km\,s^{-1}}$), and equivalent width (EQW) (Å) of the most prominent emission lines. For the spectra observed from HCT (From day 523 - 1052 in Table 6.3), the FWHM values have been corrected for broadening. However, for the spectra obtained from publicly available archives (days 1.92 and 240 in Tables 6.3), broadening correction has not been applied due to insufficient information. These measurements are essential for analyzing the properties of astronomical objects, allowing for a detailed investigation of their physical characteristics and underlying processes.

The FWHM broadening-correction of has been done using the the relation (Sagar et al., 2000);

$$FWHM_{corrected} = \frac{FWHM_{observed}}{A^{3/5}}, \tag{6.1}$$

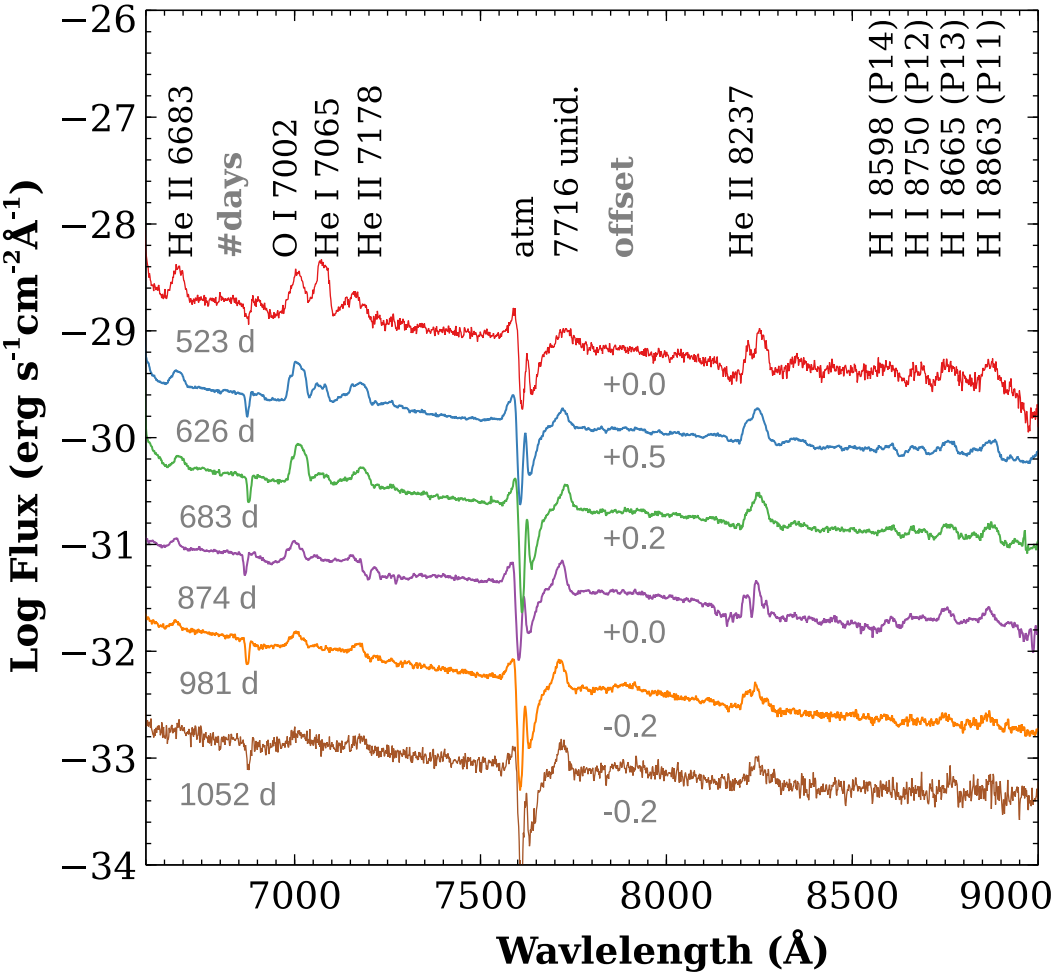

Fig. 6.10 Spectra of V1405 Cas were observed using Gr-8 from 5200 to 9000 Å. However, in this figure, we present spectra from 6600 to 9000 Å to reduce repetition of emission lines. Dates after the outburst are displayed in grey on the left side, representing: 2022 Aug 23.670 UT, 2022 Dec 3.675 UT, 2023 Jan 30.603 UT, 2023 Aug 9.891 UT, 2023 Nov 23.779 UT, and 2024 Feb 2.602 UT, in respective order from top to bottom. Each emission line is offset and indicated by grey color on the right side.

where A is the air-mass value. This correction is essential because it standardizes the observed data by removing the effects of instrumental broadening on the spectral lines. As a result, it allows for accurate comparisons with observations obtained at different times and from various directions.

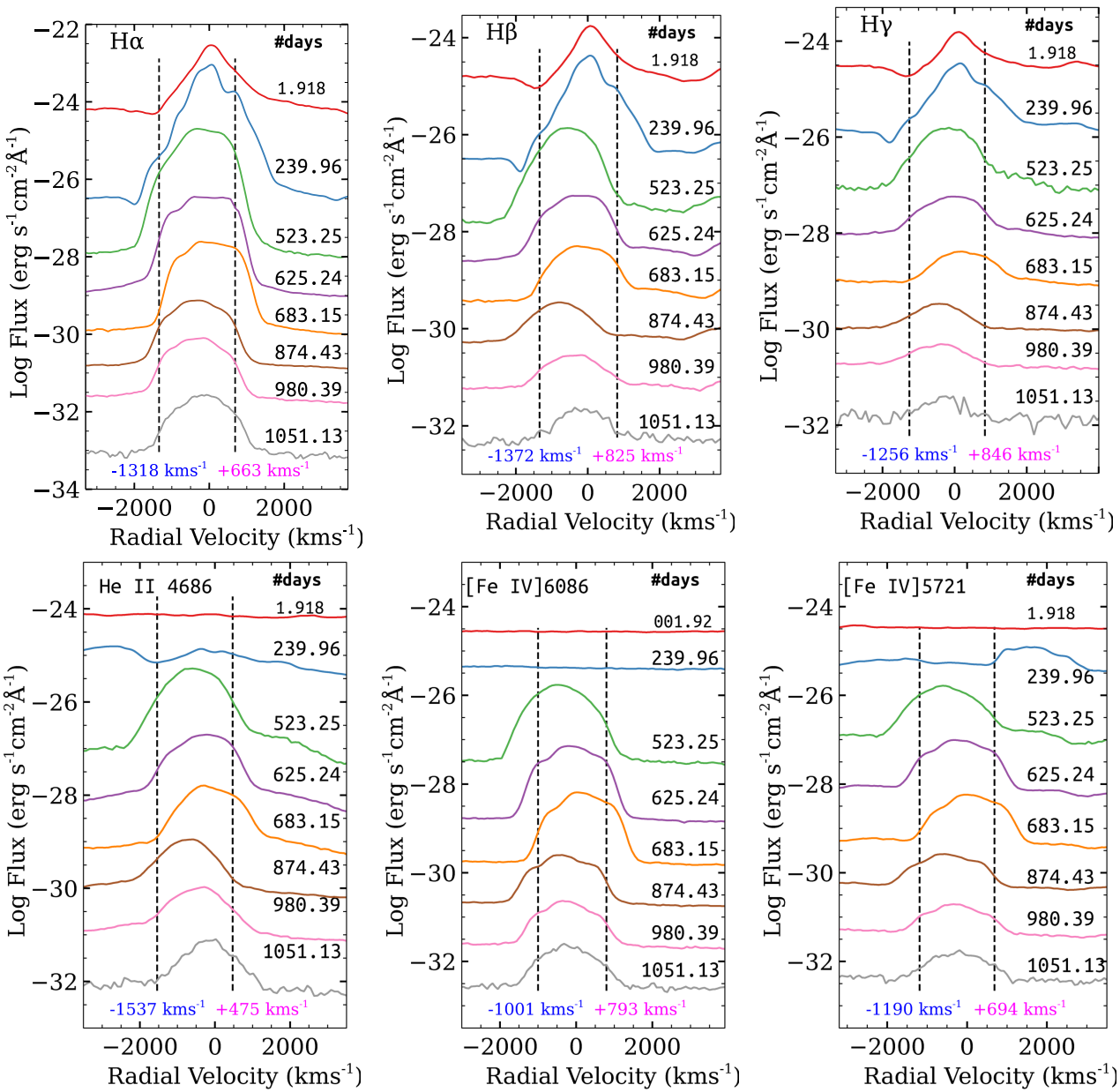

Fig. 6.11 The line profiles of H α, H β, H γ, He II 4686 Å, [Fe VII] 5721 Å, and [Fe VII] 6086 Å are shown. Two positions of heliocentric radial velocity in each profile are indicated by vertical dashed lines.

6.3.3 Photo-ionization Model

This research employs the photo-ionization code CLOUDY[5] (V17.02; Ferland et al. (2017)) to model the emission line spectra of the nova V1405 Cas. This code simulates the physical conditions of non-equilibrium gas clouds under external radiation fields, forecasting the emission line spectrum according to assumptions about the gas's physical state (ionization, density, temperature, and chemical composition). Detailed explanations about this code have been provided in our previous publications (Habtie and Das, 2024b; Habtie et al., 2024b; Pandey et al., 2022b), which we suggest referring to for further information. Similarly, Schwarz (2002); Schwarz et al. (2007); Shore et al. (2003); Vanlandingham et al. (2005); Woodward et al. (2024), and others have also utilized this code to model their spectra and extract information about various types of novae.

We made the assumption that the surface of the central white dwarf emits ionizing blackbody radiation with a temperature T_{BB} (in Kelvin) and a bolometric luminosity L_{bol} (in ergs per second), which irradiates a spherical gas geometry expanding at a velocity of v_{exp} (in kilometers per second). The cylindrical model in CLOUDY is essentially a truncated spherical model. The dimensions of this gas are determined by an inner radius r_{in} (in centimeters) and an outer radius r_{out} (in centimeters). For synthetic model spectra, we incorporate these input parameters along with the abundances of elements observed in emission lines, while other elements are maintained at their solar values as described by Grevesse et al. (2010).

The density of the ejecta is set by the total hydrogen number density, n(H) [cm^{-3}] given by,

$$\mathrm{n_H} = \mathrm{n_{H^0}} + \mathrm{n_{H^+}} + 2\mathrm{n_{H_2}} + \sum_{\mathrm{other}} \mathrm{n_{H_{other}}} \mathrm{cm}^{-3}, \tag{6.2}$$

where, $\mathrm{n_{H^0}}$, $\mathrm{n_{H^+}}$, $2\mathrm{n_{H_2}}$, and $\mathrm{n_{H_{other}}}$ respectively represent hydrogen in its neutral, ionized, molecular, and all other hydrogen-bearing molecular forms. The elemental abundances of the ejecta, relative to hydrogen, are determined by the abundance parameter.

[5] https://trac.nublado.org/

Table 6.3 De-reddened flux, FWHM (un corrected for broadening) and Equivalent width of most prominent emission lines in the spectrum of Day 1.918 (2021 March 20.342 UT)

lines	Flux ($erg\,s^{-1}$ $cm^{-2}Å^{-1}$)	FWHM ($km\,s^{-1}$)	EQW (Å)	Flux ($erg\,s^{-1}$ $cm^{-2}Å^{-1}$)	FWHM ($km\,s^{-1}$)	EQW (Å)
	Day 1.92			Day 239.97		
H α	1.30E-09	1280.359	141.1	4.23E-09	1313.271	933.90
H β	5.88E-10	1133.100	38.06	1.39E-9	1445.999	175.30
H γ	3.79E-10	1081.797	17.94	7.94E-10	1607.834	70.03
H δ	3.12E-10	1289.371	13.21	6.01E-10	1569.478	41.90
He I 5876	2.30E-10	753.063	20.16	2.49E-10	1173.2471	40.67
He I 7065	1.35E-10	808.068	15.15	1.48E-10	1477.707	41.82
He I 4471	1.61E-10	1027.287	8.43	1.28E-10	1411.765	11.25
He I 6678	1.32E-10	830.189	13.51	9.52E-11	1100.179	18.05
He I 5016	1.09E-11	931.818	7.23	-	-	-
	Day 523			Day 626		
H α	2.04E-10	1247.859	600.50	5.07E-11	1621.454	550.9
H β	5.89E-11	1334.838	108.00	2.30E-11	1706.088	98.58
H γ	2.68E-11	1419.576	41.47	1.38E-11	1853.741	44.68
H δ	1.60E-11	1431.688	22.32	9.13E-12	1850.432	23.36
He I 5876	6.82E-12	29.320	26.51	1.14E-12	32.000	7.626
He II 5412	1.11E-11	1494.909	23.47	3.98E-12	2148.660	23.15
He II 4686	7.63E-11	1510.155	134.2	4.18E-11	1940.000	176.2
[Ca] V 5288	9.49E-12	3533.486	52.92	5.20E-12	3917.419	47.77
[Fe] VI 5160	1.24E-11	2147.911	62.46	5.38E-12	2516.333	45.44
[Fe] VII 5721	2.80E-11	1504.658	63.91	1.15E-11	1629.802	69.32
[Fe] VII 6086	4.37E-11	1344.537	111.00	2.09E-11	1609.044	182.50
	Day 683			Day 874		
H α	2.49E-11	1280.177	452.9	7.38E-12	1366.890	204.8
H β	1.05E-11	1328.555	74.72	3.32E-12	1410.938	39.17
H γ	6.70E-12	1439.414	35.63	2.12E-12	1360.465	19.28
H δ	4.56E-12	1448.191	18.59	1.72E-12	1510.741	13.33
He I 5876	2.02E-13	24.910	2.289	-	-	-
He II 5412	2.58E-12	1806.458	25.58	1.09E-12	1395.711	17.95
He II 4686	1.94E-11	1400.000	131.40	6.94E-12	1490.000	77.34
[Ca] V 5288	1.43E-12	2213.588	22.11	8.59E-12	3488.757	46.58
[Fe] VI 5160	2.16E-12	2581.929	31.84	1.23E-11	2240.877	61.90
[Fe] VII 5721	2.58E-12	1806.458	25.58	2.55E-12	1513.918	49.20
[Fe] VII 6086	1.17E-11	1244.751	168.70	3.98E-12	1432.417	89.6

Table 6.3 Continued: de-reddened flux, FWHM (un corrected for broadening) and Equivalent width of most prominent emission lines in the spectrum of Day 1.918 (2021 March 20.342 UT)

lines	Flux ($erg\,s^{-1}$ $cm^{-2}Å^{-1}$)	FWHM ($km\,s^{-1}$)	EQW (Å)	Flux ($erg\,s^{-1}$ $cm^{-2}Å^{-1}$)	FWHM ($km\,s^{-1}$)	EQW (Å)
	Day 981.00			Day 1052.30		
H α	3.261E-12	1264.105	152.5	9.53E-13	1153.558	130.7
H β	2.270E-12	1333.457	31.08	2.51E-13	1276.453	19.18
H γ	1.96E-12	1395.666	17.29	2.29E-13	1524.202	14.67
H δ	1.83E-12	1644.904	12.45	3.81E-13	1677.473	22.01
He I 5876	-	-	-	-	-	-
He II 5412	4.63E-12	1974.692	27.91	1.73E-13	1201.972	17.55
He II 4686	5.34E-12	1460.000	64.33	5.68E-13	1350.000	41.5
[Ca] V 5288	9.33E-13	2183.969	18.02	1.46E-11	2411.547	29.54
[Fe] VI 5160	8.86E-13	1974.202	15.80	2.05E-11	2031.082	39.43
[Fe] VII 5721	1.30E-11	1429.574	91.35	2.51E-13	1233.489	27.92
[Fe] VII 6086	1.89E-12	1275.944	65.88	4.29E-13	1197.657	52.73

Additionally, we employ a radius-dependent density distribution governed by a power-law function. The level of clumpiness, indicating the gas proportion within the total volume, is determined by the filling factor parameter also denoted as f(r). CLOUDY employs the following two distribution functions to express the variations in density and filling factor within the ejecta: $n(r) = n(r_{in})x^{\alpha}$ for density and $f(r) = f(r_{in})x^{\beta}$ for the filling factor. where α and β represent the power-law indices and x represents the ratio of r_{in} to r_{out} of the shell. For this study we used; $\alpha = -2$ and $\beta = 0$. The value of $\alpha = -2$ was chosen to maintain a constant mass per unit volume throughout the model shell ($\dot{M}$ = const.) and a linear velocity law ($v \propto r$). On the other hand, we chose $\beta = 0$ because the filling factor of novae ejecta typically reaches a maximum of 0.1 during the outburst phase and gradually decreases as the ejecta disperses over extended distances from the source (Ederoclite et al., 2006; Shore, 2008).

The inner and outer shell radii are determined using the minimum and maximum expansion velocities obtained from the FWHM of all emission lines and the time between the outburst and discovery. But usually equating the expansion velocity with FWHM overestimates the expansion velocity, therefore we used relation (Santamaría

et al., 2024);

$$V_{exp} = \frac{FWHM}{2\sqrt{\ln 2}}. \tag{6.3}$$

Apply (Santamaría et al., 2024) equation to our broadening-corrected FWHM enables us to estimate the minimum and maximum expansion velocities, which in turn allows us to determine the inner and outer radii of the shell ejecta. The obtained minimum and maximum velocities are 791 $\mathrm{km\,s^{-1}}$and 1218 $\mathrm{km\,s^{-1}}$, respectively. Based on these values, the inner and outer radii for each epoch were estimated to be in the range of 1.63 $\times 10^{15}$cm to 7.08 $\times 10^{15}$cm , and 2.52 $\times 10^{15}$cm to 11.07 $\times 10^{15}$cm , respectively (see the values in Table 4.2). This estimate aligns well with the findings of Rudy et al. (2023), who reported an approximate value of 5.2 $\times 10^{15}$ cm based on the expansion velocity derived from Very Large Array (VLA) measurements and the GAIA distance.

The set of synthetic spectra is generated by simultaneously varying all the aforementioned input parameters in smaller increments across a wide range of values. Temperature is varied between $10^{4.5}$ and 10^{6} K, luminosity between 10^{36} and 10^{41} $\mathrm{erg\,s^{-1}}$, and ejecta density between $10^{6.5}$ and $10^{13}, \mathrm{cm^{-3}}$, along with elemental abundances. Multiple test models are iterated across all epochs numerous times before arriving at the final model. Initially, the models are visually assessed, and those not aligning with the observed spectrum are discarded. Ultimately, to assess the fitting quality, we compute the χ^2 and χ^2_{red} values of the model using the equations in eq. 4.7. Typically, σ falls within the range of 10 to 30 percent, depending on its strength relative to the continuum and its potential for blending with other spectral lines (Helton et al., 2010). Interactive flux measurements are conducted by fitting Gaussians using the *splot* task within the *onedspec* package in IRAF. An ideal model should yield a $\chi^2 \approx \nu$ (Schwarz et al., 2001). Thus, a desirable χ^2_{red} value should be low, typically ranging from 1 to 2, indicating a satisfactory and well-fitted model. The values of the best-fitting model parameters along with their corresponding uncertainties are presented in Table 4.2. These uncertainties are determined by individually varying each parameter while keeping others fixed at their best-fitting values until χ^2_{red} reaches 2, thereby establishing

parameter uncertainties. This approach results in a free parameter uncertainty of about 3σ (Schwarz et al., 2001).

In this study, we modeled a total of five spectra (epochs 1, 2, 3, 4, and 5). These spectra were recorded on days 239, 626, 683, 980, and 1051 after the outburst, respectively. Except for the spectrum observed on day 239, which covers the range from 3800 to 7550 Å, all other modeled spectra span from approximately 3700 to 9000 Å. The selection of spectra was based on availability. The observations were made in two frames: grism 7 (3700 - 7000 Å) and grism 8 (5200 - 9000 Å). After applying standard data reduction procedures of IRAF, we combined the frames of each corresponding epoch using the IRAF task *scombine*. We chose to start modeling after 239 days post-outburst because the nova is very slow and exhibited several re-brightening events. Consequently, photoionization may not have been the dominant process in the early days.

In this study, we found that a one-component model of CLOUDY is sufficient to meet our needs. Although we ran several two-component models for verification, we did not encounter any critical situations that convinced us to prefer the two-component model over the one-component model. The one-component model allowed us to generate almost all lines within a reasonably acceptable fitting range, and the two-component model did not provide any new emission lines. Therefore, we decided to stick with the one-component model and proceed with further analysis. This might indicate that the ejecta in this nova has less heterogeneity or variation compared to some other fast novae like V1674 Her. This could be attributed to the slowness of nova V1405 Cas in evolving, resulting in slower variations in density and other parameters. However, the covering factor varied slightly in each epoch and was consistently less than one in all cases (see Table 4.2).

Fig. 6.12 illustrates the best-fitting CLOUDY model profiles (shown in red) superimposed on the observed optical spectra (shown in black) for five distinct epochs. Table 6.4 presents a comparison of relative fluxes between the best-fitting model-predicted lines and the observed lines during the early phase, along with corresponding χ^2 values.

For computing χ^2 values, emission lines appearing in both observational and modelled spectra are selected. The observed and modelled line fluxes are determined using IRAF, and profiles with multiple components are decomposed using multiple Gaussian functions. To mitigate inaccuracies related to flux calibration across different epochs, flux ratios of observed and modelled emission lines relative to H β are calculated.

6.3.3.1 Temperature and Luminosity

The parameter values derived from the best-fitting CLOUDY models are presented in Table 4.2. These optimal models indicate that the effective temperature of the source increased from 3.24×10^4 K in epoch 1 to 1.55×10^5 K in epoch 5. Similarly, the luminosity of the system rose from 6.31×10^{37} erg s^{-1} during epoch 1 to 3.981×10^{38} erg s^{-1} by epoch 5. These temperature and luminosity values from the best-fitting CLOUDY model are consistent with previously estimated values of T $= 1.6 \times 10^5$ K and L $= 9.48 \times 10^{37}$ erg s^{-1} for day 863 (Rudy et al., 2023). Both the effective temperature and luminosity of the central ionizing source were lower in the initial days and increased in subsequent epochs. This rise in the central ionizing source's temperature is attributed to the compression of remaining matter within the pseudo-photosphere as the ejecta expands during its collapse. This compression leads to elevated gas temperatures, resulting in higher rates of radiation emission (Bath and Shaviv, 1976). The increased radiation output then triggers the expansion and cooling of the outer layers of the white dwarf.

6.3.3.2 Ejecta Density

Throughout epochs 1 to 5, the hydrogen density varies from 5.00×10^7 to 2.63×10^7 cm^{-3}. During the expansion phases of a nova outburst, the density of the ejected material significantly decreases over time. This happens because the ejecta expands rapidly after an outburst, with some material being absorbed by interstellar clouds or the surrounding gas from the companion star. This absorption releases additional energy from the nova mechanism, gradually shifting the atmosphere to an optically

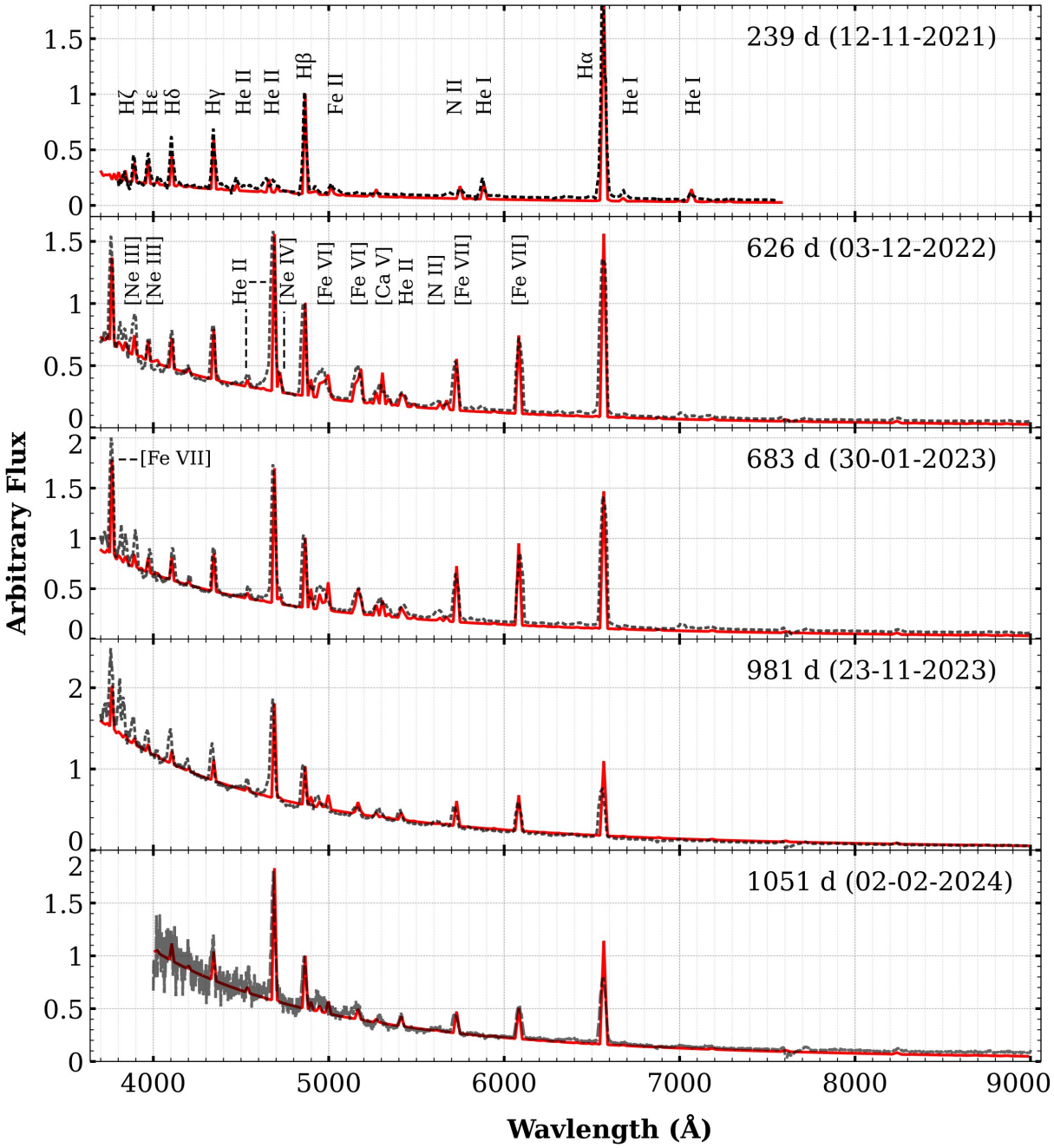

Fig. 6.12 Best-fitting CLOUDY synthetic spectrum (red solid line) plotted over the observed spectrum (dashed black line) of V1405 Cas obtained on days 239, 626, 683, 981, and 1051, from top to bottom, respectively. Both the observed and modeled spectra are normalized to H β, and the observed are spectra corrected for reddening using E(B-V) = 0.53.

thin state and reducing the density. The decreasing density exposes the ionizing radiation emitted by the central white dwarf (WD) to the expanding ejecta, leading to an increased ionization potential. This, in turn, allows the emergence of emission lines with higher ionization potentials. The density evolution in novae, along with the subsequent ionization processes, is generally due to the interaction between expanding ejecta, matter absorption, and ionizing radiation from the central WD.

6.3.3.3 Elemental Composition

The spectral modeling showed that in addition to a significant amount of H content, the ejecta is also composed of various elements such as H , He , Ne , and Ca . The model results indicated that only He appeared overabundant relative to the solar value, while all other elements were either at or below solar levels across all epochs. The He abundance in the ejecta showed a significant increase over time. For instance, on epoch 1 (day 1.92), the He /He $\odot$ ratio was 1.6, but by epoch 7 (day 1052), it had increased to 3.0, doubling from the first epoch. We found that the Fe abundance fluctuated slightly across the epochs, with a minimum Fe /Fe $_\odot$ ratio of 0.27 in epoch 4 and a maximum of 0.36 in epoch 3. The Ca abundance showed a significant decline from an initial value close to the solar value to 0.2. The Ne and N abundance remained similar to the solar value Ne $\odot$, and N $\odot$, respectively, in all seven epochs. In the model, we also set O to the solar values, even though clear and resolved lines of it were not found in the spectra.

Helium abundance across all epochs was determined by fitting the prominent He I (5876, 6678, 7065 Å) and He II (4542, 4686, 5412 Å) lines. Neon abundance was derived from [Ne III] (3869, 3968 Å) lines. Iron abundance was determined by fitting [Fe VII] 4942 Å, [Fe VII] 6087 Å, [Fe VI] 5714 Å, [Fe VI] 5159 Ålines, and [Fe II] 7155 Ålines. The calcium abundance was determined by fitting [Ca V] 5281 Åand [Ca VII] 5619 Ålines. Nitrogen abundance was estimated by fitting the [N III] 4640 Åand [N II] 5746 Ålines.

Table 6.4 Observed and best-fitting CLOUDY model line fluxes.

		Epoch 1 (239 d)			Epoch 2 (626 d)			Epoch 3 (684 d)		
Line ID	λ (Å)	Observed	modelled	χ^2	Observed	modelled	χ^2	Observed	modelled	χ^2
H ζ,[Ne III]	3889	0.257	0.156	0.451	0.740	0.682	0.117	0.367	0.279	0.191
H ϵ,[Ne III]	3970	0.340	0.200	0.876	0.283	0.1877	0.318	0.288	0.221	0.111
H δ	4101	0.440	0.274	1.228	0.424	0.292	0.605	0.378	0.298	0.159
He II	4200	-	-	-	0.249	0.119	0.578	0.085	0.099	0.005
H γ	4340	0.570	0.486	0.318	0.617	0.485	0.599	0.531	0.534	0.001
He I	4471	0.130	0.136	0.001	-	-	-	-	-	-
He II	4542	-	-	-	0.188	0.107	0.223	0.074	0.103	0.021
N III	4640	-	-	-	0.509	0.354	0.831	-	-	-
He II	4686	0.285	0.123	1.179	1.414	1.483	0.162	1.601	1.759	0.622
He I	4713	-	-	-	0.081	0.222	0.688	0.133	0.386	1.600
H β	4861	1.000	1.000	0.000	1.000	1.000	0.000	1.000	1.000	0.000
He I	4922	0.122	0.213	0.366	-	-	-	-	-	-
[Fe VII]	4942,89	-	-	-	0.694	0.998	3.197	0.674	1.181	6.419
He I	5016	0.199	0.116	0.309	-	-	-	-	-	-
[Fe VI]	5159	-	-	-	0.538	0.968	6.398	0.442	1.165	13.096
[Ca V]	5281	-	-	-	0.413	0.384	0.030	0.420	0.374	0.053
He II	5412	0.038	0.020	0.014	0.185	0.316	0.595	0.190	0.360	0.724
[Ca VII]	5619	-	-	-	0.099	0.104	0.001	.149	0.129	0.009
[Fe VI]	5714	-	-	-	0.561	0.547	0.006	0.408	0.508	0.250
[N II]	5746	0.123	0.020	0.469	-	-	-	0.379	0.433	0.073
He I	5876	0.192	0.210	0.014	-	-	-	-	-	-
[Fe VII]	6086	-	-	-	0.914	0.896	0.010	1.099	1.168	0.116
H α	6562	2.972	2.562	7.424	2.200	2.416	1.618	2.357	2.443	0.188
He I	6678	0.111	0.064	0.097	0.066	0.066	0.000	0.062	0.025	0.034
He I	7065	0.158	0.196	0.063	-	-	-	-	-	-
[Fe II]	7155	-	-	-	0.068	0.056	0.004	0.035	0.040	0.001
He II	8237	-	-	-	0.045	0.039	0.001	0.079	0.046	0.027

Table 6.4 Continued: Observed and best-fitting CLOUDY model line fluxes.

		Epoch 4 (981 d)			Epoch 5 (1051 d)		
Line ID	λ (Å)	Observed	modelled	χ^2	Observed	modelled	χ^2
H ζ,[Ne III]	3889	0.473	0.232	1.609	-	-	-
H ϵ,[Ne III]	3970	0.391	0.209	0.910	-	-	-
H δ	4101	0.759	0.332	5.020	0.122	0.091	0.634
He II	4200	0.284	0.124	0.704	0.095	0.091	0.001
H γ	4340	0.723	0.474	1.716	0.397	0.445	0.083
He I	4471	-	-	-	-	-	-
He II	4542	0.142	0.141	0.000	0.117	0.129	0.005
N III	4640	-	-	-	-	-	-
He II	4686	2.221	2.444	1.377	2.219	1.928	2.933
He I	4713	-	-	-	-	-	-
H β	4861	1.000	1.000	0.000	1.000	1.000	0.000
He I	4922	-	-	-	-	-	-
[Fe VII]	4942,89	0.916	1.004	0.215	0.914	0.536	4.928
He I	5016	-	-	-	-	-	-
[Fe VI]	5159	0.429	0.703	2.079	0.619	0.385	1.894
[Ca V]	5281	0.415	0.161	1.784	0.415	0.142	2.571
He II	5412	0.304	0.310	0.001	0.279	0.199	0.222
[Ca VII]	5619	0.136	0.082	0.082	0.195	0.050	0.724
[Fe VI]	5714	0.345	0.413	0.128	0.419	0.354	0.148
[N II]	5746	0.152	0.294	0.551	0.178	0.316	0.668
He I	5876	-	-	-	-	-	-
[Fe VII]	6086	0.846	0.727	0.388	0.835	0.819	0.009
H α	6562	1.502	1.956	5.733	1.785	2.102	3.470
He I	6678	0.039	0.029	0.003	0.076	0.031	0.069
He I	7065	-	-	-	-	-	-
[Fe II]	7155	0.0547	0.037	0.009	0.098	0.089	0.002
He II	8237	0.073	0.053	0.011	0.096	0.079	0.011

Table 6.5 Best fit CLOUDY model parameters during outburst phase (2021) Nova Cas 2021.

Parameters	Values				
	Epoch 1	Epoch 2	Epoch 3	Epoch 4	Epoch5
Blackbody Temperature ($\times 10^5$K)	0.324	1.148	1.259	1.259	1.549
Luminosity ($\times 10^{38}$ erg s^{-1})	0.631	1.122	1.259	2.512	3.981
Hydrogen density ($\times 10^6$cm^{-3})	50.12	8.913	6.309	0.302	0.263
α	-2.00	-2.00	-2.00	-2.00	-2.00
Inner radius ($\times 10^{15}$cm)^a	1.633	4.276	4.667	6.699	7.079
Outer radius ($\times 10^{16}$cm)^a	0.252	0.646	0.719	1.033	1.107
Filling Factor^a	0.10	0.10	0.10	0.10	0.10
β ^{a}	0.00	0.00	0.00	0.00	0.00
Covering factor	0.85	0.87	0.85	0.90	0.9
He/He$_\odot$	1.60	2.10	2.40	3.00	3.00
N/N$_\odot$	1.00	1.00	1.00	1.00	1.00
Fe/Fe$_\odot$	0.30	0.29	0.36	0.27	0.33
Ne/Ne$_\odot$	1.00	1.00	1.00	1.00	1.00
Ca/Ca$_\odot$	0.80	1.00	1.00	0.30	0.20
Ejected matter mass ($\times 10^{-5}$ $M_\odot$)	16.85	7.949	4.095	8.127	8.162
Number of lines	15	21	21	20	18
Number of free parameters	8	8	8	8	8
Degrees of freedom	7	13	13	12	10
$\chi^2_{\rm tot}$	12.81	20.53	23.70	22.32	18.37
$\chi^2_{\rm red}$	1.829	1.579	1.823	1.860	1.837

Note: ^{a} stands for the quantity is not considered as a free parameter.

6.3.3.4 Ejected mass Calculation

The ejecta mass in the expanding shell (M_{eje}) in a spherical volume with inner and outer radii (R_{in} and R_{out}) can be calculated in units of $M_{\odot}$ from the parameters presented in Table 4.2 using the expression:

$$M_{eje} = 4\pi \times C \times n_H \times \mathrm{cf} \times \mathrm{ff} \times R_{in}^2 \times (R_{out} - R_{in}), \tag{6.4}$$

where C is a constant representing the mass of a single hydrogen atom, equal to 1.67×10^{-24} g; 'cf' is the covering factor; n_H is the hydrogen number density; and 'ff' is the filling factor. The ejecta mass in the expanding shell at five distinct epochs; epoch 1, epoch 2, epoch 3, epoch 4, and epoch 5 are found to be; $1.063 \times 10^{-4} M_{\odot}$, $3.266 \times 10^{-4} M_{\odot}$, $3.108 \times 10^{-4} M_{\odot}$, $4.672 \times 10^{-5} M_{\odot}$, and $4.993 \times 10^{-5} M_{\odot}$, respectively.

6.4 Summary

We have investigated the spectroscopic and photometric evolution of V1674 Her, the fastest-recorded nova. We employed the ionization code CLOUDY to model the observed spectra and estimate the physical and chemical parameters of the nova system. The main findings from our analysis are summarised below:

1. We estimated the distance of this object from the earth to be $\sim 2.091 \pm 0.004$ kpc.

2. Based on the AAVSO observed data we estimated the t_2 and t_3 in reference with the last rebrightening are 164.5 and 174.6 days, respectively.

3. The He II 4686 Å [Fe VII] 3759 Å appeared as the strongest non-Balmer emission lines after day 625.

4. Photo-ionization modelling of the observed spectra through CLOUDY provided estimates for the source's temperature and luminosity, as well as the ejecta's density and elemental composition (refer to results in Table 6.5).

5. Our model, showed that He was overabundant during all time across the time span of our model covers, but all others like; Ne , O , N , and Fe , and Ca apperaed either at solar or subsolar values.

6. The ejecta mass in the expanding shell at five distinct epochs; epoch 1, epoch 2, epoch 3, epoch 4, and epoch 5 are found to be; $1.063 \times 10^{-4} M_{\odot}$, $3.266 \times 10^{-4} M_{\odot}$, $3.108 \times 10^{-4} M_{\odot}$, $4.672 \times 10^{-5} M_{\odot}$, and $4.993 \times 10^{-5} M_{\odot}$, respectively.

7 Summary and Scope of the Future Work

7.1 Summary

Novae serve as astrophysical laboratories by offering a unique environment to study a variety of fundamental processes. These include accretion, ejection, dust formation, and the interaction between outflowing ejecta and the interstellar medium in the form of shock waves. By analyzing the emitted spectra, astronomers can investigate the chemical composition, physical conditions, and velocity structures of the ejected material, gaining insights into these dynamic processes. In this thesis, observational data of various types of novae during different stages of outburst as well as during their stable state (known as the quiescent phase) have been analyzed and discussed. Spectroscopy has been the primary tool for studying the complex nature of novae for many decades because it provides a more detailed and nuanced understanding of an object's physical properties, chemical composition, and dynamic processes.

7.1.1 V1674 Her, 2021

- Nova Her 2021 (V1476 Her) was one of the most dramatic and unique events in the history of classical novae. It was the fastest classical nova ever recorded, with a decline time of $t_2 < 1$ day. This nova exhibited a rare hybrid nature, transitioning between two different classes of novae (Fe II and He/Ne type) over time. During the first 10 days, the spectra of Nova V1674 Her displayed characteristics typical

of Fe II novae. However, it then began showing higher ionized neon lines, a trait of He/Ne novae. Its extreme speed was further highlighted by the rapid succession of expansion phases, progressing from the pre-maximum stage to the coronal stage in just ∼30 days—a process that usually takes several months or even years for other novae.

- Additionally, V1674 Her was the first nova to reach the nebular phase within just 10 days after the outburst and the coronal phase in only 22 days in the optical region. It exhibited typical characteristics of neon novae, including a relatively heavy white dwarf of approximately 1.36 $M_{\odot}$, a position near the galactic center (galactic coordinates l = 048.707°, b = +06.3114°), and a light curve that showed a sharp decline in magnitude.

- Photo-ionization modeling of the observed spectra through CLOUDY provided estimates for the source's temperature and luminosity, as well as the ejecta's density and elemental composition (refer to results in Table 4.2). The model, spanning one month after the outburst, unveiled an overabundance of He , Ne , O , N , and Fe relative to solar abundances. After ∼17 d from the outburst, the Fe abundance normalized to its solar value, while the neon abundance increased by a factor of 2, favoring the transition that occurred.) Based on our CLOUDY model, the ejected mass of V1674 is predicted to be 3.42×10^{-5} $M_{\odot}$, 4.23×10^{-5} $M_{\odot}$, 4.35×10^{-5} $M_{\odot}$, 4.85×10^{-5} $M_{\odot}$, and 7.40×10^{-5} $M_{\odot}$ for epochs 1, 2, 3, 4, and 5, respectively. These values align with theoretical predictions and prior findings for this nova.

- The H α morphology of the nova ejecta during the initial month after the outburst exhibited asymmetry, featuring both bipolar and equatorial ring geometries. The presence of equatorial rings in the H α geometry suggests potential interactions of outflows with a secondary companion. We estimate the inclination angle of the ejecta geometry to be $\sim \ i = 67 \pm 1.5°$.

7.1.2 RS Ophiuchi, 2006-2021

- In this project, I studied the quiescent stage of RS Oph between the 2006 and 2021 outbursts. The study is based on spectra taken from various archival sources covering a time span of approximately 13 years, from February 22, 2008, to March 8, 2021, with intervals of about two years. This research provides a detailed analysis of the slowest spectral evolution and prominent emission line profiles. I conducted photo-ionization modeling of selected spectra, extracting information about the gradual disk formation processes, including radial increment, accretion rate variation, chemical composition of the disk, density variation in the disk, and finally, the luminosity and temperature of the system.

- The study showed that the accretion process of RS Oph between the 2006 and 2021 outbursts was highly non-uniform. Only 12% of the total mass was accreted during the first 10 years (up to July 20, 2018), while the remaining 88% was accreted in the last four years (up to August 2021). This indicates that the accretion rate was significantly faster as the nova approached the next outburst compared to the earlier stages. This acceleration in the accretion rate might be due to the enhanced gravitational pull of the white dwarf, aided by the already accreted matter. Although the mean accretion rate was also estimated, it does not necessarily imply that the accretion rate was uniform throughout the period.

- From the best-fit model parameters, I estimated the electron density (n_e) and electron temperature (T_e) in the accretion disk at various depths from the illuminated face of the disk to the white dwarf. The results clearly showed that the maximum values of electron density and electron temperature are recorded at the illuminated face of the disk ($r = r_{in}$), where $r_{in} = R_{WD}$ (White dwarf radius). Both parameters generally decrease with increasing radius, following a power-law behavior. This radial dependence of electron density and electron temperature is influenced by factors such as the mass accretion rate and the viscosity of the disk.

7.1.3 V1405 Cas, 2021

- This work is primarily based on spectroscopic data observed from the HCT. We included two spectra from archival data to cover the initial 240 days, as we were unable to observe due to the pandemic and related issues. In total, we included eight spectra spanning from day 1.98 to day 1052.

- V1405 Cas is one of the slowest recorded novae. This nova exhibited multiple brightening, with the last brightening occurring 215 days after the discovery date. The first and most significant brightening happened on day 52. We calculated the t_2 and t_3 values for the last brightening and found $t_2 = 164.5$ days and $t_3 = 174.6$ days, categorizing it as a very slow nova according to the speed classification scheme of novae.

- After evaluating the light curve and corresponding color evolution, we analyzed the spectral evolution by identifying all prominent emission and absorption lines. In the spectra, we noticed that various lower ionization recombination lines, particularly on the blue side, dominated the spectra, such as Balmer and He I lines. Gradually, higher ionized lines started appearing while the lower ionization lines diminished.

- I modeled five selected spectra spanning from day 1.98 to day 1051. We excluded the first spectrum in our list because, during the free expansion period, the process might be influenced by shocks, and the photo-ionization code we employed does not effectively account for this. From the model, we obtained various physical and chemical parameters of the shell ejecta, including density, composition, radial distances covered by the shell, and mass of the ejecta.

7.2 Future Work

- Since I started observation proposal to HCT back in 2022, about 13 nights have been allotted for me and out of that about 8 days were successful and the rest

of them wasted due to unsuitable weather condition at the observation cite. In these 8 nights I have observed various objects; including, classical nova, recurrent nova, dwarf nova and symbiotic nova. The primary plan of mine in the future is to utilize this data and keep investigating.

- In the third chapter of this thesis I have presented a spectroscopic study on V1405 Cas with a time span of 1 month following the outburst. The nova evolved very fast in just one month it passed through various stages from pre-maxima to coronal phases. It worth to explore the later stages as the nova is extremely unique and might be helpful and may provide other useful information. no many studies conducted on the later stages.

- The investigation we performed for this thesis is mainly focused spectral modeling using the 1D photo-ionization code CLOUDY and 3D morphokinematic code SHAPE. Even though these to are very useful in estimating various characteristics of the system including it is very useful in studying an important physical processes

References

Hyuga Abe et al. Evidence of hadronic origin of the gamma-ray emission from the nova RS Oph by the MAGIC telescopes. *PoS*, ICRC2023:580, 2023. doi: 10.22323/1.444.0580.

V. A. Acciari et al. Proton acceleration in thermonuclear nova explosions revealed by gamma rays. *Nature Astronomy*, 6:689–697, April 2022. doi: 10.1038/s41550-022-01640-z.

E. G. Adelberger et al. Solar fusion cross sections. II. The pp chain and CNO cycles. *Reviews of Modern Physics*, 83(1):195–246, January 2011. doi: 10.1103/RevModPhys.83.195.

I. Albanese, A. Farina, V. Andreoli, P. Ochner, and A. Reguitti. Spectroscopic follow-up observations of Nova Herculis 2021. *The Astronomer's Telegram*, 14718:1, June 2021.

G. C. Anupama and J. Mikołajewska. Recurrent novae at quiescence: systems with giant secondaries. *Astronomy & Astrophysics*, 344:177–187, April 1999. doi: 10.48550/arXiv.astro-ph/9812432.

G. C. Anupama and T. P. Prabhu. The 1985 outburst of RS Ophiuchi : spectroscopic results. *Journal of Astrophysics and Astronomy*, 10:237–255, September 1989. doi: 10.1007/BF02714998.

E. Aydi, K. V. Sokolovsky, L. Chomiuk, J. Strader, A. Kawash, K. L. Page, C. Boussin, N. Ikonnikova, K. E. Atapin, A. A. Belinski, M. A. Burlak, A. V. Dodin, N. A. Maslennikova, K. A. Postnov, S. A. Potanin, B. S. Safonov, N. I. Shatsky, A. M. Tatarnikov, S. Korotkiy, K. Z. Stanek, C. S. Kochanek, and B. J. Shappee. Multi-wavelength follow up of the very fast Nova Herculis 2021 (TCP J18573095+1653396). *The Astronomer's Telegram*, 14710:1, June 2021.

E. Aydi, L. Chomiuk, J. Strader, K. V. Sokolovsky, R. E. Williams, D. A. H. Buckley, A. Ederoclite, L. Izzo, R. Kyer, J. D. Linford, A. Kniazev, B. D. Metzger, J. Mikołajewska, P. Molaro, I. Molina, K. Mukai, U. Munari, M. Orio, T. Panurach, B. J. Shappee, K. J. Shen, J. L. Sokoloski, R. Urquhart, and F. M. Walter. Revisiting the classics: on the evolutionary origin of the 'Fe II' and 'He/N' spectral classes of novae. *Monthly Notices of the Royal Astronomical Society*, 527(3):9303–9321, January 2024. doi: 10.1093/mnras/stad3342.

J. N. Bahcall and R. M. Soneira. The universe at faint magnitudes. I. Models for the Galaxy and the predicted star counts. *Astrophysical Journal, Supplement*, 44:73–110, September 1980. doi: 10.1086/190685.

John N. Bahcall and Robert M. May. The Rate of the Proton-Proton Reaction and Some Related Reactions. *The Astrophysical Journal*, 155:501, February 1969. doi: 10.1086/149886.

C. A. L. Bailer-Jones, J. Rybizki, M. Fouesneau, M. Demleitner, and R. Andrae. Estimating Distances from Parallaxes. V. Geometric and Photogeometric Distances to 1.47 Billion Stars in Gaia Early Data Release 3. *The Astronomical Journal*, 161 (3):147, March 2021. doi: 10.3847/1538-3881/abd806.

Rahul Bandyopadhyay, Ramkrishna Das, Soumen Mondal, and Samrat Ghosh. Morphology and ionization characteristics of planetary nebulae PB 1 and PC 19. *Monthly Notices of the Royal Astronomical Society*, 496(1):814–831, July 2020. doi: 10.1093/mnras/staa1518.

D. P. K. Banerjee, R. K. Das, and N. M. Ashok. Near-infrared H- and K-band studies of the 2006 outburst of the recurrent nova RSOphiuchi. *Monthly Notices of the Royal Astronomical Society*, 399(1):357–368, October 2009. doi: 10.1111/j.1365-2966.2009.15279.x.

G. T. Bath and G. Shaviv. Classical novae - a steady state, constant luminosity, continuous ejection model. *Monthly Notices of the Royal Astronomical Society*, 175: 305–322, May 1976. doi: 10.1093/mnras/175.2.305.

Robert A. Benjamin and Harriet L. Dinerstein. Near-Infrared Spectroscopy of Classical Novae in the Coronal Phase. *The Astronomical Journal*, 100:1588, November 1990. doi: 10.1086/115619.

Charles Bertaud. Répartition des étoiles temporaires galactiques. *Annales d'Astrophysique*, 14:199, January 1951.

M. F. Bode, T. J. O'Brien, J. P. Osborne, K. L. Page, F. Senziani, G. K. Skinner, S. Starrfield, J. U. Ness, J. J. Drake, G. Schwarz, A. P. Beardmore, M. J. Darnley, S. P. S. Eyres, A. Evans, N. Gehrels, M. R. Goad, P. Jean, J. Krautter, and G. Novara. Swift Observations of the 2006 Outburst of the Recurrent Nova RS Ophiuchi. I. Early X-Ray Emission from the Shocked Ejecta and Red Giant Wind. *The Astrophysical Journal*, 652(1):629–635, November 2006. doi: 10.1086/507980.

Michael F. Bode and Aneurin Evans. *Classical Novae*. Cambridge Astrophysics. Cambridge University Press, 2 edition, 2008. doi: 10.1017/CBO9780511536168.

R. A. Booth, S. Mohamed, and Ph. Podsiadlowski. Modelling the circumstellar medium in RS Ophiuchi and its link to Type Ia supernovae. *Monthly Notices of the Royal Astronomical Society*, 457(1):822–835, March 2016. doi: 10.1093/mnras/stw001.

E. Brandi, C. Quiroga, J. Mikołajewska, O. E. Ferrer, and L. G. García. Spectroscopic orbits and variations of RS Ophiuchi. *Astronomy & Astrophysics*, 497(3):815–825, April 2009. doi: 10.1051/0004-6361/200811417.

C. Buil. RS Ophiuchi. *Central Bureau Electronic Telegrams*, 403:1, February 2006.

Yi Cao, Mansi M. Kasliwal, James D. Neill, S. R. Kulkarni, Yu-Qing Lou, Sagi Ben-Ami, Joshua S. Bloom, S. Bradley Cenko, Nicholas M. Law, Peter E. Nugent, Eran O. Ofek, Dovi Poznanski, and Robert M. Quimby. Classical Novae in Andromeda: Light Curves from the Palomar Transient Factory and GALEX. *The Astrophysical Journal*, 752(2):133, June 2012. doi: 10.1088/0004-637X/752/2/133.

Bradley W. Carroll and Dale A. Ostlie. *An Introduction to Modern Astrophysics*. Cambridge University Press, 2 edition, 2017.

A. Cassatella, B. J. M. Hassall, A. Harris, and M. A. J. Snijders. Ultraviolet Observations of the Recurrent Nova Rs-Ophiuchi in Outburst. In W. R. Burke, editor, *Recent Results on Cataclysmic Variables. The Importance of IUE and Exosat Results on Cataclysmic Variables and Low-Mass X-Ray Binaries*, page 281, January 1985.

A. Cassatella, H. J. G. L. M. Lamers, C. Rossi, A. Altamore, and R. González-Riestra. A study of the expanding envelope of Nova V1974 Cyg 1992 based on IUE high resolution spectroscopy. *Astronomy & Astrophysics*, 420:571–588, June 2004. doi: 10.1051/0004-6361:20034102.

T. Chandrasekhar, N. M. Ashok, and Sam Ragland. Near infrared coronal line emission in nova Herculis 1991. *Bulletin of the Astronomical Society of India*, 21(3-4):623–625, September 1993.

M. Chatzikos, S. Bianchi, F. Camilloni, P. Chakraborty, C. M. Gunasekera, F. Guzmán, J. S. Milby, A. Sarkar, G. Shaw, P. A. M. van Hoof, and G. J. Ferland. The 2023 Release of Cloudy. *Revista Mexicana de Astronomía y Astrofísica*, 59:327–343, October 2023. doi: 10.22201/ia.01851101p.2023.59.02.12.

Robin Ciardullo, Peter Tamblyn, and A. C. Phillips. A search for novae in M 31 globular clusters. *Publications of the Astronomical Society of the Pacific*, 102:1113, October 1990. doi: 10.1086/132739.

Donald D. Clayton. *Principles of stellar evolution and nucleosynthesis*. 1983.

M. J. Darnley, M. F. Bode, E. Kerins, A. M. Newsam, J. An, P. Baillon, V. Belokurov, S. Calchi Novati, B. J. Carr, M. Crézé, N. W. Evans, Y. Giraud-Héraud, A. Gould, P. Hewett, Ph. Jetzer, J. Kaplan, S. Paulin-Henriksson, S. J. Smartt, Y. Tsapras, and M. Weston. Classical novae from the POINT-AGAPE microlensing survey of M31 - II. Rate and statistical characteristics of the nova population. *Monthly Notices of the Royal Astronomical Society*, 369(1):257–271, June 2006. doi: 10.1111/j.1365-2966.2006.10297.x.

M. J. Darnley, V. A. R. M. Ribeiro, M. F. Bode, R. A. Hounsell, and R. P. Williams. On the Progenitors of Galactic Novae. *The Astrophysical Journal*, 746(1):61, February 2012. doi: 10.1088/0004-637X/746/1/61.

R. K. Das, N. M. Ashok, and D. P. K. Banerjee. RS Ophiuchi. *Central Bureau Electronic Telegrams*, 730:1, November 2006a.

Ramkrishna Das and Anindita Mondal. Abundance analysis of the recurrent nova RS Ophiuchi (2006 outburst). *New Astronomy*, 39:19–24, August 2015. doi: 10.1016/j.newast.2015.02.004.

Ramkrishna Das, Dipankar P. K. Banerjee, and Nagarhalli M. Ashok. A Near-Infrared Shock Wave in the 2006 Outburst of Recurrent Nova RS Ophiuchi. *The Astrophysical Journal Letters*, 653(2):L141–L144, December 2006b. doi: 10.1086/510674.

Ramkrishna Das, Dipankar P. K. Banerjee, and Nagarhalli M. Ashok. RS Ophiuchi outburst 2006: detection of a near-infrared shock wave. In *Bulletin of the Astronomical Society of India Proceedings*, volume 25 of *Bulletin of the Astronomical Society of India Proceedings*, page 50, January 2008.

M. della Valle and M. Livio. On the nova rate in the Galaxy. *Astronomy & Astrophysics*, 286:786–788, June 1994.

M. della Valle, A. Bianchini, M. Livio, and M. Orio. On the possible existence of two classes of progenitors for classical novae. *Astronomy & Astrophysics*, 266:232–236, December 1992.

Massimo della Valle and Mario Livio. The Calibration of Novae as Distance Indicators. *The Astrophysical Journal*, 452:704, October 1995. doi: 10.1086/176342.

Rebecca Diesing, Brian D. Metzger, Elias Aydi, Laura Chomiuk, Indrek Vurm, Siddhartha Gupta, and Damiano Caprioli. Evidence for Multiple Shocks from the γ-Ray Emission of RS Ophiuchi. *The Astrophysical Journal*, 947(2):70, April 2023. doi: 10.3847/1538-4357/acc105.

Carolyn L. Doherty, Pilar Gil-Pons, Lionel Siess, John C. Lattanzio, and Herbert H. B. Lau. Super- and massive AGB stars - IV. Final fates - initial-to-final mass relation. *Monthly Notices of the Royal Astronomical Society*, 446(3):2599–2612, January 2015. doi: 10.1093/mnras/stu2180.

Ronald A. Downes and Hilmar W. Duerbeck. Optical Imaging of Nova Shells and the Maximum Magnitude-Rate of Decline Relationship. *The Astronomical Journal*, 120 (4):2007–2037, October 2000. doi: 10.1086/301551.

Jeremy J. Drake, Jan-Uwe Ness, Kim L. Page, G. J. M. Luna, Andrew P. Beardmore, Marina Orio, Julian P. Osborne, Przemek Mróz, Sumner Starrfield, Dipankar P. K. Banerjee, Solen Balman, M. J. Darnley, Y. Bhargava, G. C. Dewangan, and K. P. Singh. The Remarkable Spin-down and Ultrafast Outflows of the Highly Pulsed Supersoft Source of Nova Herculis 2021. *The Astrophysical Journal Letters*, 922(2): L42, December 2021. doi: 10.3847/2041-8213/ac34fd.

Hilmar W. Duerbeck. *Novae: an historical perspective*, page 1–15. Cambridge Astrophysics. Cambridge University Press, 2 edition, 2008. doi: 10.1017/CBO9780511536168.003.

A. Ederoclite, E. Mason, M. Della Valle, R. Gilmozzi, R. E. Williams, L. Germany, I. Saviane, F. Matteucci, B. E. Schaefer, F. Walter, R. J. Rudy, D. Lynch, S. Mazuk,

C. C. Venturini, R. C. Puetter, R. B. Perry, W. Liller, and A. Rotter. Early spectral evolution of Nova Sagittarii 2004 (V5114 Sagittarii). *Astronomy & Astrophysics*, 459 (3):875–883, December 2006. doi: 10.1051/0004-6361:20065741.

A. N. Eskioglŭ. Courbes de lumière de RS Ophiuchi (1958) et de Wz Sagittae (1946). *Annales d'Astrophysique*, 26:331, February 1963.

A. Evans and R. D. Gehrz. Infrared emission from novae. *Bulletin of the Astronomical Society of India*, 40:213, September 2012.

A. Evans, C. M. Callus, J. S. Albinson, P. A. Whitelock, I. S. Glass, B. Carter, and G. Roberts. Infrared observations of the 1985 outburst of RS Ophiuchi. *Monthly Notices of the Royal Astronomical Society*, 234:755–771, October 1988. doi: 10.1093/mnras/234.3.755.

A. Evans, T. Kerr, Bin Yang, Y. Matsuoka, Y. Tsuzuki, M. F. Bode, S. P. S. Eyres, T. R. Geballe, C. E. Woodward, R. D. Gehrz, D. K. Lynch, R. J. Rudy, R. W. Russell, T. J. O'Brien, S. G. Starrfield, R. J. Davis, J. U. Ness, J. Drake, J. P. Osborne, K. L. Page, A. Adamson, G. Schwarz, and J. Krautter. Infrared observations of the 2006 outburst of the recurrent nova RS Ophiuchi: the early phase. *Monthly Notices of the Royal Astronomical Society*, 374(1):L1–L5, January 2007. doi: 10.1111/j.1745-3933.2006.00252.x.

S. P. S. Eyres, T. J. O'Brien, R. Beswick, T. W. B. Muxlow, G. C. Anupama, N. G. Kantharia, M. F. Bode, M. P. Gawroński, R. Feiler, A. Evans, M. T. Rushton, R. J. Davis, T. Prabhu, R. Porcas, and B. J. M. Hassall. Double radio peak and non-thermal collimated ejecta in RS Ophiuchi following the 2006 outburst. *Monthly Notices of the Royal Astronomical Society*, 395(3):1533–1540, May 2009. doi: 10.1111/j.1365-2966.2009.14633.x.

G. J. Ferland and G. A. Shields. Heavy element abundances of Nova Cygni 1975. *The Astrophysical Journal*, 226:172–185, November 1978. doi: 10.1086/156597.

G. J. Ferland, M. Chatzikos, F. Guzmán, M. L. Lykins, P. A. M. van Hoof, R. J. R. Williams, N. P. Abel, N. R. Badnell, F. P. Keenan, R. L. Porter, and P. C. Stancil. The 2017 Release Cloudy. *Revista Mexicana de Astronomía y Astrofísica*, 53:385–438, October 2017.

Gary J. Ferland. Systematic Effects, Unseen Phases, and Uncounted Masses in Nova Ejecta. In S. Howell, E. Kuulkers, and C. Woodward, editors, *Wild Stars in the Old West*, volume 137 of *Astronomical Society of the Pacific Conference Series*, page 165, January 1998.

John D. Fix. *Astronomy : journey to the cosmic frontier*. 2001.

Juhan Frank, Andrew King, and Derek J. Raine. *Accretion Power in Astrophysics: Third Edition*. 2002.

M. Y. Fujimoto. A Theory of Hydrogen Shell Flashes on Accreting White Dwarfs - Part Two - the Stable Shell Burning and the Recurrence Period of Shell Flashes. *The Astrophysical Journal*, 257:767, June 1982. doi: 10.1086/160030.

J. S. Gallagher and S. Starrfield. Theory and observations of classical novae. *Annual Review of Astron and Astrophys*, 16:171–214, January 1978. doi: 10.1146/annurev.aa.16.090178.001131.

Cecilia Helena Payne Gaposchkin. *The Galactic Novae*. 1957.

Robert D. Gehrz. *Infrared studies of classical novae*, page 167–193. Cambridge Astrophysics. Cambridge University Press, 2 edition, 2008. doi: 10.1017/CBO9780511536168.010.

Robert D. Gehrz, James W. Truran, Robert E. Williams, and Sumner Starrfield. Nucleosynthesis in Classical Novae and Its Contribution to the Interstellar Medium. *Publications of the Astronomical Society of the Pacific*, 110(743):3–26, January 1998. doi: 10.1086/316107.

B. P. Gerasimovic. On the classification of novae. *Popular Astronomy*, 44:78, January 1936.

J. H. Gillanders, M. McCann, S. A. Sim, S. J. Smartt, and C. P. Ballance. Constraints on the presence of platinum and gold in the spectra of the kilonova AT2017gfo. *Monthly Notices of the Royal Astronomical Society*, 506(3):3560–3577, September 2021. doi: 10.1093/mnras/stab1861.

N. Grevesse, M. Asplund, A. J. Sauval, and P. Scott. The chemical composition of the Sun. *Astrophysics and Space Science*, 328(1-2):179–183, July 2010. doi: 10.1007/s10509-010-0288-z.

H. E. S. S. Collaboration, F. Aharonian, et al. Time-resolved hadronic particle acceleration in the recurrent nova RS Ophiuchi. *Science*, 376(6588):77–80, April 2022. doi: 10.1126/science.abn0567.

Gesesew R. Habtie and R. Das. He II Emission Line Became the Most Intense Line in the Optical Spectrum of Nova V1405 Cas. *The Astronomer's Telegram*, 16496:1, March 2024a.

Gesesew R. Habtie and Ramkrishna Das. Spectroscopic Insights into the Quiescent Stages of RS Ophiuchi (2006-2021): Photoionization Modeling and Accretion Dynamics. *arXiv e-prints*, art. arXiv:2402.03234, February 2024b. doi: 10.48550/arXiv.2402.03234.

Gesesew R. Habtie, Ramkrishna Das, Ruchi Pandey, N. M. Ashok, and Pavol A. Dubovsky. Correction to: Study of the fastest classical nova, V1674 Her: photoionization and morpho-kinemetic model analysis. *Monthly Notices of the Royal Astronomical Society*, 529(2):917–917, April 2024a. doi: 10.1093/mnras/stae617.

Gesesew R. Habtie, Ramkrishna Das, Ruchi Pandey, N. M. Ashok, and Pavol A. Dubovsky. Study of the fastest classical nova, V1674 Her: photoionization and morpho-kinemetic model analysis. *Monthly Notices of the Royal Astronomical Society*, 527(1):1405–1423, January 2024b. doi: 10.1093/mnras/stad3295.

Izumi Hachisu and Mariko Kato. A Theoretical Light-Curve Model for the 1985 Outburst of RS Ophiuchi. *The Astrophysical Journal Letters*, 536(2):L93–L96, June 2000. doi: 10.1086/312736.

Izumi Hachisu and Mariko Kato. A Prediction Formula of Supersoft X-ray Phase of Classical Novae. *The Astrophysical Journal*, 709(2):680–714, February 2010. doi: 10.1088/0004-637X/709/2/680.

Izumi Hachisu and Mariko Kato. A Light Curve Analysis of Classical Novae: Free-free Emission versus Photospheric Emission. *The Astrophysical Journal*, 798(2):76, January 2015. doi: 10.1088/0004-637X/798/2/76.

Izumi Hachisu and Mariko Kato. Light-curve Analysis of Neon Novae. *The Astrophysical Journal*, 816(1):26, January 2016. doi: 10.3847/0004-637X/816/1/26.

Izumi Hachisu, Mariko Kato, and Gerardo Juan Manuel Luna. Supersoft X-Ray Light Curve of RS Ophiuchi (2006). *The Astrophysical Journal Letters*, 659(2):L153–L156, April 2007. doi: 10.1086/516838.

Margherita Hack, Pierluigi Selvelli, Antonio Bianchini, and Hilmar W. Duerbeck. Typical examples of classical novae. In *NASA Special Publication*, volume 507, pages 413–510. 1993.

T. Hamada and E. E. Salpeter. Models for Zero-Temperature Stars. *The Astrophysical Journal*, 134:683, November 1961. doi: 10.1086/147195.

Thomas E. Harrison, Jillian Bornak, Barbara E. McArthur, and G. Fritz Benedict. Hubble Space Telescope Fine Guidance Sensor Parallaxes for Four Classical Novae. *The Astrophysical Journal*, 767(1):7, April 2013. doi: 10.1088/0004-637X/767/1/7.

E. J. Harvey, M. P. Redman, P. Boumis, S. Akras, K. Fitzgerald, S. Dulaimi, S. C. Williams, M. J. Darnley, M. C. Lam, M. Kopsacheili, and S. Derlopa. Two new nova shells associated with V4362 Sagittarii and DO Aquilae. *Monthly Notices of*

the Royal Astronomical Society, 499(2):2959–2976, December 2020. doi: 10.1093/mnras/staa2896.

Coel Hellier. *Cataclysmic Variable Stars*. 2001.

L. Andrew Helton, Charles E. Woodward, Frederick M. Walter, Karen Vanlandingham, Greg J. Schwarz, Aneurin Evans, Jan-Uwe Ness, Thomas R. Geballe, Robert D. Gehrz, Matthew Greenhouse, Joachim Krautter, William Liller, David K. Lynch, Richard J. Rudy, Steven N. Shore, Sumner Starrfield, and Jim Truran. The Dusty Nova V1065 Centauri (Nova Cen 2007): a Spectroscopic Analysis of Abundances and Dust Properties. *The Astronomical Journal*, 140(5):1347–1369, November 2010. doi: 10.1088/0004-6256/140/5/1347.

M. Hernanz. Classical nova explosions. In J. M. Hameury and J. P. Lasota, editors, *The Astrophysics of Cataclysmic Variables and Related Objects*, volume 330 of *Astronomical Society of the Pacific Conference Series*, page 265, August 2005. doi: 10.48550/arXiv.astro-ph/0412333.

M. Hernanz and J. José. The recurrent nova RS Oph: A possible scenario for type Ia supernovae. *New Astronomy Review*, 52(7-10):386–389, October 2008. doi: 10.1016/j.newar.2008.06.017.

Y. Hillman, D. Prialnik, A. Kovetz, M. M. Shara, and J. D. Neill. Nova multiwavelength light curves: predicting UV precursor flashes and pre-maximum halts. *Monthly Notices of the Royal Astronomical Society*, 437(2):1962–1975, January 2014. doi: 10.1093/mnras/stt2027.

R. M. Hjellming, J. H. van Gorkom, A. R. Taylor, E. R. Sequist, S. Padin, R. J. Davis, and M. F. Bode. Radio Observations of the 1985 Outburst of RS Ophiuchi. *The Astrophysical Journal Letters*, 305:L71, June 1986. doi: 10.1086/184687.

A. J. Holloway, W. Steffen, A. Pedlar, D. J. Axon, J. E. Dyson, J. Meaburn, and C. N. Tadhunter. Kinematics of ionized gas associated with the radio nucleus and lobes in

the active galaxy IRAS 04210+0400. *Monthly Notices of the Royal Astronomical Society*, 279(1):171–179, March 1996. doi: 10.1093/mnras/279.1.171.

K. Horne and T. R. Marsh. Emission line formation in accretion discs. *Monthly Notices of the Royal Astronomical Society*, 218:761–773, February 1986. doi: 10.1093/mnras/218.4.761.

Su-Shu Huang. Profiles of Emission Lines in be Stars. *The Astrophysical Journal*, 171: 549, February 1972. doi: 10.1086/151309.

J. B. Hutchings, J. Smolinski, and J. Grygar. A spectroscopic study of Nova FH Serpentis 1970. *Publications of the Dominion Astrophysical Observatory Victoria*, 14 (2):17–43, January 1972.

Jr. Iben, Icko and Masayuki Y. Fujimoto. The evolution of nova-producing binary starspp 34-76. In Michael F. Bode and Aneurin Evans, editors, *Classical Novae*, volume 43, pages 34–76. 2008. doi: 10.1017/CBO9780511536168.005.

Jr. Iben, Icko and Alexander V. Tutukov. Model Stars with Degenerate Dwarf Cores and Helium-burning Shells: A Stationary-burning Approximation. *The Astrophysical Journal*, 342:430, July 1989. doi: 10.1086/167603.

J. José. Classical nova explosions – hydrodynamics and nucleosynthesis. *Bulletin of the Astronomical Society of India*, 40:443, September 2012.

U. S. Kamath. Observations of quiescent novae. In *Bulletin of the Astronomical Society of India Proceedings*, volume 25 of *Bulletin of the Astronomical Society of India Proceedings*, page 52, January 2008.

N. G. Kantharia, G. C. Anupama, T. P. Prabhu, S. Ramya, M. F. Bode, S. P. S. Eyres, and T. J. O'Brien. Giant Metrewave Radio Telescope Observations of the 2006 Outburst of the Nova RS Ophiuchi: First Detection of Emission at Radio Frequencies <1.4 GHz. *The Astrophysical Journal Letters*, 667(2):L171–L174, October 2007. doi: 10.1086/522201.

Mansi M. Kasliwal, Shri R. Kulkarni, Iair Arcavi, Robert M. Quimby, Eran O. Ofek, Peter Nugent, Janet Jacobsen, Avishay Gal-Yam, Yoav Green, Ofer Yaron, Derek B. Fox, Jacob L. Howell, S. Bradley Cenko, Io Kleiser, Joshua S. Bloom, Adam Miller, Weidong Li, Alexei V. Filippenko, Dan Starr, Dovi Poznanski, Nicholas M. Law, George Helou, Dale A. Frail, James D. Neill, Karl Forster, D. Christopher Martin, Shriharsh P. Tendulkar, Neil Gehrels, Jamie Kennea, Mark Sullivan, Lars Bildsten, Richard Dekany, Gustavo Rahmer, David Hale, Roger Smith, Jeff Zolkower, Viswa Velur, Richard Walters, John Henning, Kahnh Bui, Dan McKenna, and Cullen Blake. PTF 10fqs: A Luminous Red Nova in the Spiral Galaxy Messier 99. *The Astrophysical Journal*, 730(2):134, April 2011. doi: 10.1088/0004-637X/730/2/134.

Mariko Kato and Izumi Hachisu. Optically Thick Winds in Nova Outbursts. *The Astrophysical Journal*, 437:802, December 1994. doi: 10.1086/175041.

Mariko Kato and Izumi Hachisu. Recurrent novae as progenitors of Type Ia supernovae. *Bulletin of the Astronomical Society of India*, 40:393, September 2012. doi: 10.48550/arXiv.1212.2295.

D. Koester and G. Chanmugam. REVIEW: Physics of white dwarf stars. *Reports on Progress in Physics*, 53(7):837–915, July 1990. doi: 10.1088/0034-4885/53/7/001.

Robert P. Kraft. Cataclysmic Variables as Binary Stars. *Advances in Astronomy and Astrophysics*, 2:43–85, January 1963. doi: 10.1016/B978-1-4831-9920-7.50006-4.

Robert P. Kraft. Binary Stars among Cataclysmic Variables. III. Ten Old Novae. *The Astrophysical Journal*, 139:457, February 1964. doi: 10.1086/147776.

Paul Kuin, Sumner Starrfield, Marina Orio, and Kim Page. Swift UVOT photometry and spectra from V1674 Her. *The Astronomer's Telegram*, 14736:1, June 2021.

Henny J. G. L. M. Lamers and Emily M. Levesque. *Understanding Stellar Evolution*. 2017. doi: 10.1088/978-0-7503-1278-3.

J. P. Lasota, G. Dubus, and K. Kruk. Stability of helium accretion discs in ultracompact binaries. *Astronomy & Astrophysics*, 486(2):523–528, August 2008. doi: 10.1051/0004-6361:200809658.

G. R. Lauffer, A. D. Romero, and S. O. Kepler. New full evolutionary sequences of H- and He-atmosphere massive white dwarf stars using MESA. *Monthly Notices of the Royal Astronomical Society*, 480(2):1547–1562, October 2018. doi: 10.1093/mnras/sty1925.

Kwan-Lok Li. Fermi-LAT Detection of TCP J18573095+1653396 (=Nova Her 2021). *The Astronomer's Telegram*, 14705:1, June 2021.

J. D. Linford, V. A. R. M. Ribeiro, L. Chomiuk, T. Nelson, J. L. Sokoloski, M. P. Rupen, K. Mukai, T. J. O'Brien, A. J. Mioduszewski, and J. Weston. The Distance to Nova V959 Mon from VLA Imaging. *The Astrophysical Journal*, 805(2):136, June 2015. doi: 10.1088/0004-637X/805/2/136.

Itai Linial and Re'em Sari. Mass-loss through the L2 Lagrange point - application to main-sequence EMRI. *Monthly Notices of the Royal Astronomical Society*, 469(2):2441–2454, August 2017. doi: 10.1093/mnras/stx1041.

Mario Livio. Classical Novae and the Extragalactic Distance Scale. *The Astrophysical Journal*, 393:516, July 1992. doi: 10.1086/171524.

Mario Livio and James W. Truran. On the Interpretation and Implications of Nova Abundances: an Abundance of Riches or an Overabundance of Enrichments. *The Astrophysical Journal*, 425:797, April 1994. doi: 10.1086/174024.

D. K. Lynch, C. E. Woodward, T. R. Geballe, R. W. Russell, R. J. Rudy, C. C. Venturini, G. J. Schwarz, R. D. Gehrz, N. Smith, J. E. Lyke, S. J. Bus, M. L. Sitko, T. E. Harrison, S. Fisher, S. P. Eyres, A. Evans, S. N. Shore, S. Starrfield, M. F. Bode, M. A. Greenhouse, P. H. Hauschildt, J. W. Truran, R. E. Williams, R. Brad Perry, R. Zamanov, and T. J. O'Brien. Early Infrared Spectral Development of

V1187 Scorpii (Nova Scorpii 2004 No. 2). *The Astrophysical Journal*, 638(2):987–1003, February 2006. doi: 10.1086/498883.

Hiroyuki Maehara, Kenta Taguchi, Yusuke Tampo, Naoto Kojiguchi, and Keisuke Isogai. Spectroscopic classification of PNV J23244760+6111140 as a classical nova. *The Astronomer's Telegram*, 14471:1, March 2021.

K. O. Mason, F. A. Córdova, M. F. Bode, and P. Barr. Intense Soft X-rays from RS Ophiuchi during the 1985 Outburst. In M. F. Bode, editor, *RS Ophiuchi (1985) and the Recurrent Nova Phenomenon*, page 167, January 1987.

Dean B. McLaughlin. The Light Curves of Novae (continued). *Popular Astronomy*, 47: 481, November 1939a.

Dean B. McLaughlin. The Light Curves of Novae (concluded). *Popular Astronomy*, 47: 538, December 1939b.

Dean B. Mclaughlin. The Relation between Light-Curves and Luminosities of Novae. *Publications of the Astronomical Society of the Pacific*, 57(335):69, April 1945. doi: 10.1086/125689.

Dean B. McLaughlin. The Spectra of Novae. In Jesse Leonard Greenstein, editor, *Stellar atmospheres. Edited by Jesse Leonard Greenstein. Supported in part by the National Science Foundation. Published by the University of Chicago Press*, page 585. 1960.

Dean Benjamin McLaughlin. On the spectra of novae. *Publications of Michigan Observatory*, 8(12):149–194, January 1943.

J. Mikołajewska. Symbiotic Stars: Observations Confront Theory. *Baltic Astronomy*, 21:5–12, January 2012. doi: 10.1515/astro-2017-0352.

Joanna Mikołajewska and Michael M. Shara. The Massive CO White Dwarf in the Symbiotic Recurrent Nova RS Ophiuchi. *The Astrophysical Journal*, 847(2):99, October 2017. doi: 10.3847/1538-4357/aa87b6.

Lawrence A. Molnar, Daniel M. Van Noord, Karen Kinemuchi, Jason P. Smolinski, Cara E. Alexander, Evan M. Cook, Byoungchan Jang, Henry A. Kobulnicky, Christopher J. Spedden, and Steven D. Steenwyk. Prediction of a Red Nova Outburst in KIC 9832227. *The Astrophysical Journal*, 840(1):1, May 2017. doi: 10.3847/1538-4357/aa6ba7.

Anindita Mondal, G. C. Anupama, U. S. Kamath, Ramkrishna Das, G. Selvakumar, and Soumen Mondal. Optical spectroscopy of the recurrent nova RS Ophiuchi - from the outburst of 2006 to quiescence. *Monthly Notices of the Royal Astronomical Society*, 474(3):4211–4224, March 2018. doi: 10.1093/mnras/stx2988.

Anindita Mondal, Ramkrishna Das, G. C. Anupama, and Soumen Mondal. Photoionization modelling of quiescence-phase spectra of novae and a symbiotic star. *Monthly Notices of the Royal Astronomical Society*, 492(2):2326–2334, February 2020. doi: 10.1093/mnras/stz3570.

C. Morisset and L. Georgiev. A self-consistent stellar and 3D nebular model of planetary nebula IC 418. *Astronomy & Astrophysics*, 507(3):1517–1530, December 2009. doi: 10.1051/0004-6361/200912413.

P. Mróz, A. Udalski, R. Poleski, I. Soszyński, M. K. Szymański, G. Pietrzyński, Ł. Wyrzykowski, K. Ulaczyk, S. Kozłowski, P. Pietrukowicz, and J. Skowron. OGLE Atlas of Classical Novae. I. Galactic Bulge Objects. *Astrophysical Journal, Supplement*, 219(2):26, August 2015. doi: 10.1088/0067-0049/219/2/26.

U. Munari and P. Valisa. Nova Cas 2021 (=V1405 Cas) is a neon nova. *The Astronomer's Telegram*, 15796:1, December 2022.

U. Munari, A. Siviero, H. Navasardyan, and S. Dallaporta. BVI photometry and the spectroscopy of Nova Scuti 2005 N.2. *Astronomy & Astrophysics*, 452(2):567–569, June 2006. doi: 10.1051/0004-6361:20054720.

U. Munari, V. A. R. M. Ribeiro, M. F. Bode, and T. Saguner. Properties, evolution and morpho-kinematical modelling of the very fast nova V2672 Oph (Nova Oph

2009), a clone of U Sco. *Monthly Notices of the Royal Astronomical Society*, 410(1): 525–534, January 2011. doi: 10.1111/j.1365-2966.2010.17462.x.

U. Munari, P. Valisa, and S. Dallaporta. Large brightness increase of V1405 Cas (Nova Cas 2021) to naked-eye visibility. *The Astronomer's Telegram*, 14614:1, May 2021a.

U. Munari, P. Valisa, and S. Dallaporta. Spectroscopic classification of TCP J18573095+1653396 as a nova bordering naked-eye brightness. *The Astronomer's Telegram*, 14704:1, June 2021b.

Hiroyuki Naito, Akito Tajitsu, Valério A. R. M. Ribeiro, Akira Arai, Hiroyuki Maehara, Shinjirou Kouzuma, Takashi Iijima, Atsuo T. Okazaki, Makoto Watanabe, Seiko Takagi, Fumitake Watanabe, Itsuki Sakon, and Kozo Sadakane. Morpho-kinematic Modeling of the Expanding Ejecta of the Extremely Slow Nova V1280 Scorpii. *The Astrophysical Journal*, 932(1):39, June 2022. doi: 10.3847/1538-4357/ac6c82.

Michael Nauenberg. Analytic Approximations to the Mass-Radius Relation and Energy of Zero-Temperature Stars. *The Astrophysical Journal*, 175:417, July 1972. doi: 10.1086/151568.

A. J. Nayana, G. C. Anupama, Nirupam Roy, Dipankar P. K. Banerjee, Kulinder Pal Singh, L. S. Sonith, and U. S. Kamath. Shock-driven synchrotron radio emission from the 2021 outburst of RS Ophiuchi. *Monthly Notices of the Royal Astronomical Society*, 528(4):5528–5536, March 2024. doi: 10.1093/mnras/stae201.

T. Nelson, K. Mukai, M. Orio, G. J. M. Luna, and J. L. Sokoloski. X-Ray and Ultraviolet Emission from the Recurrent Nova RS Ophiuchi in Quiescence: Signatures of Accretion and Shocked Gas. *The Astrophysical Journal*, 737(1):7, August 2011. doi: 10.1088/0004-637X/737/1/7.

J. P. Ninan, D. K. Ojha, S. K. Ghosh, S. L. A. D'Costa, M. B. Naik, S. S. Poojary, P. R. Sandimani, G. S. Meshram, R. B. Jadhav, S. B. Bhagat, S. M. Gharat, C. B. Bakalkar, T. P. Prabhu, G. C. Anupama, and D. W. Toomey. TIRSPEC: TIFR

Near Infrared Spectrometer and Imager. *Journal of Astronomical Instrumentation*, 3:1450006, November 2014. doi: 10.1142/S2251171714500068.

T. J. O'Brien, M. F. Bode, R. W. Porcas, T. W. B. Muxlow, S. P. S. Eyres, R. J. Beswick, S. T. Garrington, R. J. Davis, and A. Evans. An asymmetric shock wave in the 2006 outburst of the recurrent nova RS Ophiuchi. *Nature*, 442(7100):279–281, July 2006. doi: 10.1038/nature04949.

Y. Osaki. Dwarf nova outbursts: a unification theory. In Emmi Meyer-Hofmeister and Henk Spruit, editors, *Accretion Disks - New Aspects*, volume 487, page 92. 1997. doi: 10.1007/BFb0105824.

J. P. Osborne, K. L. Page, A. P. Beardmore, M. F. Bode, M. R. Goad, T. J. O'Brien, S. Starrfield, T. Rauch, J. U. Ness, J. Krautter, G. Schwarz, D. N. Burrows, N. Gehrels, J. J. Drake, A. Evans, and S. P. S. Eyres. The Supersoft X-ray Phase of Nova RS Ophiuchi 2006. *The Astrophysical Journal*, 727(2):124, February 2011. doi: 10.1088/0004-637X/727/2/124.

Donald E. Osterbrock. *Astrophysics of gaseous nebulae and active galactic nuclei*. (university science books, Sausalito, California)., 1989.

B. Paczyński. Cataclysmic Variables Among Binary Stars. II. Physical Parameters for Novae. *Acta Astronomica*, 15:197, January 1965.

B. Paczynski. A model of accretion disks in close binaries. *The Astrophysical Journal*, 216:822–826, September 1977. doi: 10.1086/155526.

S. Padin, R. J. Davis, and M. F. Bode. RS Ophiuchi - first radio detection of a recurrent nova outburst. *Nature*, 315(6017):306, May 1985. doi: 10.1038/315306a0.

K. L. Page, M. Orio, K. V. Sokolovsky, and N. P. M. Kuin. Swift detection of super-soft X-ray emission from V1674 Her. *The Astronomer's Telegram*, 14747:1, July 2021.

K. L. Page, A. P. Beardmore, J. P. Osborne, U. Munari, J. U. Ness, P. A. Evans, M. F. Bode, M. J. Darnley, J. J. Drake, N. P. M. Kuin, T. J. O'Brien, M. Orio, S. N. Shore,

S. Starrfield, and C. E. Woodward. The 2021 outburst of the recurrent nova RS Ophiuchi observed in X-rays by the Neil Gehrels Swift Observatory: a comparative study. *Monthly Notices of the Royal Astronomical Society*, 514(2):1557–1574, August 2022. doi: 10.1093/mnras/stac1295.

Ruchi Pandey, Ramkrishna Das, Gargi Shaw, and Soumen Mondal. Photoionization Modeling of the Dusty Nova V1280 Scorpii. *The Astrophysical Journal*, 925(2):187, February 2022a. doi: 10.3847/1538-4357/ac36dc.

Ruchi Pandey, Gesesew R. Habtie, Rahul Bandyopadhyay, Ramkrishna Das, François Teyssier, and Joan Guarro Flo. Study of 2021 outburst of the recurrent nova RS Ophiuchi: Photoionization and morpho-kinematic modelling. *Monthly Notices of the Royal Astronomical Society*, July 2022b. doi: 10.1093/mnras/stac2079.

F. Paresce, M. Livio, W. Hack, and K. Korista. The structure and evolution of the Nova V1974 Cygni shell from HST observations. *Astronomy & Astrophysics*, 299: 823, July 1995.

M. Parthasarathy, David Branch, David J. Jeffery, and E. Baron. Progenitors of type Ia supernovae: Binary stars with white dwarf companions. *New Astronomy Review*, 51(5-6):524–538, June 2007. doi: 10.1016/j.newar.2007.03.001.

M. Pavana, Ramya M. Anche, G. C. Anupama, A. N. Ramaprakash, and G. Selvakumar. Optical spectroscopic and polarization properties of 2011 outburst of the recurrent nova T Pyxidis. *Astronomy & Astrophysics*, 622:A126, February 2019. doi: 10.1051/0004-6361/201833728.

M. Pavana, A. Raj, T. Bohlsen, G. C. Anupama, Ranjan Gupta, and G. Selvakumar. Spectroscopic and geometrical evolution of the ejecta of the classical nova ASASSN-18fv. *Monthly Notices of the Royal Astronomical Society*, 495(2):2075–2087, June 2020. doi: 10.1093/mnras/staa1219.

Saul Perlmutter. Supernovae, Dark Energy, and the Accelerating Universe: The Status of the Cosmological Parameters. In J. A. Janos and M. E. Peskin, editors, *Lepton and Photon Interactions at High Energies*, page 715, January 1999.

A. J. Pickles. A Stellar Spectral Flux Library: 1150-25000 Å. *Publications of the Astronomical Society of the Pacific*, 110(749):863–878, July 1998. doi: 10.1086/316197.

S. R. Pottasch. An interpretation of the spectrum of the recurrent nova RS Ophiuchi. *Bulletin Astronomical Institute of the Netherlands*, 19:227, January 1967.

V. A. R. M. Ribeiro, M. F. Bode, M. J. Darnley, D. J. Harman, A. M. Newsam, T. J. O'Brien, J. Bohigas, J. M. Echevarría, H. E. Bond, V. H. Chavushyan, R. Costero, R. Coziol, A. Evans, S. P. S. Eyres, J. León-Tavares, M. G. Richer, G. Tovmassian, S. Starrfield, and S. V. Zharikov. The Expanding Nebular Remnant of the Recurrent Nova RS Ophiuchi (2006). II. Modeling of Combined Hubble Space Telescope Imaging and Ground-based Spectroscopy. *The Astrophysical Journal*, 703(2):1955–1963, October 2009. doi: 10.1088/0004-637X/703/2/1955.

V. A. R. M. Ribeiro, M. J. Darnley, M. F. Bode, U. Munari, D. J. Harman, I. A. Steele, and J. Meaburn. The morphology of the expanding ejecta of V2491 Cygni (2008 N.2). *Monthly Notices of the Royal Astronomical Society*, 412(3):1701–1709, April 2011. doi: 10.1111/j.1365-2966.2010.18006.x.

V. A. R. M. Ribeiro, U. Munari, and P. Valisa. Optical Morphology, Inclination, and Expansion Velocity of the Ejected Shell of Nova Monocerotis 2012. *The Astrophysical Journal*, 768(1):49, May 2013. doi: 10.1088/0004-637X/768/1/49.

Michael W. Richmond, Richard R. Treffers, Alexei V. Filippenko, Young Paik, Bruno Leibundgut, Eric Schulman, and Caroline V. Cox. UBVRI Photometry of SN 1993J in M81: The First 120 Days. *The Astronomical Journal*, 107:1022, March 1994. doi: 10.1086/116915.

Adam G. Riess, Alexei V. Filippenko, Peter Challis, Alejandro Clocchiatti, Alan Diercks, Peter M. Garnavich, Ron L. Gilliland, Craig J. Hogan, Saurabh Jha, Robert P. Kirshner, B. Leibundgut, M. M. Phillips, David Reiss, Brian P. Schmidt, Robert A. Schommer, R. Chris Smith, J. Spyromilio, Christopher Stubbs, Nicholas B. Suntzeff, and John Tonry. Observational Evidence from Supernovae for an Accelerating Universe and a Cosmological Constant. *The Astronomical Journal*, 116(3):1009–1038, September 1998. doi: 10.1086/300499.

K. Rodriguez, K. D. Lee, A. C. Paquette, A. R. Sanders, and J. R. Laura. ISIS Test Data Reduction. In *5th Planetary Data Workshop & Planetary Science Informatics & Analytics*, volume 2549 of *LPI Contributions*, page 7064, June 2021.

Richard J. Rudy, John P. Subasavage, and Jon C. Mauerhan. The Rapid Formation of Coronal Lines in the Nova V1674 Herculis. *Research Notes of the American Astronomical Society*, 5(11):272, November 2021. doi: 10.3847/2515-5172/ac3c4a.

Richard J. Rudy, John P. Subasavage, and Jon C. Mauerhan. The Late-Epoch, Matter-Bounded Spectrum of the Nova V1405 Cassiopeiae. *Research Notes of the American Astronomical Society*, 7(12):277, December 2023. doi: 10.3847/2515-5172/ad1684.

Michael P. Rupen, Amy J. Mioduszewski, and Jennifer L. Sokoloski. An Expanding Shell and Synchrotron Jet in RS Ophiuchi. *The Astrophysical Journal*, 688(1): 559–567, November 2008. doi: 10.1086/525555.

R. Sagar, C. S. Stalin, A. K. Pandey, W. Uddin, V. Mohan, B. B. Sanwal, S. K. Gupta, R. K. S. Yadav, A. K. Durgapal, S. Joshi, Brijesh Kumar, A. C. Gupta, Y. C. Joshi, J. B. Srivastava, U. S. Chaubey, M. Singh, P. Pant, and K. G. Gupta. Evaluation of Devasthal site for optical astronomical observations. *Astronomy & Astrophysics Supplement*, 144:349–362, June 2000. doi: 10.1051/aas:2000213.

E. Santamaría, J. A. Toalá, M. A. Guerrero, G. Ramos-Larios, and L. Sabin. 3D physical structure and angular expansion of the remnant of the recurrent nova T

Pyx. *Monthly Notices of the Royal Astronomical Society*, 530(4):4531–4549, June 2024. doi: 10.1093/mnras/stae1139.

B. E. Schaefer. RS Ophiuchi. *IAU Cirulars*, 8396:2, August 2004.

Bradley E. Schaefer. Comprehensive Photometric Histories of All Known Galactic Recurrent Novae. *Astrophysical Journal, Supplement*, 187(2):275–373, April 2010. doi: 10.1088/0067-0049/187/2/275.

Bradley E. Schaefer. Nova Discovery Efficiency 1890-2014; Only 43%±6% of the Brightest Nova Are Discovered. In *American Astronomical Society Meeting Abstracts #224*, volume 224 of *American Astronomical Society Meeting Abstracts*, page 306.04, June 2014.

Bradley E. Schaefer, Ashley Pagnotta, and Michael M. Shara. The Nova Shell and Evolution of the Recurrent Nova T Pyxidis. *The Astrophysical Journal*, 708(1): 381–402, January 2010. doi: 10.1088/0004-637X/708/1/381.

Evry Schatzman. Remarques sur le phénomène de Nova: IV. L'onde de détonation due à l'isotope ^{3}He. *Annales d'Astrophysique*, 14:294, January 1951.

Evry L. Schatzman. *White dwarfs*. 1958.

Greg J. Schwarz. A New Abundance Analysis of the ONeMg Nova QU Vulpeculae. *The Astrophysical Journal*, 577(2):940–950, October 2002. doi: 10.1086/342234.

Greg J. Schwarz, S. N. Shore, S. Starrfield, Peter H. Hauschildt, M. Della Valle, and E. Baron. Multiwavelength analyses of the extraordinary nova LMC 1991*. *Monthly Notices of the Royal Astronomical Society*, 320(1):103–123, January 2001. doi: 10.1046/j.1365-8711.2001.03960.x.

Greg J. Schwarz, Steven N. Shore, Sumner Starrfield, and Karen M. Vanlandingham. Abundance Analysis of the Extremely Fast ONeMg Novae V838 Herculis and V4160 Sagittarii. *The Astrophysical Journal*, 657(1):453–464, March 2007. doi: 10.1086/510661.

A. W. Shafter. The Galactic Nova Rate Revisited. *The Astrophysical Journal*, 834(2): 196, January 2017. doi: 10.3847/1538-4357/834/2/196.

Allen W. Shafter. The Galactic Nova Rate. In Margarita Hernanz and Jordi José, editors, *Classical Nova Explosions*, volume 637 of *American Institute of Physics Conference Series*, pages 462–471. AIP, November 2002. doi: 10.1063/1.1518246.

S. L. Shapiro and S. A. Teukolsky. Relativistic Stellar Dynamics on the Computer. IV. Collapse of a Star Cluster to a Black Hole. *The Astrophysical Journal*, 307:575, August 1986. doi: 10.1086/164445.

M. M. Shara. A theoretical explanation of the absolute magnitude-decline time /M_{B-t} sub 3/ relationship for classical novae. *The Astrophysical Journal*, 243:926–934, February 1981. doi: 10.1086/158657.

Michael M. Shara. Masses of White Dwarfs in O-Ne-Mg Novae: Observational Constraints, Galactic $\hat{2}6$/Al, $\hat{2}2$/Na gamma-Rays, and M31 Novae. *The Astronomical Journal*, 107:1546, April 1994. doi: 10.1086/116965.

Michael M. Shara, Trisha F. Doyle, Tod R. Lauer, David Zurek, J. D. Neill, Juan P. Madrid, Joanna Mikołajewska, D. L. Welch, and Edward A. Baltz. A Hubble Space Telescope Survey for Novae in M87. I. Light and Color Curves, Spatial Distributions, and the Nova Rate. *Astrophysical Journal, Supplement*, 227(1):1, November 2016. doi: 10.3847/0067-0049/227/1/1.

Michael M. Shara, Dina Prialnik, Yael Hillman, and Attay Kovetz. The Masses and Accretion Rates of White Dwarfs in Classical and Recurrent Novae. *The Astrophysical Journal*, 860(2):110, June 2018. doi: 10.3847/1538-4357/aabfbd.

A. S. Sharov. Estimate for the Frequency of Novae in the Andromeda Nebula and our Galaxy. *Soviet Astronomy* , 16:41, August 1972.

S. N. Shore, C. Buil, P. Dubovsky, P. Berardi, M. Bajer, C. Boussin, J. Guarrò, F. Teyssier, E. Bertrand, J. M. Viannet, D. Boyd, F. Boubault, H. Allen, M. Le

Lain, P. le Dû, P. Cazzato, J. Coffin, K. Shank, E. Bressinck, O. Garde, K. Gurney, and R. Leadbeater. V1405 Cas (= PNV J23244760+6111140) now displaying Fe II emission. *The Astronomer's Telegram*, 14577:1, April 2021a.

S. N. Shore, F. Teyssier, O. Garde, S. Charbonnel, M. Bajer, C. Boussin, and H. Allen. V1405 Cas (= Nova Cas 2021) has entered a recombination phase. *The Astronomer's Telegram*, 14622:1, May 2021b.

Steven N. Shore. *Optical and ultraviolet evolution*, page 194–231. Cambridge Astrophysics. Cambridge University Press, 2 edition, 2008. doi: 10.1017/CBO9780511536168.011.

Steven N. Shore. Spectroscopy of novae – a user's manual. *Bulletin of the Astronomical Society of India*, 40:185, September 2012. doi: 10.48550/arXiv.1211.3176.

Steven N. Shore, George Sonneborn, Sumner Starrfield, Rosario Riestra-Gonzalez, and T. B. Ake. The Early Ultraviolet Spectral Evolution of Nova Cygni 1992. *The Astronomical Journal*, 106:2408, December 1993. doi: 10.1086/116812.

Steven N. Shore, Scott J. Kenyon, Sumner Starrfield, and G. Sonneborn. On the Interpretation of the Ultraviolet Spectra of Symbiotic Stars and Recurrent Novae. II. The 1985 Outburst of RS Ophiuchi. *The Astrophysical Journal*, 456:717, January 1996. doi: 10.1086/176692.

Steven N. Shore, Greg Schwarz, Howard E. Bond, Ronald A. Downes, Sumner Starrfield, A. Evans, Robert D. Gehrz, Peter H. Hauschildt, Joachim Krautter, and Charles E. Woodward. The Early Ultraviolet Evolution of the ONeMg Nova V382 Velorum 1999. *The Astronomical Journal*, 125(3):1507–1518, March 2003. doi: 10.1086/367803.

A. Skopal. Notices to investigation of symbiotic binaries IV. Optical light curves from the near-ultraviolet. *New Astronomy*, 14(3):336–340, April 2009. doi: 10.1016/j.newast.2008.10.002.

M. A. J. Snijders. Multi-frequency observations of the 1985 outburst of RS ophiuchi. *Astrophysics and Space Science*, 130(1-2):243–254, February 1987. doi: 10.1007/BF00655002.

J. L. Sokoloski, Lars Bildsten, and Wynn C. G. Ho. A search for rapid photometric variability in symbiotic binaries. *Monthly Notices of the Royal Astronomical Society*, 326(2):553–577, September 2001. doi: 10.1046/j.1365-8711.2001.04582.x.

J. L. Sokoloski, G. J. M. Luna, K. Mukai, and Scott J. Kenyon. An X-ray-emitting blast wave from the recurrent nova RS Ophiuchi. *Nature*, 442(7100):276–278, July 2006. doi: 10.1038/nature04893.

K. V. Sokolovsky, E. Aydi, L. Chomiuk, A. Kawash, J. Strader, K. Mukai, K. L. Li, A. Babul, J. L. Sokoloski, J. D. Linford, N. Ikonnikova, K. E. Atapin, A. A. Belinski, A. V. Dodin, N. A. Maslennikova, K. A. Postnov, S. A. Potanin, B. S. Safonov, N. I. Shatsky, A. M. Tatarnikov, K. L. Page, and O. V. Maryeva. Early NuSTAR and Swift X-ray detection of Nova Cassiopeiae 2021 = V1405 Cas = PNV J23244760+6111140. *The Astronomer's Telegram*, 14530:1, April 2021a.

Kirill Sokolovsky, Elias Aydi, Laura Chomiuk, Adam Kawash, Jay Strader, Aliya-Nur Babul, Jennifer Sokoloski, Justin Linford, Koji Mukai, and Kwan-Lok Li. VLA radio detection of Galactic novae V1674 Her and V1405 Cas. *The Astronomer's Telegram*, 14731:1, June 2021b.

S. Starrfield. Thermonuclear processes and the classical nova outburst. In *Classical Novae*, pages 39–60, January 1989.

S. Starrfield, J. W. Truran, J. S. Gallagher, W. M. Sparks, P. Strittmatter, and H. M. van Horn. A single-star interpretation of nova Cygni 1975. *The Astrophysical Journal Letters*, 208:L23–L25, August 1976. doi: 10.1086/182224.

S. Starrfield, W. M. Sparks, and J. W. Truran. Hydrodynamic Models for Novae with Ejecta Rich in Oxygen, Neon, and Magnesium. *The Astrophysical Journal Letters*, 303:L5, April 1986. doi: 10.1086/184642.

S. Starrfield, C. Iliadis, and W. R. Hix. The Thermonuclear Runaway and the Classical Nova Outburst. *Publications of the Astronomical Society of the Pacific*, 128(963): 051001, May 2016. doi: 10.1088/1538-3873/128/963/051001.

Sumner Starrfield, Christian Iliadis, and W. Raphael Hix. Thermonuclear processes. In Michael F. Bode and Aneurin Evans, editors, *Classical Novae*, volume 43, pages 77–101. 2008. doi: 10.1017/CBO9780511536168.006.

Sumner Starrfield, Maitrayee Bose, Christian Iliadis, W. Raphael Hix, Charles E. Woodward, and R. Mark Wagner. Hydrodynamic Simulations of Oxygen–Neon Classical Novae as Galactic ^{7}Li Producers and Potential Accretion-induced Collapse Progenitors. *The Astrophysical Journal*, 962(2):191, February 2024. doi: 10.3847/1538-4357/ad1836.

W. Steffen and N. Koning. Hybrid polygon and hydrodynamic nebula modeling with multi-waveband radiation transfer in astrophysics. *Astronomy and Computing*, 20: 87–96, July 2017. doi: 10.1016/j.ascom.2017.06.002.

W. Steffen and J. A. López. Morpho-kinematic modeling of planetary nebulae. In *Revista Mexicana de Astronomia y Astrofisica Conference Series*, volume 26 of *Revista Mexicana de Astronomia y Astrofisica Conference Series*, pages 30–31, June 2006.

Wolfgang Steffen and Nico Koning. Shape: A 3D Modeling Tool for Astrophysics. Astrophysics Source Code Library, record ascl:1204.010, April 2012.

Wolfgang Steffen, Nicholas Koning, Stephan Wenger, Christophe Morisset, and Marcus Magnor. Shape: A 3D Modeling Tool for Astrophysics. *IEEE Transactions on Visualization and Computer Graphics*, 17(4):454–465, April 2011. doi: 10.1109/TVCG.2010.62.

Richard J. Strope, Bradley E. Schaefer, and Arne A. Henden. Catalog of 93 Nova Light Curves: Classification and Properties. *The Astronomical Journal*, 140(1):34–62, July 2010. doi: 10.1088/0004-6256/140/1/34.

Qi-Bin Sun, Sheng-Bang Qian, Li-Ying Zhu, Wen-Ping Liao, Er-Gang Zhao, Fu-Xing Li, Xiang-Dong Shi, and Min-Yu Li. New evidence for the precession of tilted disc in SDSS J081256.85+191157.8. *Monthly Notices of the Royal Astronomical Society*, 526(3):3730–3743, December 2023. doi: 10.1093/mnras/stad1880.

Kenta Taguchi, Hiroyuki Maehara, Keisuke Isogai, Yusuke Tampo, Naoto Kojiguchi, Taichi Kato, and Daisaku Nogami. Spectroscopic Classification of PNV J23244760+6111140 as a classical nova (further reports). *The Astronomer's Telegram*, 14472:1, March 2021a.

Kenta Taguchi, Toshiya Ueta, and Keisuke Isogai. Spectroscopic Follow-up Observation of the 2021 outburst of the recurrent nova RS Ophiuchi. *The Astronomer's Telegram*, 14838:1, August 2021b.

Kenta Taguchi, Keiichi Maeda, Hiroyuki Maehara, Akito Tajitsu, Masayuki Yamanaka, Akira Arai, Keisuke Isogai, Masaaki Shibata, Yusuke Tampo, Naoto Kojiguchi, Daisaku Nogami, and Taichi Kato. Spectra of V1405 Cas at the Very Beginning Indicate a Low-mass ONeMg White Dwarf Progenitor. *The Astrophysical Journal*, 958(2):156, December 2023. doi: 10.3847/1538-4357/ad0133.

Akito Tajitsu, Kozo Sadakane, Hiroyuki Naito, Akira Arai, and Wako Aoki. Explosive lithium production in the classical nova V339 Del (Nova Delphini 2013). *Nature*, 518 (7539):381–384, February 2015. doi: 10.1038/nature14161.

F. Teyssier. Eruptive stars monitoring and the ARAS database. *Contributions of the Astronomical Observatory Skalnate Pleso*, 49(2):217–227, May 2019.

J. W. Truran and M. Livio. On the Frequency of Occurrence of Oxygen-Neon-Magnesium White Dwarfs in Classical Nova Systems. *The Astrophysical Journal*, 308:721, September 1986. doi: 10.1086/164544.

P. Valisa, U. Munari, S. Dallaporta, A. Maitan, and A. Vagnozzi. Atlas of photometric and spectroscopic daily monitoring of the very slow Nova Cas 2021 (=V1405 Cas)

during the first 660 days of its outburst. *arXiv e-prints*, art. arXiv:2302.04656, February 2023. doi: 10.48550/arXiv.2302.04656.

S. Van den Bergh and P. F. Younger. UBV photometry of novae. *Astronomy & Astrophysics Supplement*, 70:125–140, July 1987.

H. Van Winckel, H. W. Duerbeck, and H. E. Schwarz. An atlas of high resolution line profiles of symbiotic stars. I. Coude echelle spectrometry of southern objects and a classification system of H-alpha line profile. *Astronomy & Astrophysics Supplement*, 102:401–433, December 1993.

Justin Vandenbroucke. Nova Herculis 2021 (TCP J18573095+1653396): IceCube neutrino search. *The Astronomer's Telegram*, 14713:1, June 2021.

K. M. Vanlandingham, G. J. Schwarz, S. N. Shore, S. Starrfield, and R. M. Wagner. New Elemental Abundances for V1974 Cygni. *The Astrophysical Journal*, 624(2): 914–922, May 2005. doi: 10.1086/428895.

Karen M. Vanlandingham, Sumner Starrfield, R. Mark Wagner, Steven N. Shore, and George Sonneborn. Optical and ultraviolet spectrophotometry of the ONeMg Nova V838 Herculis 1991. *Monthly Notices of the Royal Astronomical Society*, 282(2): 563–579, September 1996. doi: 10.1093/mnras/282.2.563.

R. M. Wagner, C. E. Woodward, S. Starrfield, D. P. K. Banerjee, and A. Evans. V1674 Her is a Neon Nova. *The Astronomer's Telegram*, 14746:1, July 2021.

A. R. Walker. High-speed photometry of symbiotic stars and recurrent novae. *Monthly Notices of the Royal Astronomical Society*, 179:587–594, June 1977. doi: 10.1093/mnras/179.4.587.

Merle F. Walker. Nova DQ Herculis (1934): an Eclipsing Binary with Very Short Period. *Publications of the Astronomical Society of the Pacific*, 66(392):230, October 1954. doi: 10.1086/126703.

Frederick M. Walter, Andrew Battisti, Sarah E. Towers, Howard E. Bond, and Guy S. Stringfellow. The Stony Brook/SMARTS Atlas of (mostly) Southern Novae. *Publications of the Astronomical Society of the Pacific*, 124(920):1057, October 2012. doi: 10.1086/668404.

Brian Warner. *Cataclysmic Variable Stars*. Cambridge Astrophysics. Cambridge University Press, 1995. doi: 10.1017/CBO9780511586491.

V. Weidemann. Revision of the initial-to-final mass relation. *Astronomy & Astrophysics*, 363:647–656, November 2000.

R. E. Williams, M. Hamuy, M. M. Phillips, S. R. Heathcote, Lisa Wells, and M. Navarrete. The Evolution and Classification of Postoutburst Novae Spectra. *The Astrophysical Journal*, 376:721, August 1991. doi: 10.1086/170319.

Robert Williams. Origin of the "He/N" and "Fe II" Spectral Classes of Novae. *The Astronomical Journal*, 144(4):98, October 2012. doi: 10.1088/0004-6256/144/4/98.

Robert E. Williams. The Formation of Novae Spectra. *The Astronomical Journal*, 104: 725, August 1992. doi: 10.1086/116268.

S. C. Williams, M. F. Bode, M. J. Darnley, A. Evans, V. Zubko, and A. W. Shafter. Rapid Dust Formation in Novae: The Speed Class—Formation Timescale Correlation Explained. *The Astrophysical Journal Letters*, 777(2):L32, November 2013. doi: 10.1088/2041-8205/777/2/L32.

Marcin Wojdyr. *Fityk*: a general-purpose peak fitting program. *Journal of Applied Crystallography*, 43(5 Part 1):1126–1128, Oct 2010. doi: 10.1107/S0021889810030499. URL https://doi.org/10.1107/S0021889810030499.

C. E. Woodward, D. P. K. Banerjee, A. Evans, R. M. Wagner, and S. Starrfield. Near Infrared Coronal Line Emission in nova V1674 Herculis. *The Astronomer's Telegram*, 14741:1, June 2021a.

C. E. Woodward, D. P. K. Banerjee, T. R. Geballe, K. L. Page, S. Starrfield, and R. M. Wagner. Near-infrared Studies of Nova V1674 Herculis: A Shocking Record Breaker. *The Astrophysical Journal Letters*, 922(1):L10, November 2021b. doi: 10.3847/2041-8213/ac3518.

C. E. Woodward, D. P. K. Banerjee, R. M. Wagner, S. Starrfield, and A. Evans. Near Infrared Spectroscopy of V1674 Herculis. *The Astronomer's Telegram*, 14728:1, June 2021c.

C. E. Woodward, A. Evans, D. P. K. Banerjee, S. Starrfield, R. M. Wagner, and R. D. Gehrz. Infrared Spectroscopy of RS Oph on day +12 after the 2021 August Outburst. *The Astronomer's Telegram*, 14866:1, August 2021d.

C. E. Woodward, R. M. Wagner, S. Starrfield, V. Kumar, M. Srivastava, D. P. K. Banerjee, V. Joshi, I. IIyin, K. G. Strassmeier, and A. Evans. Further Optical Spectroscopic Observations of V1674 Herculis. *The Astronomer's Telegram*, 14723:1, June 2021e.

C. E. Woodward, A. Evans, and D. P. K. Banerjee. Late epoch near-infrared spectroscopy of V1405 Cas: The emergence of coronal line emission. *The Astronomer's Telegram*, 15540:1, August 2022a.

C. E. Woodward, R. Mark Wagner, and Sumner Starrfield. V1674 Hercules: It is Blowing out a Wind. *Research Notes of the American Astronomical Society*, 6(6): 124, June 2022b. doi: 10.3847/2515-5172/ac779d.

C. E. Woodward, G. Shaw, S. Starrfield, A. Evans, and K. L. Page. A Photoionization model for the Infrared Coronal Line Emission in the Classical Nova V1716 Scorpii. *arXiv e-prints*, art. arXiv:2404.12227, April 2024. doi: 10.48550/arXiv.2404.12227.

H. L. Worters and M. T. Rushton. Fast Hα emission line variability in RS Ophiuchi. *Monthly Notices of the Royal Astronomical Society*, 442(3):2637–2640, August 2014. doi: 10.1093/mnras/stu1049.

H. L. Worters, S. P. S. Eyres, G. E. Bromage, and J. P. Osborne. Resumption of mass accretion in RS Oph. *Monthly Notices of the Royal Astronomical Society*, 379(4): 1557–1561, August 2007. doi: 10.1111/j.1365-2966.2007.12066.x.

H. L. Worters, S. P. S. Eyres, G. E. Bromage, and J. P. Osborne. Post-Outburst Accretion Resumption in RS Ophiuchi. In A. Evans, M. F. Bode, T. J. O'Brien, and M. J. Darnley, editors, *RS Ophiuchi (2006) and the Recurrent Nova Phenomenon*, volume 401 of *Astronomical Society of the Pacific Conference Series*, page 223, December 2008.

O. Yaron, D. Prialnik, M. M. Shara, and A. Kovetz. An Extended Grid of Nova Models. II. The Parameter Space of Nova Outbursts. *The Astrophysical Journal*, 623(1): 398–410, April 2005. doi: 10.1086/428435.

R. K. Zamanov, K. A. Stoyanov, V. Marchev, M. Minev, D. Marchev, M. Moyseev, J. Marti, M. F. Bode, R. Konstantinova-Antova, and S. Stefanov. Size of the accretion disc in the recurrent nova T CrB. *arXiv e-prints*, art. arXiv:2405.11506, May 2024. doi: 10.48550/arXiv.2405.11506.

Radoslav K. Zamanov. The recurrent nova RS Oph: Flickering and Hα emission variability. *Bulgarian Astronomical Journal*, 17:59, January 2011.

Radoslav K. Zamanov and Albert Bruch. Studies of the flickering in cataclysmic variables. V. The recurrent nova T Coronae Borealis. *Astronomy & Astrophysics*, 338:988–994, October 1998.

P. Zemko, S. Ciroi, M. Orio, A. Odendaal, S. Shugarov, E. Barsukova, A. Bianchini, V. Cracco, M. Gabdeev, V. Goranskij, B. Tofflemire, A. F. Valeev, and N. Katysheva. Optical observations of 'hot' novae returning to quiescence. *Monthly Notices of the Royal Astronomical Society*, 480(4):4489–4504, November 2018. doi: 10.1093/mnras/sty2061.

Jin-Ping Zhu, Shichao Wu, Yuan-Pei Yang, Bing Zhang, He Gao, Yun-Wei Yu, Zhuo Li, Zhoujian Cao, Liang-Duan Liu, Yan Huang, and Xing-Han Zhang. Kilonova

Emission from Black Hole-Neutron Star Mergers. II. Luminosity Function and Implications for Target-of-opportunity Observations of Gravitational-wave Triggers and Blind Searches. *The Astrophysical Journal*, 917(1):24, August 2021. doi: 10.3847/1538-4357/abfe5e.

F. Zwicky. Life-Luminosity Relation for Novae. *Publications of the Astronomical Society of the Pacific*, 48(284):191, August 1936. doi: 10.1086/124698.